Deutsche Geophysikalische Gesellschaft e. V.

Protokoll über das 26. Schmucker-Weidelt-Kolloquium für Elektromagnetische Tiefenforschung

Dassel

21.-25. September 2015

ISSN 2190-7021

herausgegeben von

Marion Miensopust
Leibniz-Institut für
Angewandte Geophysik
Stilleweg 2
30655 Hannover

Michael Becken
WWU Münster
Institut für Geophysik
Corrensstraße 24
48149 Münster

Mit einem Artikel von Volker Haak zum Thema „Johann von Lamont and his magnetotelluric experiments in 1862", vorgetragen auf dem 22nd EM Induction workshop in Weimar, 2014.

Vorwort

Das 26. Schmucker-Weidelt-Kolloquium für Elektromagnetische Tiefenforschung fand vom 21. bis 25. September 2015 im CVJM – Haus Solling in Dassel im südlichen Niedersachsen statt. Das Kolloquium wurde von der Arbeitsgruppe von Andreas Hördt vom Institut für Geophysik und extraterrestrische Physik der TU Braunschweig ausgerichtet.

Um wie gewohnt durch die räumliche Nähe und die kurzen Wege viele Gelegenheiten zum Kennenlernen, für Gespräche und wissenschaftlichen Austausch zu bieten, waren auch dieses Mal alle Teilnehmenden am Tagungsort untergebracht. Der Gemeinschaftsraum und die Kegelbahn boten viel Gelegenheit, um in lockerer und persönlicher Atmosphäre Ideen auszutauschen und Kontakte zu knüpfen und zu pflegen. Darüber hinaus widmeten sich viele Teilnehmende in den Pausen mit großer Begeisterung dem Studium des Flugverhaltens von Wurfscheiben und erprobten dieses auch auf dem Discgolf-Parcour direkt vor dem Tagungsgebäude. Ein großes DANKE an die Braunschweiger für die hervorragende Vorbereitung und Durchführung des Kolloquiums und die gelungene Wahl des Tagungsortes, der mal wieder sowohl dem wissenschaftlichen Teil als auch den gemeinsamen Aktivitäten wunderbar gerecht wurde.

Die traditionelle Wanderung am Mittwochnachmittag führte durch die hügelig-waldigen Ausläufer des Solling nach Hellental. Nach einer Stärkung mit Kaffee und Kuchen im Lönskurg ging es durch den Wald zurück zum Haus Solling, wo der Tag mit einem gemeinsamen Grillabend ausklang.

Das Kolloquium wird von einer sehr aktiven Gemeinschaft getragen. Dieses Mal waren insgesamt 86 Teilnehmende aus 13 Nationen dabei (Deutschland, Tschechien, Finnland, Schweden, Schweiz, Südafrika, USA, Irland, Japan, Polen, Venezuela, Dänemark, Äthiopien). Besonders erfreulich ist, dass ein Drittel (29) der Teilnehmenden Frauen waren. Mit 19 Teilnehmerinnen und Teilnehmern war die Universität zu Köln – mal wieder – am stärksten vertreten. Neben der Universität zu Köln waren 5 weitere deutsche Universitäten (Braunschweig, Frankfurt a.M., Freiberg, Göttingen, Münster) sowie BGR, GEOMAR, GFZ und LIAG repräsentiert. Mit den ausländische Instituten sowie den Firmen und Beratern kommt man auf insgesamt 24 beteiligte Institutionen.

Das Tagungsprogramm umfasste 30 Vorträge und 44 Poster, die auf Deutsch oder Englisch präsentiert wurden. Auch dieses Mal gab es vor jeder Postersession 1- bis 2-minütige mündliche Kurzvorstellungen der Poster durch die Autoren. Die Kurzpräsentationen wurden durch das Organisationsteam technisch gut vorbereitet und haben somit die Poster für die folgenden 1,5-2 Stunden in den Fokus der Aufmerksamkeit gerückt.

Der vorliegende Kolloquiumsband umfasst 32 Beiträge. Zum ersten Mal finden sich in diesem Band neben den bisher üblichen extended Abstracts (10) auch jeweils noch eine Sammlung von Vortragsfolien (6) und Postern (16). Diese Flexibilität in den Beitragsformaten scheint ein gelungener Versuch zu sein, die bei der letzten Ausgabe drastisch zurückgegangene Zahl der Beiträge wieder auf das urspüngliche Niveau anzuheben (17 in 2013, 38 in 2011, 32 in 2009, 38 in 2007, 41 in 2005, 36 in 2003). Wir freuen uns sehr, dass wir nun wieder die Vielfalt der vorgestellten Arbeiten im gewohnten Umfang in den „blauen Bänden“ dokumentieren und dem wissenschaftlichen Austausch zur Verfügung stellen können. Wir danken allen Teilnehmern, die sich die Mühe gemacht haben, mit ihren extended Abstracts, Folien und Postern dazu beizutragen.

Zusätzlich zu den Beiträgen, die auf dem Kolloquium vorgestellt wurden, haben wir in diesen „blauen Band“ auch einen Artikel von Volker Haak aufnehmen können, der sich mit den frühen magnetotellurischen Arbeiten von Johann von Lamont beschäftigt. Volker Haak’s Artikel basiert auf einem Vortrag, den er auf dem 22nd EM Induction workshop 2014 in Weimar gehalten und den er nun mit viel Mühe schriftlich aufgearbeitet hat.

Bei Herrn Bertelmann von der Bibliothek des GFZ Potsdam bedanken wir uns für die professionelle Unterstützung und die Gewährleistung der Online-Verfügbarkeit unseres Kolloquiumsbandes und bei Tobias Lindau für die HTML-Programmierung der Webseite dieses Bandes.

Marion Miensopust und Michael Becken
Hannover und Münster, im Mai 2016

Inhaltsverzeichnis

Extended Abstracts

Influence of steel infrastructure on transient electromagnetic fields

Matthias Bär, Jana Börner, Ralph-Uwe Börner, and Klaus Spitzer

TU Freiberg, Institut für Geophysik und Geoinformatik

1 Summary

Geophysical measurements for monitoring the processes of CO_2-sequestration or enhanced oil recovery usually take place on active or abandoned oil respectively gas fields. Considering the amount of steel infrastructure in the subsurface of these investigation sites it is crucial to take account of the effect of steel infrastructre on electromagnetic fields. Therefore we present three-dimensional finite element (FE) simulations of transient electromagnetic fields in the present of steel infrastructure. As a first approach we consider two common scenarios. The first scenario covers the case of surface transient electromagnetic measurements with a crossing pipeline beneath a receiver profile. The second scenario covers borehole transient electromagnetic measurements in a partially steel cased borehole. We demonstrate that steel infrastructure has a significant effect on the electromagnetic response.

2 Introduction

A large-scale borehole transient electromagnetic (TEM) field campaign is planned at a pilot CO_2-sequestration site in Alberta, Canada. The target area, however, contains an extensive steel infrastructure consisting of three oil pipelines (partially intersecting) as well as two full cased injection wells of 500 m (see Fig. 1 Injection well 1) and 300 m (see Fig. 1 Injection well 2) depth. Setting up a transmitter loop without having steel infrastructure beneath it, is almost impossible due to the limitations of the test site and the required survey layout. The test site has the dimension of 1000×1000 m^2. Therefore it is necessary to investigate the influence of various steel constructions (pipelines, steel casing) on TEM data. We present three-dimensional finite element (FE) simulations of transient electromagnetic fields for several receiver locations (M-4 to M4) considering steel infrastructure in the subsurface.

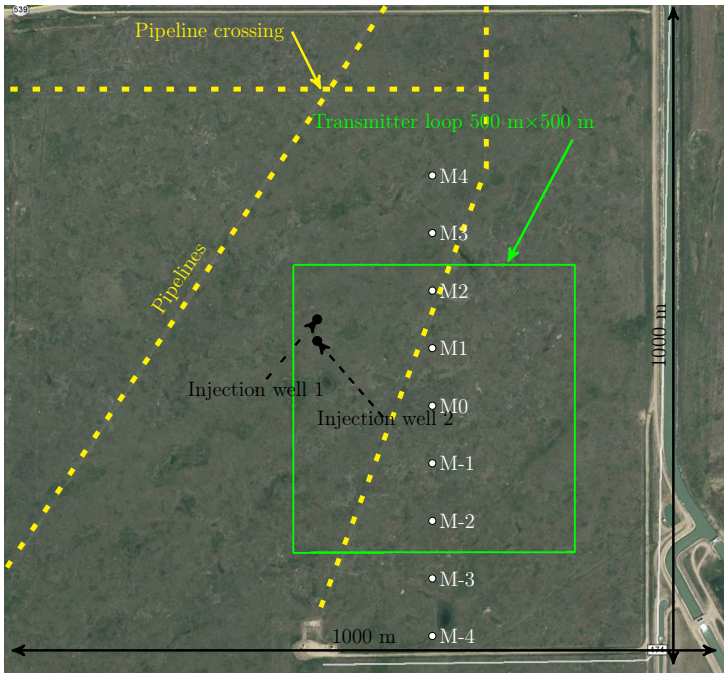

Figure 1: Plan view of the CO_2-sequestration site Brooks, Alberta(CA)

3 Model domain and parameters

The first model covers the case of a pipeline beneath the source crossing a receiver profil. As a first approximation the pipeline is a solid cylinder with a diameter of 2 m and an installation depth of 6 m. It strikes from south west to north east (Fig. 2). The model consists of a 5 km × 5 km × 2.5 km air halfspace and a 5 km×5 km×2.5 km subsurface. The transmitter is a square loop with a side length of 500 m centered at the point (0, 0, 0). The finite element grid employed for the numerical simulation consists of 2 306 479 tetrahedra (Fig. 3).

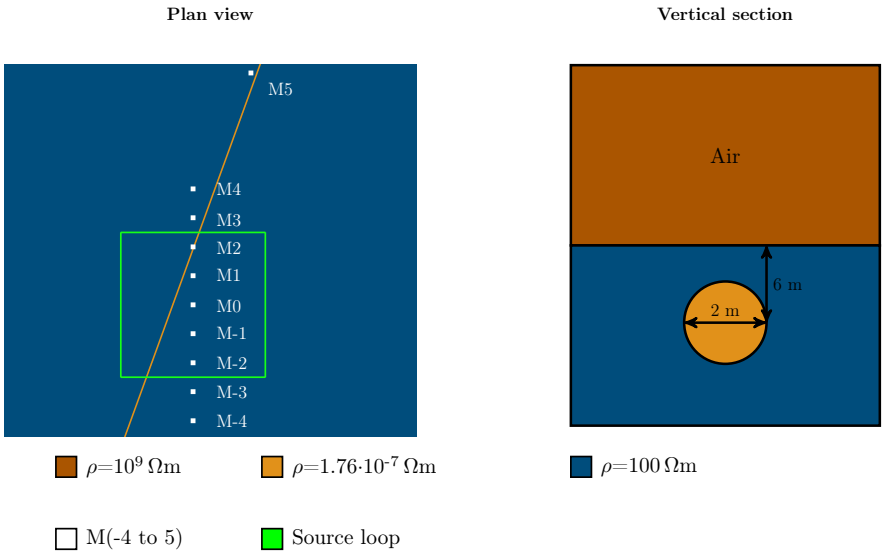

Figure 2: Parameter model of a pipeline crossing beneath the transmitter loop.

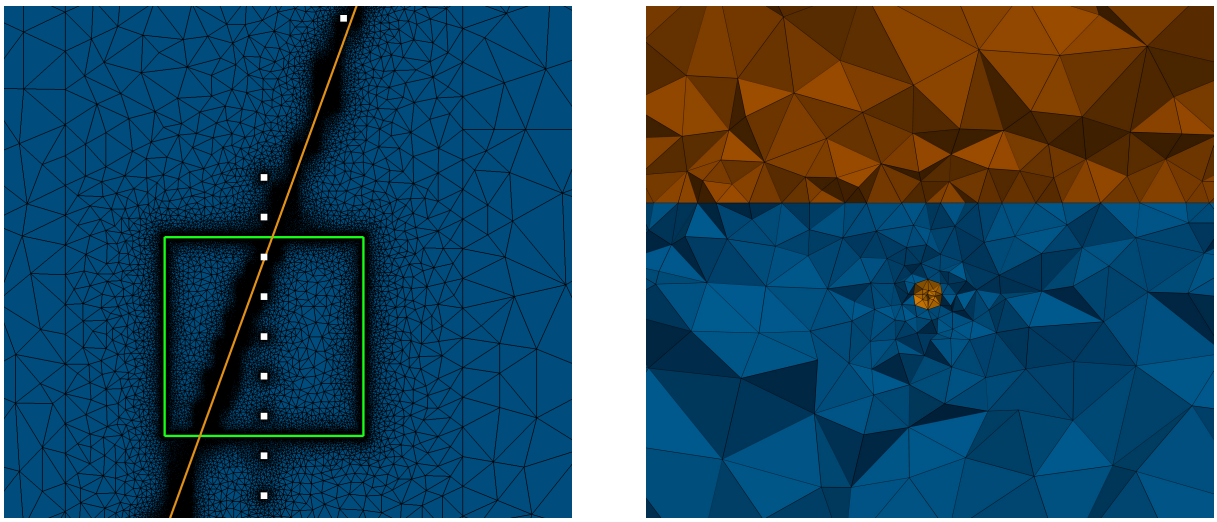

Figure 3: Pipeline model: Trace of the tetrahedral mesh at the plane z = 0 (left) and vertical section of the FE mesh along the plane x = 0.

The second model covers the case of a steel cased borehole. The model consists of a 2 km × 2 km ×1 km air halfspace and a 2 km × 2 km × 1 km subsurface in which a 200 m deep borehole with a diameter of 1 m is embedded. The casing of the borehole is 50 m long with a casing width of 10 cm (see Fig.4). The borehole is located at (x=200 m y=0 m z=0 m). The transmitter is a square loop with a side length of 100 m centered at the point (0, 0, 0). The finite element grid employed for the numerical simulation consists of 1 934 820 tetrahedra (Fig. 5).

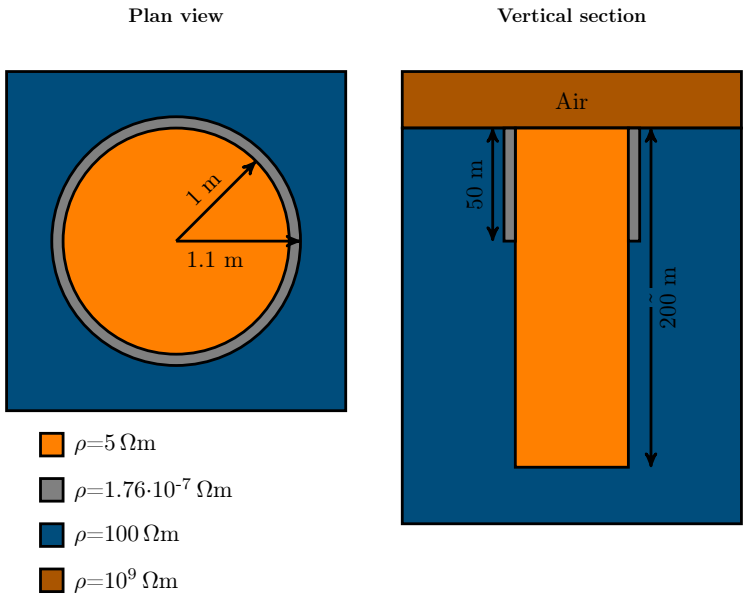

Figure 4: Model scheme and parameters for the cased borehole model

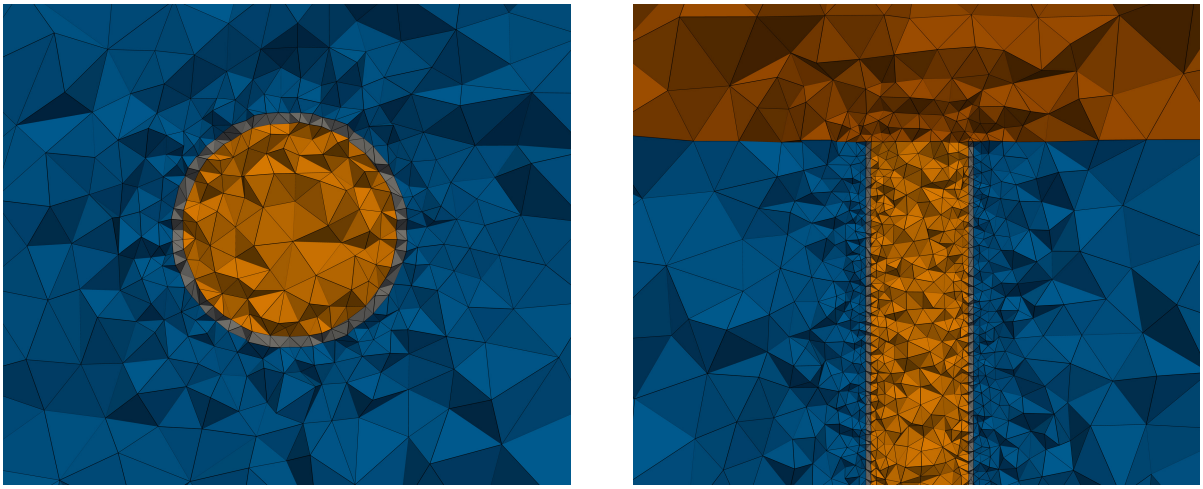

Figure 5: Cased borehole model: Trace of the tetrahedral mesh at the plane z = 0 (left) and vertical section of the FE mesh along the plane x = 0.

4 Simulation results

To solve the 3-D forward modelling problem we employ an approximation to the matrix exponential function using a Rational Arnoldi method (Börner, Ernst, and Güttel 2015). The mesh for scenario 1 consists of 2 306 479 tetrahedral elements which after discretizaton using linear Nedelec elements results in 2 696 577 degrees of freedom. Figure 6 shows the results of the simulation at the points M0, M-1, M1, M-3, M-4 (see Fig. 2). The black line denotes the analytical solution for a 100 Ωm homogeneous halfspace in the center of a circular loop with radius 282 m. The red line represents the numerical solution of the model with homogeneous conductivity distribution. The numerical solution of the actual conductivity model (Fig. 2) is represented by the blue line.
The mesh for scenario 2 consists of 1 934 820 tetrahedral elements which after discretizaton using linear Nedelec elements results in 2 271 984 degrees of freedom. Figure 7 shows the results of the simulation for different points inside the borehole (A - at surface, B - within, C - just below casing, D and E - far away). The black line denotes the analytical solution for a 100 Ωm homogeneous halfspace and a vertical magnetic dipole source. The red line represents the numerical solution of the model with homogeneous conductivity distribution. The numerical solution of the actual conductivity model (Fig. 4) is represented by the blue line.

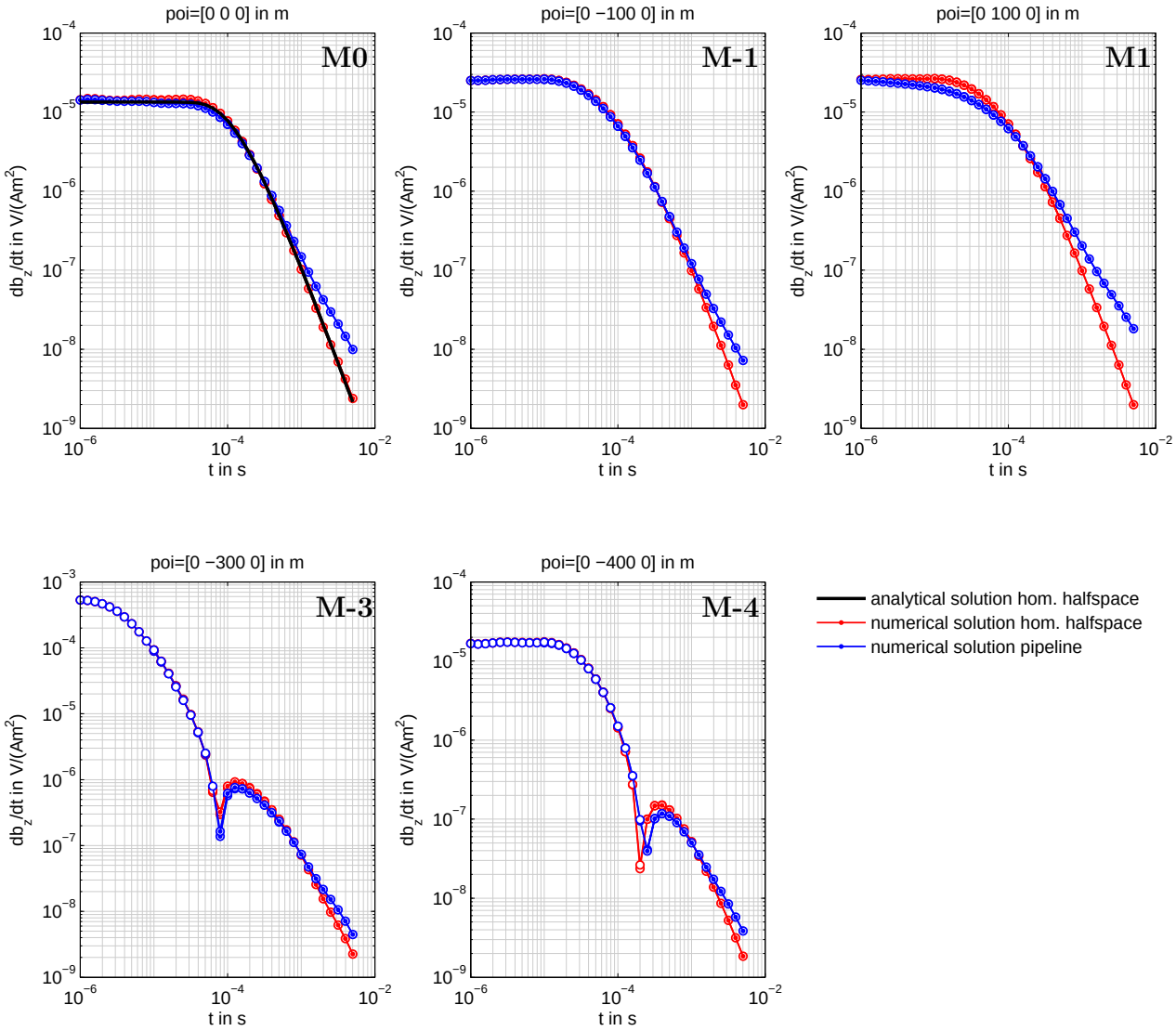

Figure 6: Simulation results for the pipeline model

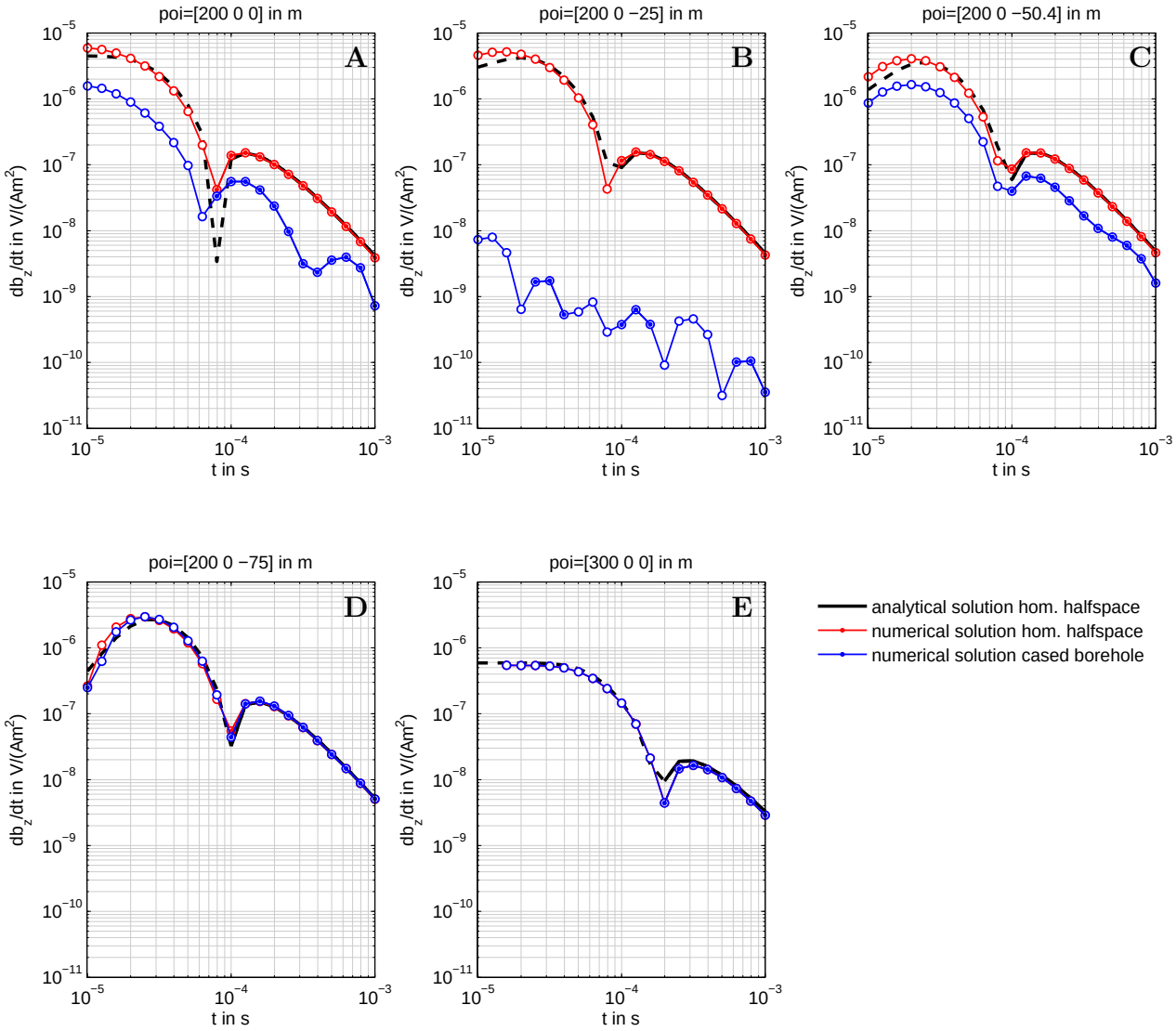

Figure 7: Simulation results for the cased borehole model

5 Conclusion

We have carried out three-dimensional transient electromagnetic finite element simulations for various steel constructions in the subsurface. Our computations demonstrate that steel infrastructure may shield, shift and/or distort the TEM response given the discretisation errors from the large conductivity contrasts are still moderate. However, a quantitative statement is not possible at this point. This is subject to intensive studies of the numerical error using e.g., a posteriori error estimators, appropiate boundary conditions for perfect conductors, and sequences of increasing conductivity contrasts. Mesh refinement close to large conductivity contrasts is crucial. The mismatch between the numerical solution for the homogeneous halfspace (red line) and the analytical solution for the homogeneous halfspace (black line) in the early times for scenario 2 (Fig. 7) indicates that further efforts have to be made with respect to the mesh size and quality.

References

Börner, Ralph-Uwe, Oliver G Ernst, and Stefan Güttel (2015). "Three-dimensional transient electromagnetic modelling using Rational Krylov methods". In: *Geophysical Journal International* 202.3, pp. 2025–2043.

Electrical phenomena during CO_2 sequestration – a pore scale view

Jana H. Börner[1], Volker Herdegen[1], Jens-Uwe Repke[1,2], Klaus Spitzer[1]

[1] Technical University Bergakademie Freiberg
[2] now at Technical University Berlin

Summary

The electrical rock conductivity is a sensitive indicator for CO_2 migration processes. CO_2 dissolves into the pore water in large amounts and provides additional charge carriers due to the dissociation of carbonic acid.

We present laboratory measurements of the spectral complex electrical conductivity of water-bearing sand samples during exposure to and flow-through by carbon dioxide. Pressures up to 300 bar and temperatures up to 80°C were applied. Steady-state experiments serve for investigating the physicochemical equilibrium of the fluid phases. Dynamic experiments aim at analyzing the impact of partial saturation and chemical interaction on complex conductivity.

The steady-state dissolution experiments show that besides the conductivity-increasing dissociation a second opposing process may be observed which results in a significant reduction of conductivity at high salinities despite the added CO_2. We explain our observations with a semi-analytical formulation for the electrical conductivity taking into account the interactions of ion and neutral species.

A significant reduction of saturation is observed during CO_2 flow and drainage. The spectral complex conductivity maps both changes in saturation and chemical interaction.

1 Introduction

The presence of the reactive gas carbon dioxide (CO_2) in pore space gives rise to a network of physical and chemical processes [Börner et al., 2013], which all act on the complex electrical rock conductivity σ^*

$$\sigma^* = \sigma' + i\sigma'' \quad . \tag{1}$$

We carried out static dissolution experiments to tackle pore water conductivity σ_w and dynamic flow-through experiments with quartz sand to investigate the three-phase system.

We summarize the processes involved from a pore scale perspective. Furthermore, our laboratory observations, data and results regarding the real part of conductivity σ', the imaginary part of conductivity σ'' and the pore water conductivity σ_w are presented.

2 Effect of CO_2 on rock conductivity

2.1 Partial saturation

CO_2 is forced into the pore space of the storage formation. A connected flowing phase forms due to the pressure gradient. When no pressure gradient is applied, the non-wetting CO_2 forms bubbles in the pore centers. Character and efficiency of the phase replacement depend on pressure, temperature, CO_2 mass flow and pore space characteristics [Sarmadivaleh et al., 2015, Börner et al., 2016].

During flow chemical interaction between gas and pore water take place. Also, water dissolves in the CO_2. This may lead to drying out of connate interface water.

During injection, CO_2 partially replaces the pore water of the storage formation and consequently reduces rock conductivity σ^* according to [Archie, 1942, Vinegar and Waxman, 1984]:

$$\sigma' = S_{\mathrm{w}}^{n}\Phi^{m}\sigma_{\mathrm{w}} + S_{\mathrm{w}}^{k}\sigma'_{\mathrm{if}} \tag{2}$$

$$\sigma'' = S_{\mathrm{w}}^{k}\sigma''_{\mathrm{if}} \tag{3}$$

where S_{w} denotes water saturation, Φ is porosity, m is the cementation exponent, n and k are the real and imaginary part saturation exponent, respectively, and σ'_{if} and σ''_{if} denote the real and imaginary part, respectively, of interface conductivity at full saturation.

Due to its reactive nature the presence of CO_2 affects not only the saturation S_{w} but also pore water conductivity, pH and the grain–water interface. The main task of electromagnetic monitoring techniques is to correctly reconstruct $S_{\mathrm{CO2}} = 1 - S_{\mathrm{w}}$ from conductivity measurements.

2.2 Dissolution and dissociation

CO_2 is highly soluble in water. The amount of carbon dioxide, which is dissolved in a pore water with known sodium chloride (NaCl) content at thermodynamic equilibrium ($CO_{2(aq)}$), is a function of pressure p, temperature T and salinity c_{NaCl} [e.g. Duan et al., 2006]:

$$c_{\mathrm{CO2}} = f(p, T, c_{\mathrm{NaCl}}) \ . \tag{4}$$

The dissolved CO_2 forms uncharged aqueous complexes. A small portion of the $CO_{2(aq)}$ forms carbonic acid (H_2CO_3), which is unstable. The carbonic acid dissociates into protons, hydrocarbonate and carbonate ions:

$$\mathrm{CO_{2(aq)} + H_2O} \overset{K_1}{\rightleftharpoons} \mathrm{H^+ + HCO_3^-} \tag{5}$$

$$\mathrm{HCO_3^-} \overset{K_2}{\rightleftharpoons} \mathrm{H^+ + CO_3^{2-}} \tag{6}$$

These ions occur in addition to the self dissociation of water and anions and cations of dissociated salts. Consequently, they act on the pore water conductivity σ_{w}. As a result of the dissociation the pH decreases as well. The formation and dissociation of carbonic acid under pressure results in a significantly reduced pH of the CO_2-rich pore water (computed with PHREEQC: ~3.0).

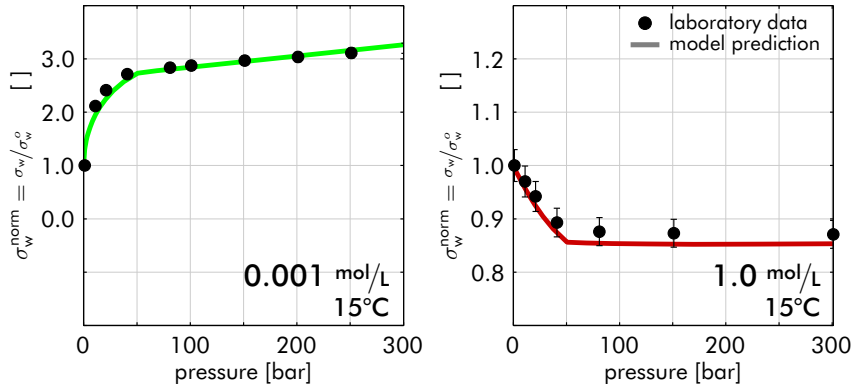

Fig. 1: Change in electrolyte conductivity due to CO_2 dissolution and dissociation at 0.001 M NaCl (left) and 1 M NaCl (right).

2.3 Inner surface area variation

The complex interface conductivity in clean sands is caused by the electrical double layer, which forms at the contact of the quartz grains and the conductive pore water.

Interface conductivity depends on salinity, grain roughness (i.e. inner surface area) and pH. It depends less strongly on water saturation than the electrolytic conductivity. A decrease in pH causes a decrease in σ'' [Skold et al., 2011]. Furthermore, the low-pH environment due to CO_2 dissolution and dissociation may trigger changes of the rock matrix [Wigand et al., 2008], which would result in an increased inner surface area, and consequently affects the imaginary part of conductivity σ'' in multiplie ways [Börner et al., 2016].

3 Results

Static dissolution experiments were carried out in order to investigate the impact of CO_2 on pore water conductivity [for experimental details see Börner et al., 2015a]. For salinities below 0.6 g/l we observe an increase in pore water conductivity σ_w with pressure (*'low salinity regime'*, Fig. 1, left). This is expected, since the additional ions from dissociation contribute to σ_w. For solutions with $c_{NaCl} \geq 5.8$ g/l we observe an unexpected behavior. No conductivity increase occurs (*'high salinity regime'*, Fig. 1, right). Instead, σ_w decreases by up to 15% [Börner et al., 2015a]. This behaviour is due to a decrease in ion mobility, which dominates the electrolyte conductivity at high salinities despite the added charge carriers.

The effect of CO_2 dissolution and dissociation on pore water conductivity σ_w may be predicted for all salinities based on physicochemical properties by the following model [Börner et al., 2015a]:

$$\sigma_w^{norm}(p, T, c_{NaCl}) = \frac{\sigma_w}{\sigma_w^o} = \frac{1}{\sigma_w^o} \sum_{i=1}^{2} [\Lambda_i \gamma_i \alpha_i c_i] \quad . \tag{7}$$

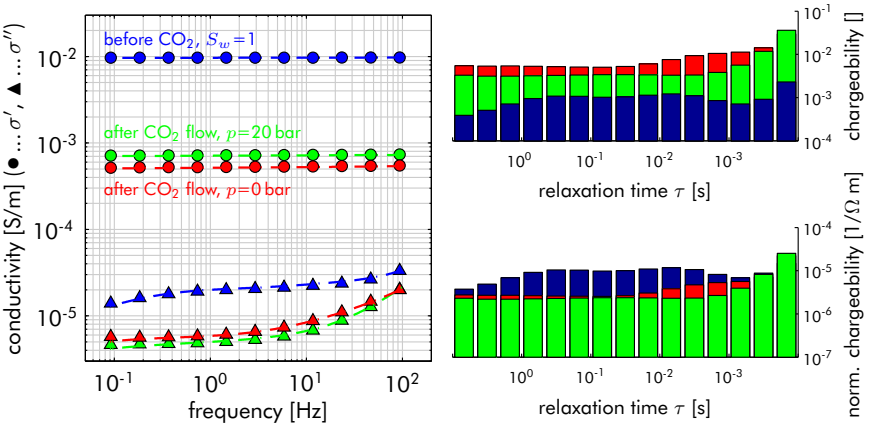

Fig. 2: Conductivity spectra (left) and according Debye decomposition (right) of a flow through experiment with CO_2 at 20 bar and 15°C.

Here, σ_w denotes the electrolyte conductivity with CO_2, σ_w^o is the initial electrolyte conductivity. Λ denotes molar conductivity, γ is the activity coefficient, α is the degree of dissociation and c is concentration. The activity coefficients γ_i of NaCl and dissociated CO_2 are described by:

$$\ln(\gamma_{NaCl}) = \ln(\gamma^o_{NaCl}) - g_{12}c_{CO2} - h_{12}c^2_{CO2} \tag{8}$$

$$\ln(\gamma_{CO2}) = \ln(\gamma^o_{CO2}) - g_{21}c_{NaCl} - h_{21}c^2_{NaCl} \quad . \tag{9}$$

The parameters g_{ij}, h_{ij} and Λ_{CO2} are determined by a least squares inversion. A purely empirical formulation is also available (with empirical parameters q_i; for parameter values and details see Börner et al. [2015a]):

$$\sigma_w^{norm}(p, T, c_{NaCl}) = 1 + \frac{q_1 + q_2T + q_3p}{c_{NaCl}} \left(1 - e^{-(q_4+q_5T)p}\right) - (q_6 + q_7T)\left(1 - e^{-q_8p}\right) \quad . \tag{10}$$

When interpreting measurements of complex rock conductivity σ^* in terms of saturation the reactive nature of CO_2 has to be considered. CO_2 flow, the resulting partial saturation, dissolution/dissociation and pH act on the spectral complex conductivity of a sand sample. σ' and σ'' react differently (Fig. 2, left; 20 bar, 15°C, 0.2 g/l NaCl).

The impact of chemical interaction on the three-phase system of CO_2–electrolyte–sand may be deduced from the flow experiments (for experimental details see Börner et al. [2016]). As expected, the surfaces of the quartz sand used for our experiments are not affected by the CO_2 or the low pH of the pore water under pressure (see secondary electron micrographs in Fig. 3). Changes in the imaginary part of conductivity σ'' may be related to chemical effects, therefore. This does not hold for reactive rock matrices.

Chemical interaction may be quantified by comparing the complex conductivity under pressure to the complex conductivity after depressurization at the end of the flow experiments. During pressure release saturation remains the same and CO_2 degasses. Nevertheless, σ' and σ'' change [Börner et al., 2016]. For all pressures and temperatures, σ' reflects the salinity regime predicted by our model (Eqs 7 – 10). At the same time σ'' increases stably due to the change in pH from acidic back to near neutral during degassing. It is known that a lowering of the pH-value causes a reduction of the imaginary part of conductivity σ''. This effect is also

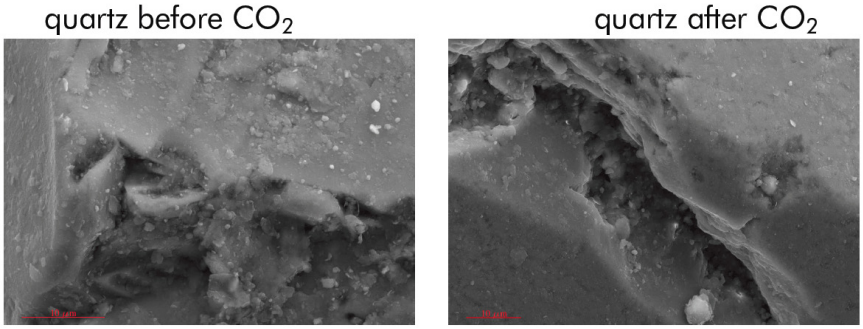

Fig. 3: Secondary electron micrographs of the sample material before (left) and after (right) exposure to CO_2 (courtesy of Dr. Franziska Wilke, GFZ Potsdam).

detectable for the CO_2–electrolyte–sand system. Taking into account the chemical interaction allows for reliably reconstruction the sample saturation from electrical measurements. A Debye decomposition approach might help to separate physical and chemical effects (Fig. 2, right).

4 Conclusions

The electrical rock conductivity is a sensitive indicator for CO_2 migration processes and interactions between the phases of the system CO_2 - pore water - sand. Our experimental results reveal the complicated network of processes, which occur simultaneously, and influence the electrical rock conductivity in multiple ways.

The dominating effect is the reduction of pore water saturation due to the injection of CO_2. This is the basis for electromagnetic monitoring techniques [Börner et al., 2015b]. For the correct calculation of pore contents the chemical interaction between the reactive CO_2 and the pore water have to be taken into account.

The dissociation of carbonic acid adds charge carriers to the pore water. Depending on salinity either the additional conductivity contribution causes an increased pore water conductivity or the mutual impeding of all species results in a decrease in pore water conductivity. We provide a model to predict these effects.

In our study the imaginary part of conductivity is dominated by the chemical interaction processes. It reflects the change in pH caused by the formation of carbonic acid. Measuring the SIP response bears the potential to better differentiate between saturation and chemical effects. This may improve the saturation reconstruction.

Literatur

G. E. Archie. The electrical resistivity log as an aid in determining some reservoir characteristics. *Transactions of the American Institute of Mining, Metallurgical and Petroleum Engineers*, 146(146):54–62, 1942.

J. H. Börner, V. Herdegen, J.-U. Repke, and K. Spitzer. The impact of CO_2 on the electrical properties of water bearing porous media - laboratory experiments with respect to carbon capture and storage. *Geophysical Prospecting*, 61:446–460, 2013.

J. H. Börner, V. Herdegen, J.-U. Repke, and K. Spitzer. The electrical conductivity of CO_2–bearing pore waters at elevated pressure and temperature: a laboratory study and its impli-

cations in CO_2 storage monitoring and leakage detection. *Geophysical Journal International*, 203:1072–1084, 2015a.

J. H. Börner, F. Wang, J. Weißflog, M. Bär, I. Görz, and K. Spitzer. Multi-method virtual electromagnetic experiments for developing suitable monitoring designs: A fictitious CO_2 sequestration scenario in Northern Germany. *Geophysical Prospecting*, 63:1430–1449, 2015b.

J. H. Börner, V. Herdegen, J.-U. Repke, and K. Spitzer. Spectral induced polarization of the three-phase system CO_2–brine–sand under reservoir conditions. *Geophysical Journal International*, under review, 2016.

Z. Duan, R. Sun, C. Zhu, and I. Chou. An improved model for the calculation of CO_2 solubility in aqueous solutions containing Na^+, K^+, Ca^{2+}, Mg^{2+}, Cl^- and SO_4^{2-}. *Marine Chemistry*, 98:131–139, 2006.

M. Sarmadivaleh, A. Al-Yaseri, and S. Iglauer. Influence of temperature and pressure on quartz-water-CO_2 contact angle and CO_2-water interfacial tension. *Journal of Colloid and Interface Science*, 441:59–64, 2015.

M. Skold, A. Revil, and P. Vaudelet. The pH dependence of spectral induced polarization of silica sands: Experiment and modeling. *Geophysical Research Letters*, 38, 2011. L12304.

H. J. Vinegar and M. H. Waxman. Induced polarization of shaly sands. *Geophysics*, 49(8): 1267–1287, 1984.

M. Wigand, J.W. Carey, H. Schütt, E. Spangenberg, and J. Erzinger. Geochemical effects of CO_2 sequestration in sandstones under simulated in situ conditions of deep saline aquifers. *Applied Geochemistry*, 23:2735–2745, 2008.

Waiting for the Storm – Geomagnetic Activity and its Influence on Magnetotelluric Transfer Functions

M. Cembrowski[1], A. Junge[1], P. Hering[1], E. Vilamajo [2]
[1] Institute of Geosciences, Geophysics, Goethe University Frankfurt am Main, Germany
[2] Departament de Geodinàmica i Geofísica, Universitat de Barcelona, Spain

Introduction

The Magnetotelluric (MT) method uses time variations of the Earth's magnetic field which induce electrical currents in the conductive Earth [Simpson and Bahr, 2005; Chave and Jones, 2012; Viljanen, 2012]. By means of the relation between the resulting horizontal magnetic and electric fields one can estimate the conductivity as a function of spatial position. Electromagnetic fluctuations with periods higher than 1 s are caused by the interaction of the solar wind and the Earth's magnetosphere and ionosphere. The fluctuations depend on variations in density, velocity and magnetic field intensity of the solar wind, whereupon the largest geomagnetic field variations occur during so called magnetic storms. Hereby an enhanced ring current is formed by ions and electrons located between 3–8 R_E.
Variations of the magnetic fields caused by the dynamic variations of space plasma are defined as signal, whereas the fluctuations originated from artificial sources are termed as electromagnetic noise, since often they are undesired signals violating the plane wave assumption. Quiet geomagnetic periods are characterized by a low signal level which can lead to the degradation of response quality due to the increased uncertainty on spectral estimates.
By means of MT data recorded during a field work in the Central Pyrenees we show how a time period of geomagnetic activity influences the horizontal magnetic fields and can dramatically improve the quality of impedances.

Field course

In the course of the field work in the Central Pyrenees in May and June 2015 an approximately 120 km North-South profile was set up consisting of 12 long period MT stations. The data generally show a low signal-to-noise ratio which results in impedances of low quality. Exemplarily we show the data of station MT6 that was located above the axial zone of the orogen and recorded the magnetic and electric field components for almost 16 days. During the first 13 days the horizontal magnetic field variations show a regular pattern characterized by the diurnal changes (*Sq*) of the total magnetic field (Fig. 1). On the 14th and 15th day the horizontal field variations show some disturbances. The amplitude of the North component initially increases, followed by an abrupt decrease and a recovery phase. The East component does not exhibit variations as strong as in the North component, yet a general increase of activity can be observed. This behavior of the magnetic variations shows the typical features of a magnetic storm and we therefore examine the geomagnetic activity that was recorded for this period of time.

Dst Index

Gonzalez et al. (1994) characterize a geomagnetic storm by an interval of time of intense and long-lasting interplanetary convection. Through a substantial energization in the magnetosphere-ionosphere system an intensified ring current then can cause the Earth magnetic field exceed some key threshold which is quantified by the storm time *Dst* index.

For the derivation of the *Dst* index magnetometer stations near the equator are used (Hermanus, Kakioka, Honolulu, San Juan) with sufficient distance from the auroral and equatorial electrojets. For these locations, after the removal of the regular daily variation, the north component of the magnetic field variation is dominated by the ring current. The *Dst* is presented as the hourly average of this perturbation. Values of the *Dst* index less than -100 nT are referred to as an intense storm, a *Dst* between -50 nT and -100 nT indicates a moderate storm, and weak storms are those between -30nT and -50nT. Undisturbed time intervals are represented by a value of 0, whereas the mean *Dst* is between -20 nT and -10 nT. The reason for the negative values is the enhanced magnetic ring current field being opposed to the Earth's magnetic field.

Figure 2 shows the real-time *Dst* index during the recording time of station MT6. Note that the real-time *Dst* index is a preliminary value giving a momentary overview of the ring current's intensity. For the first 13 days of the recording the indices feature values higher than -20 nT indicating a period of low ring current activity. At day 14 the *Dst* index reaches values below -50 nT revealing the occurrence of a moderate magnetic storm. This pattern is very similar to that of the North component of the magnetic field observed in the Pyrenees.

K_p Index

In contrast to the *Dst* index illustrating the activity of the ring current, the K_p index represents the overall geomagnetic activity. It is deduced from the 3-hour range *K* Index that was proposed by Bartels et al. (1939) and it is a measure of the magnetic variability at individual observing stations. In the same contribution Bartels et al. (1939) additionally suggested to use the K indices from a network of stations to obtain a planetary index of geomagnetic activity. The K_p Index was finally introduced by Bartels (1949) and is the mean standardized *K* Index from 13 geomagnetic observatories. It is expressed in third of a unit and ranges from 0 to 9 with values of 0-1 characterizing periods of quiet geomagnetic activity, 2-4 moderate activity, and 5-9 indicating disturbances.
The K_p Index during the recording of station 6 is illustrated in Figure 3 and shows the time period of increased activity during the last days with the K_p value >5 marking the start time of the magnetic storm. For the first 13 days of recording the index shows the low geomagnetic activity.

On the basis of the *Dst* and the K_p Indices we divide the magnetic time series into a part of low geomagnetic activity (Fig. 1 - green box) and a part of increased geomagnetic activity (Fig. 1 – red box).

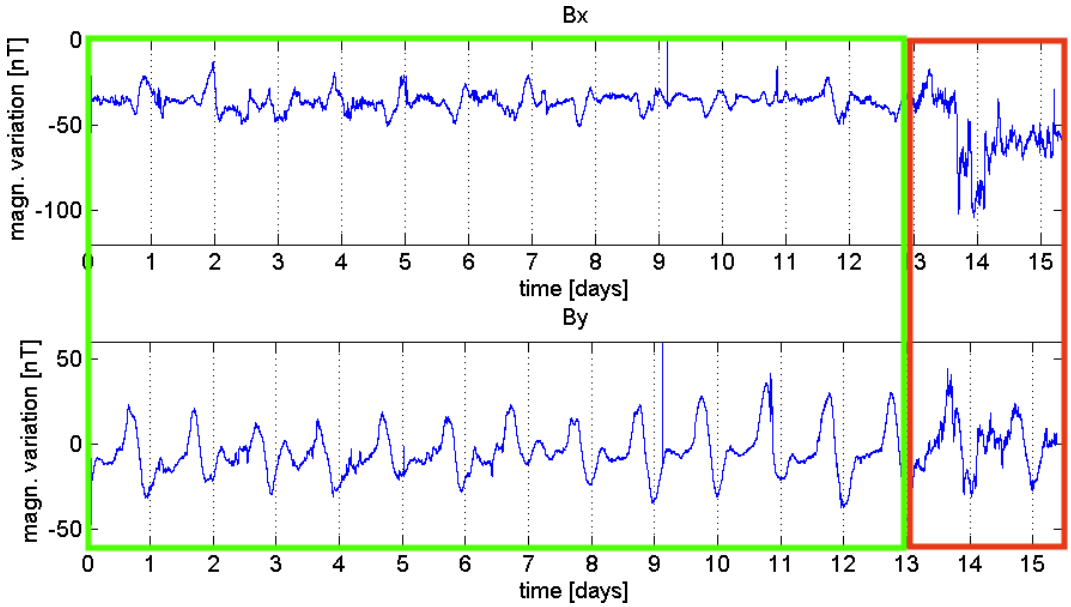

Fig. 1: Horizontal magnetic field variations at station 6. Start time of station: 2015/05/25, 14:00:00. The green box indicates a period of low geomagnetic activity. The red box marks a period of high geomagnetic activity.

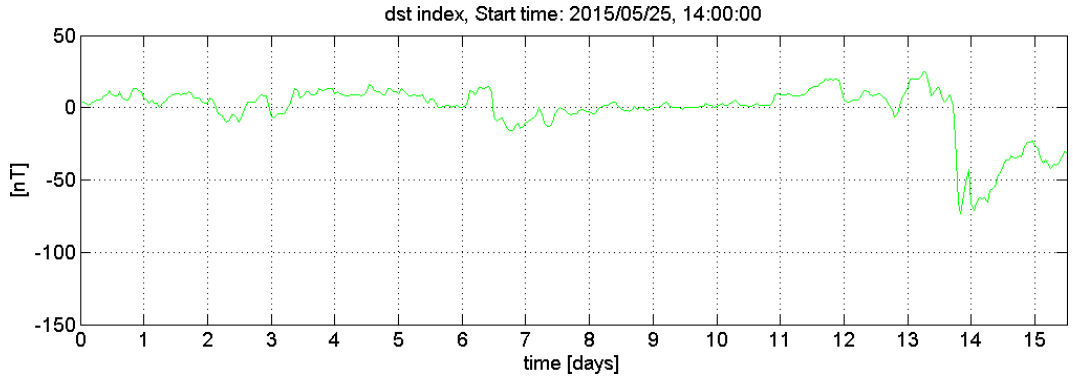

Fig. 2: Real-time *Dst* index during recording of station 6 (25th of May 2015 to 10th of June 2015). Data source: World Data Center for Geomagnetism, Kyoto (http://wdc.kugi.kyoto-u.ac.jp/dst_realtime/201505/index.html).

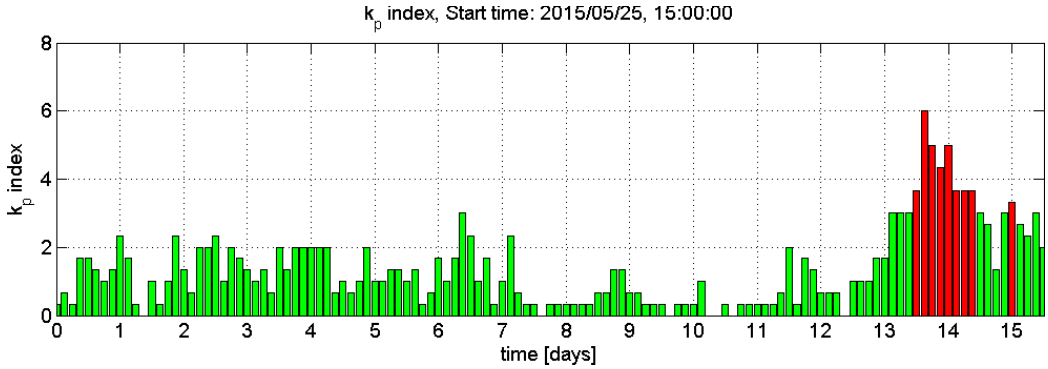

Fig. 3: *Kp* Index during recording of MT6. An index of >5 indicates a geomagnetic storm. Red bars mark K_p Indices >3. Data source: Deutsches GeoForschungsZentrum, Potsdam (ftp://ftp.gfz-potsdam.de/pub/home/obs/kp-ap/tab/).

Power spectra

In the following we process the time series separately with respect to low and high magnetic activity.

Figure 4 shows the power spectra for the magnetic (left) and the electric field variations (right). The different components are illustrated in grey with their mean values plotted in blue (section with low activity) and red (section with increased activity). Both spectra were calculated for a representative time section of 40 h, respectively. The magnetic field spectra are significantly enhanced for the active period with dominating North component due to the East-West orientated ring current.

The spectra for the electric field variations are very similar (Fig. 4 right) with the East component of the electric field variations for the increased activity section dominating, which corresponds to the enhanced magnetic north component. The power spectra reveal that the increased geomagnetic activity strongly affects the power spectra of the magnetic fields, but for the electric fields only a small influence is visible. A possible reason is that the electric field variations are mainly dominated by noise.

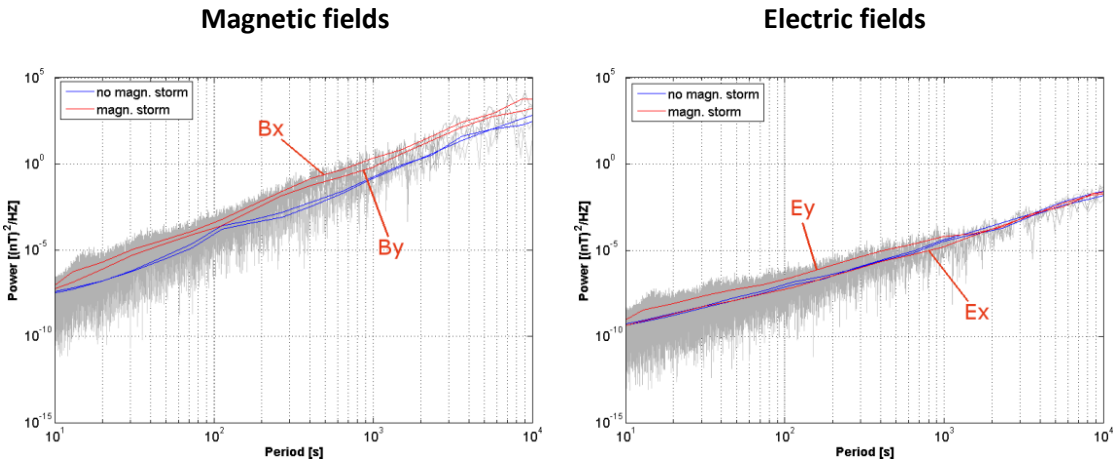

Fig. 4: Power spectra from a time segment of 40 h from the period of low (blue) resp. high (red) geomagnetic activity. The power spectra are shown for the horizontal magnetic and electric field variations.

Partial Coherency

The coherency is a measure of the linear correlation between two time series and takes values between 0 (no correlation) and 1 (perfect correlation). The coherency can be interpreted as a measure of the noise level of the time series. The partial coherency, that is used to classify time intervals, illustrates the correlation between an input (magnetic) field and an output (electric) field under the consideration of the second input field. It is calculated from the time intervals' univariate and bivariate coherencies.

Figure 5 shows the partial coherencies between E_x and B_y (red) as well as between E_y and B_x (blue) for a period of 10 s. The time series was divided up into time windows of 1000 samples each and partial coherencies were calculated for every time interval. The partial coherencies

correlate with the observed *Kp* Indices with both showing two distinct peaks during the period of high geomagnetic activity, possibly revealing a magnetic substorm at day 15. The part of low geomagnetic activity (green box) is characterized by partial coherencies taking values mostly below 0.2 and indicating a low signal-to-noise ratio. Here the time series, particularly the electric field variations (as seen in Figure 4), are dominated by noise. For the period of high activity the partial coherencies exhibit values significantly higher than for the low activity period with the yx-component dominating and confirming the dominating power spectra for the east component of the electric field.

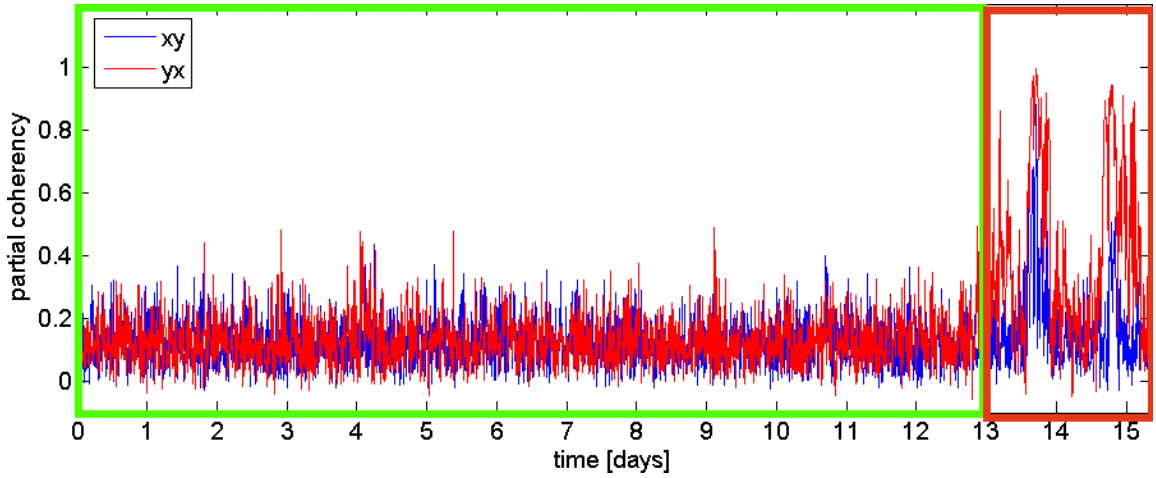

Fig. 5: Partial coherency for a period of 10 s. The time series was divided up into time windows of 1000 samples each and partial coherencies were calculated. Red: E_x, B_y. Blue: E_y, B_x. The green and red box mark the periods of low and high geomagnetic activity, respectively.

Transfer Function

When determining the transfer functions the partial coherencies serve as a criterion for the selection of time windows that are included in the calculation [Löwer, 2014]. Dependent on the target frequency the time series are divided into a specific number of time windows for which, after being transformed into the frequency domain, transfer functions are calculated, respectively. The final transfer function is calculated from the individual transfer functions with a median estimator and by setting limits for a minimum partial coherency only time windows with a high partial coherency are included into the calculations. This way the impedances can be estimated from the horizontal magnetic and electric fields and apparent resistivities and phases can be determined.

Figure 6 shows the transfer functions for the low (left) and high (right) geomagnetic activity for station 6. Even though the low activity period comprises 13 days contrary to about 2.5 days of measurement for the active period, transfer functions for the active period are of higher quality with smoother curves and smaller errors. Particularly the yx component is of better

quality, since, as already discussed above, the ring current mainly produces strong variations in the B_x and the E_y components.

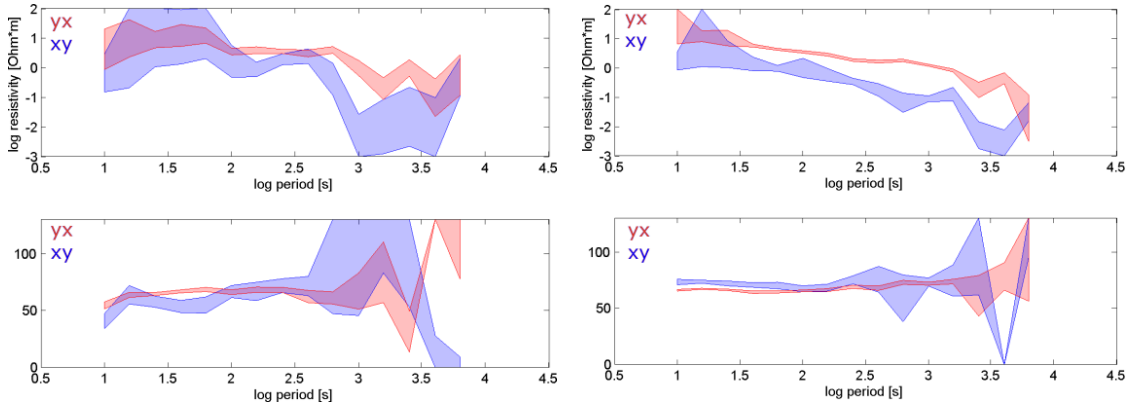

Fig. 6: Transfer functions for low (left) and high (right) geomagnetic activity.

Conclusions

A field work was conducted in the Central Pyrenees at which several long period magnetotelluric stations were set up. By examining the measured magnetic field variations it can be observed that the time series are mainly characterized by a regular pattern including the diurnal changes of the total magnetic field. Only towards the end of the campaign some disturbances are present. The geomagnetic activity represented by the *Dst* and the K_p indices confirm the observations and reveal the occurrence of a moderate geomagnetic storm originated from an intensified ring current. The high geomagnetic activity results in an enhancement of the magnetic power spectra, particularly for the magnetic north component, since the enhanced magnetic ring current field is opposed to the Earth's magnetic field. Moreover involves the high activity an increase in partial coherencies between the observed magnetic and electric fields, as the signal-to-noise ratios are enhanced. The resulting transfer functions for the 2.5 days period of high geomagnetic activity therefore feature a higher quality than for the 13 days of low activity.

References

- Bartels, J., Heck, N. A., & Johnston, H. F. (1939), The three-hour-range index measuring geomagnetic activity. Terrestrial Magnetism and Atmospheric Electricity, 44(4), 411-454.
- Bartels J. (1949), The standardized index, Ks, and the planetary index, Kp, IATME Bull. 12b, p. 97, Int. Union of Geod. and Geophys., Paris.
- Chave, A. D., Jones, A. G. (2012), Chapter 1: Introduction to the magnetotelluric method, in The Magnetotelluric Method - Theory and Practice, Editoren: A. D. Chave und A. G. Jones, Cambridge University Press, S. 1-18.
- Gonzalez, W. D., Joselyn, J. A., Kamide, Y., Kroehl, H. W., Rostoker, G., Tsurutani, B. T., & Vasyliunas, V. M. (1994), What is a geomagnetic storm?, Journal of Geophysical Research: Space Physics, 99(A4), 5771-5792.

- Löwer, A. (2014), Magnetotellurische Erkundung geologischer Großstrukturen des südwestlichen Vogelsberges mit anisotroper, dreidimensionaler Modellierung der Leitfähigkeitsstrukturen, Dissertation, Goethe-Universität Frankfurt am Main.
- Simpson, F., Bahr, K. (2005), Practical Magnetotellurics, Cambridge University Press.
- Viljanen, A. (2012), Chapter 3B: Description of the magnetospheric/ionospheric sources, in The Magnetotelluric Method - Theory and Practice, Editoren: A. D. Chave und A. G. Jones, Cambridge University Press, S. 1-18.

Determining upper mantle electrical conductivity from solar quiet (Sq) variations

Martina Guzavina[1], Michael Becken[2], Alexey Kuvshinov[1], Stephan Koch, Christoph Püthe

1. ETH Zürich, Institute of Geophysics, Zürich, Switzerland
2. Westfälische Wilhelms-Universität Münster, Institute of Geophysics, Münster, Germany

Extended abstract

The interactions of the solar radiation with the internal magnetic field of the Earth produce a current system in the ionosphere at the altitude between 90 and 130 km, called solar quiet (Sq). The Sq current system has a double vortex structure, with an anticlockwise direction of rotation in the Northern and clockwise in the Southern hemisphere. Observed from outside the Earth, the Sq vortexes are bound to the side of the Earth where the Sun is currently shining at. The double vortex structure of the Sq current system in the clearest form develops on magnetically quiet days and the most reliable source description is achieved during geomagnetically truly quiet days. In order to pick such days, we rely on the '*aa*' geomagnetic activity index, which measures variations of the geomagnetic field intensity over the course of a three-hour interval in nT with respect to a Greenwich day. Because Sq current system is characterized by its strong daily variability, only single day magnetic recordings can be analyzed at a time. The period of geomagnetic field variations caused by the Sq source ranges between 3 and 24 hours, therefore using Sq as an induction source can provide information about the electrical conductivity distribution within the range of approximately 100 - 600 km depth and thus constrain the physical conditions and in particular the water content within the upper mantle.

We implement Schmucker's (1999a) parametrization of this complex source in spherical harmonics. The parametrization utilizes a superposition of six time-harmonics '*p*' with periods of 24 h, 12 h, 8 h, 6 h, 4.8 h and 4 h, where each time-harmonic is assigned with an individual subset of 11 to 12 spherical harmonic (SH) functions. Here, p=1 corresponds to T=24h, p=2 to T=12h etc. Schmucker's scheme yields total of 71 SH terms for a complete source description. The main part of Sq source is governed by the so-called dominant terms, which describe variations occurring at the speed of the Sun. There is one such term for each time-harmonic, defined as time-harmonic '*p*' equal to SH order '*m*' with SH degree '*n*' equal to m+1. Exemplary, the dominant term of the first time-harmonic p=1 is pnm=121.

A common way of estimating the Sq source is the potential method by Gauss (1839). Within this method the measured geomagnetic fields are expressed in terms of the magnetic potential, which can be separated into parts of external (inducing) and internal (induced) origin described by external and internal coefficients respectively. The accuracy of the separation and of the estimated coefficients strongly depends on a dense observatory distribution around the world, which is not provided in the oceans and in the Southern hemisphere. Therefore, only low-order SH coefficients are estimated accurately. However, in order to describe the spatial details of the 3-D ocean effect (an effect observed in the recordings from coast-close stations due to large conductivity contrasts between the continents and the oceans), high-order SH coefficients are required.

Source estimates can be substantially improved by taking into account additional (a priori) information. A method, which makes use of such a priori information has been introduced by Koch and Kuvshinov (2013) for the Sq source. Unlike the potential method, S3D approach estimates the source coefficients by expressing the measured magnetic fields as a product of a priori computed responses of the Earth to unitary sources. A priori assumptions on the Earth include a thin uppermost layer of 2-D conductance and a 1-D conductivity model underneath.

We perform a global estimation of the Sq source field using S3D method. Our data set consists of geomagnetic field recordings from ground-based geomagnetic observatories active between 2000 and 2010 and we exclude observatories outside ± 6° and ± 60° geomagnetic latitude range to prevent disturbances from polar and equatorial jets. Afterwards, we estimate novel transfer functions originally introduced by Püthe et al. (2015), which relate the individual source coefficients and the local vertical geomagnetic fields.

Our transfer functions correspond to inductive responses of the Earth and relate local daily vertical magnetic fields from geomagnetic observatories and the global daily Sq source coefficients for a specified time-harmonic. The amount of the obtained transfer functions is equivalent to spherical harmonic terms used per time-harmonic. To acquire between 11 or 12 unknowns at a time, the transfer functions were estimated in a multivariate regression for many single day recordings. The obtained estimates are local and independent of the source structure of specific day.

We determine stable transfer function estimates for the first three time-harmonics for all geomagnetic observatories, but should treat higher time-harmonic estimates with more caution. Because we cannot obtain a stable solution for the highest time-harmonics and therefore the smallest periods of the source, most likely we cannot accurately determine the conductivity distribution in the uppermost part of the Sq sensitivity range. Some of our transfer function estimates show a latitudinal trend expressed by descending transfer function values towards lower geomagnetic latitudes. We are able to remove the trend by restricting data to the geomagnetic latitude range between ± 6° and ± 45°, thus minimizing an influence from the polar electrojet. Remarkably, our estimates remain stable despite a sparser observatory coverage. Furthermore, we establish an interdependence between the a priori 1-D conductivity model used and the obtained transfer function values.

Our 1-D deterministic inversion for mantle conductivity yields local 1-D conductivity models comparable to global Schmucker's (1999b) model, which, as in this work, was obtained from observatory data for the Sq source, but with a different type of inductive responses. The changes in the inversion models caused by different starting models happen almost completely outside the Sq sensitivity range. The amount of terms however has a more notable effect on the inversion results, since the inversion models not only shift towards more conductive or more resistive values, but the kinks in the model shift in depth as well. Though for stations with good data fit these changes are modest although present.

In the future work we intend to invert for conductivity at coast-close stations. So far we have inverted starting from a homogeneous half-space, however for coast-close stations this leads to false results. Instead, a layer at fixed depth and of fixed conductivity which represents the ocean should be implemented into the starting model. This type of inversion is referred to as quasi 1-D inversion. Furthermore, we could repeat the inversion for transfer functions estimated from the source within the ± 6° and ± 45° geomagnetic latitude range. Also, we plan to invert probabilistically, so that instead of a single model a whole range of possible models which explain the data would be estimated.

Literature:

Gauss, C. F. (1839). Allgemeine Theorie des Erdmagnetismus. Resultate aus den Beobachtungen des magnetischen Verein imJahre 1838.

Koch, S. and Kuvshinov, A. (2013). Global 3-D EM inversion of Sq variations based on simultaneous source and conductivity determination: concept validation and resolution studies. *Geophysical Journal International*, 195: 98-116.

Püthe, C., Kuvshinov, A., and Olsen, N. (2015). Handling complex source structures in global EM induction studies: from C-responses to new arrays of transfer functions. *Geophysical Journal International*, 201(1): 318-328.

Schmucker, U. (1999a). A spherical harmonic analysis of solar daily variations in the years 1964-1965: response estimates and source fields for global induction – I. methods. *Geophysical Journal International*, 136(2): 439-454.

Schmucker, U. (1999b). A spherical harmonic analysis of solar daily variations in the years 1964-1965: response estimates and source fields for global induction - II. results. *Geophysical Journal International*, 136(2): 455-476.

Multivariate processing of magnetotelluric data – comparison and interpretation of measurement results from the Westerwald (Germany)

Philip Hering[1], Andreas Junge[1], Nynne Lauritsen[2], Annika Löwer[1]

(1) Institute of Geosciences, Applied Geophysics, Goethe University Frankfurt am Main, Germany
(2) DTU Space, Technical University of Denmark, Denmark

Summary

During the processing of magnetotelluric (MT) data, frequency-dependent, complex transfer functions between magnetic (B) and electric (E) fields are calculated. The transfer functions provide information about the conductivity of the subsurface and thus are of crucial importance. In some cases the data processing proves to be difficult, since the recorded time series can be heavily contaminated by anthropogenic noise signals, e. g. galvanic currents or near field sources. Several methods, like robust or remote reference processing, address these problems, however in case of coherent noise sources they might fail (*Junge, 1996*). Therefore a new multivariate processing scheme based on an eigenvalue decomposition method (*Egbert, 1997*) was developed within an AMT study in the Westerwald, Germany (*Hering, 2015*). The results are presented for frequencies between 10 Hz and 5 kHz. The choice of the noise model is crucial for noise being coherent between different channels at a local site but incoherent to that at remote sites. For an unfavorable signal-to-noise ratio, however, the results of the eigenvalue analysis might be misleading, e. g. if the two dominant eigenvalues are taken as an indication for homogeneous source fields. Furthermore the magnetic and electric field polarizations from the Westerwald data set were analyzed. The results show distinct preferential directions and may be related to artificial source fields. As a consequence the far field assumption has to be checked for subsequent data interpretation.

Introduction

Principally the evaluation of magnetotelluric data is based on the calculation of transfer functions (TF) between electric and magnetic fields. For example the measured horizontal electric and magnetic field components (E_x and E_y, resp. B_x and B_y) are related by the frequency dependent impedance tensor ($\underline{Z}$) (e. g. *Tikhonov and Berdichevsy, 1966*):

$$\begin{pmatrix} E_x \\ E_y \end{pmatrix} = \begin{pmatrix} Z_{xx} & Z_{xy} \\ Z_{yx} & Z_{yy} \end{pmatrix} \begin{pmatrix} B_x \\ B_y \end{pmatrix} \quad (1)$$

All the variables are defined in frequency domain and the components $Z_{i,j}$ (i = x,y and j = x,y) of the impedance tensor represent the magnetotelluric transfer functions. The complex impedance values are visualized by the period (T) dependent phase- (φ) and apparent resistivity- (ρ_a) curves:

$$\varphi_{ij} = tan^{-1} \frac{\mathfrak{C}(\tilde{Z}_{ij})}{\Re(\tilde{Z}_{ij})} \quad (2)$$

$$\rho_{a,ij} = 0.2\, T\, |Z_{ij}|^2 \quad (3)$$

Generally $Z_{i,j}$ are estimated by a bivariate linear approach resulting from eq. (1), where the electric fields are assumed to contain noise while the magnetic fields are regarded as noise-free. Noise in the magnetic channels violates this assumption and causes the underestimation of the transfer functions (bias effects). One way to handle this problem is the remote reference method (e. g. *Gamble et al., 1979*). Subsequently robust methods can be applied to the processing scheme by predefined selection criterions choosing short time windows of the entire time series (e. g. *Junge, 1992*, *Ritter et al., 1998*, *Löwer, 2014*). A commonly used criterion is based on coherency between the electric and magnetic fields. Generally this method yields good results, but in case of coherent noise between the electric and magnetic field channels, it might fail. This also applies to the remote reference method mentioned before: if the noise is coherent between the local and the remote site (e.g. if the distance between the local and the remote site is too small), the method yields unsatisfying results.

In June/July 2014 magnetotelluric measurements were performed in the Westerwald, which is part of the Rhenish Massif in central Germany. The survey area was located at a geological fault zone with steeply dipping shales near the surface. The measurement campaign aimed at the detection of three-dimensional, anisotropic conductivity structures and the comparison with geoelectric measurements in the same area. As the experiment focused on the near-surface, mainly frequencies between 10 Hz and 5 kHz were investigated.
In **Fig. 1** transfer functions resulting from a standard robust processing scheme (*Löwer, 2014*) are shown for the off-diagonal tensor elements. Beside large scatter, the phases take very low values which is most commonly a clear indication for anthropogenic noise sources and nearfield effects. For further investigation of the nature of the noise sources, a multivariate processing scheme is presented in the next section (following *Egbert, 1997*).

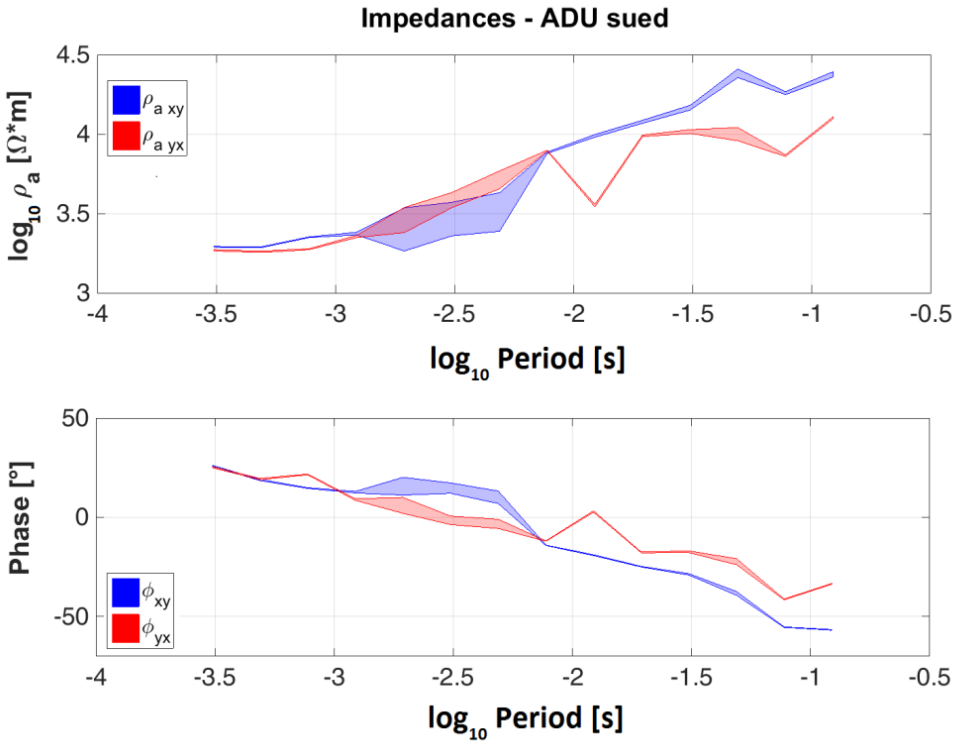

Fig. 1: Transfer functions for site "ADU sued" (Westerwald campaign 2014) as phase- and ρ_a-curves with 95%- confidence intervals (shaded areas) . The time series had been bandpass filtered (LP: 5 kHz, HP: 6 Hz) and the processing consisted of a robust bivariate calculation of the transfer functions based on a coherency selection criterion.

Multivariate processing

Following *Egbert* (*1997*) the multivariate processing scheme is based on the idea of using as many stations and channels (generally 3 magnetic and 2 electric channels for each station) as possible in view of detecting and removing incoherent noise from the data. The processing algorithm detects the number of independent polarizations within the source field by solving a generalized eigenvalue problem. With absent coherent noise and for a homogeneous source, not more than two dominant Eigenvalues significantly larger than 1 should occur (*Egbert, 1997*).
Equation (4) describes the idea behind the processing for a given data vector X_i of MT observations $e_{j,i}$ and $b_{j,i}$.

$$X_i = \begin{pmatrix} e_{1,i} \\ b_{1,i} \\ \vdots \\ e_{J,i} \\ b_{J,i} \end{pmatrix} = \begin{pmatrix} \xi_{1,1} \\ \eta_{1,1} \\ \vdots \\ \xi_{J,1} \\ \eta_{J,1} \end{pmatrix} * \beta_{1,i} + \begin{pmatrix} \xi_{1,2} \\ \eta_{1,2} \\ \vdots \\ \xi_{J,2} \\ \eta_{J,2} \end{pmatrix} * \beta_{2,i} + \varepsilon_i = U\beta_i + \varepsilon_i \qquad (4)$$

With *J* as the number of stations *j*, *i*: index of the time segment, e and b the Fourier coefficients of the electric and magnetic fields, β describing the two polarizations of the natural MT-source fields, ε as the residual, containing all noise parts.

Equation (5) allows for coherent noise being attributed to the signal, as in practice both cannot be distinguished easily. The residual ε is reduced to the incoherent noise part.

$$X_i = U\beta_i + V\gamma_i + \varepsilon_i = [U \quad V]\begin{bmatrix}\beta_i \\ \gamma_i\end{bmatrix} + \varepsilon_i = W\alpha_i + \varepsilon_i \tag{5}$$

Now *U* contains the natural signal and *V* contains the coherent noise, γ_i represents the polarizations of the noise source fields whereas α_i is the vector combining natural and noise source field polarizations

Before starting the eigenvalue analysis, all time series are bandpass filtered. Then the whole processing is performed in the frequency domain evaluating each target frequency separately. Initially the spectral density matrix (*S*) is calulated containing all the cross- and auto spectra from all the channels:

$$S = \begin{bmatrix} b_{x1,i} * b^*_{x1,i} & b_{y1,i} * b^*_{x1,i} & \cdots & e_{xK,i} * b^*_{x1,i} & e_{yK,i} * b^*_{x1,i} \\ b_{x1,i} * b^*_{y1,i} & b_{y1,i} * b^*_{y1,i} & & e_{xK,i} * b^*_{y1,i} & e_{yK,i} * b^*_{y1,i} \\ \vdots & & \ddots & \vdots & \\ b_{x1,i} * e^*_{xK,i} & b_{y1,i} * e^*_{xK,i} & \cdots & e_{xK,i} * e^*_{xK,i} & e_{yK,i} * e^*_{xK,i} \\ b_{x1,i} * e^*_{yK,i} & b_{y1,i} * e^*_{yK,i} & & e_{xK,i} * e^*_{yK,i} & e_{yK,i} * e^*_{yK,i} \end{bmatrix} \tag{6}$$

With *e, b* the electric and magnetic field Fourier coefficients, *K* the number of channels (generally 5**J*)

The spectral density matrix is normalized by the noise covariance matrix ΣN (see next chapter) and the eigenvalue problem (7) can be formulated:

$$S * u = \lambda * \Sigma_N * u \tag{7}$$

Here λ contains all the eigenvalues which can be interpreted as a signal to incoherent noise ratio and *u* stands for the corresponding eigenvectors. In case that only two dominant eigenvalues exist, the rescaled data vector *U (*see (4)) is derived from the two corresponding eigenvectors represented by *U'*.

$$U = \Sigma_n^{1/2} * U' * (U' * \Sigma_n^{-1} * U')^{-1} \tag{8}$$

In the last step, transfer functions *Z* for each site *J* are calculated from *U* accounting for the particular electric and magnetic fields:

$$Z_J = \begin{bmatrix}\xi_{xJ1} & \xi_{xJ2} \\ \xi_{yJ1} & \xi_{yJ2}\end{bmatrix} * \begin{bmatrix}\eta_{xJ1} & \eta_{xJ2} \\ \eta_{yJ1} & \eta_{yJ2}\end{bmatrix}^{-1} \tag{9}$$

Two different models for incoherent noise estimation

The estimation of the noise covariance matrix is of essential importance for the calculation of reliable transfer functions. In the following we present two models for to assess the incoherent noise level for each of the observed field components.

In a first approach we assume incoherent noise between all the existing field components. The noise covariance matrix (ΣN) is calculated by a multiple linear regression for each component (*k*) against the remaining (*K-1*) components. The variances of the residuals are summarized by:

$$\Sigma_N = \begin{bmatrix} \sigma_1^2 & 0 & \cdots & 0 & 0 \\ 0 & \sigma_2^2 & & 0 & 0 \\ \vdots & & \ddots & \vdots & \\ 0 & 0 & \cdots & \sigma_{K-1}^2 & 0 \\ 0 & 0 & & 0 & \sigma_K^2 \end{bmatrix} \quad (10)$$

With: $\sigma_1^2 \ldots \sigma_k^2$ as the noise variances for each component.

Allowing for coherent noise between the field components at each station, the multiple linear regression is modified such that each of the 5 components of the station is predicted by the (K-5) components of the remaining sites. The modified analysis yields the covariance matrix for each site which can be summarized by the block diagonal matrix:

$$\Sigma_N = \begin{bmatrix} \sigma_1^2 & \sigma_{1,2}^2 & \sigma_{1,3}^2 & & & 0 & 0 & 0 \\ \sigma_{2,1}^2 & \sigma_2^2 & \sigma_{2,3}^2 & \cdots & & 0 & 0 & 0 \\ \sigma_{3,1}^2 & \sigma_{3,2}^2 & \sigma_3^2 & & & 0 & 0 & 0 \\ & \vdots & & \ddots & & \vdots & & \\ 0 & 0 & 0 & & \sigma_{K-2}^2 & \sigma_{K-2,K-1}^2 & \sigma_{K-2,K}^2 \\ 0 & 0 & 0 & \cdots & \sigma_{K-1,K-2}^2 & \sigma_{K-1}^2 & \sigma_{K-1,K}^2 \\ 0 & 0 & 0 & & \sigma_{K,K-2}^2 & \sigma_{K,K-1}^2 & \sigma_K^2 \end{bmatrix} \quad (11)$$

With each components' variances of the residuals on the main diagonal and the covariances on the off diagonals.

The application of covariance model (11) proved to be crucial for the transfer function estimation of some of our data sets.

Results

The multivariate processing scheme was applied to data sets from the MT survey in the Westerwald in 2014. They were obtained at two stations ("ADU sued" and "ADU west") which were approximately 350 m apart. At both sites 3 magnetic (H_x, H_y, H_z) and two electric field (E_x, E_y) components were recorded with a sampling rate of 16 kHz. The length of the time series was 15 minutes with noise occurring permanently during the observation period. Therefore the division into individual subintervals was omitted. Before the multivariate processing the data was bandpass filtered (LP: 6 kHz, HP: 10 Hz).

The Eigenvalues resulting from two different noise models are compared and presented in Fig. 2. Noise model 1 refers to the simple case (cf. equation (10)) and yields more than 2 dominant eigenvalues for the whole frequency range (Fig. 2(a)). We assume that the data is strongly influenced by coherent noise signals. The calculation of the data vector *U* (eq. (8)), using the two largest eigenvectors results in impedances which are highly contaminated, especially the phase curves (**Fig. 3**). Using the noise covariance matrix of model 2 (cf. equation (11)) produces two dominant eigenvalues clearly separated from the remaining eigenvalues (Fig. 2(b)). Therefore we assume that they represent the polarizations of the source field. Noise model 2 improves the impedances significantly (**Fig. 4**), also with respect to the standard robust processing procedure (**Fig. 1**). Nevertheless, the phase curves still decay steeply towards zero with decreasing frequency, which can be an indication for nearfield effects. Furthermore the polarization directions of the electric (E) and magnetic (B) fields were analyzed. They were calculated for each Fourier coefficient according to *Fowler (1967*) (eq. (12), shown for the electric field):

$$\Psi = \tan^{-1}\left(\frac{2*\Re(E_x*E_y^*)}{|E_x|^2-|E_y|^2}\right) \qquad (12)$$

They have distinct preferential directions as well for the electric as for the magnetic field (Fig.5). As for natural source fields the polarization directions of the magnetic field are assumed to be randomly distributed, we suspect that the transfer functions related to the two dominant eigenvalues result from artificial source fields. This would implicate that the two dominant eigenvalues do not necessarily indicate homogeneity of the source field. The origin of the artificial signals is uncertain. They could be led back to the disadvantageous signal-to-noise ratio due to the AMT-dead-band between 1 kHz and 5 kHz. Another explanation could be an electric current channeling effect due to the steeply inclined shales at the near surface. This assumption could be an interesting target for a theoretical study.

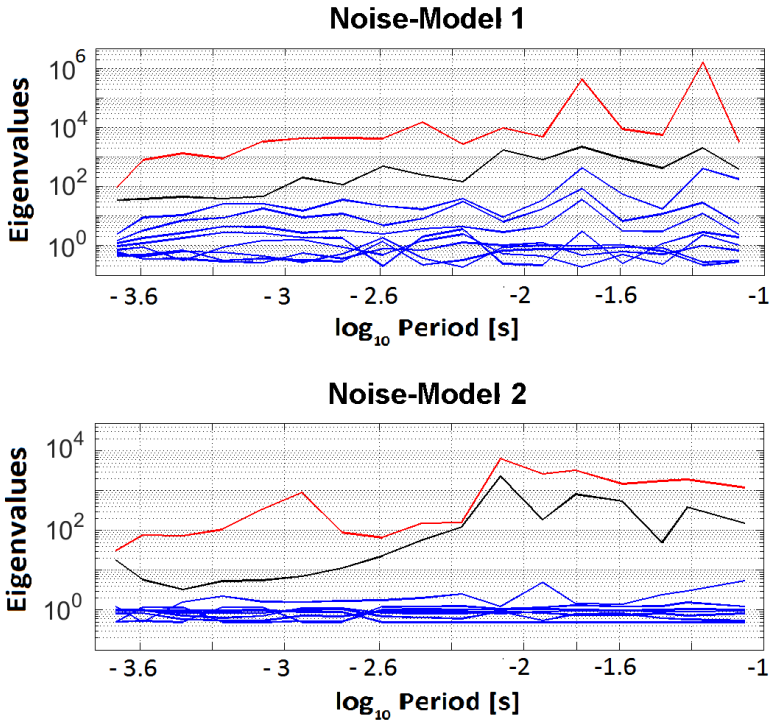

Fig. 2: Eigenvalue analysis using two different Noise-Models. Dominant eigenvalues 1 and 2 are marked in red and black. The calculation is based on data observed at stations "ADU sued" and "ADU west" from the measurement campaign in the Westerwald (2014). **Top (a)**: Only incoherent parts of the noise. **Bottom (b)**: Coherent noise allowed within one station.

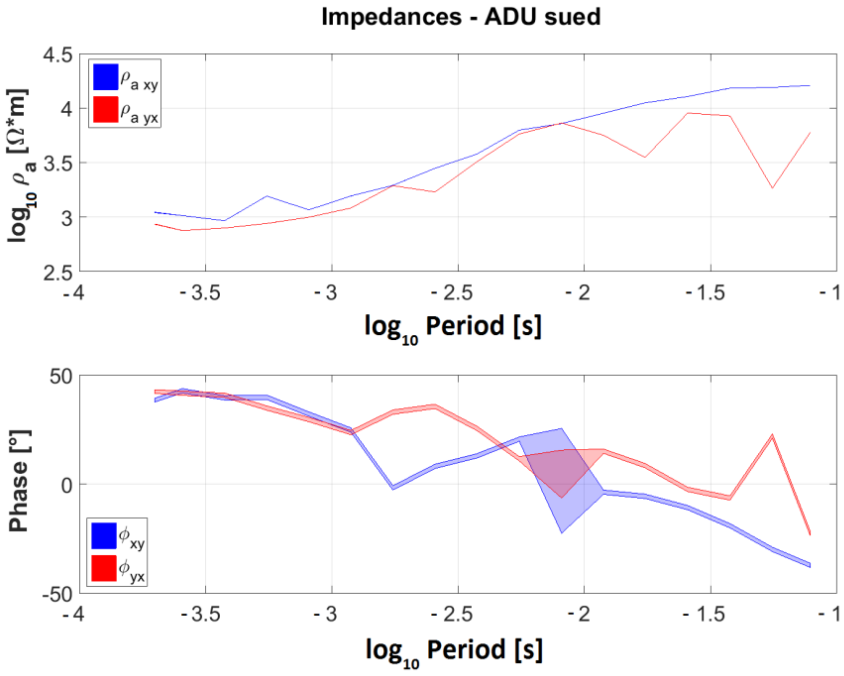

Fig. 3: Transfer functions for site "ADU sued", shown in form of phase- and ρ_a- curves from **Noise-Model 1**. The shaded areas represent the 95%- confidence intervals. The multivariate processing was performed using the stations "ADU sued" and "ADU west" from the 2014-measurement campaign in the Westerwald.

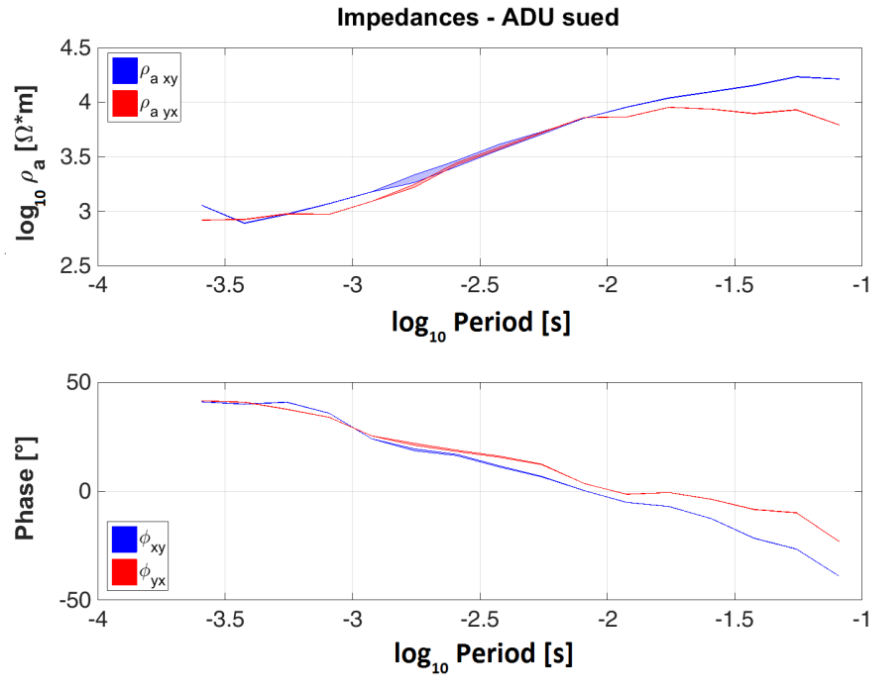

Fig. 4: Transfer functions for site “ADU sued” as in Fig.3 using **Noise-Model 2**.

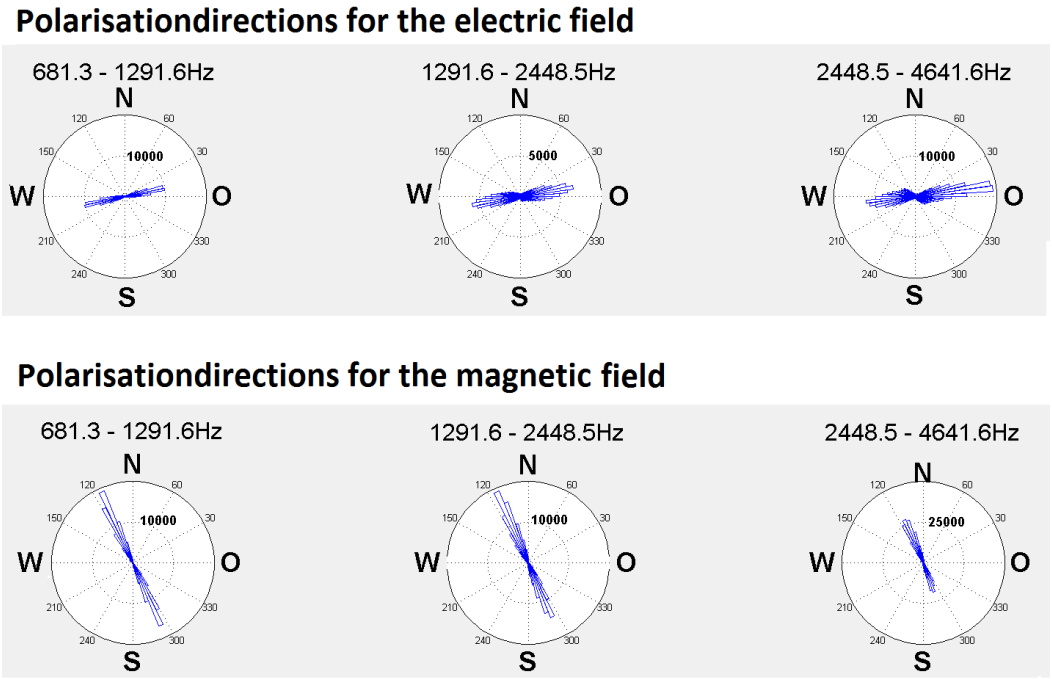

Fig 5: Polarizations of the electric (**top**) and magnetic fields (**bottom**) from station “ADU sued” are showing strongly preferred directions. The polarization direction of the fields was calculated for each Fourier coefficient. The results are summarized in three rose plots with frequency ranges above 680 Hz and a cluster width of 4°.

Conclusions

The presented multivariate processing scheme removes incoherent noise from the data and indicates the presence of coherent noise sources. The example from the Westerwald shows a significant improvement for the transfer function estimation compared to the standard robust single site processing. Here the choice of the noise model is of crucial importance. Using a noise covariance matrix which considers coherent noise signals between the field-components observed at one station is strongly recommended. However, two distinct dominant eigenvalues might also represent a high anthropogenic noise level in case of very weak natural signals. It is recommended to check the polarization directions of the magnetic fields for distinct preferred directions which might indicate strong influence from anthropogenic noise. In case of the data set from the Westerwald, the recorded signals were mostly referred to artificial source fields. As a consequence the interpretation of the data was restricted to frequencies above 1 kHz to fulfill the far field assumption.

Literature

Egbert, G. (1997), *Robust multiple-station magnetotelluric data processing*, Geophys. J. Int. 130, 475-496

Fowler, R., Kotick, B. and Elliot, R. (1967), *Polarization analysis of natural and artificially induced geomagnetic micropulsations*, J. geophys. Res. 72

Gamble, T., Goubau, W. und Clarke, J. (1979), *Magnetotellurics with a remote reference*, Geophysics 44**,** 53-68.

Hering, Ph. (2015), *Magnetotellurische Messungen im Westerwald - Eine Studie zur Detektion und Minimierung von anthropogenen Rauschsignalen*, Master-Thesis (in German), Goethe University Frankfurt am Main

Junge, A. (1992), *Erweiterte Auswerteverfahren in Göttingen*, Tagungsband, 14. Kolloquium Elektromagnetische Tiefenforschung in Borkheide, Deutsche Geophysikalische Gesellschaft, ISSN: 0946 7467

Junge, A. (1996), *Characterization of and correction for cultural noise*, Surv. Geophys. 17, 361–391

Löwer, A. (2014), *Magnetotellurische Erkundung geologischer Großstrukturen des südwestlichen Vogelsberges mit anisotroper, dreidimensionaler Modellierung der Leitfähigkeitsstrukturen*, PhD-Thesis (in German), Goethe University Frankfurt am Main

Ritter, O., Junge, A. and Dawes, G. J. (1998), *New equipment and processing for magnetotelluric remote reference observations*, Geophys. J. Int. 132**,** 535-548

Tikhonov, A. N. und Berdichevsky, M. (1966), *Experience in the use of magnetotelluric methods to study the geological structures of sedimentary basins*, Izv. Acad. Sci. USSR, Phys. Solid Earth 2**,** 34-41

3D MT Modelling in West Greenland Considering the Influence of Fjord Systems and Ocean.

N. L. B. Lauritsen[1], P. Hering[2], A. Junge[2], J. Matzka[3], and N. Olsen[1]

[1]*DTU Space, Technical University of Denmark, Denmark*
[2]*Institue of Geosciences, Goethe Universität Frankfurt am Main, Germany*
[3]*GFZ Potsdam, Germany*

Introduction

Collecting magnetotelluric data in Greenland give rise to different challenges. Here we investigate one of the challenges, how a fjord system connected to the ocean can affect induction arrows around the fjord, by numerical simulations for periods of 1s, 10s and 100s. The results are induction arrows from a magnetotelluric data set collected in West Greenland in the summer 2013, with stations along the shoreline of the fjords between the towns of Kangerlussuaq and Aasiaat, see Figure 1. The setup consisted of 10 LMT stations on a 100 km profile with equipment kindly supplied by the GIPP at GFZ Potsdam (2015).

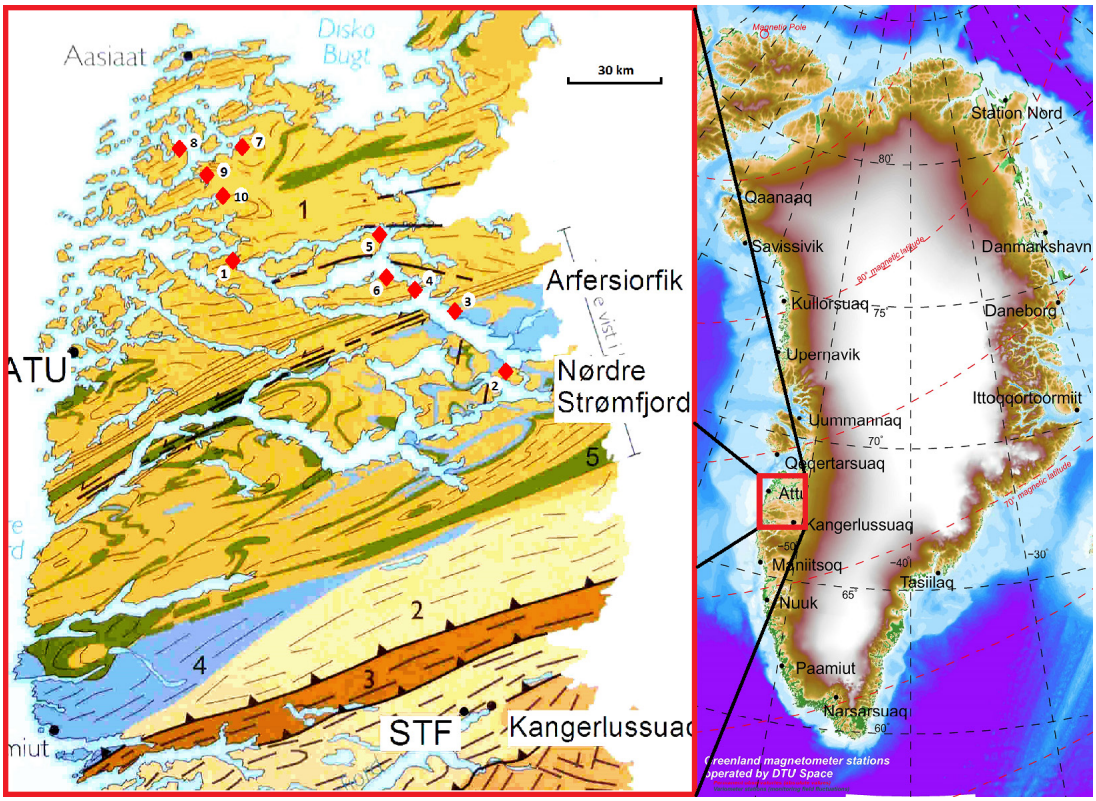

Figure 1: Left Red diamonds indicate the locations of the 10 stations at Arfersiorfik fjord. Geological map from van Gool in Henriksen (2008). **Right** Red square indicates the left-side maps location together with permanent DTU Space magnetometer stations.

Model study: the impact of fjords on MT transfer functions

We have conducted a model study with a simplified bended fjord, with or without connection to the ocean, to investigate how seawater of the fjord affects the induction arrows along the shoreline. The COMSOL Multiphysics v. 5.2 (2015) software is used to perform the modeling. The cross section of the fjord is set to a rectangle, 2 km width and 200 m depth.
Figure 2, left column, illustrates a fjord with no connection to the ocean, with the three panels presenting induction arrows for periods of 1s, 10s or 100s. The background color displays the magnitude of the induction, with the highest induction concentrated along the shoreline, but especially on the inside of the bend of the fjord. The real part of the induction arrows, illustrated as red arrows in Figure 2, will point away from conductive material (Wiese convention). Focusing first on the period of 1s, it is clear that the arrows along the shoreline (not towards the ends) are larger than 1, which is the maximum limit we normally expect from geology. For longer periods, 10s and 100s, the magnitude decreases fast and is negligible at long periods. Therefore, the induction caused by the fjord is most distinct for short periods, when the station is located very close to the shoreline.

The induction arrows change if the fjord is connected to the ocean. Figure 2, right column, illustrates thisfor periods 1s, 10s and 100s. Focusing on the period of 1s, the largest magnitude of the induction has shifted closer to the ocean, however the highest value is twice as large as in the bend. The magnitude in the bend is approximately the same value as in the situation without the ocean, but the difference is along the shoreline. The magnitude and the real induction arrows are very large all along the shoreline, whereas for the fjord without an ocean it decreases when moving away from the bend.
For the period of 10s, the magnitude is approximately the same in the bend, but the real induction arrows are larger. Induction from the fjord is completely disguised in the induction originating from the ocean, for the period of 100s,.
The induction from a fjord is therefore very high in low and medium periods and it can transverse further into a big fjord system when connected to the ocean, because of currents channeling.

Comparison with observations

The results of the model study illustrates the importance of modeling fjords in the vicinity of stations. The area of the magnetotelluric survey from West Greenland is traversed with a complex fjord system, see Figure 1. We have therefore tried to model the fjord system to account for the effect. As the bathymetry of the fjord system is not currently known different depths were tested and an average value of 100 m was selected.
Additionally, the model also consists of a model of the ocean created with the bathymetry from GEBCO world map (2014).
Figure 3 illustrates the model with a background resistivity of 100Ωm and a resistivity of the water (fjord and ocean) of 0.25Ωm. The induction arrows from this model are illustrated in Figure 4 together with the data response for three stations, station 8, 9 and 10 in the survey, see location in Figure 1.

Both station 9 and 10 illustrate a transition between conductive and resistive material to the north west of their location, which in the long periods is boundary to the ocean and for shorter periods is boundary to the fjord. The model responses agree with the data, the arrows

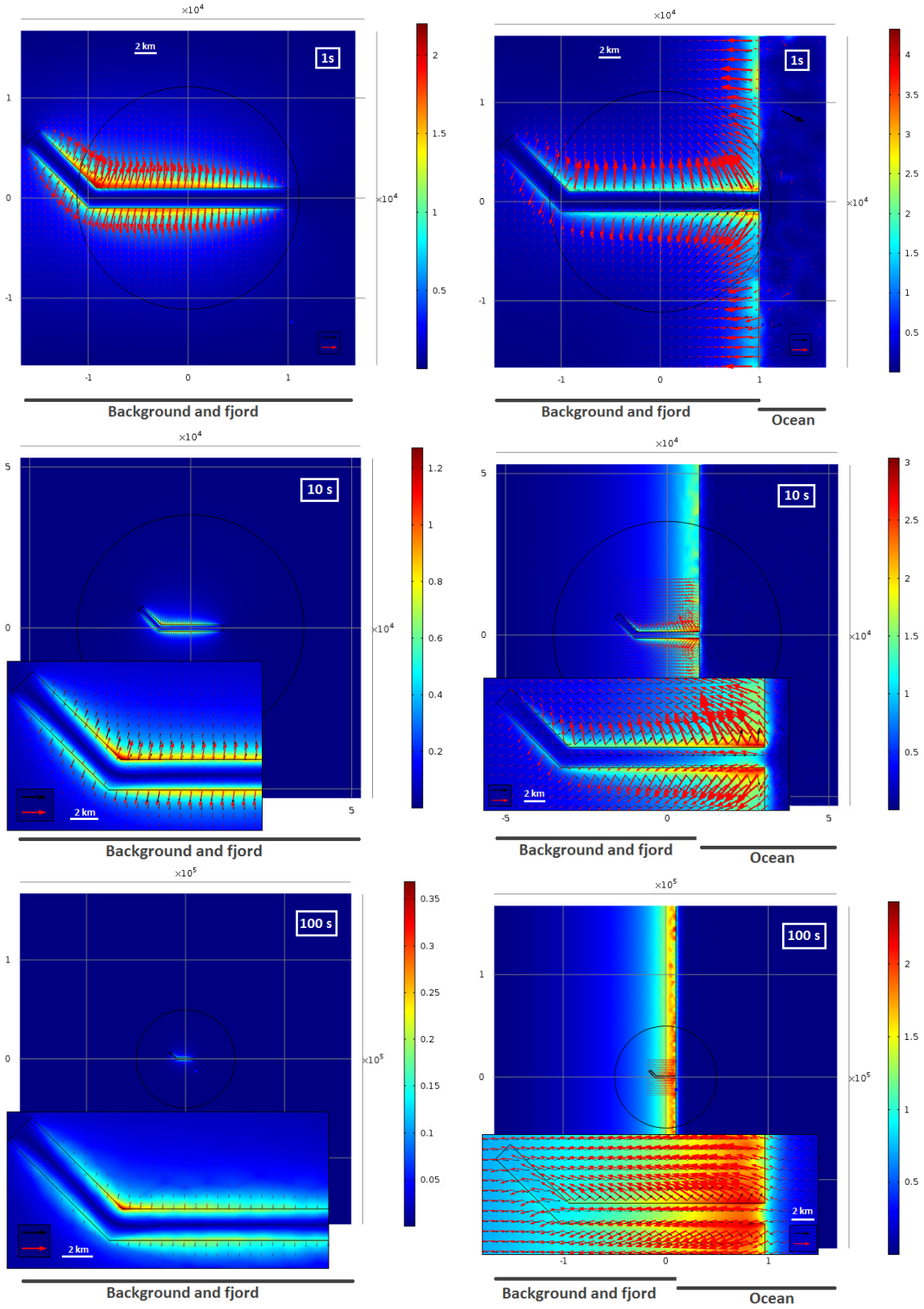

Figure 2: Left Models of a closed fjord, and **Right** model of a fjord connected to an ocean, for three different periods 1s, 10s and 100s. The color represents the magnitude of the total magnetic field and the red (black) arrows represents the real (imaginary) induction arrow. The four bottom figures display a zoom in of the fjord. Scale shown by unit arrows in each figure.

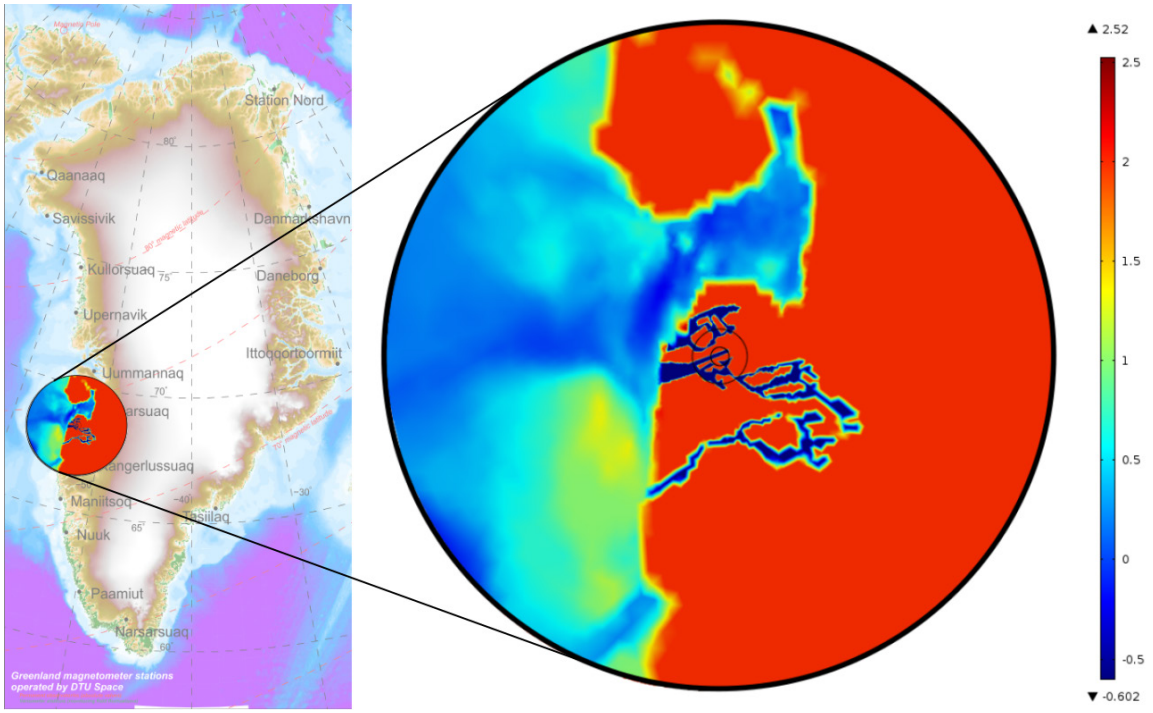

Figure 3: Left The resistivity distribution of the model located in its geographical surroundings. **Right** A close-up of the resistivity of the model, with a background resistivity of 100Ωm.

have the same direction in the real part, although not the same magnitude. Station 8 behaves differently, it illustrates a boundary between conductive and resistive material to the east in short periods and to the north west in long periods, with a smooth transition in between. This is present both in the data and the model. This can be explained by the location of station 8, which is on a small island within the fjord. There is a larger water area to the east and a large island to the west, which explains the rotation of the arrows with period.
Even though the model and data differ from each other with respect to the direction, they reveal the same pattern.

The model consists only of a homogeneous background, ocean and fjords and does not include any geological bodies. The considerable contribution originating from the ocean and fjords has to be considered definitely when explaining the observed data by conductivity models. To achieve a reasonable data fit shaping the fjord in the model as truly as possible is important.

References

COMSOL Multiphysics v. 5.2. (2015). COMSOL AB, Stockholm, Sweden. (`www.comsol.com`)

GEBCO world map. (2014). (www.gebco.net)

GFZ Potsdam. (2015). *Geophysical Instrument Pool Potsdam (GIPP).* http://www.gfz-potsdam.de/en/section/geophysical-deep-sounding/infrastructure/geophysical-

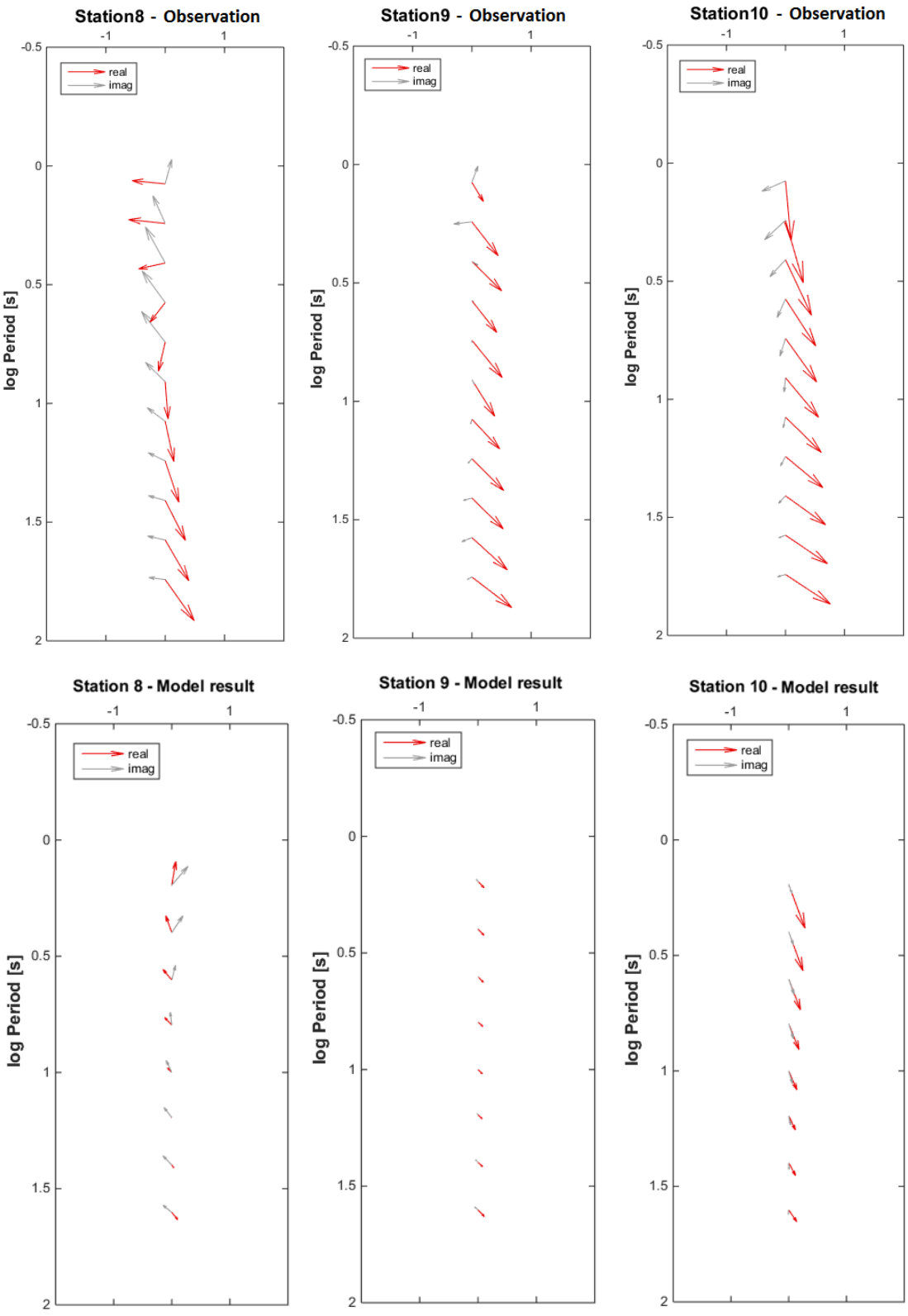

Figure 4: Observed (Top) and model (Bottom) induction arrows of station 8, 9 and 10.

instrument-pool-potsdam-gipp/instruments/gipp-mt/. ([Online; accessed 08-December-2015])

Henriksen, N. (2008). *Geological History of Greenland*. Geological Survey of Denmark and Greenland (GEUS).

Von der Punkt- zur Flächenlösung:

Simulation eines vertikalen magnetischen Dipols mittels einer analytischen Punktlösung unter Verwendung eines Quadraturverfahrens

S.Malecki, R.-U. Börner und K. Spitzer
Institut für Geophysik und Geoinformatik, TU Bergakademie Freiberg

1 Zusammenfassung

In der Geoelektromagnetik werden oft großflächige Quellen, beispielsweise Leiterschleifen, näherungsweise als Punktquellen aufgefasst. Diese Annahme ist jedoch nur für hinreichend große Entfernungen zwischen Quelle und Messpunkt zulässig.
Da die Messung mit relativ kleinen Spulen durchgeführt werden, die Sendespulen aber bis zu 10 000 m^2 Spulenfläche aufweisen, liegt es nahe, das Reziprozitätsprinzip auszunutzen, um Sender und Empfänger zu vertauschen. So wird das Feld eines Sendedipols am Ort des eigentlichen Empfängers genutzt, um über die Lösung dieses Dipols am Ort des eigentlichen Senders zu integrieren. Die Integrationsfläche entspricht dabei der Fläche der eigentlichen Sendeschleife. Dabei kann die Lösung des Dipols entweder analytisch über homogenen oder geschichteten Leitfähigkeitsmodellen oder numerisch über beliebigen Leitfähigkeitsverteilungen berechnet werden.
Um den Einfluss der Spulengeometrie abzuschätzen, genügt meist die Auswertung der analytischen Lösung. Die numerische Integration geschieht dabei durch eine zweidimensionale Gaußquadratur. Eine Konvergenzstudie zeigt die Abhängigkeit der Genauigkeit dieses Ansatzes von der Knotenzahl der Gaußquadratur in Verbindung mit ausgewählten Entfernungen zwischen Senderzentrum und Messpunkt.

Schlagwörter: Gauß-Legendre-Quadratur, magnetischer Dipol, analytische Punktlösung, Konvergenz

2 Einleitung

Das Institut für Geophysik und Geoinformatik der TU Bergakademie Freiberg verfügt über einen schnellen analytischen 1-D Code zur Berechnung transienter elektromagnetischer Felder in horizontal geschichteten Medien für einen punktförmigen, vertikalen magnetischen Dipol.
In der Praxis sind diese magnetischen Quellen nicht punktförmig, sondern großflächige, auf der Erdoberfläche ausliegende Leiterschleifen. Es sollen die Grenzen der häufig getroffenen Annahme einer Punktquelle gezeigt werden. Weiterhin wird das Konvergenzverhalten einer 2-D Gauß-Legendre-Quadratur dieser Punktlösung in Abhängigkeit von Knotenzahl und Abstand zum VMD-Zentrum vorgestellt.
Auf Grundlage der Konvergenzstudie können Empfehlungen für eine hinreichende Anzahl an Quadraturpunkten gegeben werden.

3 Modellbeschreibung

Grundlage der Simulationsrechnungen ist ein analytischer 1-D Vorwärtsoperator für die Berechnung der Felder eines punktförmigen, vertikalen magnetischen Dipols (VMD). Eine quadratische Drahtschleife (100 m × 100 m) auf einem homogenen Halbraum ($\rho = 100\,\Omega\,\mathrm{m}$) bilden den zu approximierenden VMD und das zugehörige Leitfähigkeitsmodell.
Die Anzahl n der Quadraturpunkte (Knoten) ist variabel. Die Punktaufteilung innerhalb der Fläche des VMD (vgl. Abbildung 1) erfolgt durch eine Gauß-Legendre-Quadratur.

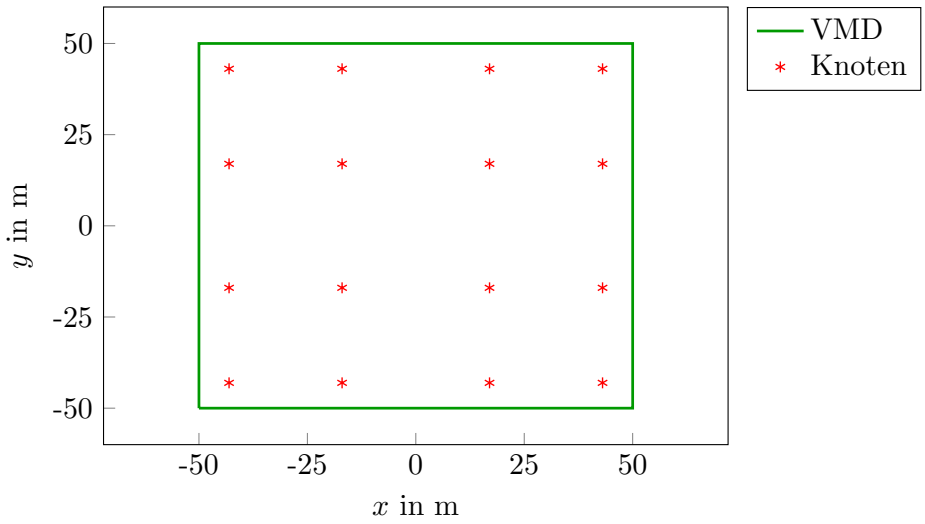

Abbildung 1: Beispiel zur Verteilung der Knoten innerhalb der Fläche des VMD: Die Anordnung der Knoten wird durch eine 2-D Gauß-Legendre-Quadratur festgelegt. Im Beispiel hat diese Quadratur den Polynomgrad $n = 4$. Dies entspricht 4×4 Knoten innerhalb der Fläche des VMD.

In der Konvergenzstudie wird die Anzahl der Knotenpunkte von $n = 1$ bis auf $n = 35$ erhöht und mit einer Quadraturlösung für $n = 100$ verglichen. Diese Referenzlösung umfasst 10 000 Punkte innerhalb einer Fläche von $10\,000\,\mathrm{m}^2$. Die verschiedenen Quadraturlösungen werden für steigende Abstände zwischen VMD-Zentrum und Messpunkt berechnet (vgl. Abbildung 2).

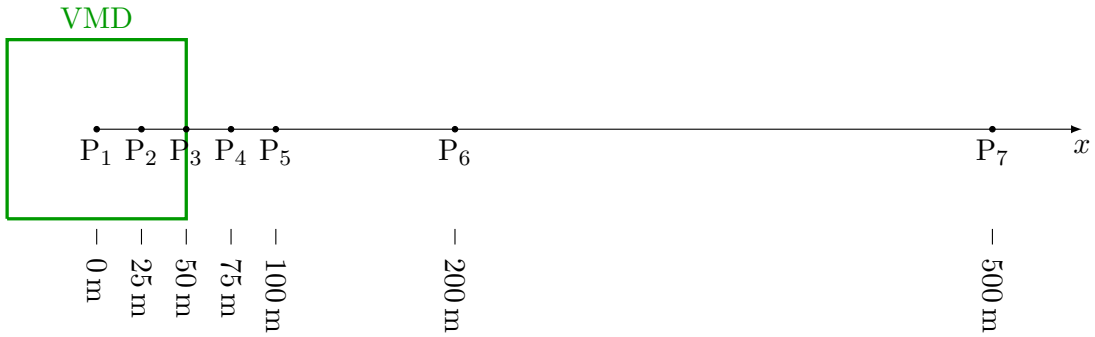

Abbildung 2: Draufsicht: Die Quadratur des quadratischen VMD (grün, 100 m × 100 m) wird an den Beobachtungspunkte P_i ausgewertet. Sie liegen sowohl innerhalb als auch außerhalb der Fläche des VMD und sind in wachsenden Abständen entlang der x-Achse verteilt.

4 Theorie

Die Gauß-Quadratur ist ein Verfahren zur numerischen Integration. Die Stammfunktionen sind meist unbekannt oder nur mit großem Aufwand berechenbar. Das Ziel der Gauß-Quadratur ist eine möglichst gute Näherung für das Integral I einer Funktion $g(x)$ zu finden.
In einem ersten Schritt wird das Integral der Ausgangsfunktion $g(x)$ durch das Integral

$$I = \int_a^b f(x)\,\rho(x)\;\mathrm{d}x = \int_a^b g(x)\;\mathrm{d}x \tag{1}$$

ersetzt und numerisch gelöst. Die stetige Gewichtsfunktion $\rho(x)$ ist dabei stets positiv.
Im zweiten Schritt erfolgt die Approximation der Funktion $f(x)$ durch ein Polynom n-ten Grades

$$I = \int_a^b f(x)\,\rho(x)\;\mathrm{d}x \approx \int_a^b p_n(x)\,\rho(x)\;\mathrm{d}x = I_n, \tag{2}$$

wobei der Grad n des Polynoms die Genauigkeit der Approximation direkt beeinflusst. Das Polynom $p_n(x)$ lässt sich in innerhalb bestimmter Grenzen durch

$$\int_{-1}^1 p_n(x)\,\rho(x)\;\mathrm{d}x = \sum_{i=1}^n f(x_i)\,\omega_i \tag{3}$$

exakt numerisch integrieren. Werden als Polynomfunktion $p_n(x)$ Legendre-Polynome verwendet, kann die Gewichtsfunktion im normierten Intervall $[-1,1]$ durch $\rho(x) \equiv 1$ definiert werden. Das Gleichungssystem (3) ist dann eindeutig lösbar und dessen Gewichte ω_i sind stets positiv (vgl. Bärwolff [2007]).

Aus der eindimensionalen Quadraturformel (3) lässt sich eine Gauß-Quadratur für einen Rechteckbereich konstruieren. Die Gewichte ω_i werden nun als Vektoren entlang der x- bzw. y-Achse

$$\boldsymbol{\omega_x} = [\omega_1, \omega_2, \ldots, \omega_n]^\top \quad \text{und} \quad \boldsymbol{\omega_y} = [\omega_1, \omega_2, \ldots, \omega_m]^\top \tag{4}$$

aufgefasst. Die Matrix

$$\boldsymbol{\Omega} = \boldsymbol{\omega_x} \cdot \boldsymbol{\omega_y}^\top \tag{5}$$

beinhaltet alle Gewichte im Integrationsgebiet (vgl. [Engeln-Müllges et al., 2011]). Gleichzeitig sind mit den Vektoren

$$\boldsymbol{x} = [x_1, x_2, \ldots, x_n]^\top \quad \text{und} \quad \boldsymbol{y} = [y_1, y_2, \ldots, y_m]^\top \tag{6}$$

die Koordinaten der Knotenpunkte innerhalb des Integrationsgebietes gegeben. Ein bestimmtes Zweifachintegral kann durch die Näherung

$$\int_{-1}^1 \int_{-1}^1 h(x,y)\;\mathrm{d}x\,\mathrm{d}y \approx \sum_{i=1}^n \sum_{j=1}^m \Omega_{i,j} h(x_i, y_j) \tag{7}$$

numerisch berechnet werden. Die Berechnung erfolgt zunächst im normierten Intervall $[-1,1] \times [-1,1]$. Es lassen sich jedoch auch Flächenintegrale mit den Integrationsgrenzen $[a,b] \times [c,d]$

$$\int_a^b \int_c^d h(x,y)\;\mathrm{d}x\,\mathrm{d}y \approx \sum_{i=1}^n \sum_{j=1}^m \Omega_{i,j} h\left(\frac{b-a}{2}x_i + \frac{a+b}{2}, \frac{d-c}{2}y_j + \frac{c+d}{2}\right) \tag{8}$$

auf dieses normierte Intervall abbilden.

5 Konvergenzstudie

Die Konvergenzstudie zeigt das Fehlerverhalten verschieden genauer Approximationen des VMD bezüglich eines Referenzdipols. Der Referenzdipol ist durch eine Gaußquadratur mit $n \times n = 100 \times 100$ Knoten approximiert. In der Fläche des quadratischen VMD ($10\,000\,\mathrm{m}^2$) sind somit 10 000 Knotenpunkte eingetragen.
Beginnend mit $n = 1$ Knoten, wird für jeden Punkt P_i (vgl. Abbildung 2) die Quadraturlösung berechnet und mit der Referenzlösung verglichen. Die Norm der Differenz

$$\Delta\dot{B} = \left\| \dot{B}_{100} - \dot{B}_n \right\|_2 \tag{9}$$

ist in Abbildung 3 dargestellt.

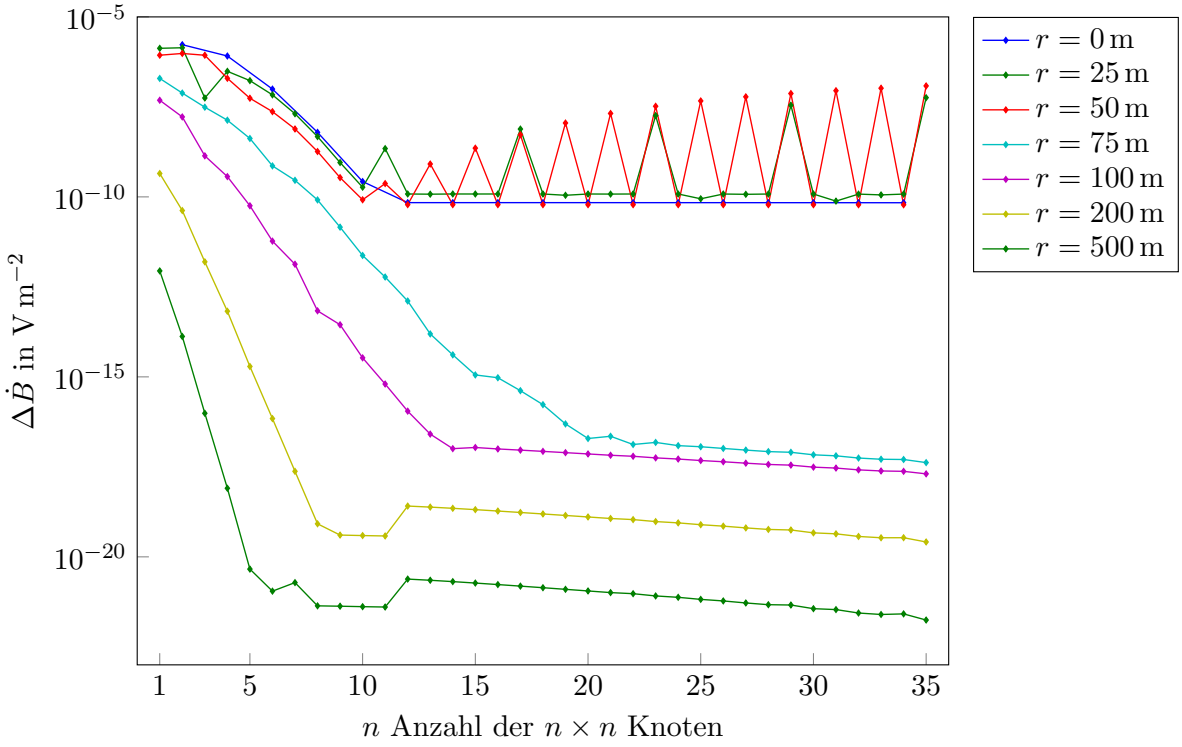

Abbildung 3: Die Abweichungen des Quadraturergebnisses von der Referenzdipollösung wurden für die Abstände $0\,\mathrm{m} \leq r \leq 500\,\mathrm{m}$ bei $z = 0\,\mathrm{m}$ berechnet. Als Referenz dient ein Dipol, der mit 100×100 Gaußpunkten approximiert wurde. Das Hintergrundmodell ist ein homogener Halbraum mit $\rho = 100\,\Omega\,\mathrm{m}$.

In Abbildung 3 beginnt der Fehler der Lösungen für $r = 25\,\mathrm{m}$ und $r = 50\,\mathrm{m}$ ab einer Knotenanzahl von $n = 10$ zu ozillieren. Dies ist im zufälligen Zusammentreffen der Punkte P_2 bzw. P_3 mit Quadraturpunkten begründet. (vgl. Abbildung 4 und Abbildung 5)
Diese Punkte liegen nicht exakt aufeinander, jedoch dicht genug um einen großen, die Quadraturlösung verfälschenden, Einfluss zu haben.
Sollten sie sich zufällig an gleicher Stelle befinden, so würde an dieser Stelle eine Singularität entstehen. Sie macht die Quadraturlösung für diesen speziellen Fall unbrauchbar.

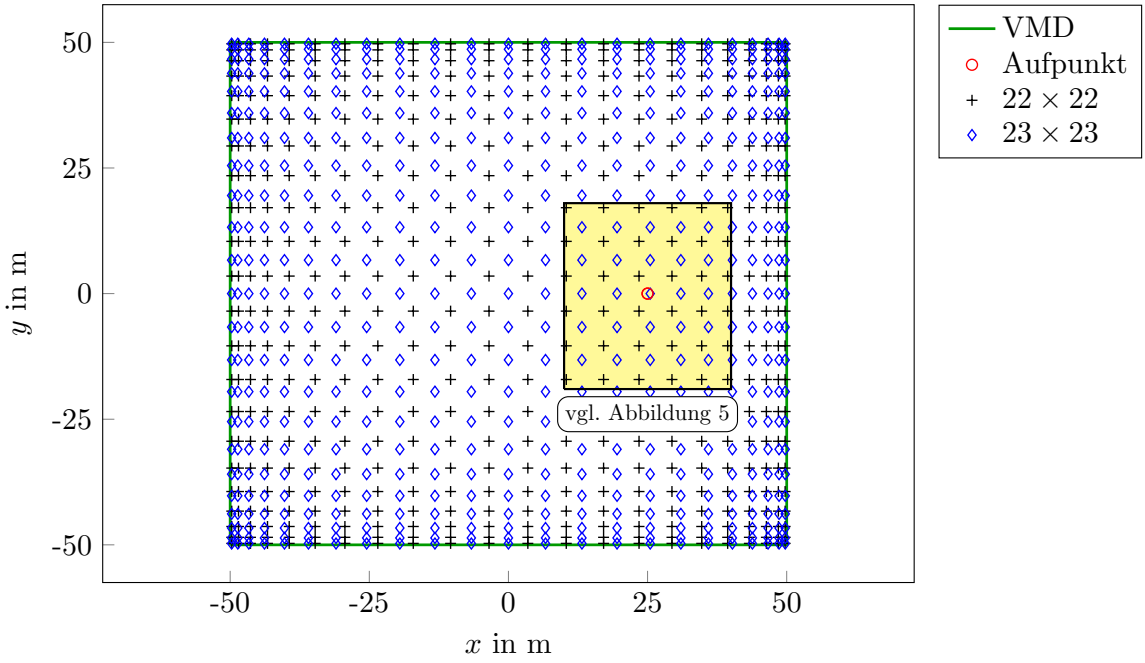

Abbildung 4: Innerhalb des VMD sind die Quadraturpunkte sowohl für $n = 22$ als auch für $n = 23$ eingetragen. Der Aufpunkt P_2 ist in Rot markiert. Die unmittelbare Nähe zu einem Punkt der Quadratur vom Grad $n = 23$ ist in dem gelb markierten Bereich zu sehen. Der sehr geringe Abstand ist in der vergrößerten Ansicht in Abbildung 5 deutlicher zu erkennen.

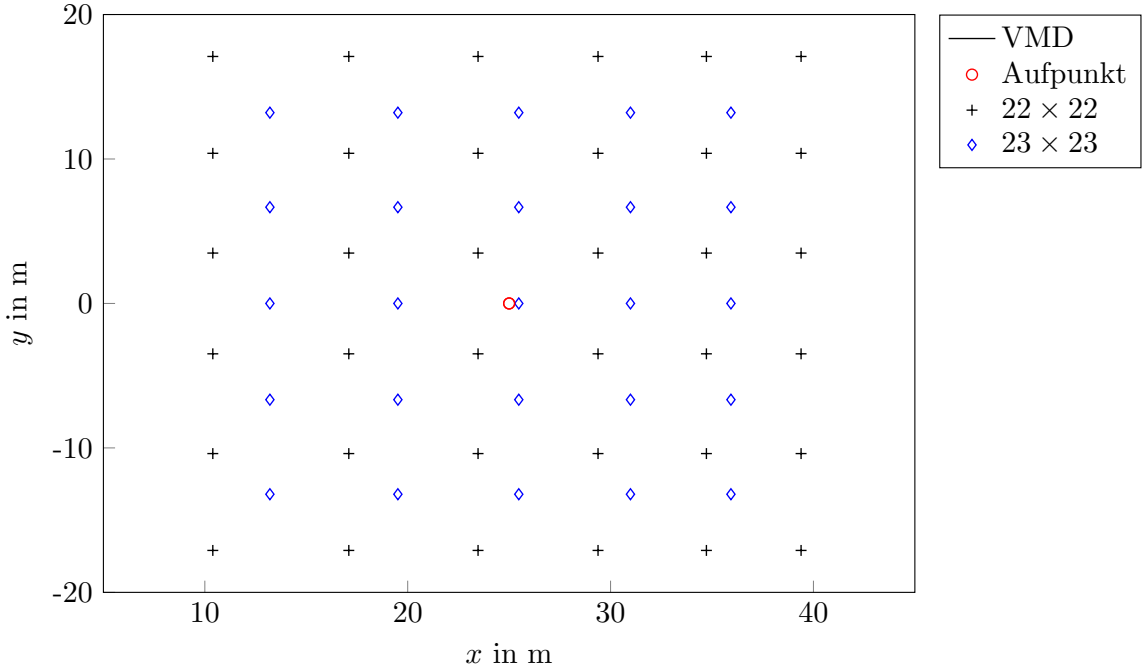

Abbildung 5: Ausschnitt aus Abbildung 4: Der Abstand zwischen Aufpunkt und Quadraturpunkt beträgt 0,48 m.

6 Zusammenfassung

Es konnte am Beispiel eines $100\,\mathrm{m} \times 100\,\mathrm{m}$ großen VMD gezeigt werden, dass die Verwendung einer Punktlösung zur Approximation einer Flächenlösung mittels einer Gauß-Legendre-Quadratur möglich ist.
Die Anzahl notwendiger Knoten kann dabei in Abhängigkeit vom Abstand r auf $5 \leq n \leq 10$ beschränkt bleiben. Eine Erhöhung der Knotenzahl darüber hinaus ergibt keine signifikanten Genauigkeitssteigerungen.
Bei der Quadratur ist darauf zu achten, dass der Aufpunkt nicht mit einem Quadraturpunkt zusammenfällt.

Literatur

G. Bärwolff. *Numerik für Ingenieure*. Spektrum Akademischer Verlag, 2007.

G. Engeln-Müllges, K. Niederdrenk, and R. Wodicka. *Numerik-Algorithmen*. 10. Auflage. Springer-Verlag, 2011.

Electric and electromagnetic investigation of a karst system

Marion P. Miensopust[1], Jan Igel[1], Thomas Günther[1], Raphael Dlugosch[1], and Sarah Hupfer[1]

[1]*Leibniz Institute for Applied Geophysics, Hannover, Germany*

1 Motivation

Dissolution of rocks such as anhydrite, gypsum, limestone, dolomite or salt rock enlarges fractures or pore space and finally results in voids and cavities within karst rocks. Especially in populated areas such collapses may have catastrophic consequences, but the current knowledge about the evolution, governing processes and capabilities of prediction are insufficient. Geophysical methods can contribute to the understanding, first of all by detailed investigation of known sinkhole structures and - later on - by monitoring areas of high risk as well as localising those areas before a surface expression is visible. As voids and cavities are often fluid- or air-filled (or both) and the electrical properties of the fluid and air are in many cases significantly different to those of the surrounding karst rocks, electric and electromagnetic methods such as, e.g., electrical resistivity tomography (ERT), ground-penetrating radar (GPR) and nuclear magnetic resonance (NMR) are potentially useful tools for the investigation of sinkhole structures. In the case study presented here we focus on the application of electric and electromagnetic methods on the karst system of the Innerste Mulde in Lower Saxony which is surface-mapped by numerous sinkhole structures.

2 Geological Setting

The Innerste Mulde is a trough structure along the northern rim of the Harz Mountains in Northern Germany. It comprises steeply dipping, jointed Pläner limestone of Turonian age which host a karst water system bound to this limestone of the western flank of the Innerste Mulde. The subsurface karst system is about 27 km long and can be traced on surface by numerous sinkholes and collapse structures. Close to the village of Altwallmoden an anticline (i.e., the Lutterer Sattel) extends into the Innerste Mulde and causes steepening of the stratification and hence a narrowing flow channel of the karst system. Therefore, a part of the water emerges in karst springs near Altwallmoden, the remaining water reappears in the springs of Baddeckenstedt further north (Knolle & Jacobs, 1988).
The so-called Kirschensoog (Figure 1) is an elongated elliptic sinkhole structure of approximately 75 m length and 20 m width. It is one of the karst springs near Altwallmoden. At the southern end the base of the spring is about 5 m below the surrounding surface and flattens towards the north. It only temporarily yields water, e.g., in times of snow melting or after heavy rain fall.
In February and early March 2015, the Kirschensoog itself and also the discharging brook were water filled. Towards mid March the water level dropped quickly and the brook

Figure 1: Temporary karst spring Kirschensoog. Water level changed visibly within a few days and first the discharge and later the spring itself fell dry. Viewing directions are indicated in Figure 2.

and large parts of the Kirschensoog fell dry. In May, the entire trough was completely dry. Figure 1 shows the spring at different water levels. The feeding system of this spring is still under speculation but obviously the spring acts like a pressure relief valve of the subsurface karst water system which might go along with larger water-filled cavities in the surrounding.

3 Field Studies

Figure 2 shows the location of the Kirschensoog and the positions of the ERT and GPR profiles as well as the 2D survey setups for surface NMR (SNMR). In total, ERT data were acquired along four profiles using Wenner-alpha and Wenner-beta electrode arrays with 140 electrodes and 2 m electrode spacing. Figure 3 shows inversion results of all four ERT profiles stitched together. The resistivity models show 3D structures and dipping features. The obtained resistivity of the limestone seems rather low suggesting possible fluid- or clay-filled fissures and fractures. Additional field and laboratory studies are required to confirm or disprove this interpretation.
Three ERT profiles and one additional profile were also investigated using GPR with antenna frequencies from 20-400 MHz. The covering soil causes strong attenuation and, therefore, restricted the penetration depth of the signal. Figure 4 shows an example of 200 MHz GPR data where the cover layer is thin (approx. less than 0.5 m). The dipping reflectors – coinciding with the dipping features of the ERT models – are possibly related to the bedding of the limestone or fluid-filled fractures. To determine the dipping direction

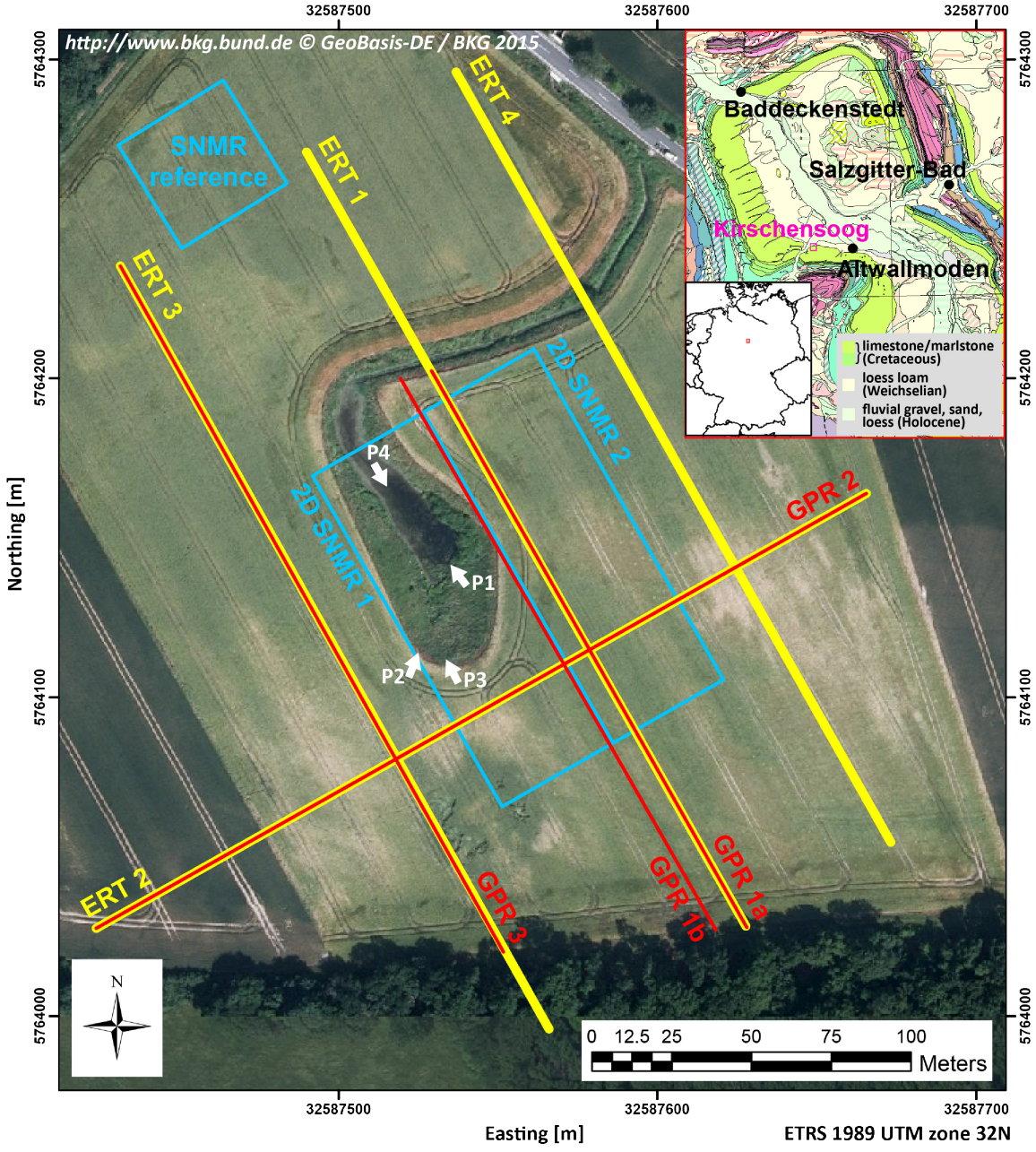

Figure 2: Survey area (magenta rectangle on geological map) and locations of ERT (yellow) and GPR (red) profiles as well as 2D SNMR survey setups (blue). White arrows P1 - P4 indicate approximate viewing directions of the pictures in Figure 1. Inlay: Geological map (NIBIS map service of LBEG) - shown area is indicated as red rectangle on the small map of Germany.

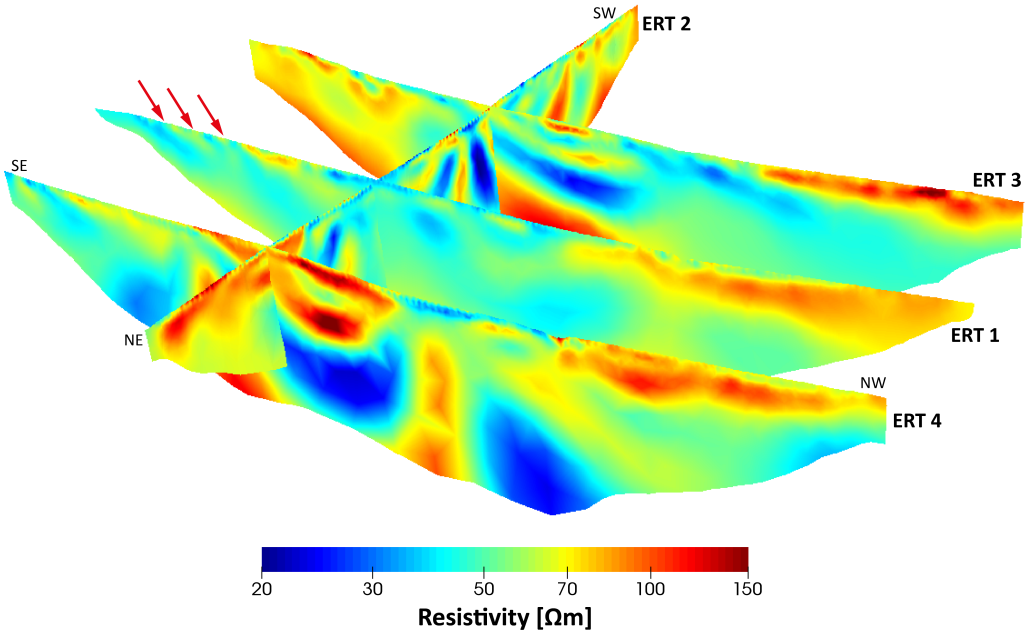

Figure 3: Resistivity models based on 2D inversion of four ERT profiles using BERT (Günther et al., 2006). Topography was considered during inversion as well as both Wenner-alpha and Wenner-beta data. Red arrows exemplarily indicate dipping structures (also seen as reflectors in GPR data – Figure 4).

additional measurements are required (e.g., focused 3D GPR measurements).
2D SNMR surveys were conducted (above and east to the karst spring) according to a loop layout suggested by Jiang et al. (2015), i.e., using a 120 m × 40 m transmitter loop while recording simultaneously at six overlapping 40 m × 40 m receiver coils and one reference loop (for noise cancellation). No signal of free water could be observed. Hence, if the spring is fed by a large-scale (several meters in each dimension) water-filled cavity, it must be either located further away from the karst spring or in greater depths (several tens of meters or more) or both as deducted from synthetic studies.

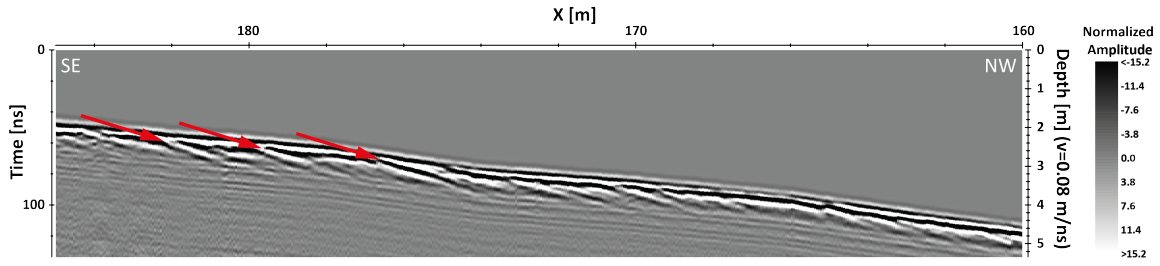

Figure 4: GPR data (200 MHz; SE end of profile GPR 1a; processed using REFLEXW (Sandmeier, 2014)) shows dipping reflectors (exemplary indicated by red arrows; also seen in resistivity models - Figure 3) in areas of thin soil cover.

4 Laboratory Studies

Soil and rock samples were taken for laboratory analysis to complement the field data and support their interpretation. The soil samples of the clay-rich cover layer were subject to three types of laboratory measurements. Firstly, laboratory 4-point-resistivity measurements resulted in approximately 20 Ωm (about 50 mS/m) which is common for clay-rich soil. Secondly, the dielectric spectroscopy revealed a wave attenuation of about 50-60 dB/m. This confirms the results of TDR probe measurements in the field and explains the limited depth of investigation using GPR. And finally, laboratory NMR (Figure 5 bottom right; green line) only detected very little free but mostly claybound water. But the latter cannot be detected in the field by surface NMR.

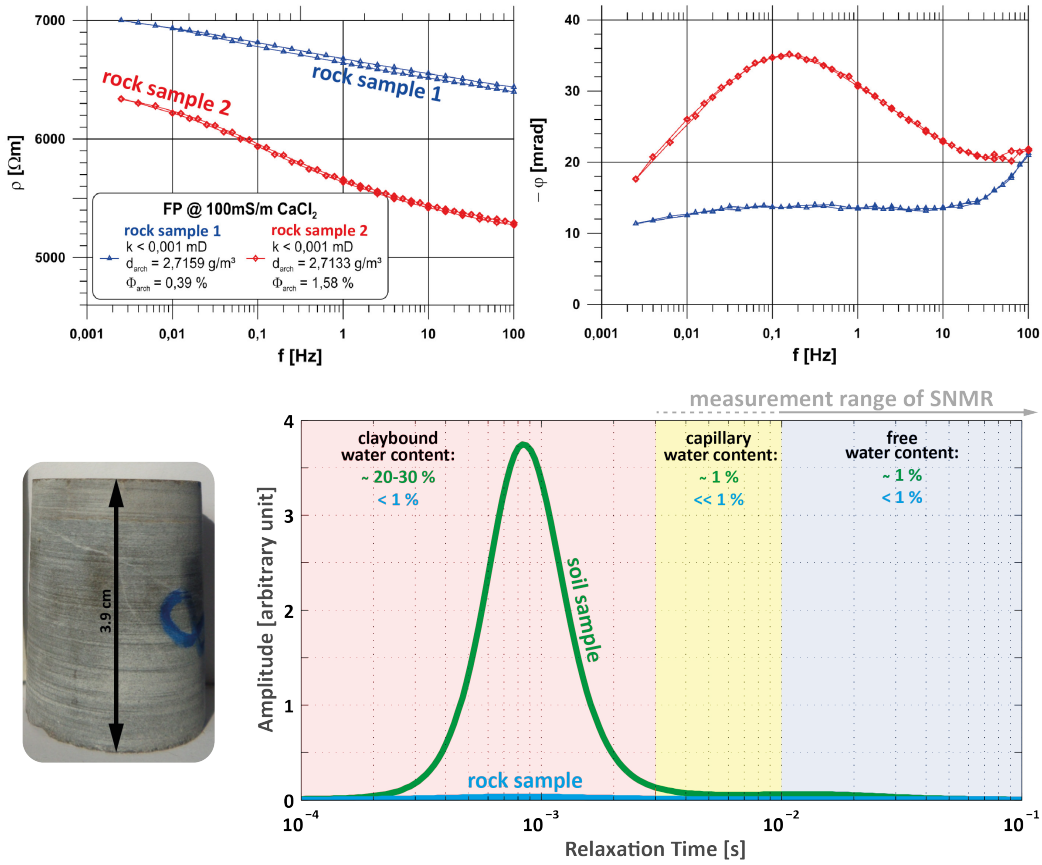

Figure 5: Laboratory results. *Top*: IP spectra of two saturated limestone samples with electrical resistivity (left) and phase shift (right) in dependence on frequency f. The related petrophysical results namely hydraulic permeability k, Archimedean density d_{arch} and Archimedean porosity Φ_{arch} of both samples are specified. *Bottom left*: Limestone sample from survey area. *Bottom right*: Exemplary NMR relaxation time distributions of a soil sample with in-situ moisture content (green) and a saturated rock sample (cyan). Values for claybound, capillary and free water content were deducted based on measurements of three soil and five rock samples.

The rock samples were also analysed by different laboratory methods. Only very little water – less than 1% of free and claybound water – were detected by laboratory NMR (Figure 5 bottom right; cyan line). Pycnometer and permeameter studies showed that

the limestone samples are dense rocks with little porosity and low permeability. Spectral induced polarisation (IP) measurements (Figure 5 top) showed very high resistivities ($> 5000\,\Omega$m) suggesting that the rock samples are very dense. At the same time there is a distinct phase maximum observed at f = 0.2 Hz which is rather unusual for dense rocks.

5 Interpretation and Outlook

The dipping structures obtained in the resistivity models as well as in the GPR data are possibly related to the bedding of limestone or fissures/fractures. The rather low in-situ resistivity might be an indication of disruption and presence of fluids or clay-filled fractures. On the other hand, SNMR observed no signal of capillary nor free water and, therefore, a large-scale water-filled cavity in close proximity of the spring in shallow depth can be excluded. But it is still unclear why the resistivity of the limestone obtained in the field is significantly lower compared to the laboratory results. Is the studied sample representative for the formation? Can those differences be explained solely by rock moisture? Further measurements and analyses are needed to enhance understanding. For example, a focused high resolution 3D ERT and GPR investigation of an area with thin soil cover might be useful to obtain detailed information about the bedding and fissure system of the limestone. Furthermore, additional measurements at different targets within this karst system are intended, e.g. close to a deep not-filled sinkhole with steep edges (offering outcrop information to support interpretation) or in between individual sinkholes within a closely spaced sequence (looking for possible causes of the aligned appearance of the sinkholes at this location).

6 Acknowledgements

We would like to thank Robert Meyer and Dieter Epping for their support during the fieldwork and Cynthia Minnich and Markus Loewer for the dielectric spectroscopy of the soil samples. We very much appreciate the permission and concessions by Konrad Wolf to measure on his land.

References

Günther, T., Rücker, C., & Spitzer, K.(2006). 3-D modeling and inversion of DC resistivity data incorparating topography - Part II: Inversion. *Geophysical Journal International*, *166*(2), 506-517.

Jiang, C., Müller-Petke, M., Lin, J., & Yaramanci, U. (2015). Magnetic resonance tomography using elongated transmitter and in-loop receiver arrays for time-efficient 2-D imagging of subsurface aquifer structures. *Geophysical Journal International*, *200*(2), 824-836.

Knolle, F., & Jacobs, F.(1988). Die Karstgrundwassergewinnung am nördlichen Harzrand (Niedersachsen, Bundesrepublik Deutschland) und ihre Gefährdung. *Die Höhle*, *39*(3), 81-89.

Sandmeier, K.-J. (2014). *REFLEXW 7.5 - Windows 9x/NT/2000/XP/7/8- program for the processing of seismic, acoustic or electromagnetic reflection, refraction and transmission data.* (manual)

Crustal structure of the southern Polish Basin imaged by magnetotelluric surveys

Anne Neska[1], Waldemar Jóźwiak[1], and Borys Ladanivskyy[2]

[1]Institute of Geophysics, Polish Academy of Sciences, Warsaw, Poland, *anne@igf.edu.pl*
[2]Carpathian Branch of Subbotin Institute of Geophysics, National Academy of Sciences of Ukraine, Lviv, Ukraine

Abstract

The aim of this study is to provide a continuation to the electromagnetic investigation of the Teisseyre-Tornquist Zone (TTZ). The TTZ is a tectonic boundary crossing Poland in NW-SE direction. Intense research of this zone has taken place in Pomerania (NW Poland) in the past, resulting in spatially coinciding conductivity anomalies and seismic transition zones that are interpreted in terms of a collision zone of ancient continents and micro-plates. Here we present three new two-dimensional magnetotelluric models across the TTZ in central and SE Poland. Signatures of the tectonic border continue to be visible in these models, even if with modifications that increase with distance to the NW Polish models. Furthermore, we observe a not drastic but clear spatial deviation to the tectonic picture derived from seismics that deserves further attention.

1. Introduction: Geological and Geophysical Context

The target of this study, the Polish Teisseyre-Tornquist Zone (Fig. 1), has a scientific history of more than one hundred years. It cannot be recalled here, important aspects of it can be found in Krolikowski (2006) and Dadlez (2013). The key point is the controversy where the margin of the Precambrian East-European Craton (EEC) is and if there is a belt of Caledonian rocks in front of it. The problem is that the basement (presumably an assemblage of terranes accreted to Baltica in the Early Paleozoic) is not accessible to direct observation since it is covered by younger sediments. These sediments form the Polish Basin, the easternmost part of the epicontinental Permian Basin that extends through West and Central Europe (Van Wees et al. 2000). The siliciclastic rocks, carbonates, and thick evaporates are of Mesozoic and mainly Upper Permian (Zechstein) age. The axial and deepest part of the Polish Basin, called the Mid-Polish Trough, was inverted in Late Cretaceous-Paleocene times and is characterized by a complex system of salt structures. Especially (but not only) in this region the sediments reach such thicknesses that even boreholes cannot penetrate them (Fig. 2).

Hence geophysics is the only way to assess the question of ancient tectonic boundaries. Surveying the magnetic anomaly (Tornquist 1908) was the first method, or attempt, to define this border. A glimpse on a modern magnetic map of Poland (Fig. 3, Petecki et al. 2003) suggests that two regions have to be distinguished, one to the NE characterized by positive anomalies and strong heterogeneities, and the other one to the SW that is rather homogeneous and carries a negative anomaly. This division is such fundamental that it can even be seen from space and satellites (cf. Maus et al. 2002). The interpretation that the "positive" side is of Precambrian and the "negative" one of Paleozoic age is hence not surprising and has been pointed out by Petecki (2001a, b, in Krolikowski 2006). However, the tectonic picture shown in Fig. 1 is not based on the magnetic anomaly, but mainly on seismics. This method observes different Moho depths and crustal velocities on both sides of a broad transition zone with rather complicated structure, the course of which roughly follows the magnetic picture, especially in NW Poland (e.g. Janik et al. 2002, Guterch & Grad 2006). It is mainly this seismic transition zone that is referred to and mapped as TTZ today and which is a part of the Trans-European Suture Zone (TESZ) extending from the British Islands to the Black Sea. In NW Poland (Pomerania) as well as more to the west in NE Germany also magnetotelluric investigations gave results that were interpreted in terms of an ancient suture zone (Ernst et al. 2008, Schafer et al. 2011, in Neska 2016, Fig. 4).

Figure 1 Tectonic sketch of Poland after Guterch et al. (2003)

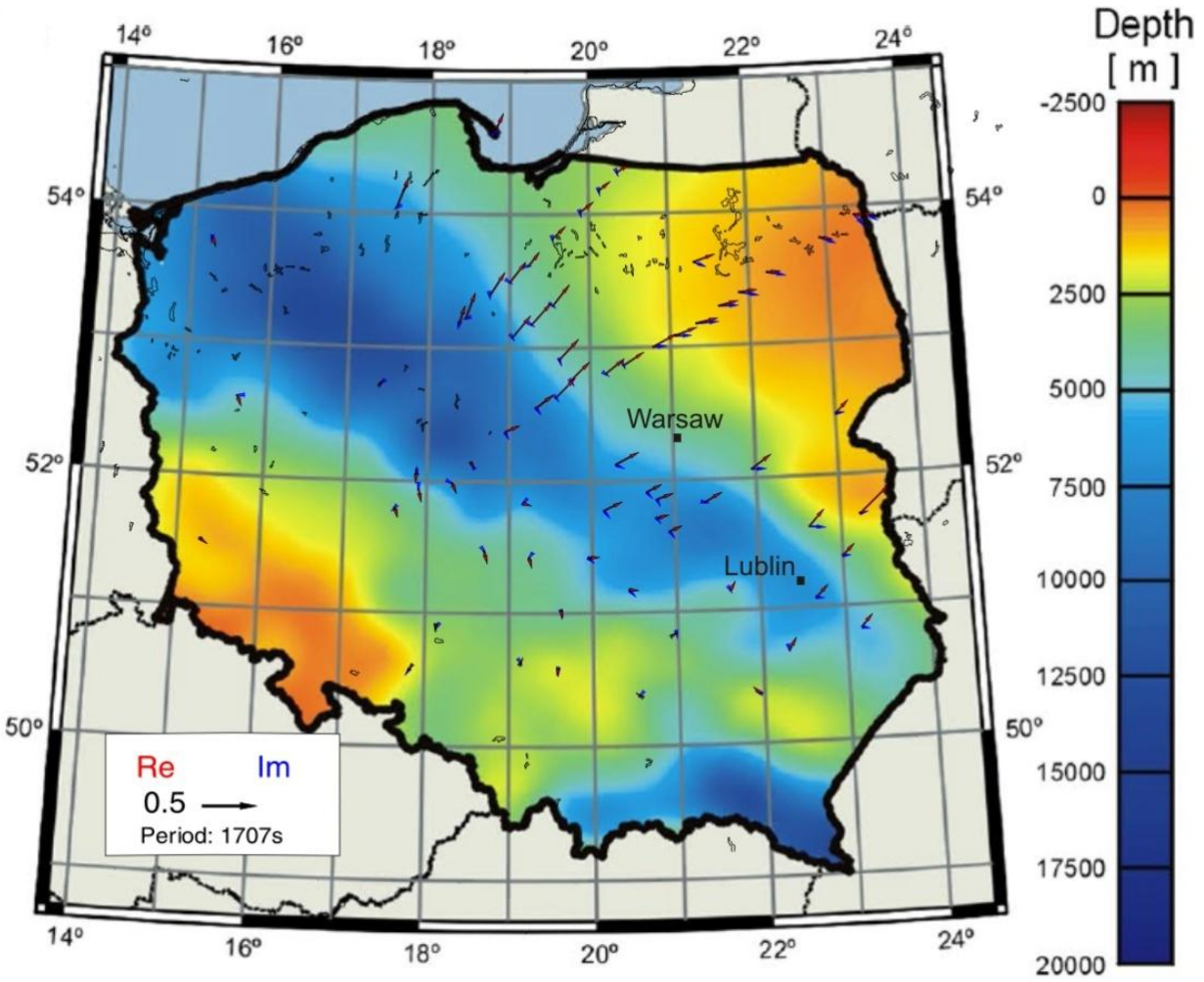

Figure 2 Map of sediment thickness to basement in Poland (Grad & Polkowski 2015) with induction arrows at 1700s superimposed on it. Note that for most regions real (red) arrows point away from greater depths and are perpendicular to isolines, but not for the Lublin Basin south of Warsaw.

2. Resistivity models for central and south-east Poland

New resistivity models (Fig. 4) have been obtained from three profiles in central and SE Poland that are described in the following. The first profile (no. 3 on Fig. 4) lies on a line running diagonally through Poland from SW to NE. It has a length of just under 300 km, consists of 13 stations, and coincides roughly with a seismic profile referred to in the literature as P4 (e.g., Guterch et al. 2006). Stations were measured partly in 1999 (NE part of profile) and partly in 2013/14 (in the SW). Data were processed with Egbert's code (Egbert & Booker 1986) and the remote-reference technique resulting in a consistent set of transfer functions covering almost the whole LMT range (10-10,000 s). The average strike direction has been determined to N15°W and transfer functions were rotated accordingly. A two-dimensional inversion of TE and TM mode and tipper has been performed by

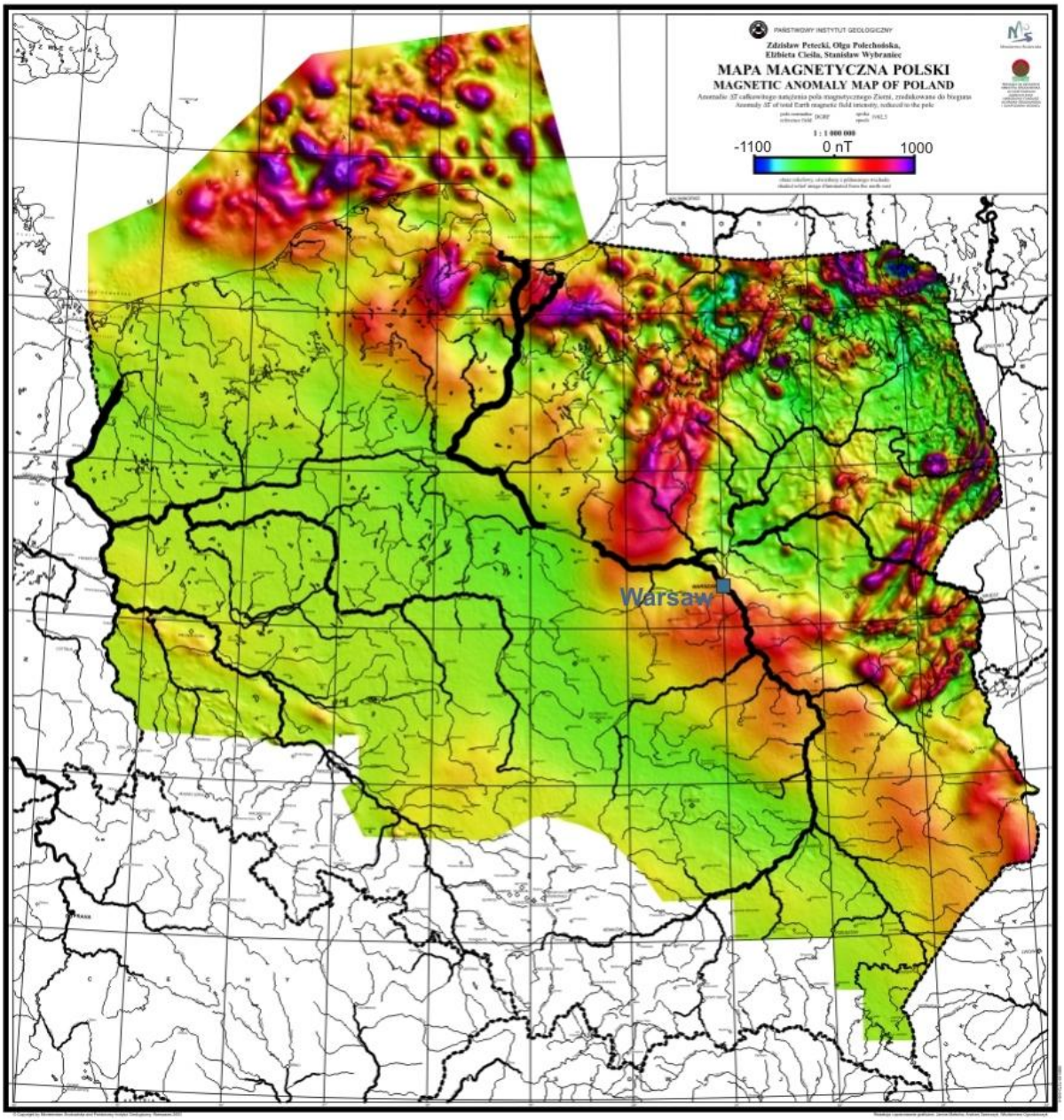

Figure 3 Magnetic map of Poland (Petecki et al. 2003, modified)

means of the REBOCC code (Siripunvaraporn & Egbert 2000). The final model has an RMS value of 2.19. The influence of the TE mode had to be somewhat limited by means of an enlarged error floor of 50 per cent for apparent resistivities and 5° for phases (while 20 per cent and 2° where used for the TM mode and 0.04 for both real and imaginary tippers) and by using an inversion result of only TM mode and tipper as starting model for the final joint inversion of all three transfer functions.

The next profile CZ-SI (after the towns Czestochowa and Siedlce, no. 4 on Fig. 4) comprises five stations distributed over a length of 200 km on a line running roughly 60 km south of Lodz and Warsaw. The LMT data were measured in 2012 and processed, again, with Egbert & Booker (1986). One station had serious problems with data quality. For the complete dataset, transfer functions below a few hundred seconds hint at another strike direction than longer periods, where it amounts, again, to N15°W. Hence only transfer functions (TE mode and tipper) >300s were subjected to a two-dimensional inversion by means of the REBOCC code after appropriate rotation. The final model had an RMS of 7.39 per cent which sounds much but is partly a result of the rather strict error floor (10 per cent for apparent resistivities, 3° for phases, 0.03 for tippers), and bad fitting concerns apparent resistivities much more than phases and tippers. The large station distance, the missing short-period range, and the data quality problems led to a model that is less informative than the other ones presented here (note that the uppermost 10 km are not resolved and not shown here), but the difference to the previous model (see next section) is constrained.

The last profile named C05 (no. 5 in Fig. 4) was measured in 2006. Five LMT stations were distributed over 180 km along a line some dozens of km off the Polish-Ukrainian border. The data were processed with a code described in Korepanov et al. (2014) and checked with Egbert & Booker (1986) and Egbert (1997), transfer functions were rotated accordingly to the strike direction of N30°W. Two-dimensional inversion of all three transfer functions was carried out with the REBOCC code and converged well with a final RMS of 1.07 after operations to down-weight the influence of the TE mode similarly as described for the first model.

All models shown in Fig. 4 (with the exception of CZ-SI) show shallow, high-conductive surface layers that can be assigned to the sediments. These contain a known aquifer of high salinity that extends through the whole North-German-Polish Basin (cf. Neska 2016 and citations therein). In lower crustal to upper mantle depth we find high (several hundred Ωm) to very high (up to 10,000 Ωm) resistivity values. Their lateral differences and their interruptions by deep-reaching areas of moderate resistivity deserve further consideration which, however, exceeds the scope of this work. Most interesting in terms of the question whether Pomeranian structures do continue in the new models are mid-crustal conductors with resistivity values not higher than about 2 Ωm. Such low resistivities are most likely due to a combination of ionic and electronic conduction. The latter is (if of larger scale) bound to an interconnected network of graphite or pyrrhotite which can develop from an original material rich in alum or black shale under metamorphic conditions of a collision zone and in the middle crust (Schafer 2011 and citations therein). Such a high-conducting structure that is indicative of a tectonic collision is undoubtedly present in the diagonal profile, it is (at most) slightly indicated in CZ-SI, and it is absent in C05. Implications are discussed in the next section.

3. Discussion, Conclusions, and Outlook

The prominent high-conductive anomaly in mid-crustal depth associated with the TESZ in Pomerania remains visible on the mid-Polish profile with very similar depth (10-20 km) and resistivity values (< 2 Ωm). This suggests that the underlying tectonic structure is of the same nature

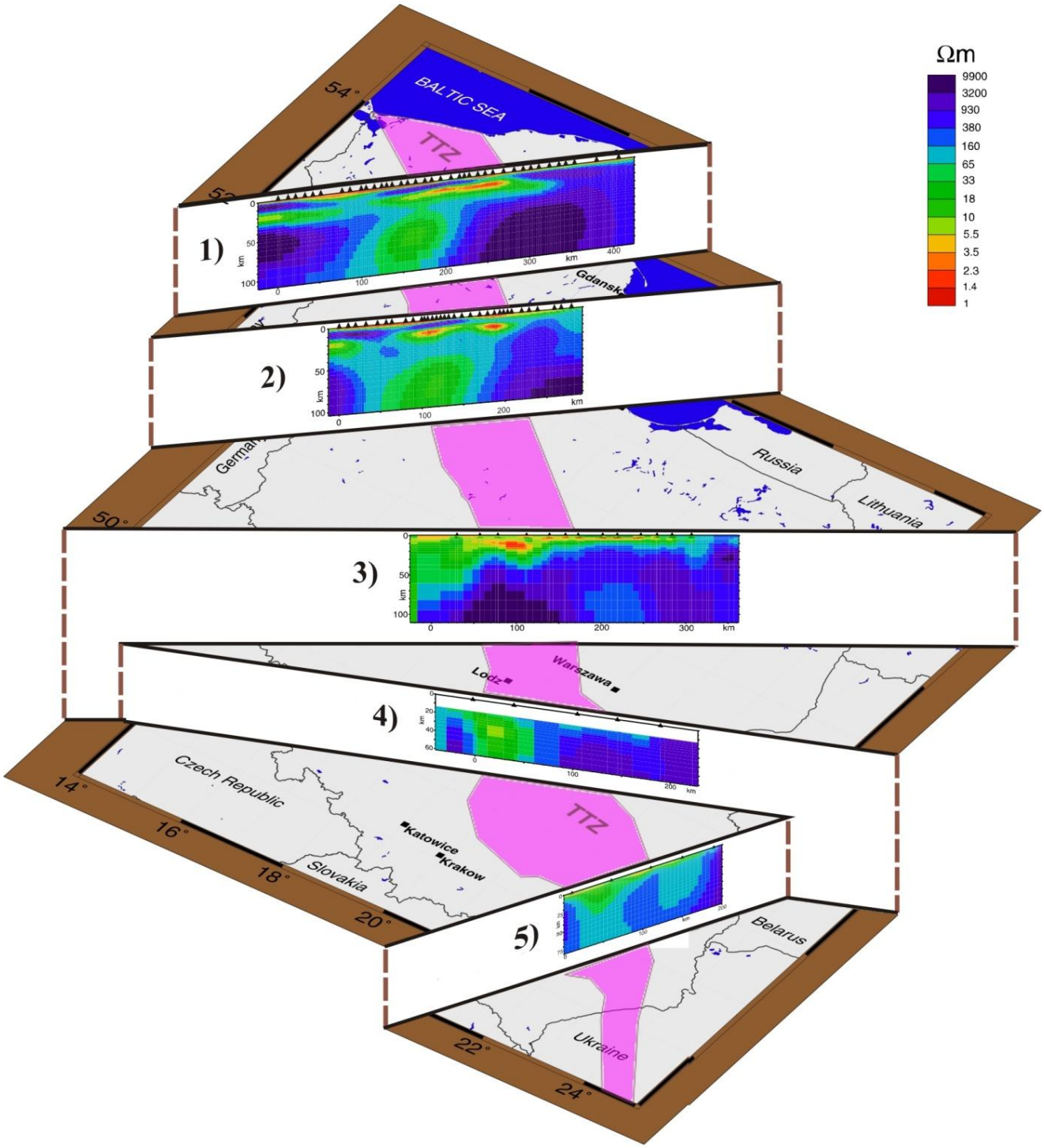

Figure 4 Two-dimensional models of electrical resistivity related to their location in Poland and to the Teisseyre-Tornquist-Zone (TTZ, in pink color) according to Fig. 1. The models LT7 (1) and P2 (2, both after Ernst et al. 2008), mid- or diagonal Polish one (3), CZ-SI (4), C05 (5) have equal resistivity and vertical scales. Note the spatial coincidence of the NE boundary of the TTZ with conductive mid-crustal zones for (1) and (2) and the slight deviation between them for (3), (4), and (5).

in both places, which is what one would expect from the known tectonic picture. In central Poland the anomaly appears relatively focused, whereas it has a laterally relatively extended, even bimodal, structure in Pomerania (where, however, a model regularization that promotes horizontal smoothing has been used, Ernst et al. 2008). This double anomaly can be interpreted as connected to two orogenic events or their remnants, the NE one to the Caledonian Deformation Front and the southern one to the Variscan Deformation Front following Jozwiak (2012) and Narkiewicz & Dadlez (2008). The convergence of both deformation lines in central Poland suggested by the singular anomaly is in accordance with expectations from the general tectonic picture. Another interesting point is that above the anomaly, resistivity is enhanced in comparison to the horizontal surrounding. This can be explained as a consequence of salt tectonics, which is characteristic of this part of the Polish Basin, during a later geologic epoch. Details will be treated in a separate work.
The next profile to the SE referred to as CZ-SI shows another picture. A zone of enhanced conductivity is present in a location (to the W of the model) not conflicting with an interpretation as a continuation of the previously discussed anomalies. On the other hand, its depth (~30 km) and resistivity (5-10 Ωm) characteristics is too different to reflect just the same 2D structure intersected in another place. Comparison with the mapped conductivity anomaly pattern (Fig. 5) rather suggests that this conductive zone could be the end of the anomaly (or anomalies) encountered to the NW. To settle this and to overcome the problems about the deviating strike direction at short periods a three-dimensional study of this area is necessary. This remains a task for the near future.

The model to the SE (C05) is characterized by a trough-like structure with ~30 km depth and moderate resistivities of a few tens of Ωm. High-conductive layers are found only very close to surface. Thereby this model confirms the results of older, adjacent profiles on both sides of it (Adam et al. 1997, Pushkarev et al. 2007). According to this, very low resistivities of ~1 Ωm at mid-crustal depths as in NW and central Poland can be ruled out for this region.

Hence in NW to central Poland the TESZ is accompanied by prominent mid-crustal conductivity anomalies and in the SW only by moderate ones. A further difference between both regions comprises the relation to the tectonic model that is based on seismics. The TESZ according to seismic models (e.g., Blundell et al. 1992, Guterch et al. 2003 and citations therein) and the TESZ indicated by the position of conductivity anomalies coincide spatially very well in Pomerania (Fig. 4). In central and SW Poland there is a slight but systematic deviation between both zones. The zones of enhanced conductivity lie within the “seismic” TESZ, but not directly in front of the presumed EEC boundary as in the NW. The distance between both patterns amounts to ~80 km on the mid-Polish profile (for comparison, the maximal difference between this border after various authors is just under 50 km, in Grad & Polkowski 2015) and it does not decrease to the SE. Generally speaking, the slight sinistral turn that the seismic TTZ performs between Warsaw and the Holy Cross Mountains (the latter are marked with brown color in Fig. 1) is not observed in the running of mid-crustal conductive zones. Interestingly, this area is in gravity (Malopolska High, Krolikowski 2006) and magnetic maps (Petecki et al. 2003) characterized by strong positive anomalies which are indicative of a magmatic intrusion. Similar anomalies visible on the EEC in NW Poland are interpreted as caused by Vendian (i.e. Precambrian) rifting magmatism (Krolikowski 2006). On the other hand, seismic authors describe this area as a sedimentary basin

filled with up to 10 km thick sediments and sometimes refer to it as the Lublin Basin[1] (in Grad & Polkowski 2015) which, astonishingly, does not influence the resistivity pattern imaged by induction arrows (Fig. 2) and the HMT (Fig. 5). This means that the pleasant situation of Pomerania, where various geophysical results allow for a consistent tectonic interpretation, does not simply continue. Rather the pictures delivered by various geophysical methods in central to SW Poland demand another way of tectonically relevant integration than in the NW. Another light is shed on the tectonic interpretation of the TTZ by Berthelsen (1998) and Mazur et al. (2015) who suggest that the (seismic) TTZ is a Precambrian intra-EEC suture and the proper Caledonian suture between EEC and Paleozoic Europe is situated much more to the west and not as evident in seismic sections due to thick younger sediments.

From a magnetotelluric point of view we can say that, if the TTZ was marked in accordance with the resistivity pattern instead of seismic velocities, the resulting picture in central and SE Poland would be different and much more similar to the division suggested by the magnetic map (Fig. 3).

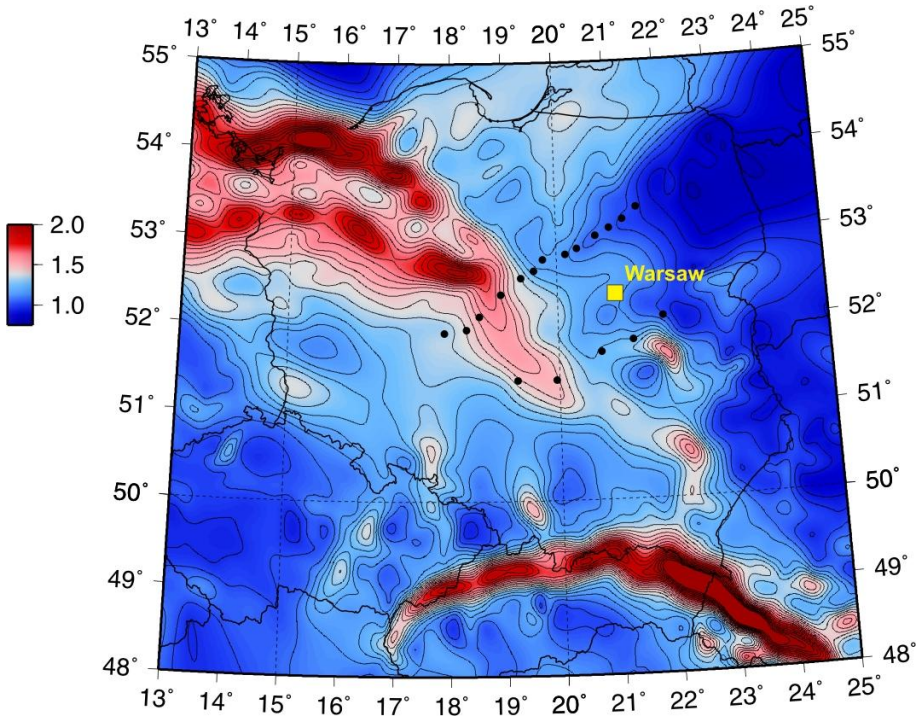

Figure 5 Amplitude of the maximum eigenvalue of the Horizontal Magnetic Tensor (HMT, Jozwiak 2012) at 1800s for Poland. Black points are stations of the diagonal and CZ-SI profiles (3 and 4 in Fig. 4). Note that the running of the well-conducting anomaly that extends from NW to central and SE Poland (red and light-red colors) differs from the northern margin of the TTZ (cf. Fig. 1) at latitudes of both profiles.

[1] Note that the according to our knowledge original, or underlying, tectonic outline of Central Europe by Berthelsen (http://www.oberrheingraben.de/Tektonik/Karte%20Gebirgsbildungen%20Europa.htm) does not interpret this region south of Warsaw as either Precambrian or Paleozoic basement, but describes it only in terms of seismics (i.e., greater Moho depth) and later tectonic events (Upper Cretaceous-Paleocene basin uplift).

Acknowledgements

This work was supported within statutory activities No 3841/E-41/S/2016 and by grant No 2011/01/B/ST10/07046 of the Ministry of Science and Higher Education of Poland. It has been partially financed from the funds of the Leading National Research Centre (KNOW) received by the Centre for Polar Studies for the period 2014-2018.

References

Ádám, A., Ernst, T., Jankowski, J., Jozwiak, W., Hvozdara, M., Szarka, L., Wesztergom, V, Logvinov, I., and Kulik, S. (1997), Electromagnetic induction profile (PREPAN95) from the East European Platform (EEP) to the Pannonian Basin, *Acta Geodaetica et Geophysica Hungarica* **32**, 203-223.

Berthelsen, A. (1998), The Tornquist Zone northwest of the Carpathians: an intraplate pseudosuture, *GFF* **120**, 223-230, doi: 10.1080/11035899801202223.

Blundell, D. J., Freeman, R., Mueller, S., and Button, S., eds. (1992), A Continent Revealed: The European Geotraverse, Structure and Dynamic Evolution. Cambridge University Press.

Dadlez, R. (2000), Pomeranian Caledonides (NW Poland), fifty years of controversies: a review and a new concept, *Geol Quart* **44 (3)**, 221-236.

Egbert, G.D. and Booker, J.R. (1986), Robust estimation of geomagnetic transfer functions, *Geophysical Journal of the Royal Astronomical Society* **87**, 173-194.

Egbert, G.D. (1997), Robust multiple-station magnetotelluric data processing, *Geophys J Int* **130**, 475–496.

Ernst, T., Brasse, H., Cerv, V., Hoffmann, N., Jankowski, J., Jozwiak, W., Kreutzmann, A., Neska, A., Palshin, N., Pedersen, L. B., Smirnov, M., Sokolova, E., and Varentsov, I. M. (2008), Electromagnetic images of the deep structure of the Trans-European Suture Zone beneath Polish Pomerania, *Geophys Res Lett* **35**, L15307, doi: 10.1029/2008GL034610.

Grad, M. and Polkowski, M. (2015), Seismic basement in Poland, *Int J Earth Sci (Geol Rundsch)*, doi: 10.1007/s00531-015-1233-8.

Guterch, A., Grad, M., Spicak, A., Bruckl, E., Hegedus, E., Keller, G.R., Thybo, H., and CELEBRATION 2000, ALP 2002, SUDETES 2003 Working Groups (2003), An Overview of Recent Seismic Refraction Experiments in Central Europe , *Stud. Geophys. Geodet.* **47**, 651-657.

Guterch, A. and Grad, M. (2006), Lithospheric structure of the TESZ in Poland based on modern seismic experiments, *Geol Quart* **50(1)**, 23-32.

Janik, T., Yliniemi, J., Grad, M., Thybo, H., and Tiira, T. (2002), Crustal structure across the TESZ along POLONAISE'97 seismic profile P2 in NW Poland, *Tectonophysics* **360**, 129-152, doi: 10.1016/S0040-1951(02)00353-0.

Jankowski, J., Ernst, T., and Jóźwiak, W. (2004), Effect of thin near-surface layer on the geomagnetic induction arrows: An example from the East European Platform, *Acta Geophysica Polonica* **52 (3)**, 349-361.

Jozwiak, W. (2012), Large-Scale Crustal Conductivity Pattern in Central Europe and Its Correlation to Deep Tectonic Structures, *Pure and Applied Geophysics* **169**, 1737-1747.

Korepanov, V., Ladanivskyy, B., and Leonov, S. (2014), New user-friendly program for field data processing, Extended Abstract, 22nd Electromagnetic Induction Workshop, Weimar, Germany, 24 – 30 August 2014.

Królikowski, C. (2006), Crustal-scale complexity of the contact zone between the Palaeozoic platform and the East-European Craton in the NW Poland, *Geol Quart* **50**, 33–42.

Maus, S., Rother, M., Holme, R., Luhr, H., Olsen, N., and Haak, V. (2002), First scalar magnetic anomaly map from CHAMP satellite data indicates weak lithospheric field, *Geophys Res Lett* **29(14)**, doi: 10.1029/2001GL013685.

Mazur, S., Mikolajczak, M., Krzywiec, P., Malinowski, M., Buffenmyer, V., and Lewandowski, M. (2015), Is the Teisseyre-Tornquist Zone an ancient plate boundary of Baltica?, *Tectonics* **34 (12)**, 2465–2477, doi: 10.1002/2015TC003934.

Narkiewicz, M., and Dadlez, R. (2008), Geological regional subdivision of Poland: general guidelines and proposed schemes of sub-Cenozoic and sub-Permian units, *Prz. Geol.* **56**, 391–397, in Polish with English abstract.

Neska, A. (2016), Conductivity Anomalies in Central Europe, *Surveys in Geophysics* **37 (1)**, 5-26, doi: 10.1007/s10712-015-9349-8

Petecki, Z. (2001a), Magnetic evidence for deeply buried crystalline basement southwest of the Teisseyre-Tornquist Line in NW Poland, *Acta Geoph Pol.* **4**, 509–515.

Petecki, Z. (2001b), Charakter i geometria podloza magnetycznego NW Polski, Panstw. Inst. Geol., Centr. Arch. Geol. Warszawa.

Petecki, Z., Polechonska, O., Ciesla, E., and Wybraniec, S. (2003), Magnetic map of Poland, scale 1:500,000, Pol Geol Ins, Warsaw.

Pushkarev, P. Yu., Ernst, T., Jankowski, J., Jozwiak, W., Lewandowski, M., Nowozynski, K., and Semenov, V.Yu. (2007), Deep resistivity structure of the Trans-European Suture Zone in Central Poland, *Geophys J Int* **169**, 926-940.

Schäfer, A., Houpt, L., Brasse, H., Hoffmann, N., and EMTESZ Working Group (2011), The North German Conductivity Anomaly revisited, *Geophys J Int* **187**, 85-98, doi: 10.1111/j.1365-246X.2011.05145.x.

Siripunvaraporn, W. and Egbert, G. (2000), An efficient data-subspace inversion method for 2-D magnetotelluric data. *Geophysics* **65(3)**, 791-803.

Tornquist, A. (1908), Die Feststellung des Südwestrandes des baltisch-russischen Schildes und die geotektonische Zugehörigkeit der ostpreussischen Scholle, *Schriften der Phys.-Ökonomischen Gesellschaft* **49 (1)**, 1–12, Königsberg.

Van Wees, J.D., Stephenson, R.A., Ziegler, P.A., Bayer, U., McCann, T., Dadlez, R., Gaupp, R., Narkiewicz, M., Bitzer, F., and Scheck, M. (2000), On the origin of the southern Permian Basin, Central Europe, *Marine Pet Geol* **17(1)**, 43-59.

Evaluation of a SQUID-based receiver for transient electromagnetics in Bad Frankenhausen, Germany

Raphael Rochlitz[1], Thomas Günther[1], Matthias Queitsch[2], Nina Kukowski[2], Andreas Chwala[3], and Ronny Stolz[3]

[1]*Leibniz Institute for Applied Geophysics - Hannover, Germany*
[2]*Friedrich Schiller University - Jena, Germany*
[3]*Leibniz Institute of Photonic Technology - Jena, Germany*

Abstract

Within the framework of the multidisciplinary research project called INFLUINS, INtegrated FLUid dynamics IN Sedimentary basins, we use a highly sensitive magnetic field receiver based on Superconducting Quantum Interference Devices (SQUIDs) for the transient electromagnetic method and compare its performance specifications with a commercially available induction coil.
Four fixed loops TEM measurements with 10 - 20 receiver stations each have been conducted along a survey line perpendicular to the known geologic strike direction at the test site *Esperstedter Ried* in Northern Thuringia, Germany.
The signals of the SQUID receiver provide significantly better quality and are less affected by natural and man-made noise sources than the ones of the induction coil, which is proved by data error and noise measurement analysis. As a result, the 1D inverse modeling results of the SQUID data show lower misfit ratios and are more reliable compared to the coil.

1 Introduction

In transient electromagnetic (TEM) surveys, usually the time derivative dB_z/dt of the vertical magnetic field component B_z is recorded with induction coil receivers. Alternatively, it is possible to measure directly the vector components B_x, B_y and B_z with magnetic field sensors, so-called magnetometers, which shows several advantages pointed out by Asten & Duncan, (2012).
Until 1990, only induction coil receivers were used for TEM due to the fact that magnetic field sensors did not provide the desired accuracy to compete with them (Telford, 1990). Especially since the beginning of the 21st century, the development of highly accurate B-field receivers based on Superconducting QUantum Interference Devices (SQUIDs) lead to new opportunities for TEM measurements.
Today, especially low- and high-temperature supcerconductor SQUIDs, named LTS and HTS, are in routine field use as receivers for TEM exploration surveys (Le Roux & Macnae, 2007; Chwala et al., 2011; Vallée et al., 2011; Smith, 2014). In all these studies, LTS SQUID sensors clearly outperform other magnetic field receivers such as HTS SQUIDs, optically pumped magnetometers (OPM) and fluxgate magnetometers as well as conventional or specially developed induction coils.

Successful exploration studies in low-noise areas are described by Le Roux & Macnae, (2007), Webb & Corscadden, (2009) and Smit & Le Roux, (2009). In this work, we applied an LTS SQUID based magnetometer for TEM in a culturally disturbed environment, the test site *Esperstedter Ried*, and evaluate the performance specifications of this SQUID receiver in comparison with a commercially available induction coil.
Subsequently, the survey area and the field measurements are introduced. Afterwards, decay curves, data errors, noise records and first inverse modeling results are presented. It is concluded with a summary of important results and an outlook towards future work.

2 Survey details

2.1 Investigation area

The survey area, which includes the Esperstedter Ried, is situated in the East of Bad Frankenhausen (Fig. 1) in northern Thuringia, Germany. This area is of great interest for geological surveys due to subrosion effects, observed since decades (PGL, 1926). For our TEM survey, especially two facts are important. On the one hand, saline waters, which even reach the surface, lead to a highly conductive overburden, and thus, to theoretical advantages for the *B*-field receiver (Asten & Duncan, 2012). On the other hand, data of an additional seismic and large-scale ERT survey, described by Rochlitz, (2015), are available at the test site, which enables to better interpret the recorded TEM data.

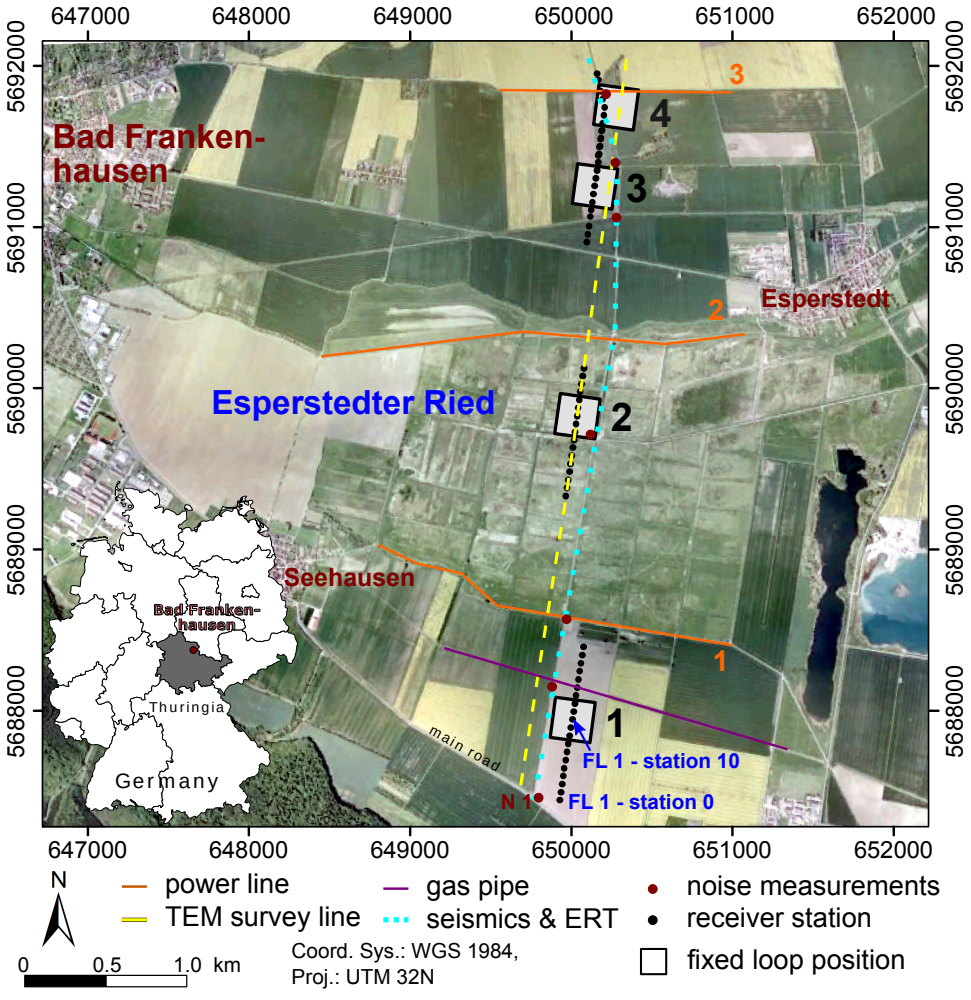

Figure 1: Test site *Esperstedter Ried* near Bad Frankenhausen and survey design.

2.2 Instruments

The transmitter equipment, depicted in Fig. 2 a), consists of the following instruments:

- 9 x 12 V batteries
- Crone - PEM transmitter - max. current: 20 A
- EMIT - SMARTem transmitter controller - waveform adjustment and timing

The receiver systems, shown in Fig. 2 b), are described below:

- 3-component LTS SQUID receiver
- Supracon - SQUID sensor controller, called OrangeBox
- 1-component (B_z) Crone receiver coil
- EMIT SMARTem24 field computer - 12 channels with 24 bit ADCs

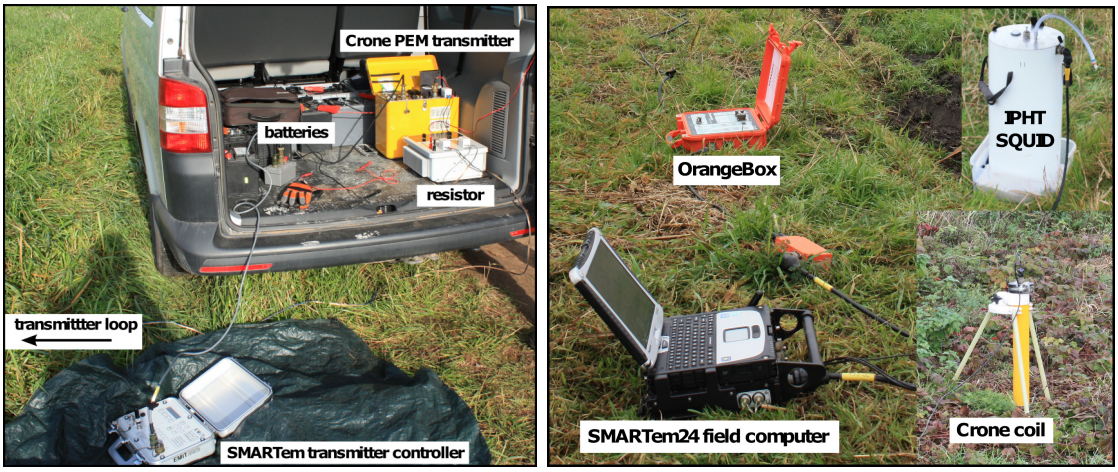

(a) Transmitter unit **(b)** Receiver unit

Figure 2: TEM instruments.

2.3 Survey information

The survey took place from 17th - 21st November 2014. In order to reach an optimum signal to noise ratio (SNR) with a maximum amount of measured data, we decided for the fixed loop configuration, which provides a comparatively high source signal strength with low logistic effort, since the transmitter loop (Tx) needs to be placed only once to cover 1 km of the survey line. Four fixed loops with 10 - 20 receiver stations each were placed along a survey line (Fig. 1) with gaps due to power lines and gas pipes. Furthermore, noise measurements were conducted in order to characterize the two different receiver systems and the electromagnetic noise at different locations within the test site. Important survey parameters are listed below:

- Transmitter current: 11.8 - 11.0 A (decreasing with battery voltage)
- Transmitter loop size: 250 x 250 m, receiver station offset: 50 m
- 50 % duty cycle: 2 s / 0.5 Hz, downward ramp: 85 μs
- Number of gates: 39
- Number of stacks within one reading: 128
- Number of readings: 5 - 11 depending on noise level

3 Results

3.1 Noise measurements

In Figs. 3 a) and b), the noise record N 1 (Fig. 1) at FL 1 adjacent to the main road, is presented in time and frequency domain, respectively. As expected, only the horizontal components of the SQUID as well as the coil are affected by sferics (Fig. 3 a). The SQUID-Z signal is approximately constant over time, whereas the coil signal varies, which can be attributed to the traffic and the higher spatial sensitivity of the coil. Especially at frequencies less than 100 Hz and explicitly at 50 Hz, the SQUID-Z noise is significantly lower, as can be observed in Fig. 3 b).

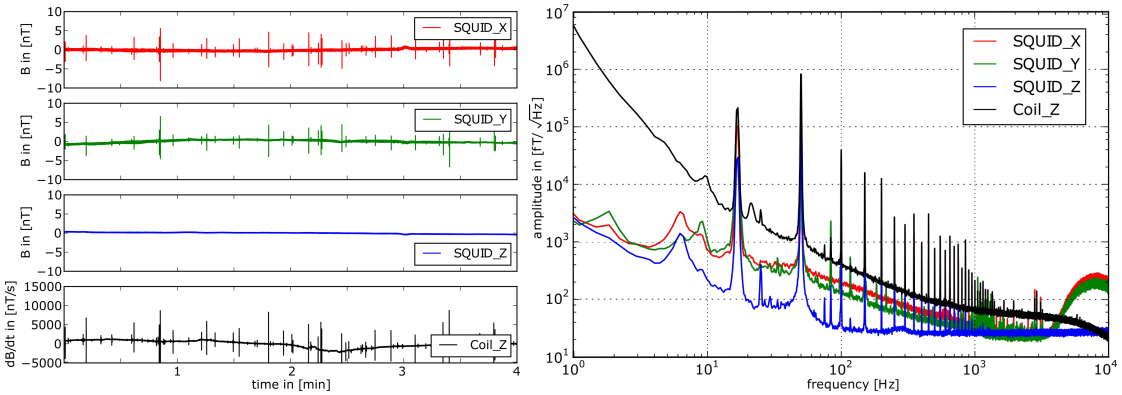

(a) **(b)**

Figure 3: Noise measurements in 50 m distance to the main road: a) time-domain, b) frequency-domain.

3.2 SQUID and coil decays

As an example, decay curves of both receivers are depicted at two locations: the central loop position of FL 1 (Fig. 4 a) and the receiver station adjacent to the main road (Fig. 4 b). The Z-component of the SQUID sensor shows a significantly better data quality compared to the coil at times later than 100 ms at both positions. The horizontal components are added for the sake of completeness, but are not discussed for brevity.

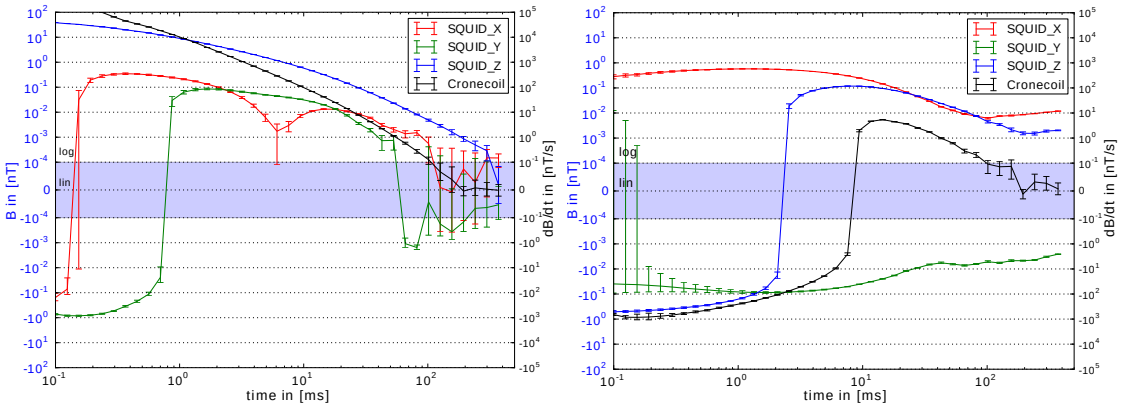

(a) FL 1 - station 10, central loop pos. (Fig. 1) **(b)** FL 1 - station 0, adjacent to main road (Fig. 1)

Figure 4: Decay curve examples.

3.3 Data errors

In order to deliver a quantitative representation of data errors, the normalized standard deviation was calculated for every time gate at all receiver stations. In Fig. 5, the percentage data error is illustrated for the Z-components of all receiver stations at FL 1. Overall, the SQUID sensor shows better data quality after 100 ms (red line in Fig. 5). Furthermore, it is less affected by the gas pipe and the power line, but shows higher data errors at early times < 10 ms close to the road. The noisy gates around the polarity switch at out-of-loop receiver positions occur earlier in the B-field signal. Thus, there is an advantage at late times, especially at offsets greater than 300 m to the center of Tx.

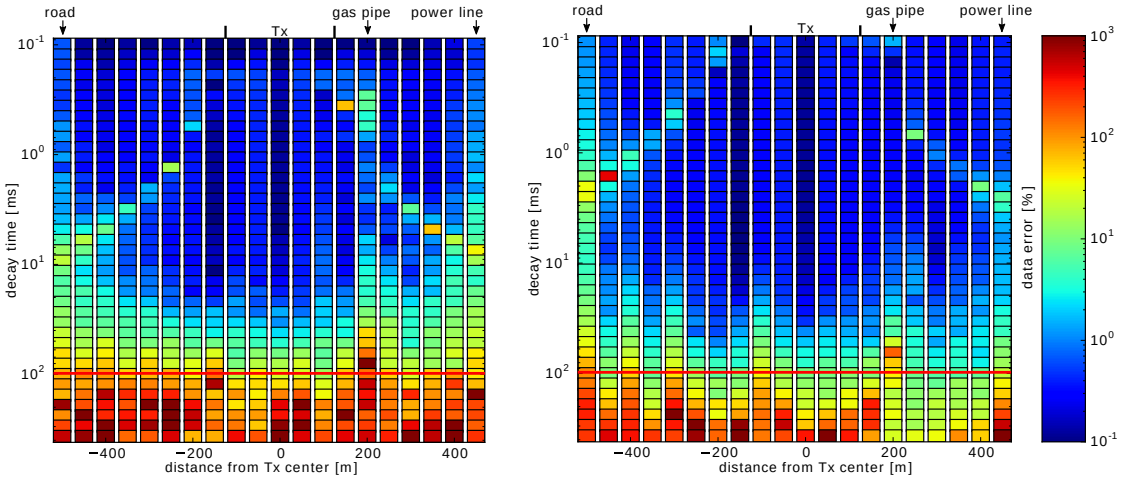

(a) Coil **(b)** SQUID-Z

Figure 5: Data errors (normalized standard deviation) for each time gate and every receiver station of FL 1, red line = 100 *ms* decay time.

3.4 Inverse modeling results

In general 1D Levenberg-Marquardt inverse modeling results by using the code *Beowulf* (Raiche, 2008) do not significantly vary in terms of layer depths and resistivities between coil and SQUID-Z data. An example, the 1D inverse modeling results of the FL 1 dataset, based on the same starting model, is presented in Fig. 6. The 1D starting model with 7 layers is based on a trial-and-error fit at the central loop position of Fl 1. For more information, it is referred to Rochlitz, (2015).

The coil data inversion (Fig. 6 a) shows more artifacts, which occur at the road, the gas pipe and the power line, whereas inverse modeling results of the SQUID-Z component (Fig. 6 b) are solely disturbed by the gas pipe. Furthermore, in the central part, the obtained resistivity distribution from the SQUID-Z data appears more consistent in respect to an approximately 1D subsurface structure in the uppermost 300 m (Rochlitz, 2015).

In order to gain a first quantitative view of the inversion quality, it is possible to calculate the misfit ratio between the measured data and the final forward response for each time gate and receiver station. The misfit ratios according to the previously presented *Beowulf* 1D inverse modeling results of Fl 1 are depicted in Fig. 7. Considering the logarithmic color scale, the overall misfit ratio of the SQUID data inversion (Fig. 7 b) is significantly lower than the one of coil data inversion (Fig. 7 a).

Another important fact is that the misfit ratio related to the SQUID shows nearly a Gaussian distribution. Exceptions occur only due to the gas pipe and polarity switches. In contrast, particularly at early times until 1 ms, the misfit ratio related to the coil is systematically biased according to in-loop and out-of-loop receiver stations. Surprisingly, this fact has no noticable impact on the inverse modeling results, depicted in Fig. 6.

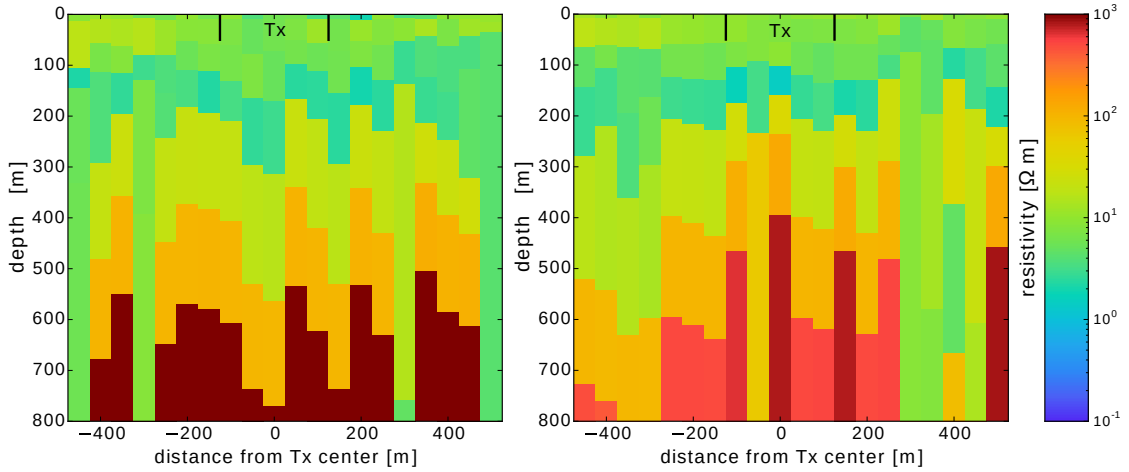

(a) Coil **(b)** SQUID-Z

Figure 6: Coil and SQUID-Z 1D inversion results of the FL 1 dataset

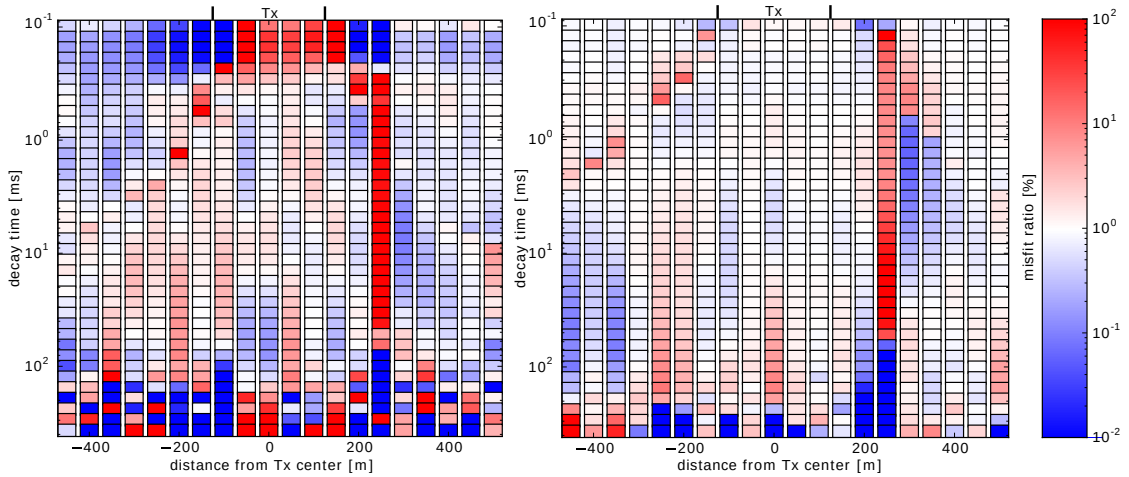

(a) Coil **(b)** SQUID-Z

Figure 7: Coil and SQUID-Z inversion misfit ratio according to the results in Fig. 6.

4 Summary and Outlook

We applied an LTS SQUID-based magnetic field receiver in comparison with a commercially available induction coil for TEM measurements. It was focused on the presentation of the results according to the datasets of FL 1. Nevertheless, the obtained results, summarized subsequently, are valid for the data of the other 3 fixed loop positions within our test site as well (Rochlitz, 2015).

The SQUID sensor shows advantages over the coil in every respect: The average usable decay time range of the SQUID is significantly larger, as can be inferred from decay and data error figures. The better data quality can be first explained by theoretical advantages, especially the slower decaying B-field (Asten & Duncan, 2012). Second, in particular the SQUID-Z component is less affected by sferics, traffic and power lines than the coil, as noise measurements indicate. Furthermore, 1D *Beowulf* inversion results of the SQUID have advantages over the coil with respect to misfit ratios and reliability of the 1D approach.

A more detailed description of the inverse modeling procedure and the geological interpretation of the final inversion results along the survey line in accordance with the seismic and ERT data (section 2.1) can be obtained in Rochlitz, (2015).
Inverse modeling of SQUID and coil data with alternative software is still in progress. Most important, in order to gain maximum advantage of using the LTS SQUID, the 3-component data should be inverted altogether. It is assumed that the uncertainty, which results from the principle of equivalence, will be reduced. Furthermore, it would be advantageous to consider data errors and apply a laterally constrained 1D inverse modeling procedure.

Acknowledgements

The Leibniz Institute of Photonic Technology and the Supracon AG as well as the Friedrich Schiller University Jena provided not only the instruments for this TEM study, but also supported conducting the survey. Special thanks goes to Frank Bauer and Stefan Dunkel. The survey was funded by the Federal Ministry of Education and Research (BMBF) as part of INFLUINS (grant 03IS2091A).

References

Asten, M. W., & Duncan, A. C. (2012). The quantitative advantages of using B-field sensors in time-domain EM measurement for mineral exploration and unexploded ordnance search. *Geophysics*, *77*(4), WB137–WB148.

Chwala, A., Smit, J., Stolz, R., Zakosarenko, V., Schmelz, M., Fritzsch, L., et al. (2011). Low temperature SQUID magnetometer systems for geophysical exploration with transient electromagnetics. *Superconductor Science and Technology*, *24*(12), 125006 ff.

Le Roux, C., & Macnae, J. (2007). SQUID sensors for EM systems. In *Exploration in the new millennium: Proceedings of the fifth decennial international conference on mineral exploration* (pp. 417–423).

PGL - Preußische Geologische Landesanstalt. (1926). *Erläuterungen zur Geologischen Karte von Preußen und benachbarten deutschen Ländern.* Berlin.

Raiche, A. (2008). The P223 software suite for planning and interpreting EM surveys, PREVIEW. *Australian Society of Exploration Geophysicists*, *Issue 132*, 25-30.

Rochlitz, R. (2015). *Squid-based transient electromagnetics in an area with highly conductive overburden - a case study from Bad Frankenhausen, Thuringia.* Master's thesis, FSU Jena, Germany.

Smit, J., & Le Roux, T. (2009). TDEM survey at Shea Creek uranium deposit utilising a low-temperature superconductor SQUID. In *11th SAGA biennial technical meeting and exhibition.*

Smith, R. (2014). Electromagnetic induction methods in mining geophysics from 2008 to 2012. *Surveys in Geophysics*, *35*(1), 123–156.

Telford, W. M. (1990). *Applied geophysics.* Cambridge England New York: Cambridge University Press.

Vallée, M. A., Smith, R. S., & Keating, P. (2011). Metalliferous mining geophysics—state of the art after a decade in the new millennium. *Geophysics*, *76*(4), W31–W50.

Webb, M., & Corscadden, B. (2009). A case study of deep electromagnetic exploration in conductive cover. *ASEG Extended Abstracts*, *2009*(1), 1–11.

Präsentationsfolien

Main advantages of performing joint inversion of MT data with GTF and HMT data: Results from a synthetic case study and real data

Joan Campanyà i Llovet, Xènia Ogaya, Alan G. Jones[1], Volker Rath & Jan Vozar

Dublin Institute for Advanced Studies (DIAS), Ireland
[1]Now at: Complete MT solutions, Ottawa, Canada

DIAS
Institiúid Ard-Léinn Bhaile Átha Cliath
Dublin Institute for Advanced Studies

(campanya@cp.dias.ie)

TYPES OF EM DATA

MT Impedance Tensor (Z) and (Z_0)

$$\begin{pmatrix} e_x(\omega) \\ e_y(\omega) \end{pmatrix} = \begin{pmatrix} Z_{xx}(\omega) & Z_{xy}(\omega) \\ Z_{yx}(\omega) & Z_{yy}(\omega) \end{pmatrix} \begin{pmatrix} h_x(\omega) \\ h_y(\omega) \end{pmatrix}$$

Geomagnetic Transfer Function (GTF)

$$h_z(\omega) = \begin{pmatrix} W_x(\omega) & W_y(\omega) \end{pmatrix} \begin{pmatrix} h_x(\omega) \\ h_y(\omega) \end{pmatrix}$$

Inter-station Horizontal Magnetic Tensor (HMT)

$$\begin{pmatrix} h_x^A(\omega) \\ h_y^A(\omega) \end{pmatrix} = \begin{pmatrix} M_{xx}(\omega) & M_{xy}(\omega) \\ M_{yx}(\omega) & M_{yy}(\omega) \end{pmatrix} \begin{pmatrix} h_x^B(\omega) \\ h_y^B(\omega) \end{pmatrix}$$

Reference site

Acquisition of **E** and **H** fields time variations

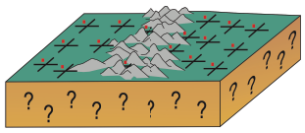

Relations between **E** and **H** fields time variations

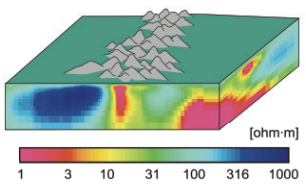

TYPES OF EM DATA

MT Impedance Tensor (Z) and (Z_0)

$$\begin{pmatrix} e_x(\omega) \\ e_y(\omega) \end{pmatrix} = \begin{pmatrix} Z_{xx}(\omega) & Z_{xy}(\omega) \\ Z_{yx}(\omega) & Z_{yy}(\omega) \end{pmatrix} \begin{pmatrix} h_x(\omega) \\ h_y(\omega) \end{pmatrix}$$

Geomagnetic Transfer Function (GTF)

$$h_z(\omega) = \begin{pmatrix} W_x(\omega) & W_y(\omega) \end{pmatrix} \begin{pmatrix} h_x(\omega) \\ h_y(\omega) \end{pmatrix}$$

Inter-station Horizontal Magnetic Tensor (HMT)

$$\begin{pmatrix} h_x^A(\omega) \\ h_y^A(\omega) \end{pmatrix} = \begin{pmatrix} M_{xx}(\omega) & M_{xy}(\omega) \\ M_{yx}(\omega) & M_{yy}(\omega) \end{pmatrix} \begin{pmatrix} h_x^B(\omega) \\ h_y^B(\omega) \end{pmatrix}$$

Reference site

GTF and HMT

Can be easily acquired during the MT survey

No dependence of electric field galvanic distortion

Provides information even when the electric fields are poor

EXPERIMENT

MT profiles in a 3D environment. MT profiles crossing the area of interest, independent of the dimensionality of the geoelectrical structures

Zo

Zo+GTF+HMT

Z

Z+GTF+HMT

Synthetic model

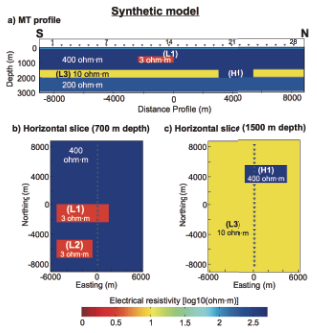

Real data

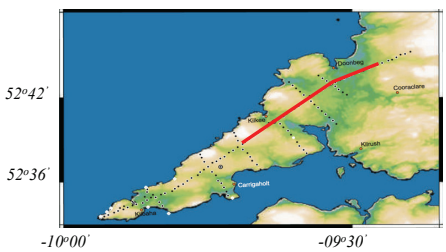

SYNTHETIC MODEL

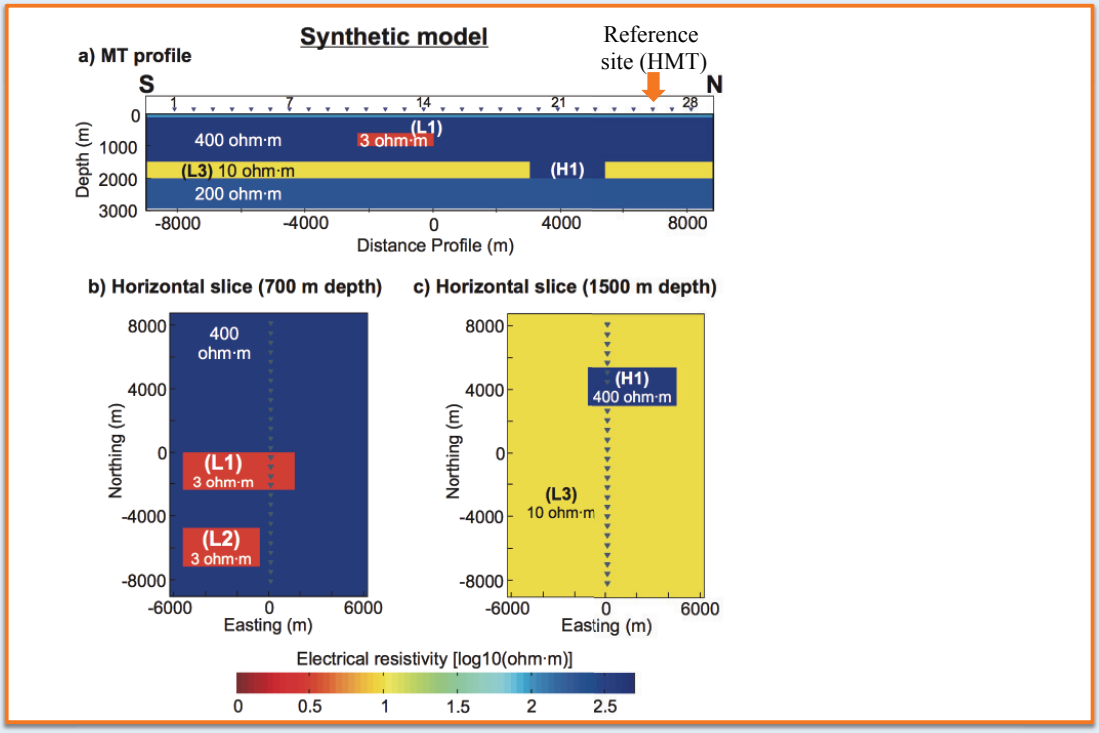

SYNTHETIC MODEL

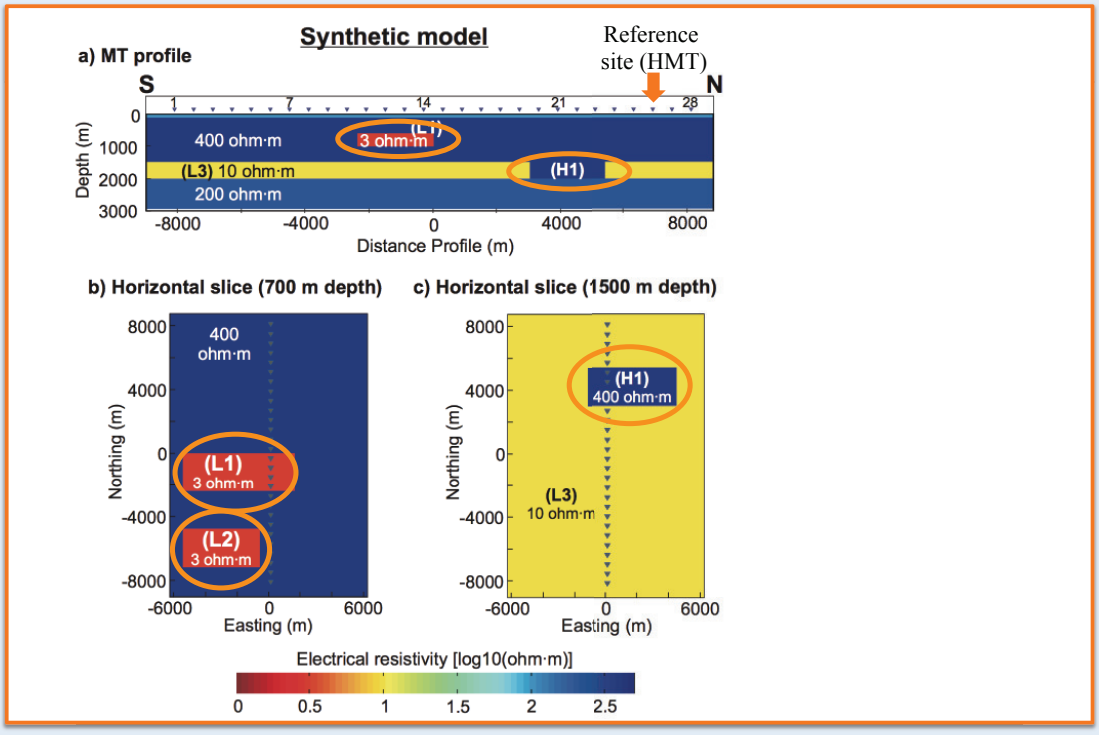

SYNTHETIC MODEL

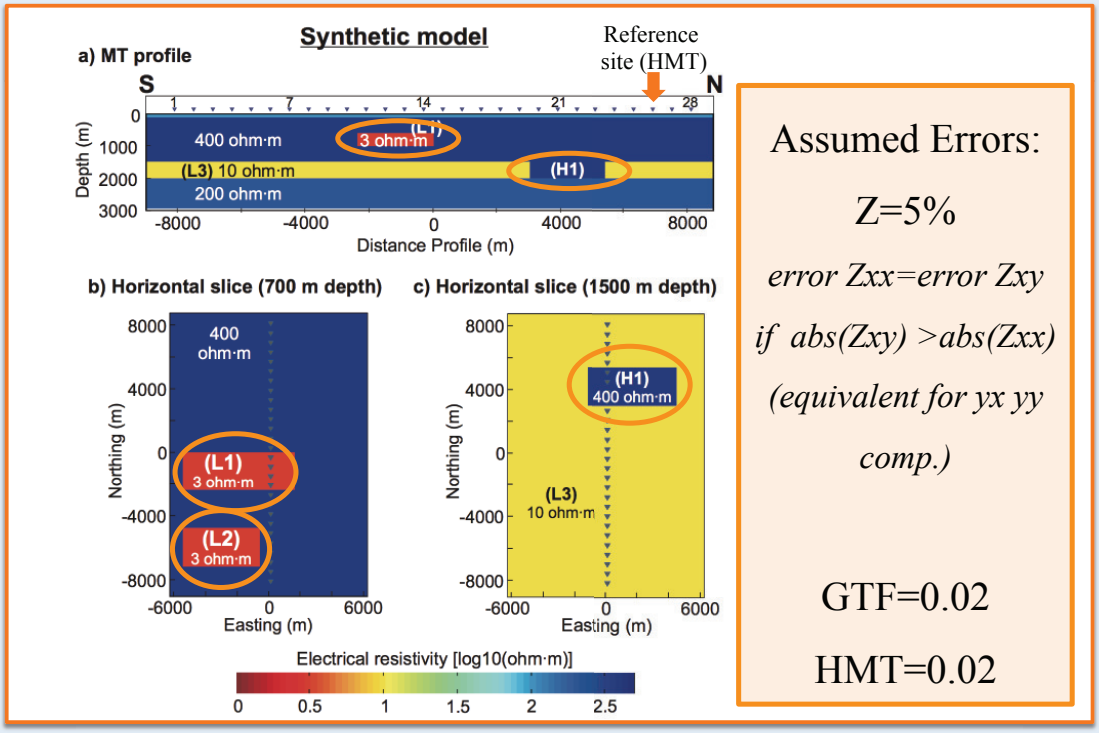

Assumed Errors:

Z=5%

error Zxx=error Zxy

if abs(Zxy) >abs(Zxx)

(equivalent for yx yy comp.)

GTF=0.02

HMT=0.02

SENSITIVITY ANALYSIS

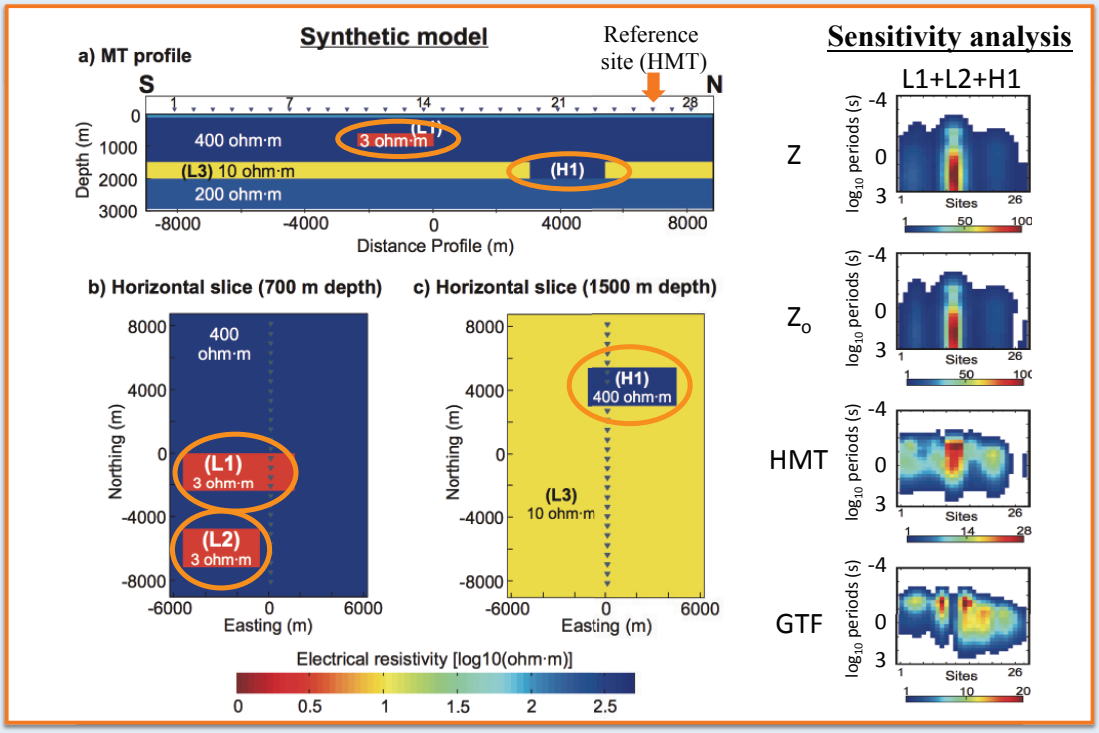

DIMENSIONALITY ANALYSIS

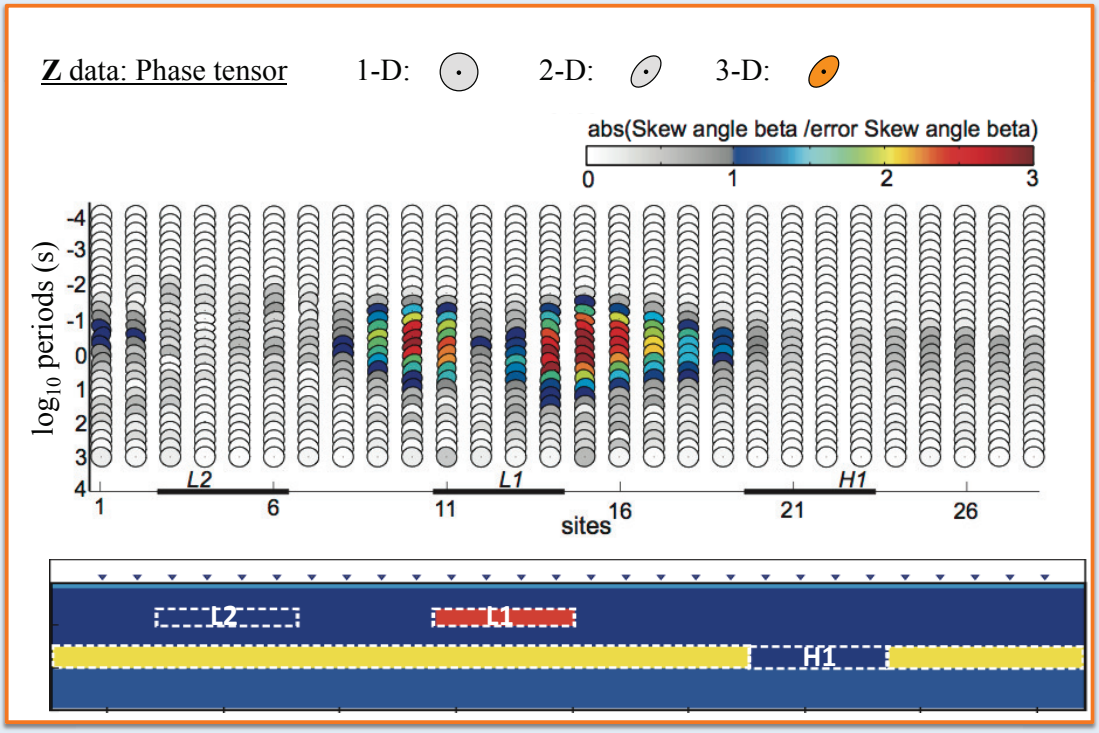

DIMENSIONALITY ANALYSIS

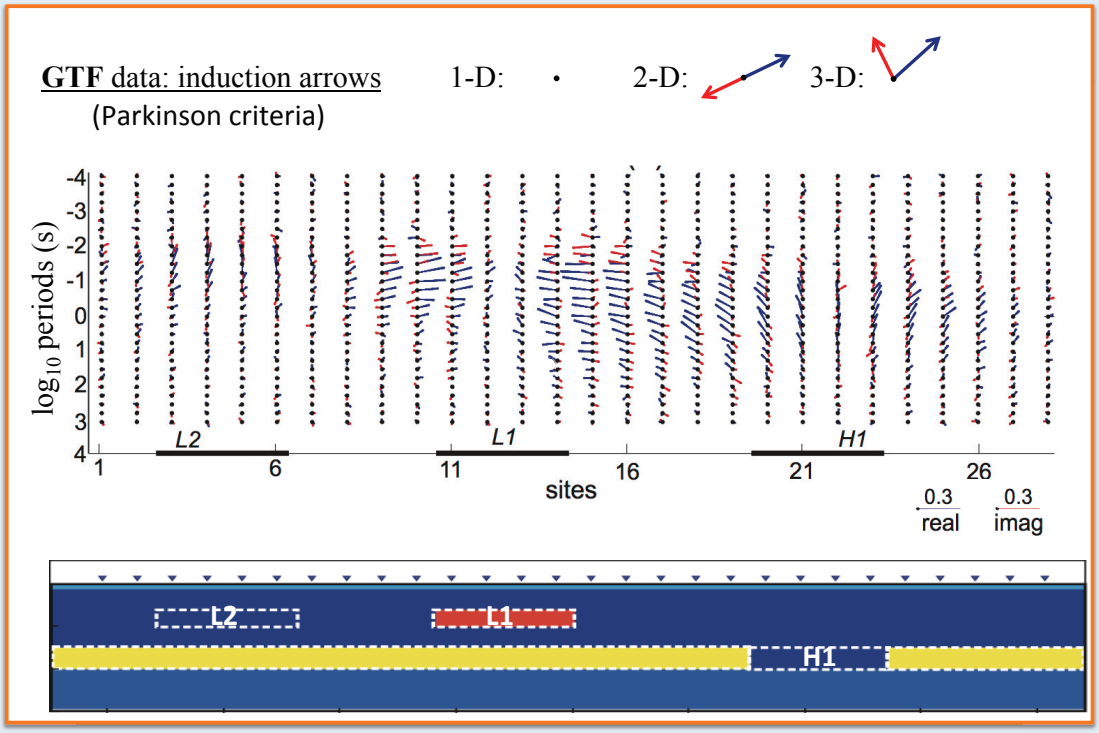

DIMENSIONALITY ANALYSIS

HMT data: HMT variations 1-D: • 2-D: 3-D:

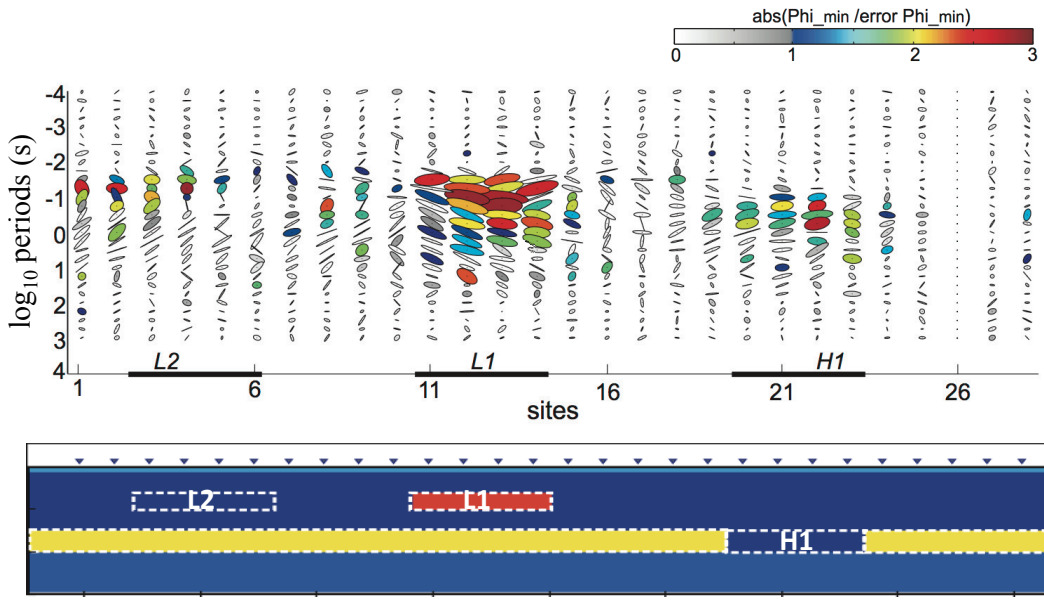

RECOVERING THE SUBSURFACE

3-D INVERSION

Z_o Z

Z_o+GTF+HMT Z+GTF+HMT

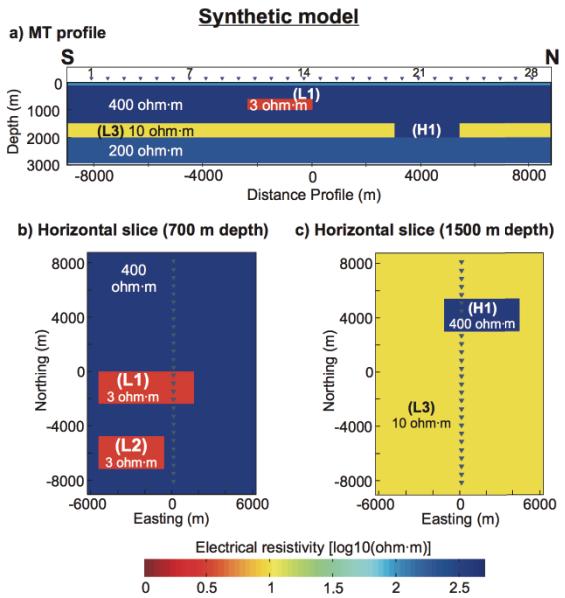

RECOVERING THE SUBSURFACE

3-D INVERSION

Z_o Z

Z_o+GTF+HMT Z+GTF+HMT

- Errors randomly introduced to better simulate real situations
  (Z=5%, GTF=0.02, HMT=0.02)
- Error floors: Z=5%, GTF=0.02, HMT=0.02
- Period range 0.001 s – 30 s
- ModEM algorithm

(Egbert and Kelbert, 2012; Kelbert et al., 2014)

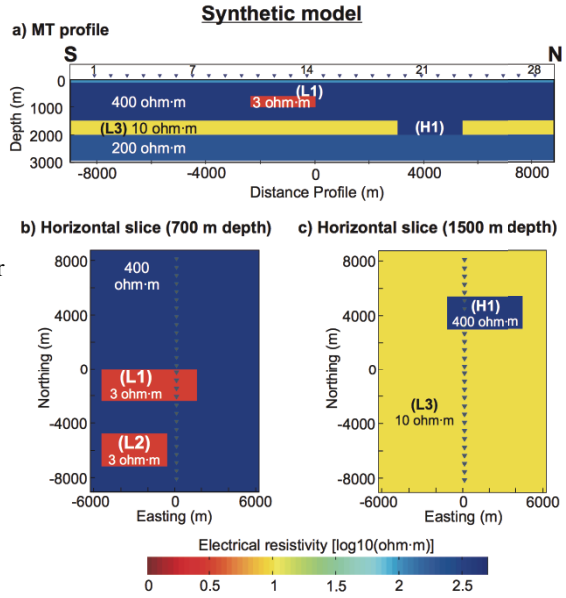

RECOVERING THE SUBSURFACE

3-D INVERSION

Structures below the profile

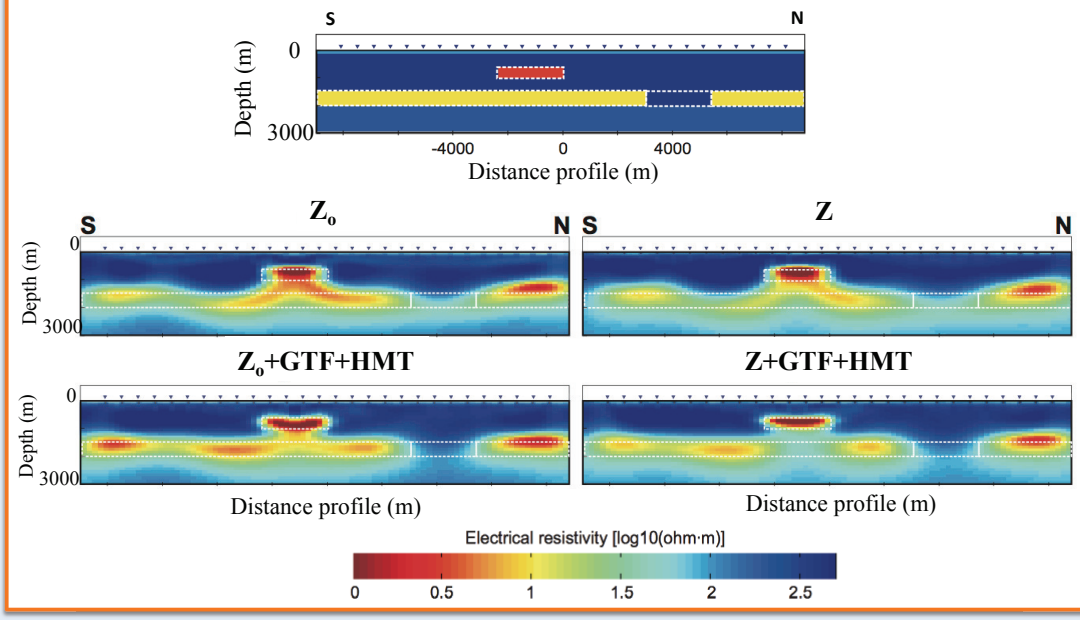

RECOVERING THE SUBSURFACE

3-D INVERSION

Structures off-profile

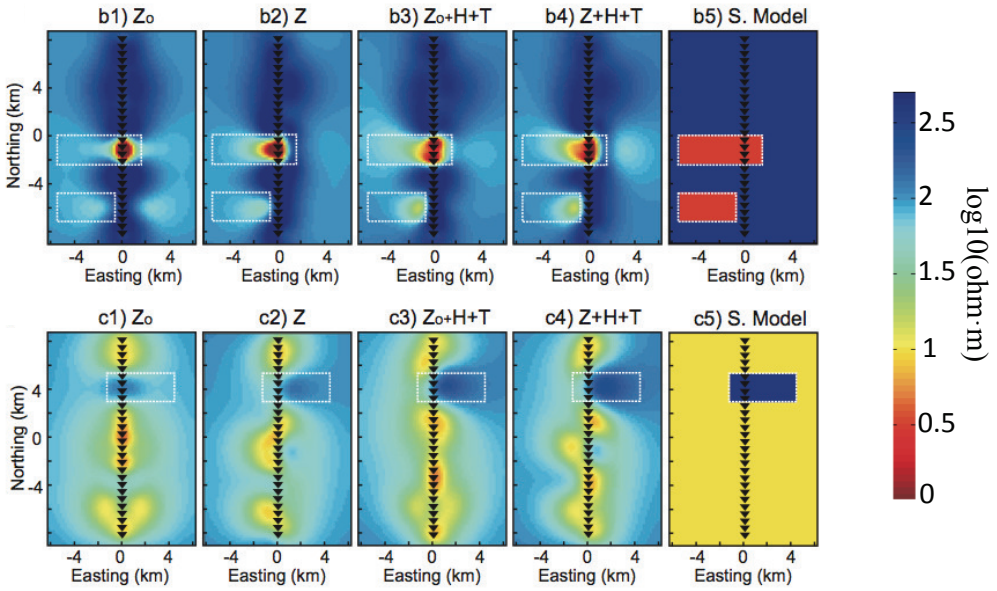

RECOVERING THE SUBSURFACE

3-D INVERSION

Fit of the Data

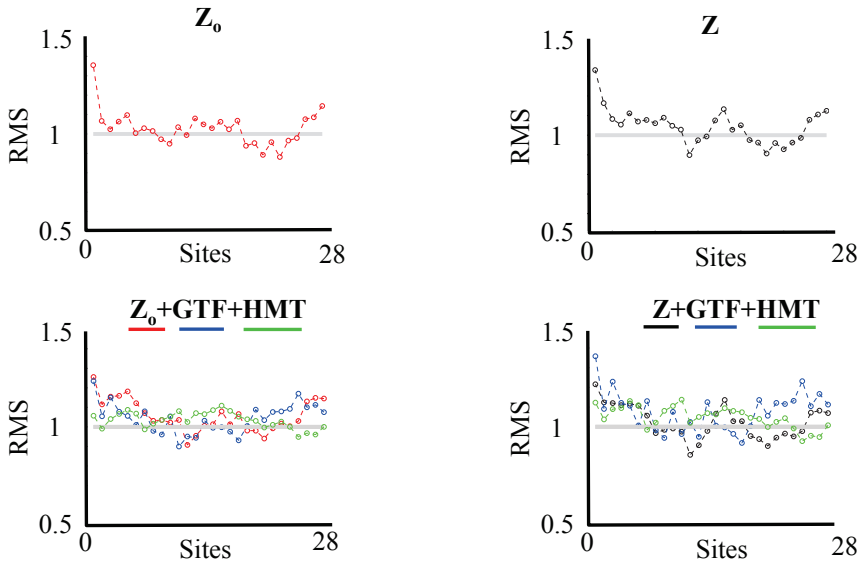

RECOVERING THE SUBSURFACE

3-D INVERSION

Fit of the Model

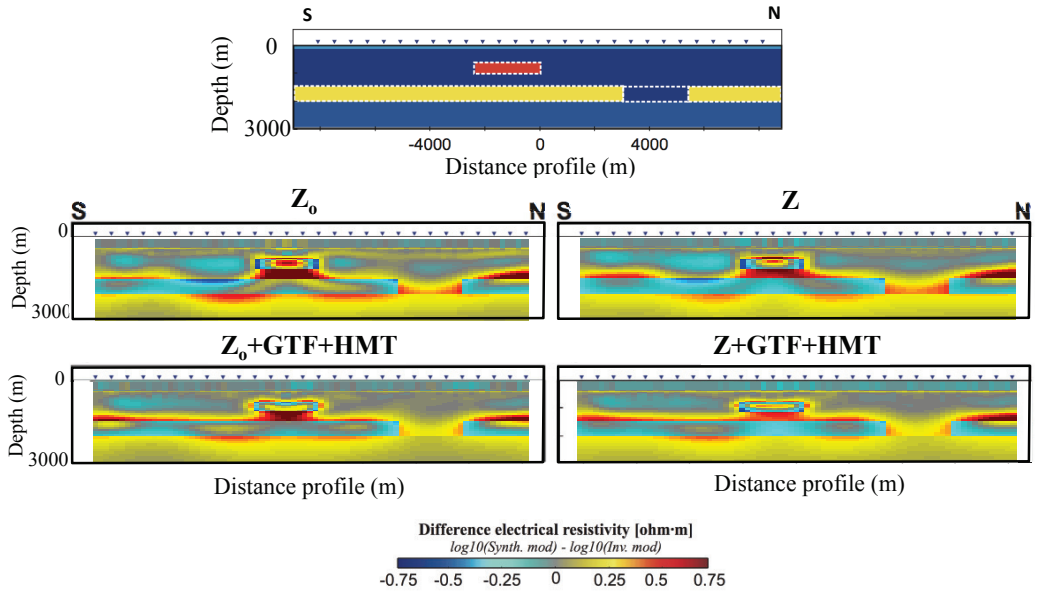

MAIN ADVANTAGES

3-D INVERSION

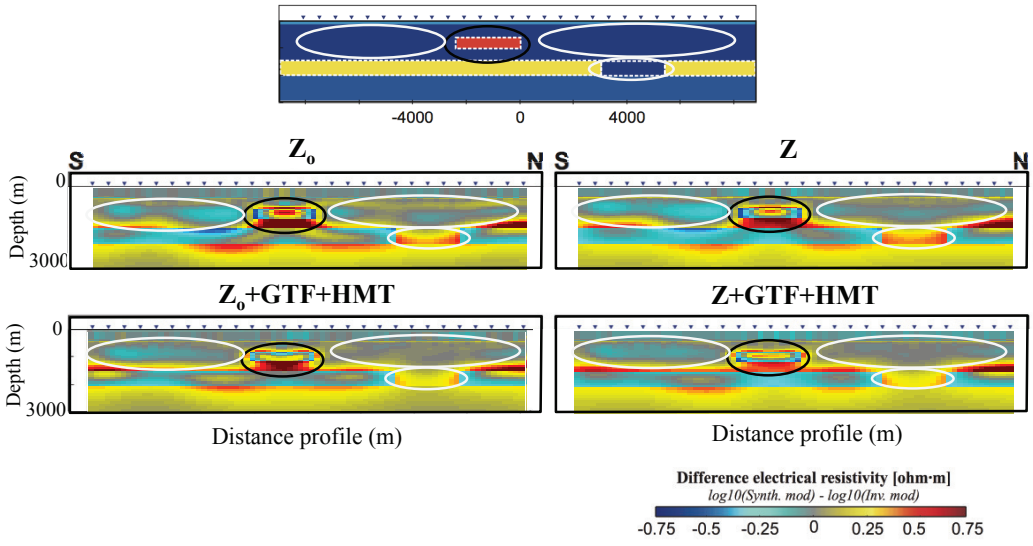

More accurate characterization of the electrical resistivity values

MAIN ADVANTAGES

3-D INVERSION

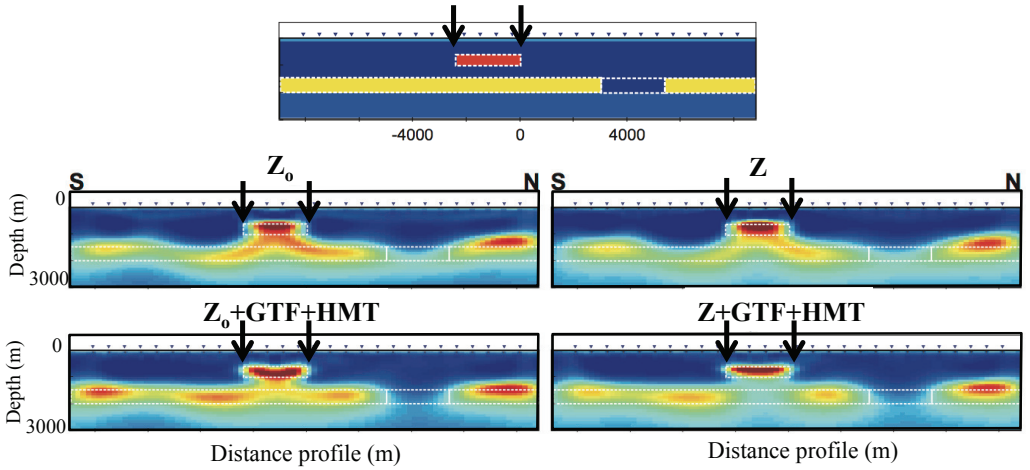

Better definition of the bottom and lateral boundaries of low electrical resistivity anomalies

MAIN ADVANTAGES

3-D INVERSION

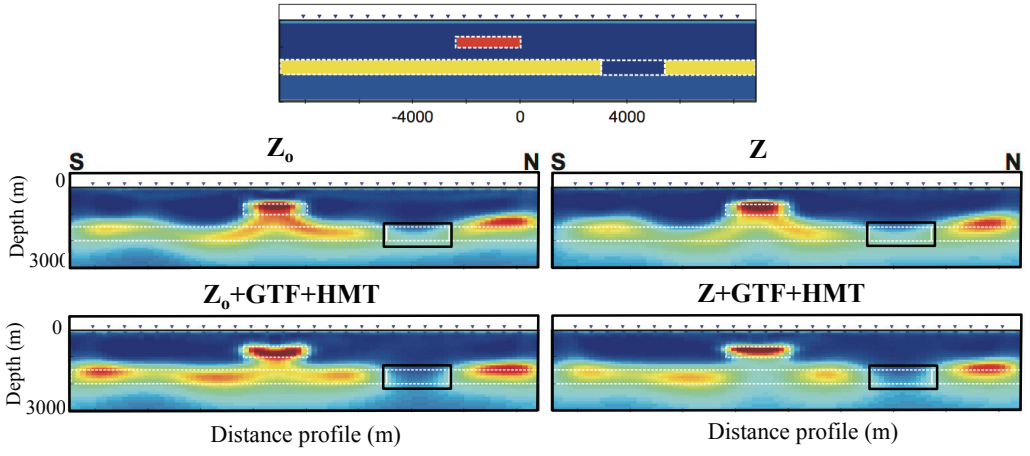

Superior capacity recovering high electrical resistivity anomalies that are difficult to recover by using Z or Z_o data alone.

MAIN ADVANTAGES

3-D INVERSION

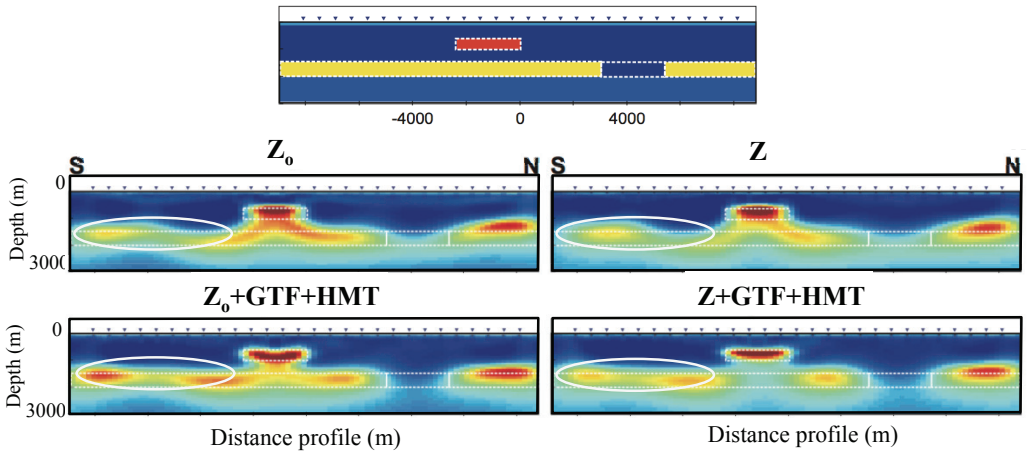

Better definition of the lateral continuity of electrical resistivity structures

EXAMPLE with REAL DATA

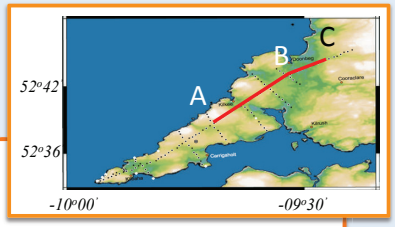

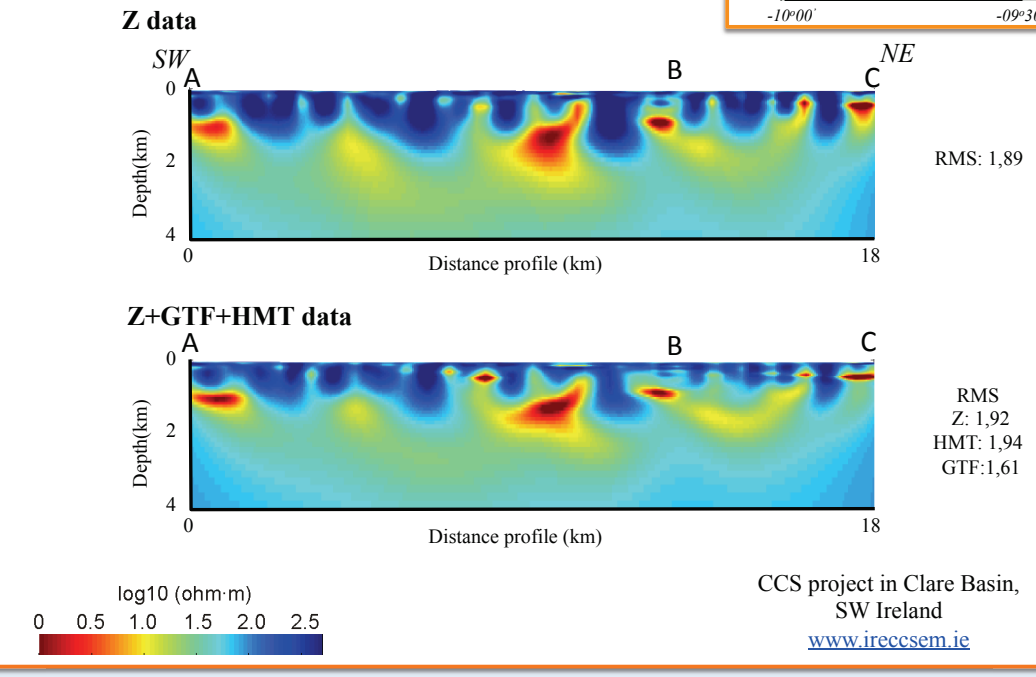

CCS project in Clare Basin, SW Ireland
www.ireccsem.ie

MANY THANKS!

Main improvements

1) More accurate characterization of the electrical resistivity values.

2) Better definition of the bottom and lateral boundaries of the low electrical resistivity anomalies.

3) Superior capacity recovering high electrical resistivity anomalies that usually cannot be recovered by using Z or Z_o data alone.

4) Better define the lateral continuity of electrical resistivity structures.

e-mail: campanya@cp.dias.ie

Paper submitted in GJI

Joint ERT and AMT measurements in an active volcano area

Colin Hogg, Duygu Kiyan, Sveta Byrdina, Jean Vandemeulebrouck,
Volker Rath & Furnas Working Group

DIAS Institiúid Ard-Léinn Bhaile Átha Cliath Dublin Institute for Advanced Studies

ISTerre Institut des Sciences de la Terre

CV ARG

cnrs

Université de Savoie Chambéry Annecy

IRD Institut de recherche pour le développement

22 September, 2015
Dassel, Germany

Introduction to survey area - Furnas Caldera

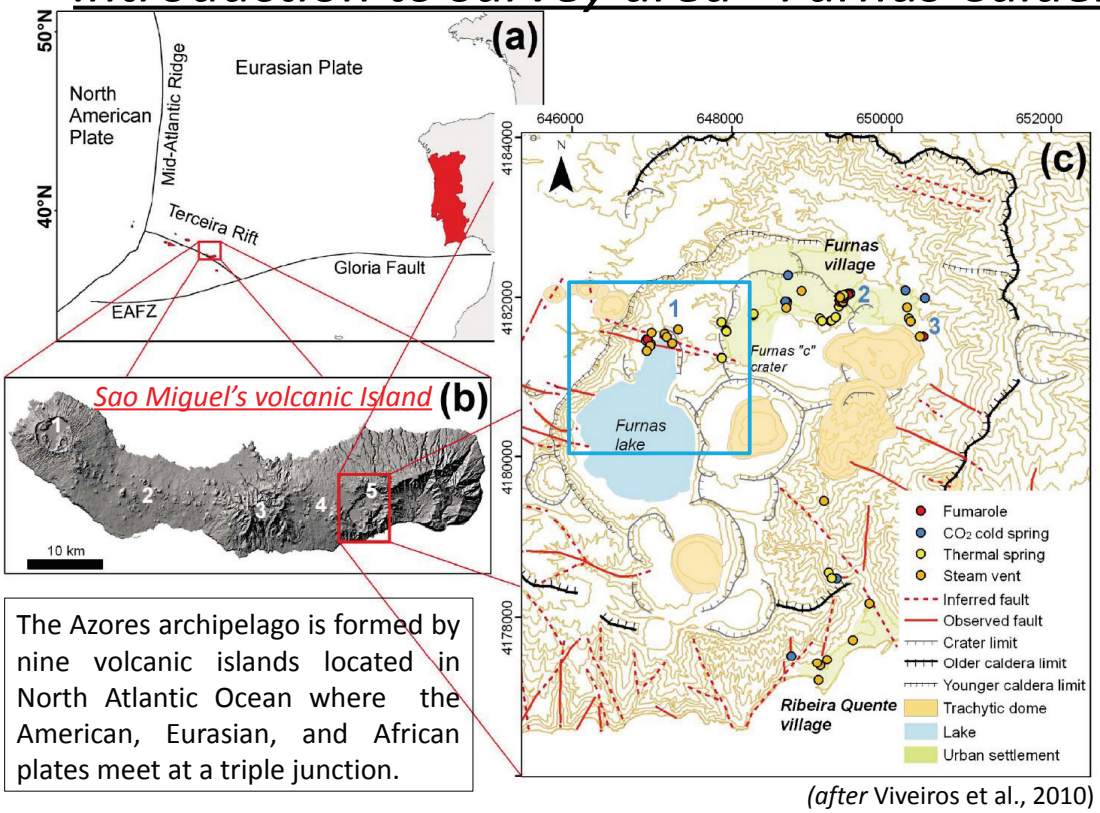

The Azores archipelago is formed by nine volcanic islands located in North Atlantic Ocean where the American, Eurasian, and African plates meet at a triple junction.

(after Viveiros et al., 2010)

Motivation

Characterize the extent, geometry and depth of the hydrothermal system manifested by strong diffuse degassing

Survey area – Furnas Caldera

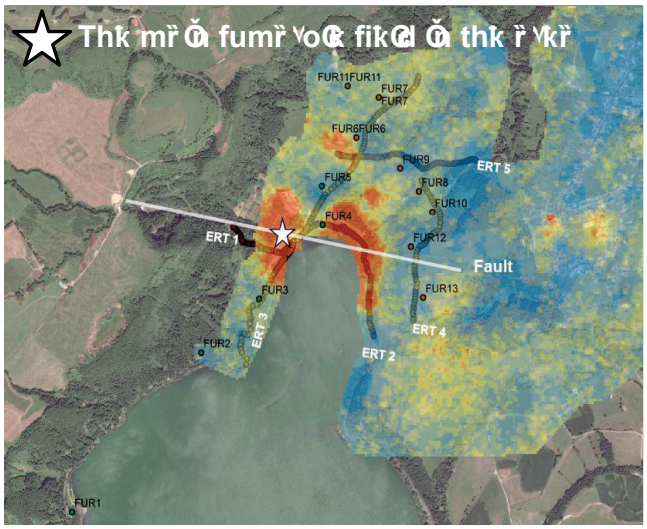

- Furnas consists of a steep-sided caldera complex 8 x 5 km across WNW-ESE trending dip-slip faulting crosses the volcanic edifice.
- Fumerolic fields estimated aquifers 100 – 200 m depth and proposed to be supplied with gas from plutonic bodies cooling at greater depths (*Ferreira and Oskarsson, 1999, Viveiros et al., 2010).* Intensive CO_2 outgassing.

AMT measurements

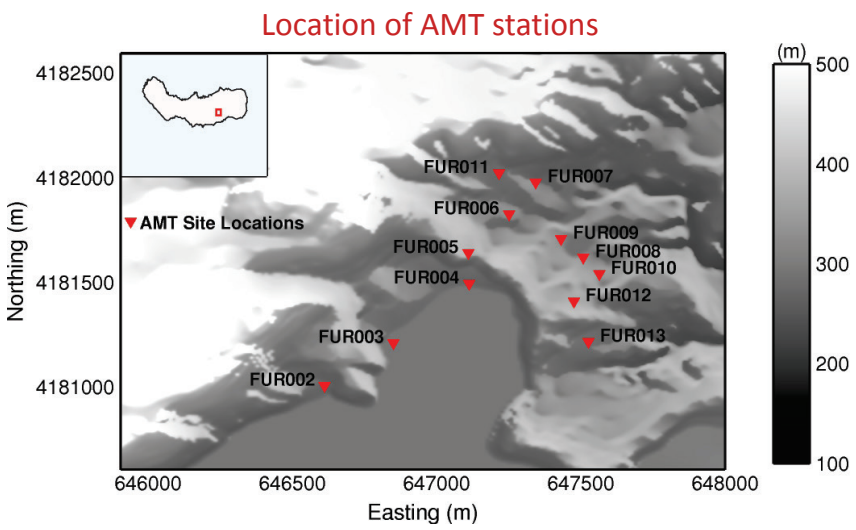

- 13 AMT sites in total with remote reference site (FUR001 & REM sites not plotted)
- on average 10 hours over night recordings
- site spacing: Approx. 100 - 150 m
- high quality data between the period range of 0.0001 s and 1 s

FURNAS AMT data

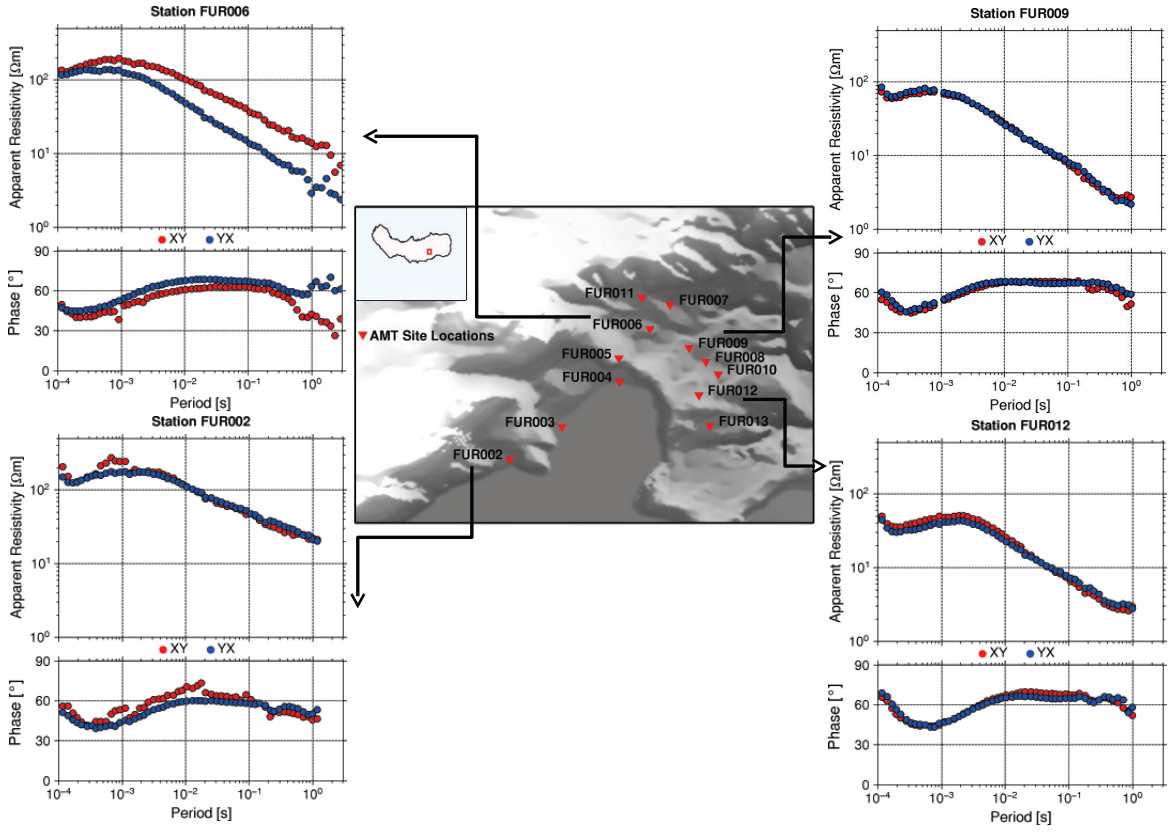

What do induction arrows indicate?

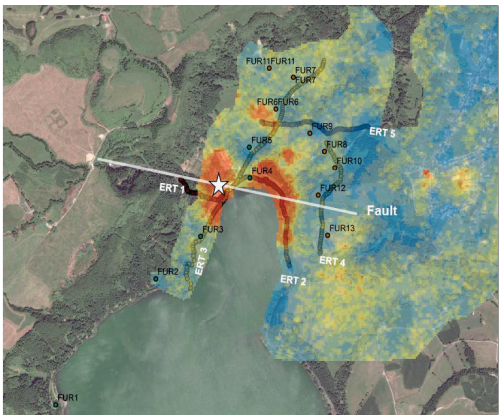

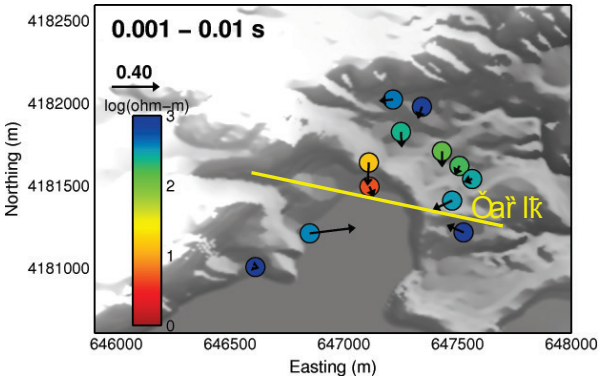

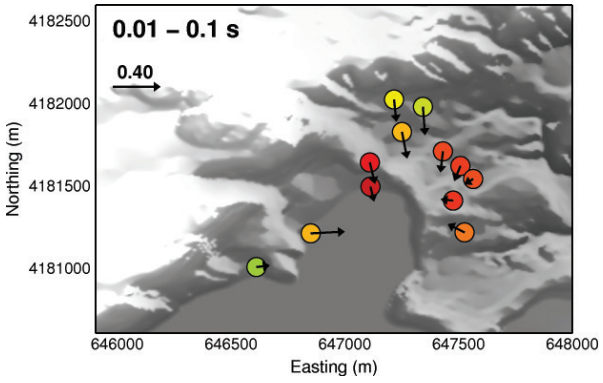

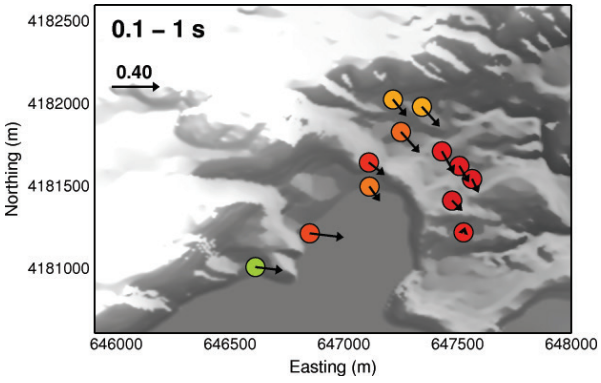

How deep are we seeing?

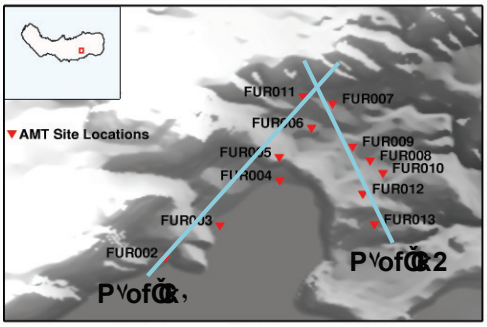

Induction depths ⇳ longer periods are necessary!

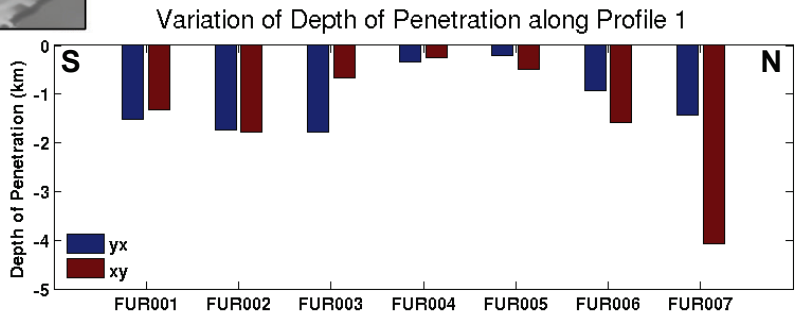

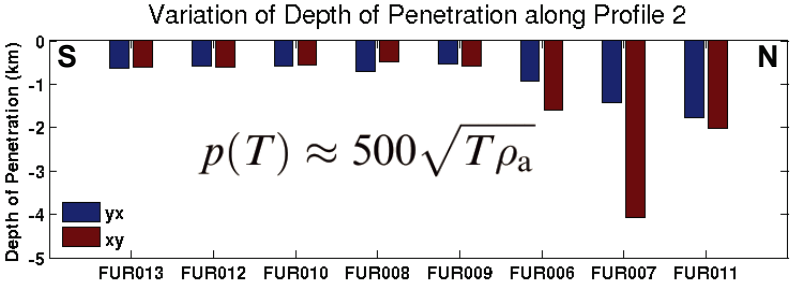

$$p(T) \approx 500\sqrt{T\rho_a}$$

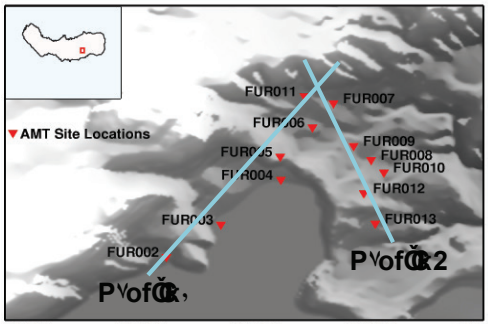

Phase Tensor Analysis

Data at long periods indicate 3D structure(s) inferred from high skew angles

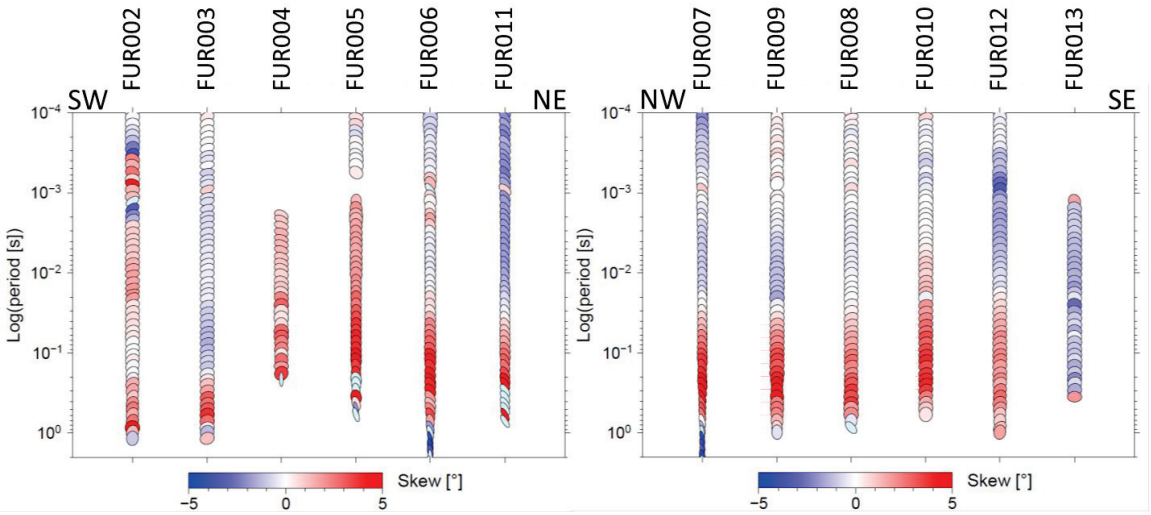

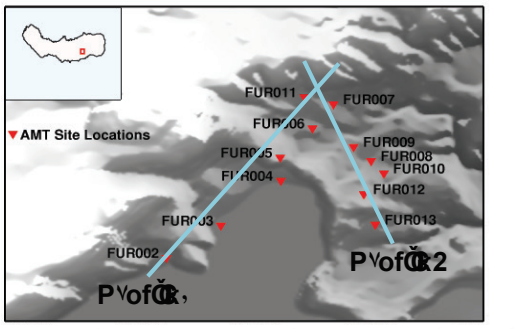

Dimensionality Analysis

Black circles outline areas where the minimum phase value is greater than 50° correspond to the region of high conductivity imaged in the preliminary 1D and 2D models.

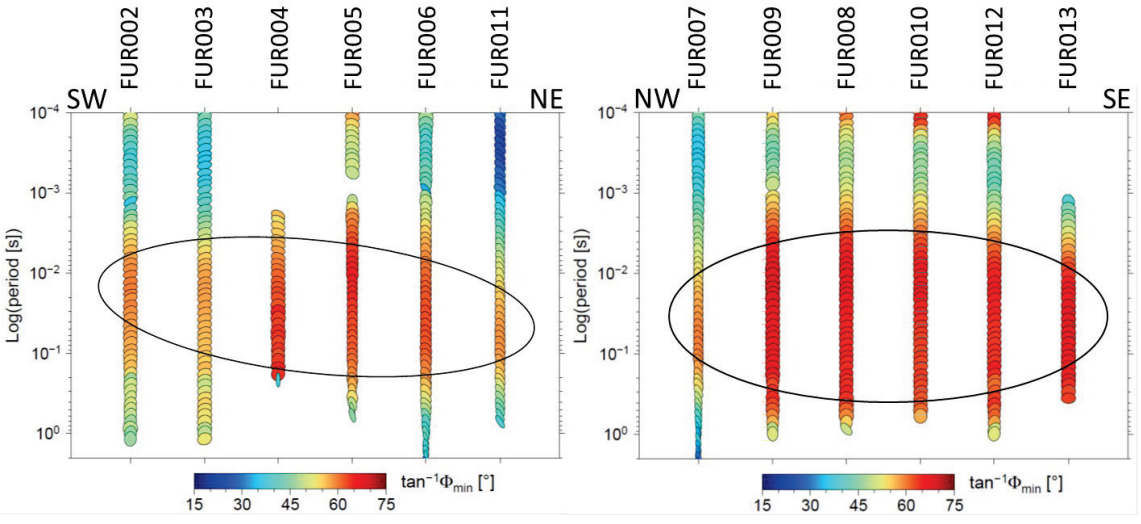

1-D Models

Cross-sections of edited Furnas AMT responses were modelled using both Occam and sharp-boundary 1-D modelling approaches

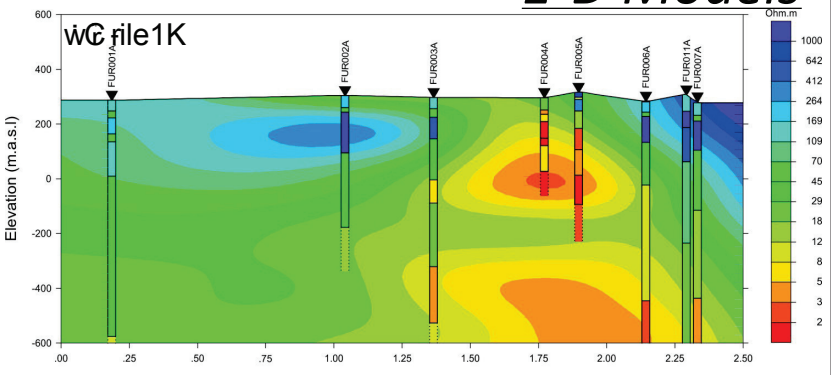

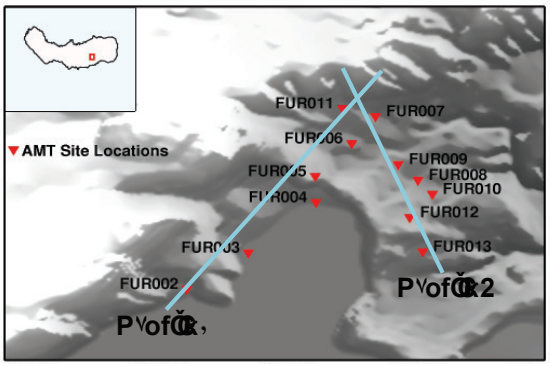

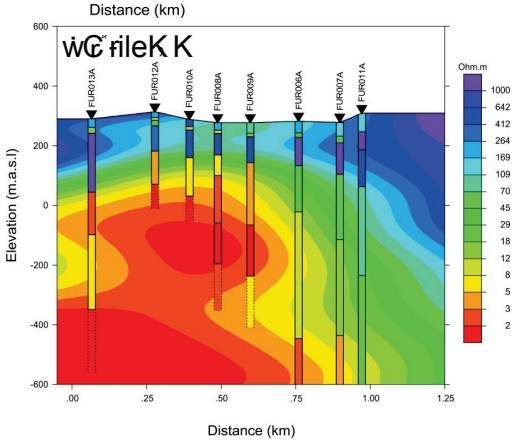

ERT measurements

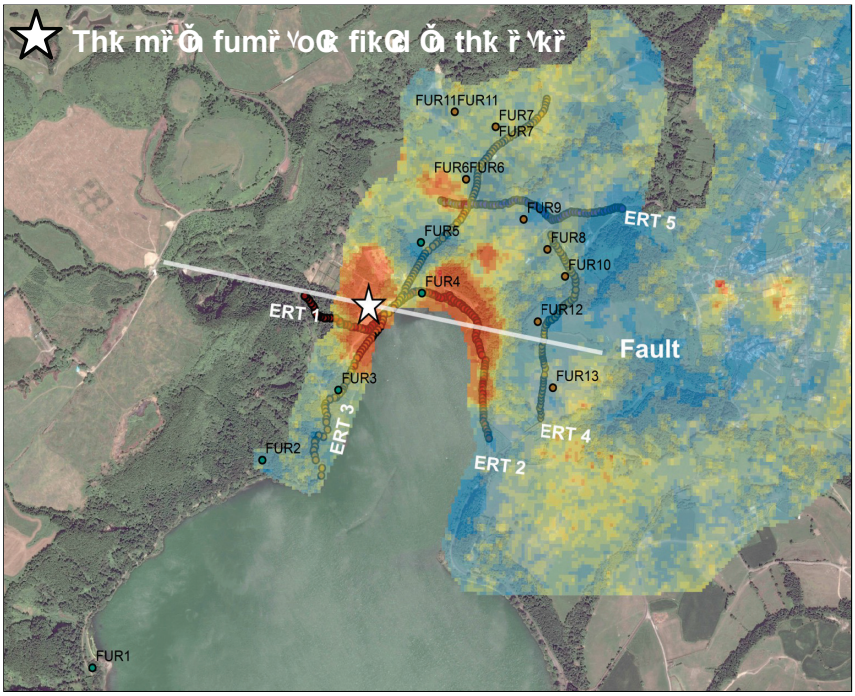

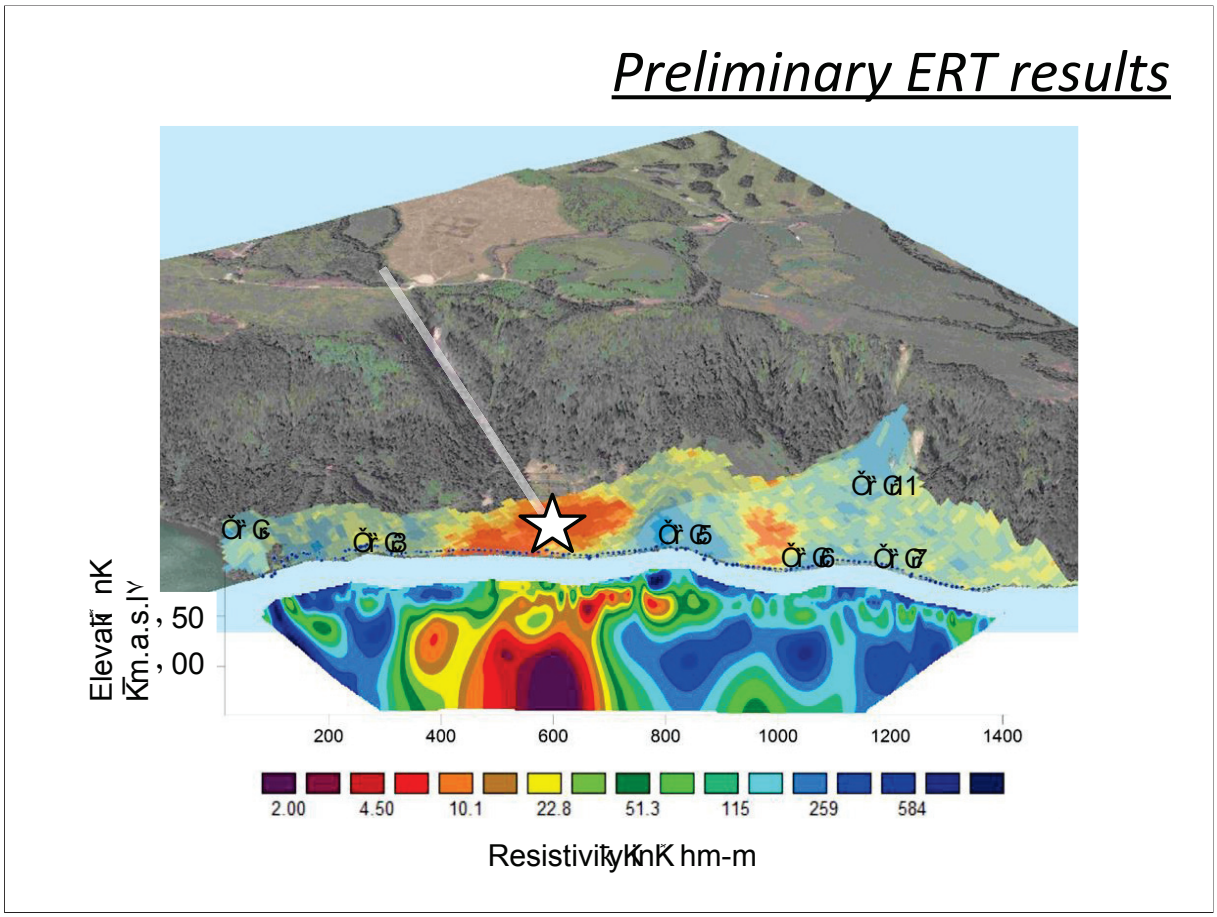
Preliminary ERT results
200
400
600
800
1000
1200
1400
2.00
4.50
10.1
22.8
51.3
115
259
584

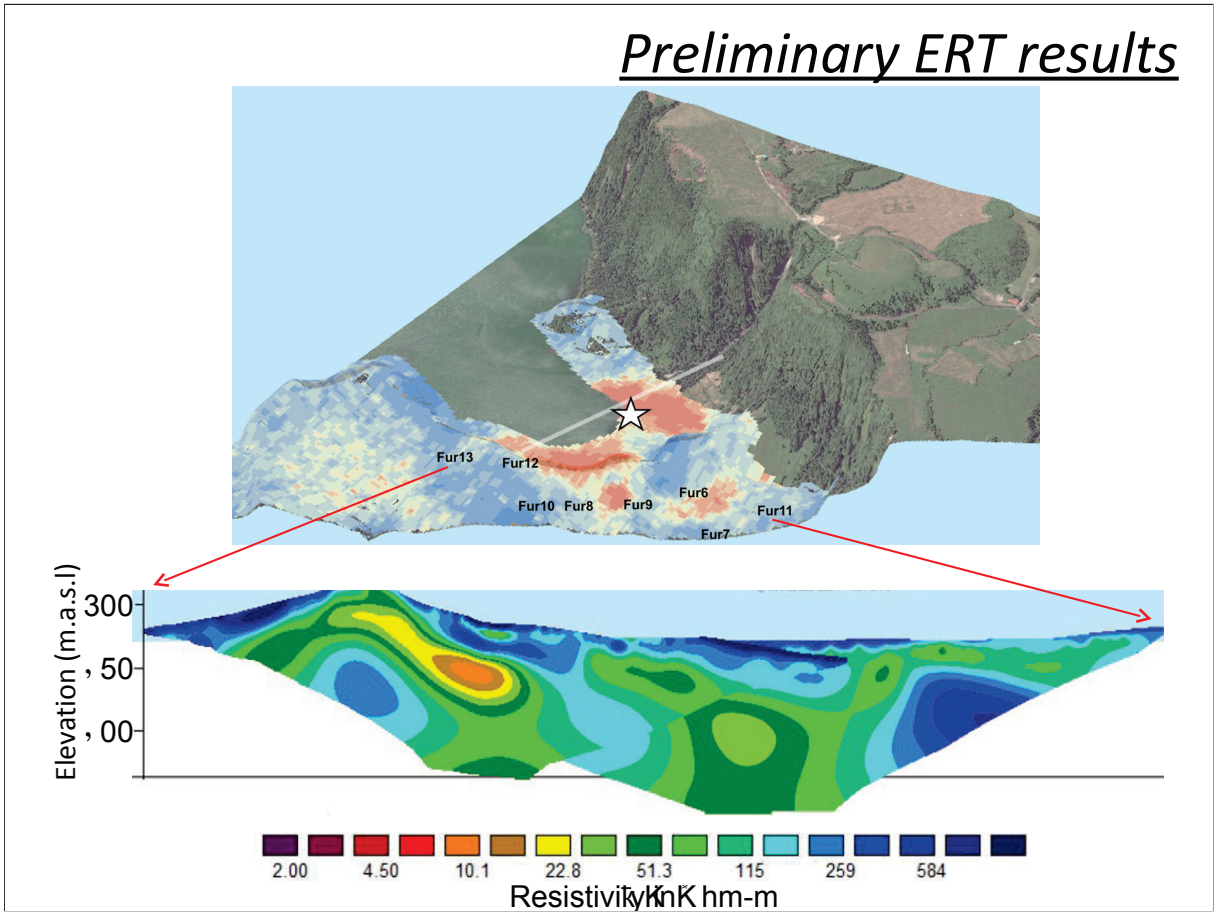
Preliminary ERT results
Fur13
Fur12
Fur10
Fur8
Fur9
Fur6
Fur11
Fur7
Elevation (m.a.s.l)
300
, 50
, 00
2.00
4.50
10.1
22.8
51.3
115
259
584

Preliminary 2-D inversion results: Profile 1

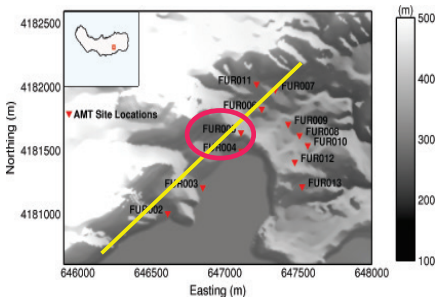

Profile 1 average strike angle of 72° East of N.
Inverted using smooth model inversion code (WinGLink software package, Rodi Mackie, 2001).
10kHz to 0.1Hz, app. resistivity and phase. Error floors for phase and apparent resistivity data: 5%, 10% for both TM and TE modes.
Regularization parameter: ¯Ł 3.0
Starting model: 100 ohm-m

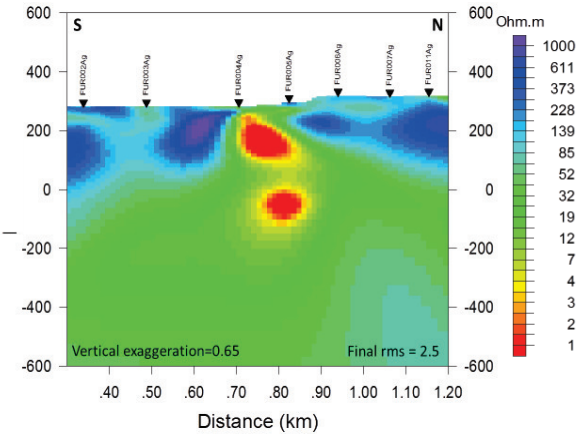

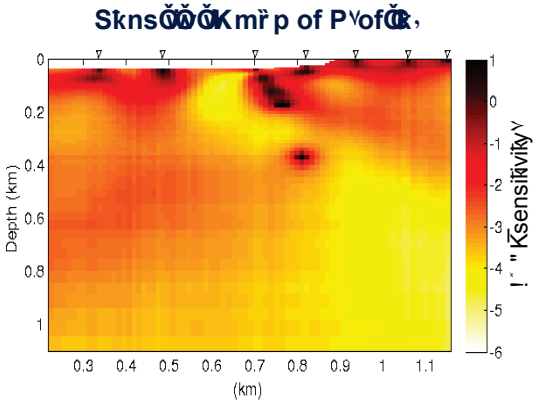

On-going & future research

(a) Complete 2-D inverse modelling of MT responses

(b) Investigating distortion effects on MT responses by 3-D modelling of high resolution topography data (e.g., Stark et al., 2013) including Lake Furnas bathymetry (also for future 3-D models)

(c) New field measurements (extended area, broad band instruments) and more ERT also in/on the lake

(d) Some ideas for *feasible joint inversion* of AMT and ERT data
- "joint inversion" vs "data fusion" (non-invasive)
- reduced models combined with probabilistic methods
- improved regularization

(a) and (b) completed as of April, 2016


THANKS!

26. Schmucker-Weidelt-Kolloquium für elektromagnetische Tiefenforschung, 23.09.2015, Dassel

Das magnetische Joch und andere Gründe zur Betrachtung von MT-Quellsignalen

Anne Neska

Instytut Geofizyki Polskiej Akademii Nauk

Diese Kiewer Konstruktion wird im Volksmund als Joch bezeichnet, lateinisch “iugum”

Zwei unter einem Joch zusammengespannte Tiere heißen auf lateinisch “coniugati”

(Bild entfernt um Urheberrechtsprobleme auszuschließen)

“Konjugierte Punkte” gibt es auch im Geomagnetismus; so nennt man die Fußpunkte einer Feldlinie

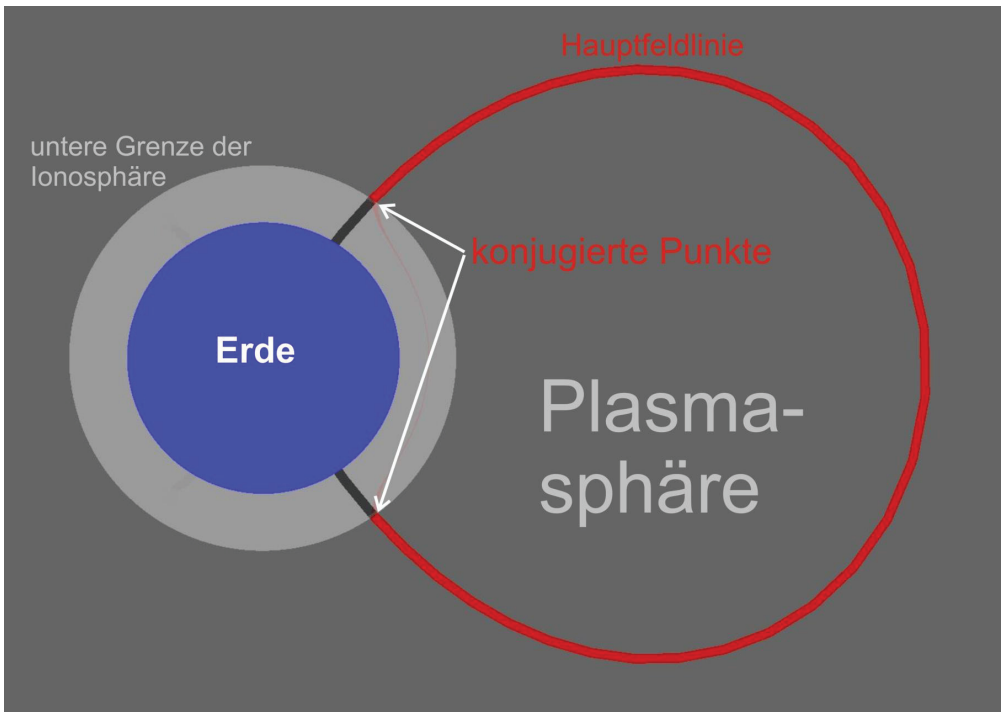

- In einem Medium, das durch ein Plasma in einem statischen Magnetfeld charakterisiert ist, können sich magnetohydrodynamische (MHD) Wellen ausbreiten.

- Stehende MHD-Wellen, die sich entlang der Hauptfeldlinien in der Plasmasphäre ausbreiten, werden auch als Feldlinienresonanzen bezeichnet; sie werden als Quellen der geomagnetischen Pulsationen (pc und pi, mit Perioden von 0,2 – 600 s) betrachtet.

- Diese Pulsationen sind das wichtigste Quellsignal für den kurzperiodischen LMT-Bereich.

Beispiele für INTERMAGNET-Observatorien an konjugierten Punkten

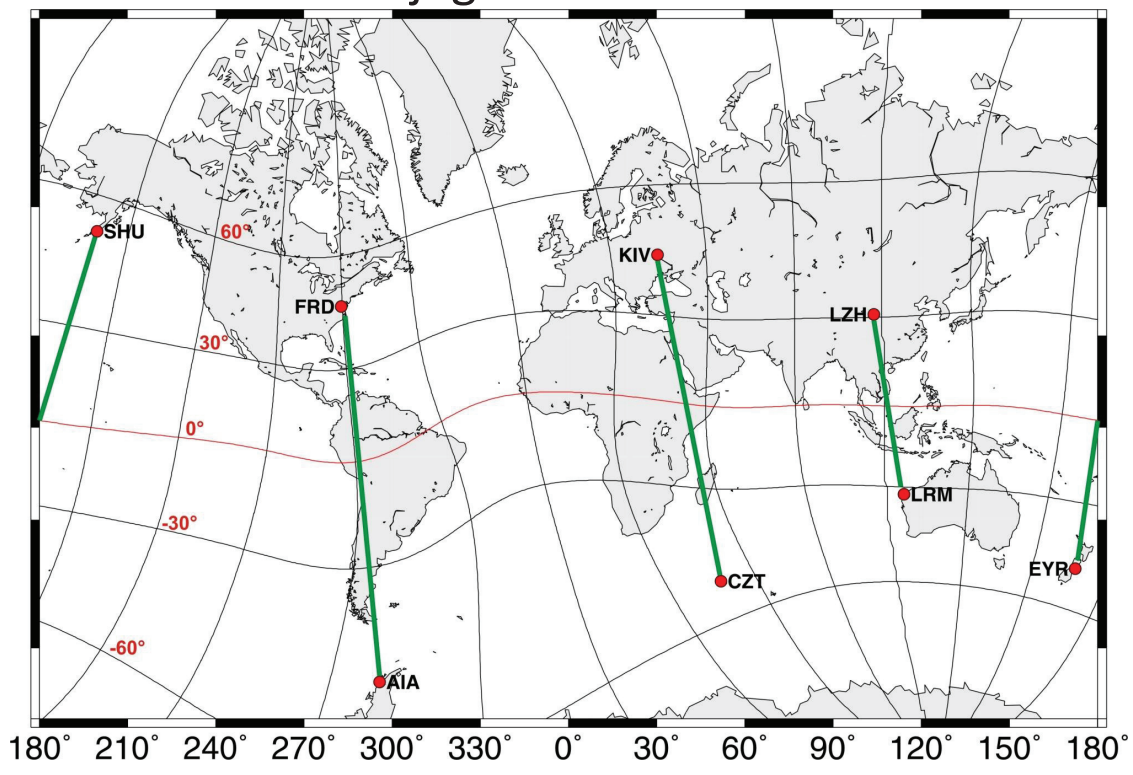

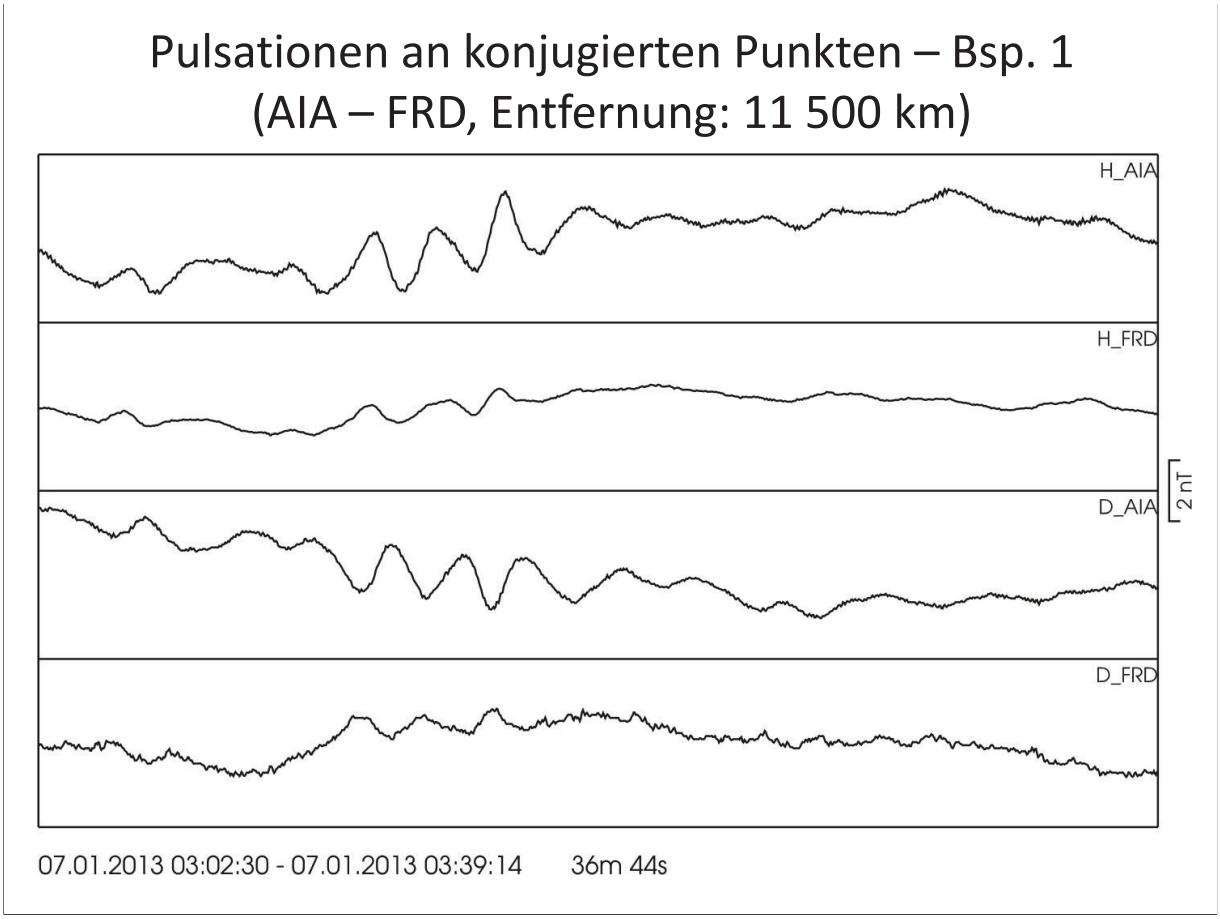
Pulsationen an konjugierten Punkten – Bsp. 1
(AIA – FRD, Entfernung: 11 500 km)
H_AIA
H_FRD
D_AIA
D_FRD
2 nT
07.01.2013 03:02:30 - 07.01.2013 03:39:14 36m 44s

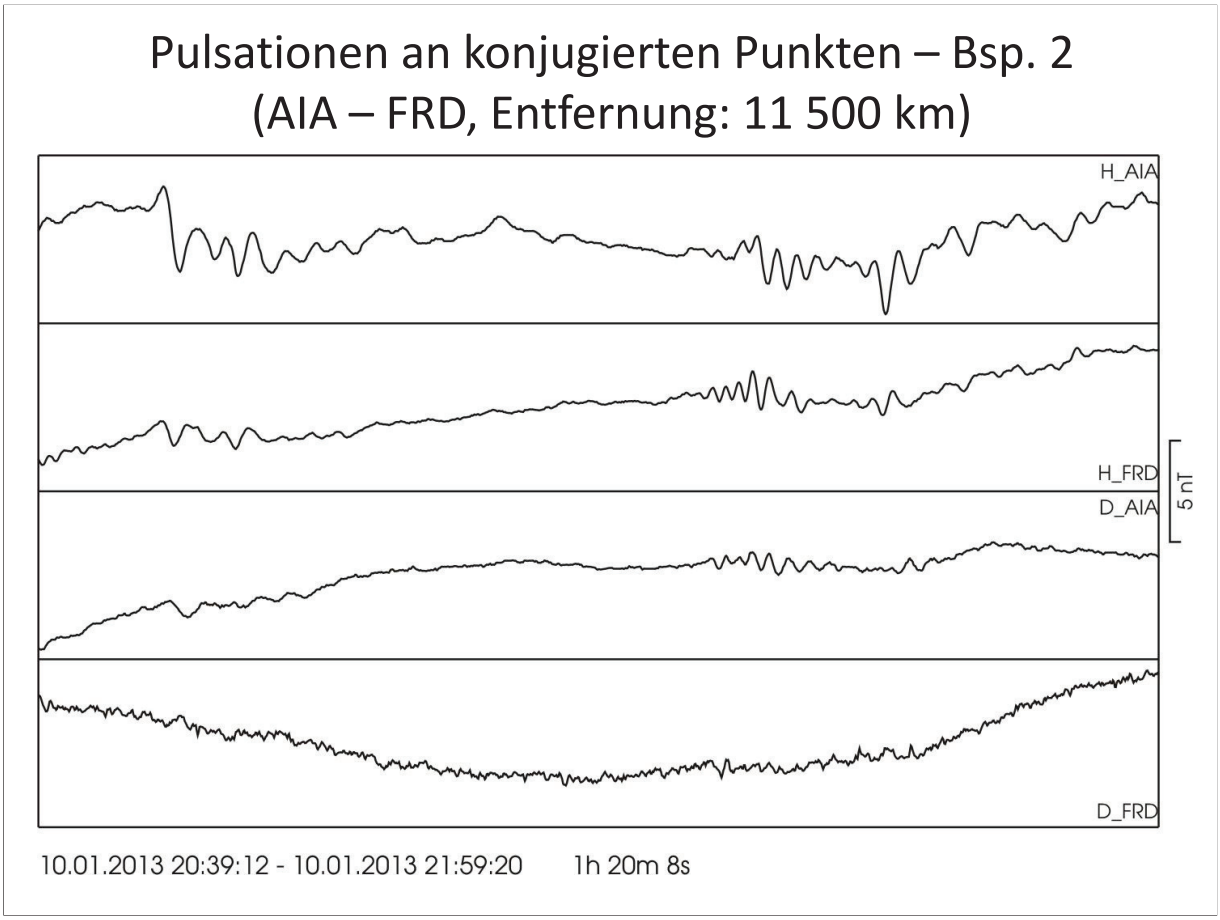
Pulsationen an konjugierten Punkten – Bsp. 2
(AIA – FRD, Entfernung: 11 500 km)
H_AIA
H_FRD
D_AIA
D_FRD
5 nT
10.01.2013 20:39:12 - 10.01.2013 21:59:20 1h 20m 8s

Pulsationen an konjugierten Punkten – Bsp. 3 (AIA – FRD, Entfernung: 11 500 km)

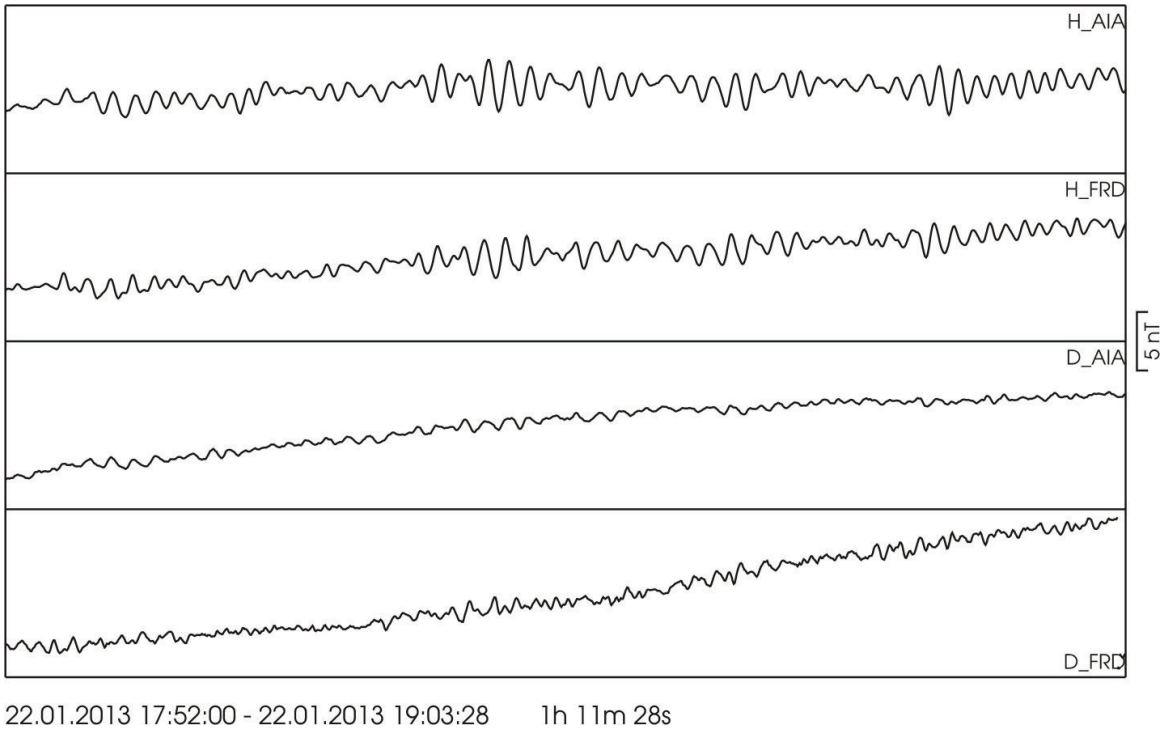

Eignet sich eine Station am konjugierten Punkt als Referenz für den Bereich der Pulsationen? Sondierungskurven aus Ostpolen:

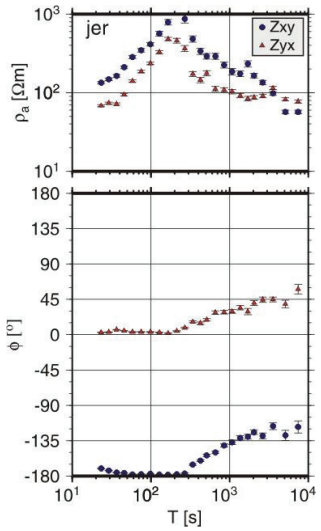

Single-site mit eindeutigen Gleichstrombahn-Verzerrungen

Eignet sich eine Station am konjugierten Punkt als Referenz für den Bereich der Pulsationen? Sondierungskurven aus Ostpolen:

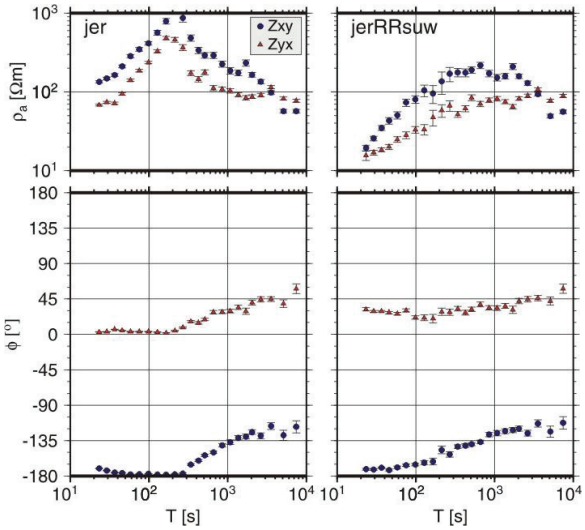

Single-site mit eindeutigen Gleichstrombahn-Verzerrungen

Klassisches RR mit Referenz aus der Region

Eignet sich eine Station am konjugierten Punkt als Referenz für den Bereich der Pulsationen? Sondierungskurven aus Ostpolen:

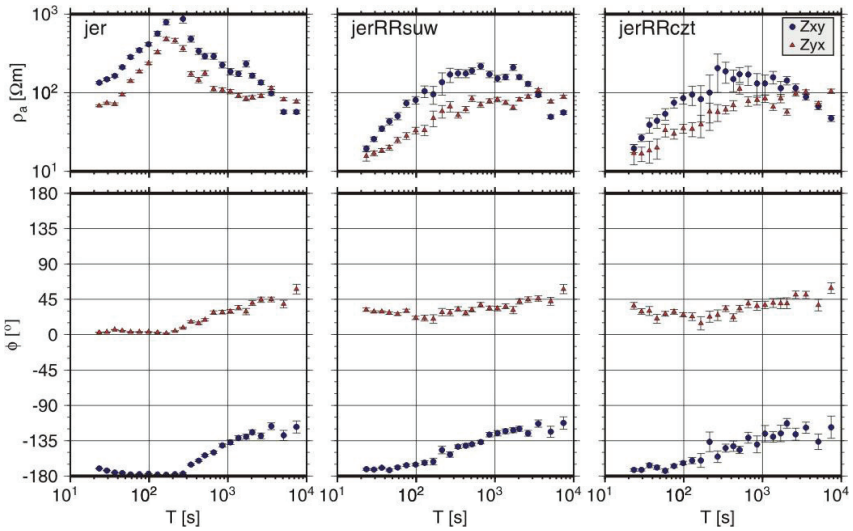

Single-site mit eindeutigen Gleichstrombahn-Verzerrungen

Klassisches RR mit Referenz aus der Region

RR mit Referenz vom konjugierten Punkt auf den Crozet-Inseln

- Pulsationen an konjugierten Punkten sind in ähnlichem Maße kohärent wie man es bei benachbarten Stationen erwarten würde.

- Daher eignen sich “konjugierte” Stationen prinzipiell als Referenzen im Rahmen des RR-Verfahrens. Dies gilt natürlich nur für den Periodenbereich der Pulsationen (0,2 – 600 s).

Schumann-Resonanzen: Grundlagen I

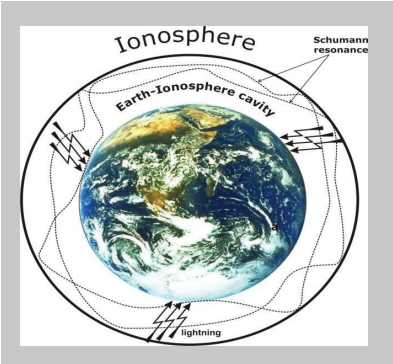

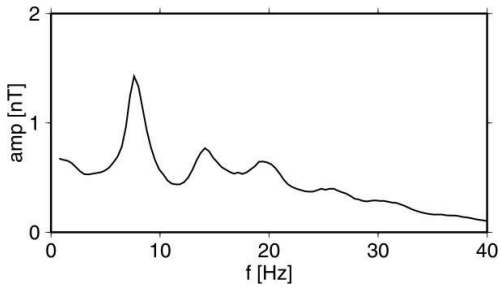

Maxima bei ca. 7, 14, 21 , … Hz
im Amplitudenspektrum
(hier: Hx, Hornsund, Spitzbergen)

Schumann-Resonanzen: Grundlagen II

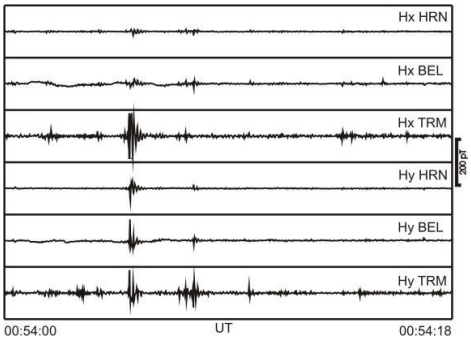

Die Aufzeichnungen verschiedener Stationen sind stark kohärent, da sie bestimmte Ereignisse zeitgleich sehen (HRN-Spitzbergen, BEL-Polen, TRM-Tarimbecken, China). Dies ermöglicht weltweites RR und sogar eine Bestimmung des Einschlagsortes.

Schumann-Resonanzen: Grundlagen II

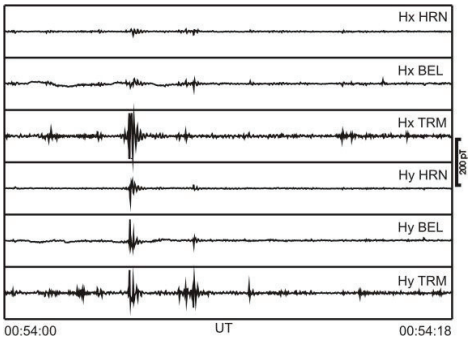

Die Aufzeichnungen verschiedener Stationen sind stark kohärent, da sie bestimmte Ereignisse zeitgleich sehen (HRN-Spitzbergen, BEL-Polen, TRM-Tarimbecken, China). Dies ermöglicht weltweites RR und sogar eine Bestimmung des Einschlagsortes.

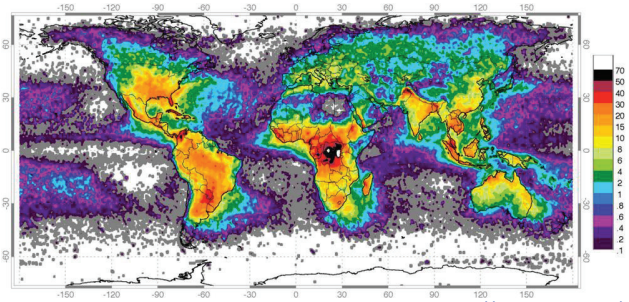

Blitze pro Jahr und km^2 (http://www.nasa.gov/centers/goddard/news/topstory/2004/0621lightning_prt.htm, Wikipedia)

Schumann-Resonanzen: Grundlagen II

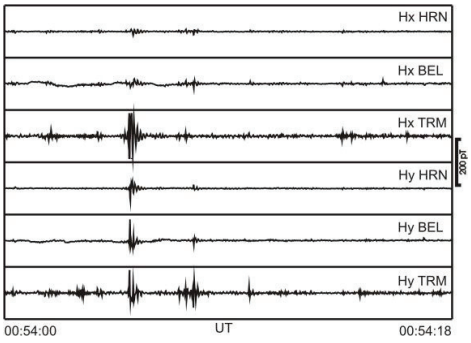

Die Aufzeichnungen verschiedener Stationen sind stark kohärent, da sie bestimmte Ereignisse zeitgleich sehen (HRN-Spitzbergen, BEL-Polen, TRM-Tarimbecken, China). Dies ermöglicht weltweites RR und sogar eine Bestimmung des Einschlagsortes.

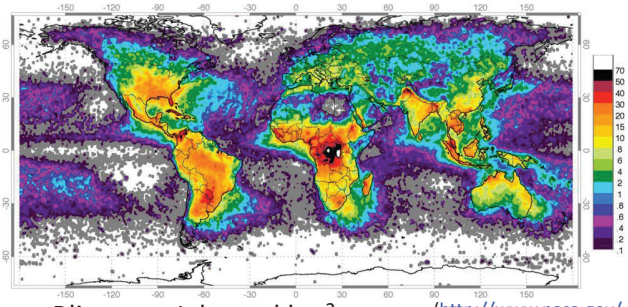

Blitze pro Jahr und km^2 (http://www.nasa.gov/centers/goddard/news/topstory/2004/0621lightning_prt.htm, Wikipedia)

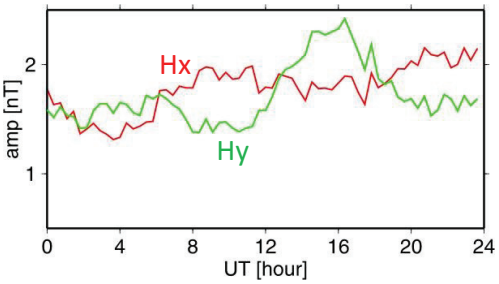

Tageszeitabhängigkeit der Intensität der ersten Schumann-Resonanz-Mode (Hornsund, Spitzbergen, 13. 05. 2011)

Afrikanische Blitze verbessern nachmittags das Signal-Rausch-Verhältnis für Zxy in Europa:

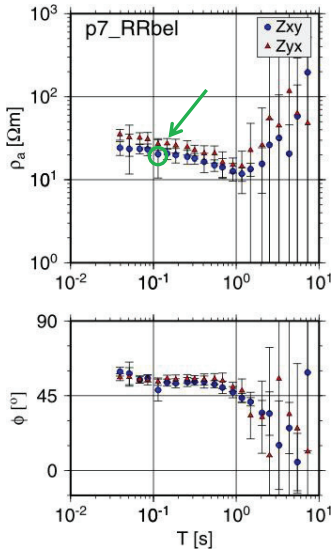

Teil einer Sondierungskurve aus NW-Polen

Afrikanische Blitze verbessern nachmittags das Signal-Rausch-Verhältnis für Zxy in Europa:

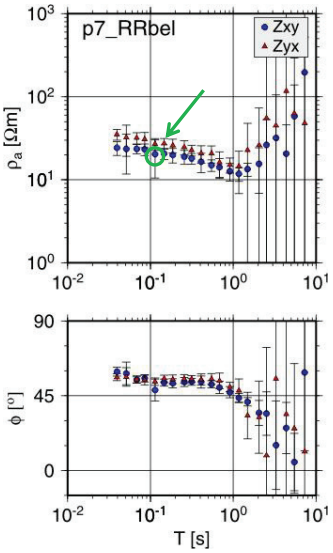

Teil einer Sondierungskurve aus NW-Polen

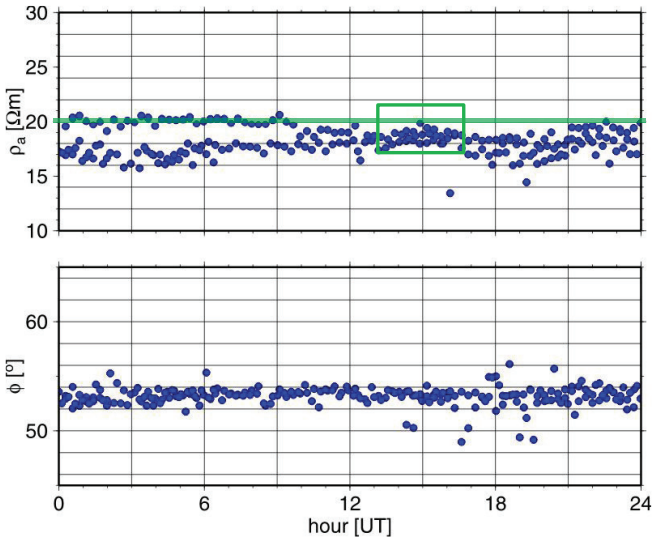

Der Zxy-Wert (single-site) bei 8 Hz dieser Station auf Grundlage von 20-min-Zeitreihen in Abhängigkeit von der Tageszeit

- Die zeitlich und räumlich ungleichmäßige Verteilung der Schumann-Resonanz-Quellen ist (bei entsprechender Bearbeitung) in den statistischen Eigenschaften von MT-Übertragungsfunktionen nachweisbar.

- Bei Problemen, die eine mögliche Nicht-Stationarität von Übertragungsfunktionen betreffen, sollte der Betrachtung der Quellen eine gewisse Bedeutung eingeräumt werden.

Eine

Danksagung

geht an

- **INTERMAGNET**, das Netzwerk für hohe Standards in der Observatoriumsarbeit, sowie die nationalen Institute, die die Observatorien betreiben, deren Daten hier verwendet wurden,
- **Jürgen Matzka** *(Deutsches GeoForschungsZentrum, Observatorium Niemegk)* für Hilfe beim Umgang mit geomagnetischen Koordinaten,
- **Mariusz Neska** *(Institut für Geophysik der Polnischen Akademie der Wissenschaften, Observatorium Belsk)*, da er Abbildungen zum Thema Schumann-Resonanzen beigesteuert hat,
- **Vladimir Bakhmutov** *(Institute of Geophysics at the National Academy of Sciences of the Ukraine, Kiev)*, **Vaclav Červ** *(Geophysical Institute, Academy of Sciences of the Czech Republic, Prague)* und **Yixian Xu** *(Subsurface Multi-scale Imaging Laboratory of Hubei Province, China University of Geosciences, Wuhan)*, da sie Daten zur Verfügung gestellt haben,
- **KNOW** (Krajowy Naukowy Ośrodek Wiodący), aus dessen Mitteln für das Zentrum für Polarstudien meine Teilnahme am Kolloquium finanziert wurde.

WESTFÄLISCHE WILHELMS-UNIVERSITÄT MÜNSTER

GEOPHYSIK WWU MÜNSTER

Magnetotelluric inversion with wavelet sparsity regularization

C. Nittinger[1], M. Becken[1]

[1]University of Münster, Institute of Geophysics, Correnstr. 24, 48149 Münster,

Contact: cnittinger@wwu.de

23.09.2015

EMTF 2015

Smoothing regularization in Magnetotellurics – an inevitable tool?

Occam's inversion: A practical algorithm for generating smooth models from electromagnetic sounding data

Steven C. Constable*, Robert L. Parker*, and Catherine G. Constable*

ABSTRACT

…tigate a new algorithm for computing regularized solutio…
…sional magnetotelluric inverse problem. The algorithm employs a…
…gradients (NLCG) scheme to minimize an objective function that p…
…als and second spatial derivatives of resistivity. We compare this al…

Occam's inversion to generate smooth, two-dimensional models from magnetotelluric data

C. deGroot-Hedlin* and S. Constable*

Abstract

…hree-dimensional magnetotelluric (MT) minimum structure inversion alg…
…t of the Occam approach. Computational costs associated with construct…
…el-space Occam approach to 3D MT inversion impractical. These diffic…
…matrix dimensions depend on the size of the data set, rather than the numl…
…space it becomes feasible to invert modest 3D MT data sets on a PC. To r…
…on is used for the iterative forward modeling code used to compute t…
…tational time by more than 70%, without affecting the inversion results.…
…asonable fits can be obtained within a small number of iterations, with…
…essary structure and find the model with minimum norm.
…4 Elsevier B.V. All rights reserved.

Magnetotelluric inversion for minimum structure

J. Torquil Smith* and John R. Booker*

ABSTRACT

Structure can be measured in terms of a norm of the derivative of a model with respect to a function of depth $f(z)$, where the model $m(z)$ is either the conductivity σ or $\log \sigma$. An iterative linearized algorithm can find models

Others result in s… quencies, a "red" fit… robust statistic is us… be made acceptably …

Regularization is needed for a stable solution

Regularization

- Inverse problem:

$$min\{\underbrace{\| G(m)-d^{obs} \|_2^2}_{data\ term} + \underbrace{\lambda \Phi(m)}_{regularization}\}$$

- Objective: smoothest possible representation of the model that fits the data
- non-linear and ill-posed problem

  → infinite number of solutions

- L2-Norm: $\Phi(m)=\sqrt{\sum |m|^2}$

  → smoothness

How to describe a resistivity model?

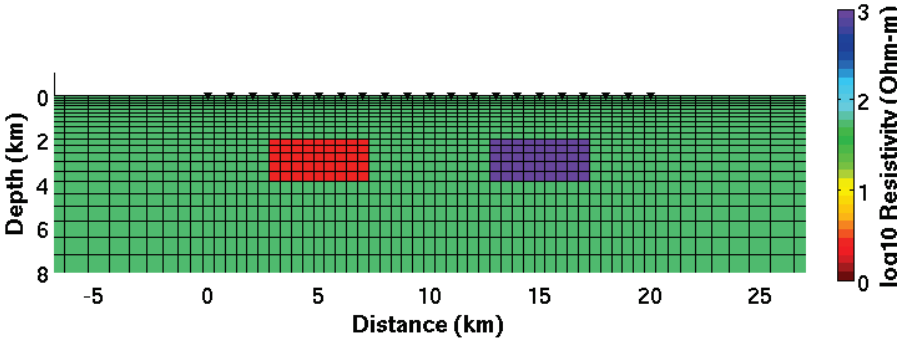

Usual inversion grid:

- Piecewise constant functions
- **Many** Blocks

Compressed model described by wavelets: [Daubechies, 1992]

$$m(x) = \sum_j^M c_j \Phi_j(x) = \underbrace{\sum_j a_j \Phi_j(x)}_{Approximation.\ Coeffs.} + \underbrace{\sum_j \sum_k d_k^j \Psi_{j,k}(x)}_{Detail\ Coeffs.}$$

j - translation
k - scale

- **few** coefficients

  → no loss of Information

Can we benefit from sparse inversion?

Sparse Inversion: Regularize for sparsity of wavelet coefficients

→ applications in various fields: medical imaging, image processing, signal analysis, seismic tomography

- No structural penalty
- Model structures dependent on chosen wavelet basis
  → can be sharp, smooth or both.

Regularization

- Inverse problem:

$$min\{\underbrace{\| G(c) - d^{obs} \|_2^2}_{data\ term} + \underbrace{\lambda \Phi(c)}_{regularization}\}$$

- Objective: **sparsest** possible representation of the model that fits the data
- L2-Norm: $\Phi(m) = \sqrt{\sum |m|^2}$
  → smoothness
- L1-Norm: $\Phi(c) = \sum |c|$
  → sparsity

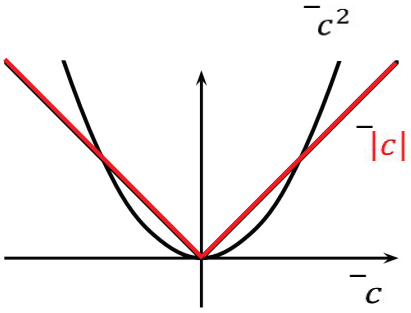

Objective function in Wavelet domain

$$\Phi(c,m) = \| G(m) - d^{obs} \|_2^2 \quad + \quad \lambda \| c \|_1^1$$

- Wavelet Transformation: $m = Rc$
- Finite element forward code by Lee et al. (2009)

Block model domain

$G(m)$

$J(m)$

Wavelet domain

$G(Rc)$

$J(c) = J(m)R$

$$\Phi(c) = \| W_e(G(c) - d^{obs}) \|_2^2 \quad + \quad \lambda \| c \|_1^1$$

Gauss Newton approach to solve linearized objective

- Linearized Iteration step:

$$\| W_e(J(c^k)c^{k+1} - \hat{d}(c^k)) \|_2^2 \quad + \quad \lambda \| c^{k+1} \|_1^1 \quad \rightarrow \; min.$$

$$\hat{d}(c^k) = d^{obs} - G(c^k) + J(c^k)c^k$$

- Solve with iterative soft thresholding (IST) by Daubechies et al. (2004)

$$c_{n+1}^{k+1} = Shrink_\lambda\left(c_n^{k+1} + (W_e J(c^k))^T (W_e(\hat{d}(c^k) - J(c^k)c_n^{k+1}))\right)$$

$$\text{Shrink}_\lambda(c) = \begin{cases} c - \lambda & c \geq \lambda \\ 0 & |c| \leq \lambda \\ c + \lambda & c \leq -\lambda \end{cases}$$

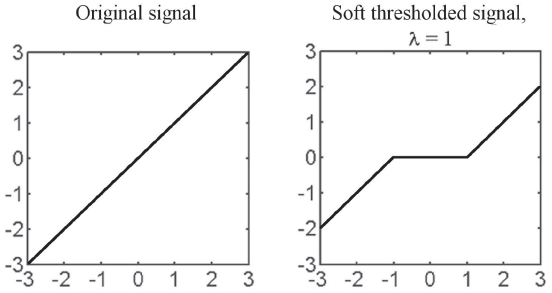

Inversion of magnetotelluric data in a sparse model domain

Sparsity regularization

Model Representation

Synthetic examples

Wavelet functions

Simple Haar wavelet (only vertical):

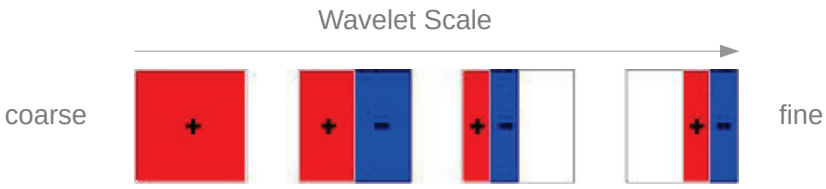

Complex dual tree wavelets [Kingsbury, 2001; Selesnik et al., 2005]:

Real

Imaginary

Absolute

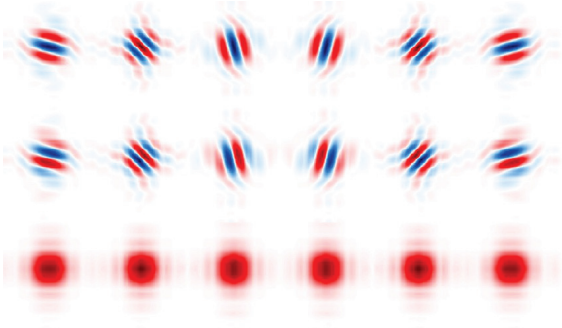

$$Dm = c$$

$$m = Rc$$

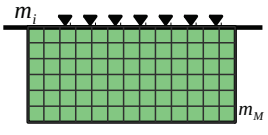

[Loris et al., 2007]

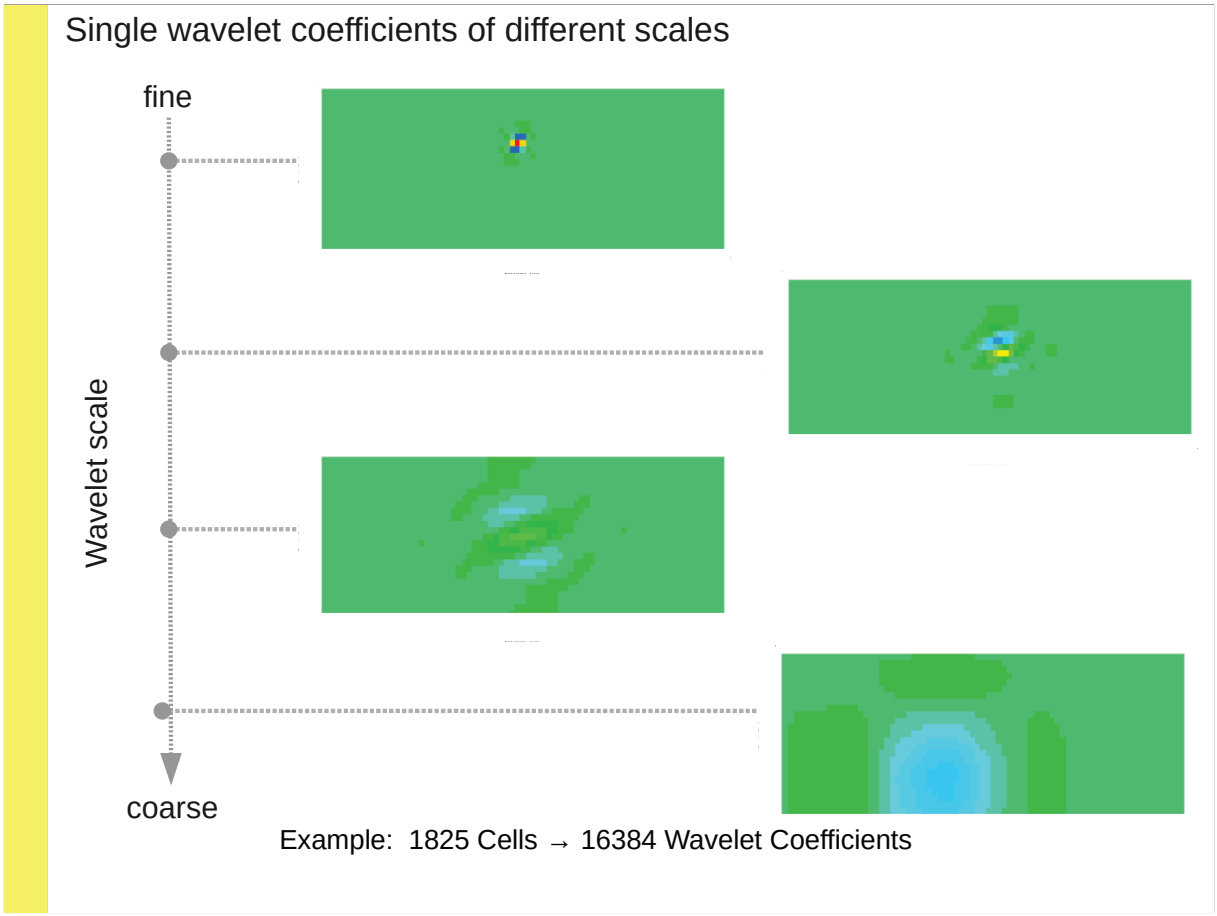

Single wavelet coefficients of different scales
fine
Wavelet scale
coarse
Example: 1825 Cells → 16384 Wavelet Coefficients

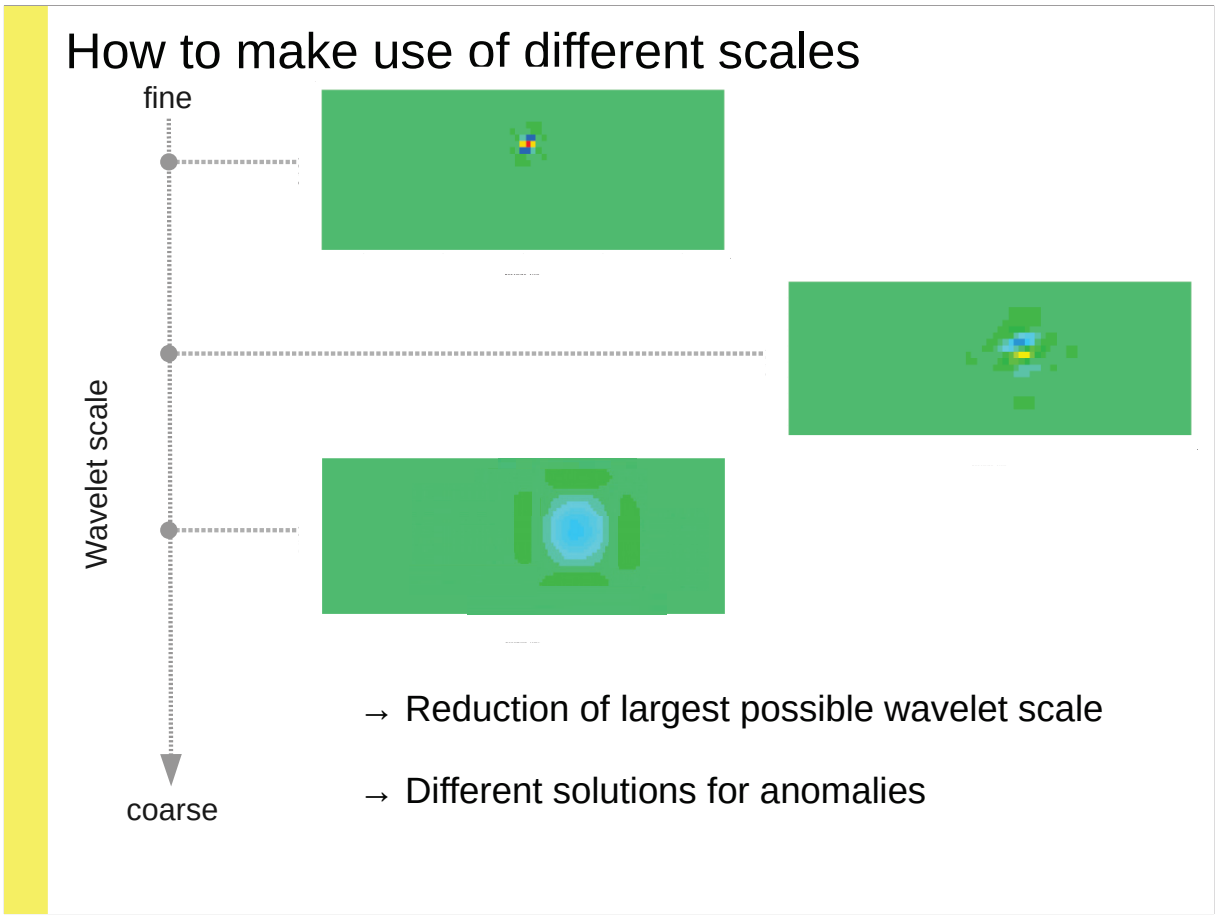
How to make use of different scales
fine
Wavelet scale
coarse
→ Reduction of largest possible wavelet scale
→ Different solutions for anomalies

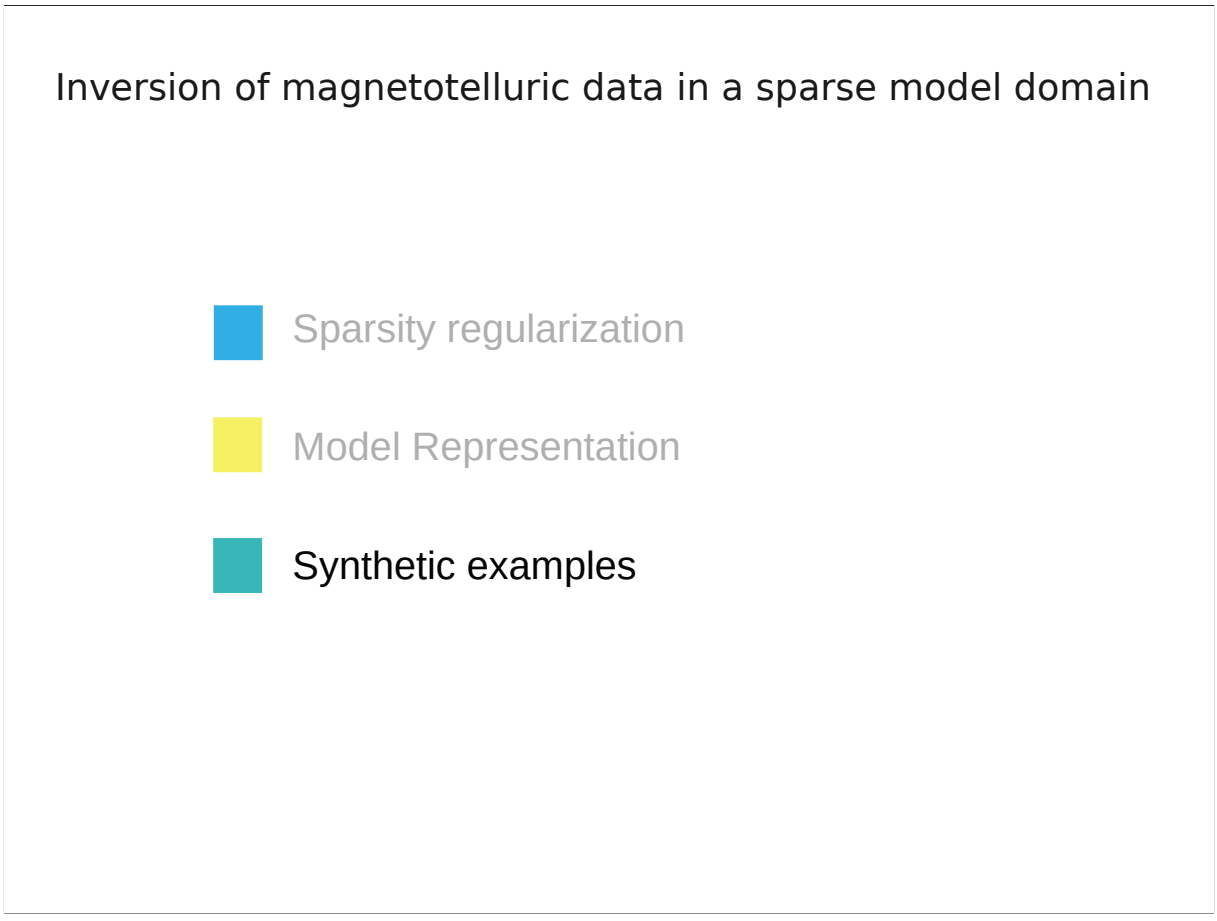
Inversion of magnetotelluric data in a sparse model domain
Sparsity regularization
Model Representation
Synthetic examples

True model

Errors: App. Res. 5%
Phase 1°
Tipper 0.05

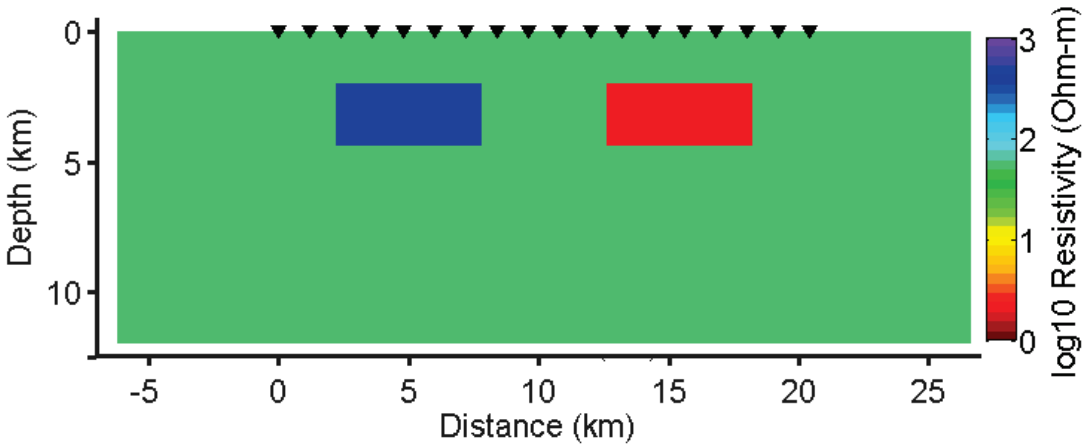

Grid: 55x20 uniform cell sizes of 600m
Freq.: 0.1s-100s

Sparsity of Iteration steps

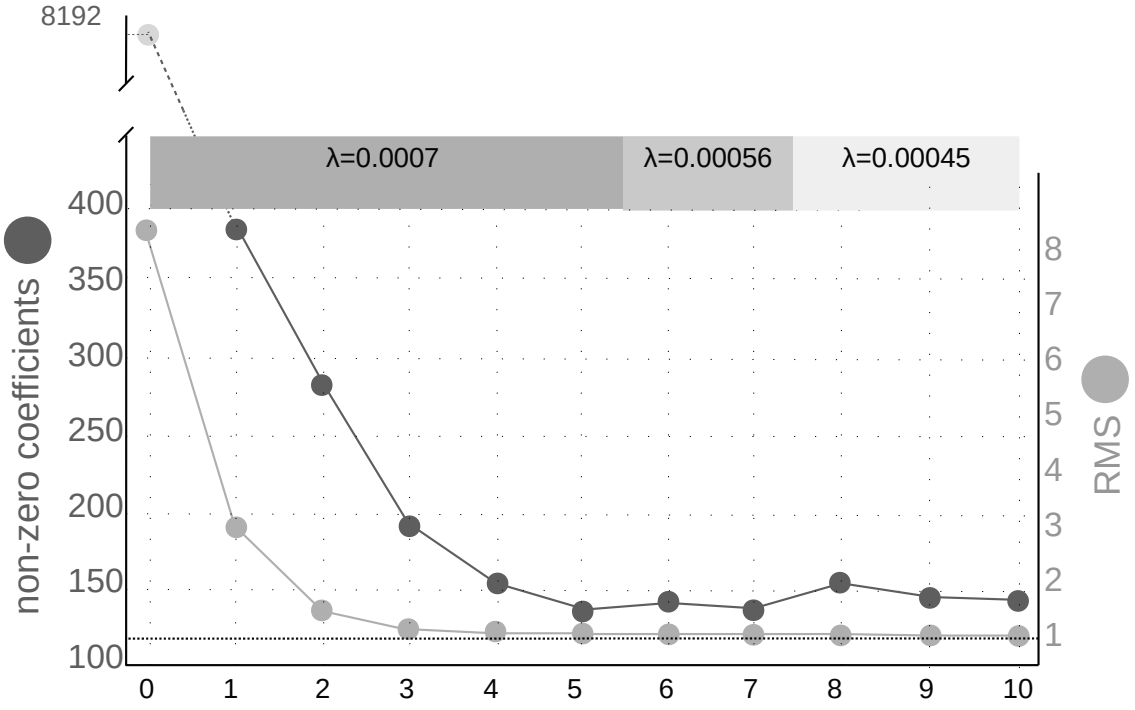

Inverse model

Coeffs: 143 RMS: 1.03

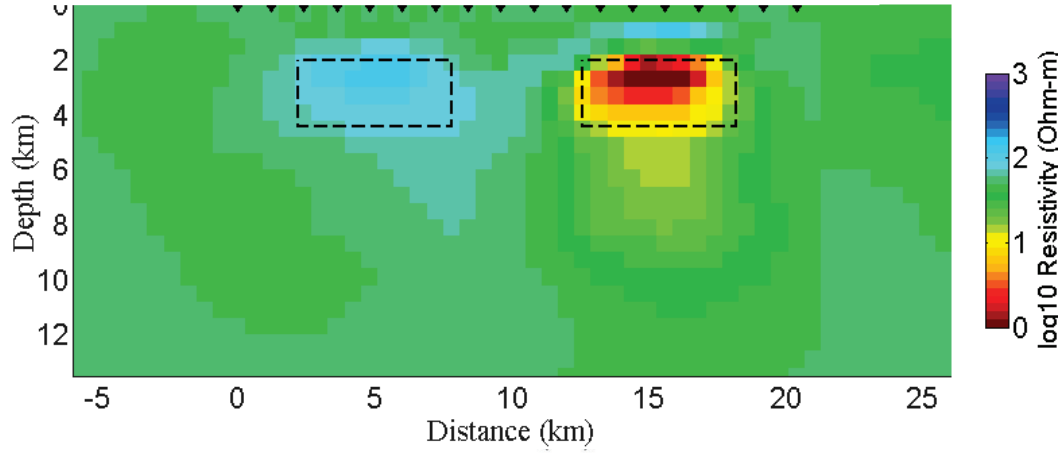

Inverse model

Coeffs: 143 RMS: 1.03

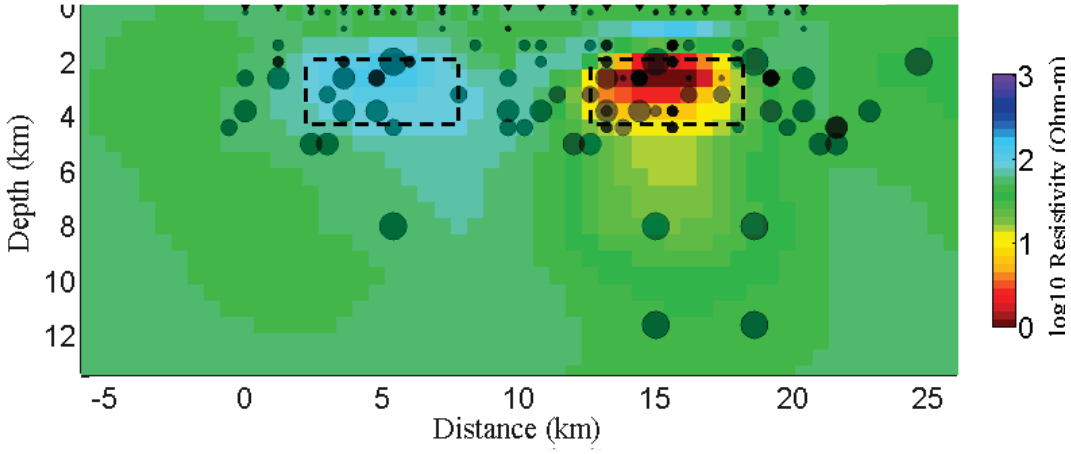

True model

Errors: App. Res. 5%
Phase 1°
Tipper 0.05

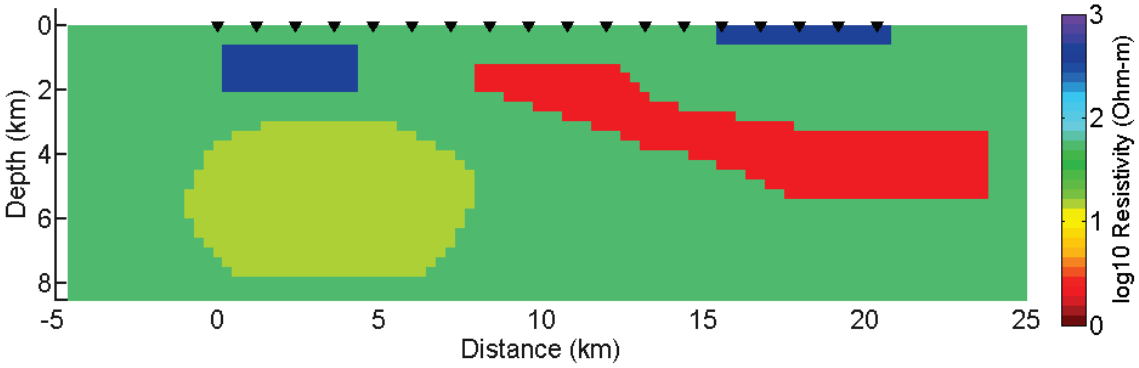

Inverse model

Coeffs: 199 RMS: 1.05 Max scale: 4

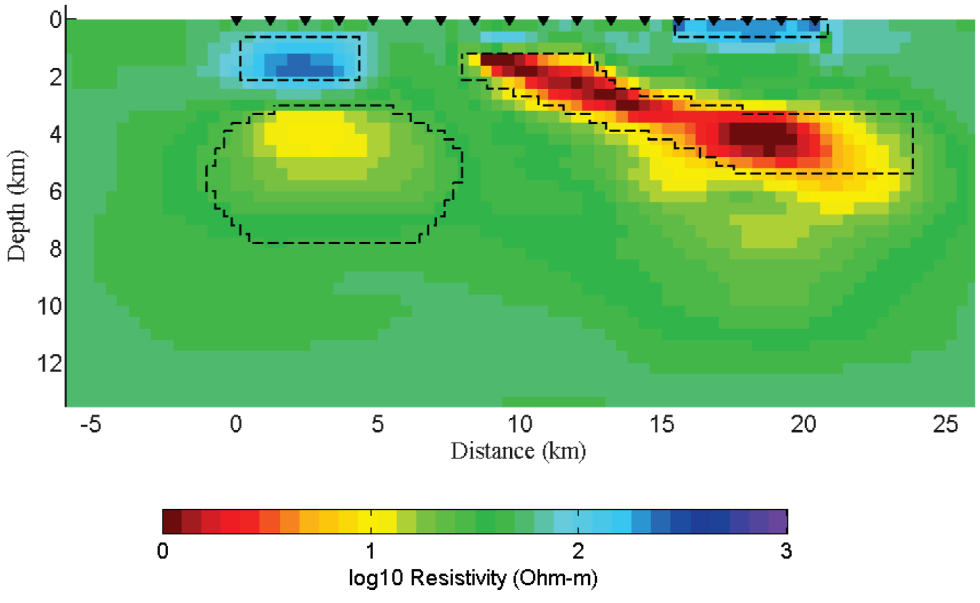

Inverse model

Coeffs: 199 RMS: 1.05 Max scale: 4

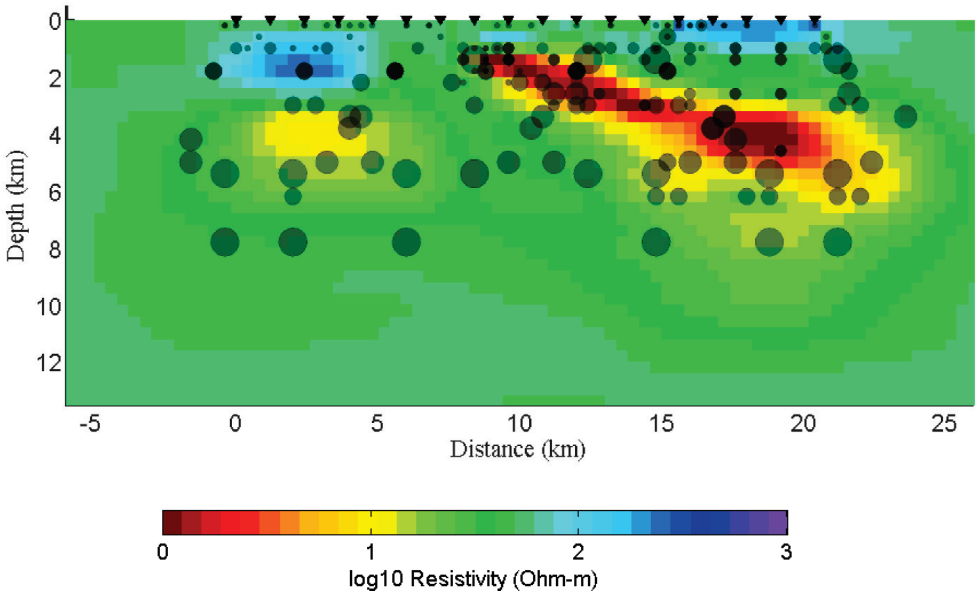

Reduction of maximal scale

Maxlvl: 4 RMS: 1.05 Coeffs.: **199**

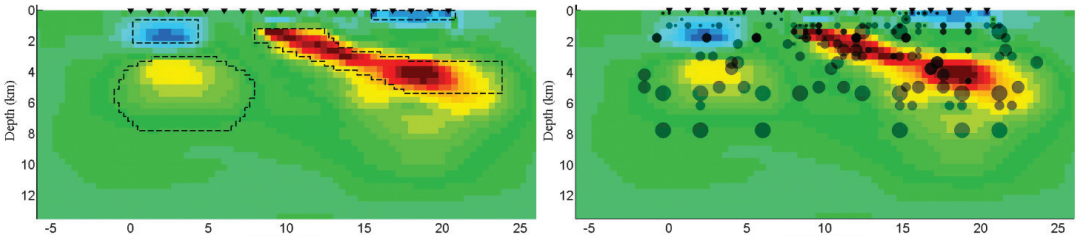

Maxlvl: 3 RMS: 1.06 Coeffs.: **180**

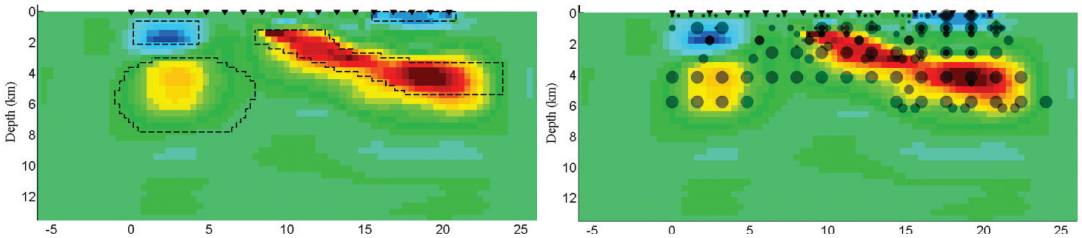

Maxlvl: 2 RMS: 1.05 Coeffs.: **285**

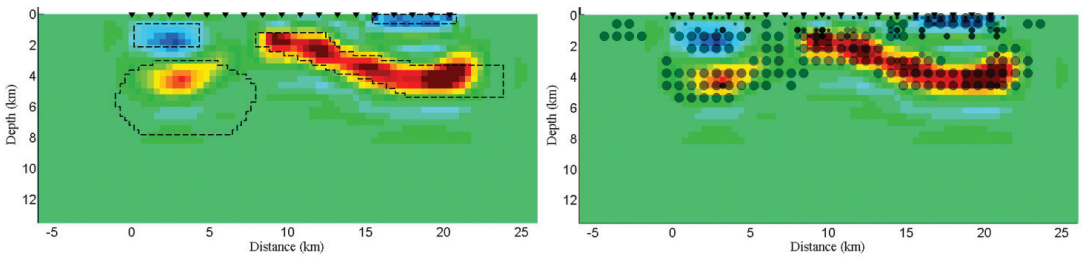

Smooth Inversion model is very similar

RMS: 1.02

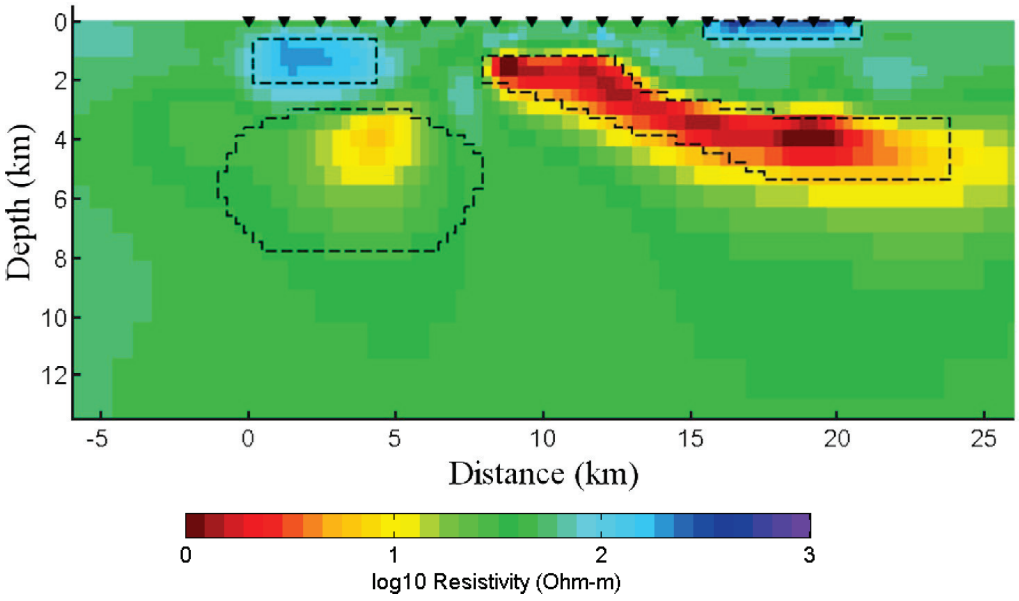

The Haar wavelet representation

Coeffs: 96 RMS: 1.05 Max Scale: 4

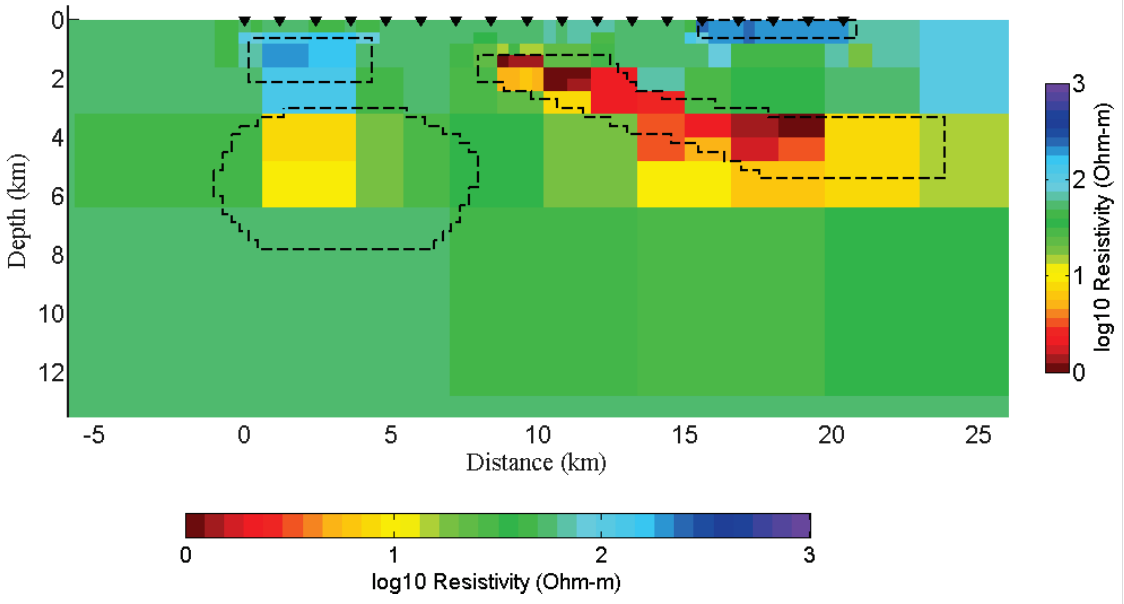

Inverse model

Maxlvl: 4 RMS: 1.05 Coeffs.: **199**

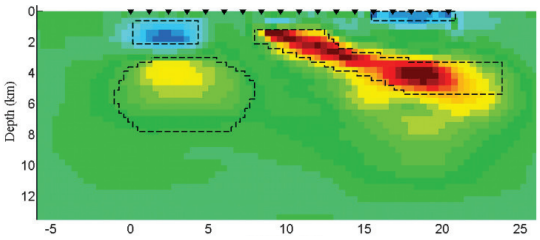

Maxlvl: 3 RMS: 1.06 Coeffs.: **105**

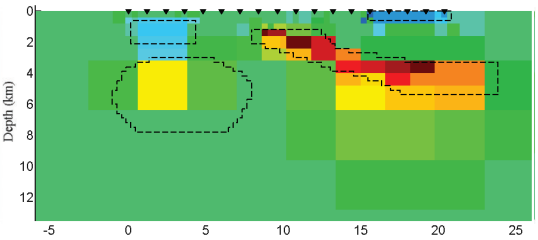

Maxlvl: 3 RMS: 1.06 Coeffs.: **180**

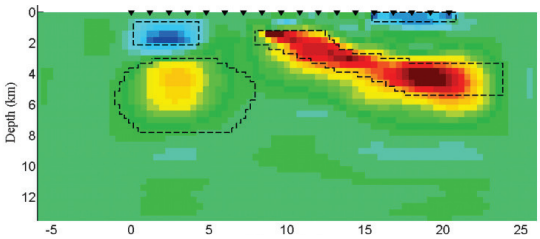

Maxlvl: 2 RMS: 1.06 Coeffs.: **118**

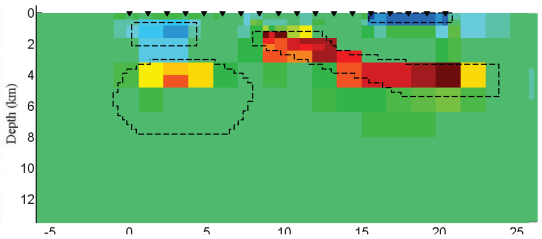

Maxlvl: 2 RMS: 1.05 Coeffs.: **285**

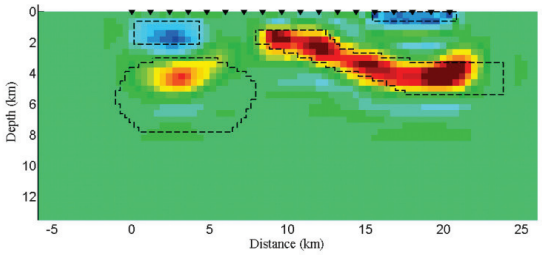

Maxlvl: 1 RMS: 1.05 Coeffs.: **181**

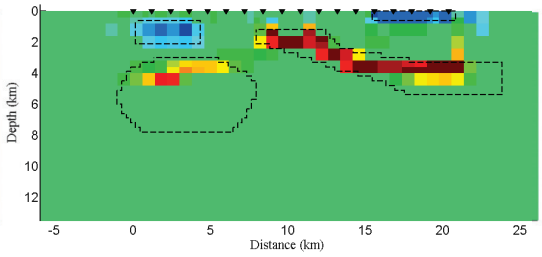

Summary

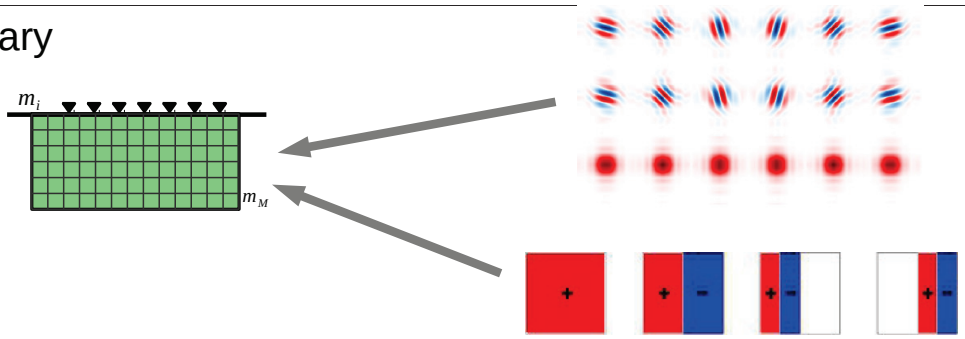

L1-Norm Regularization of *c*: $\Psi(c) = \lambda \| c \|_1^1$

Sparse inversion model

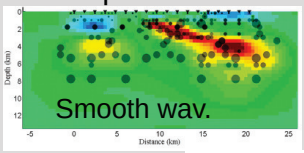

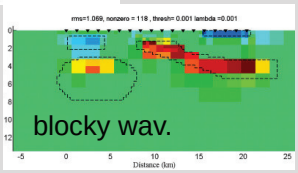

Model Evaluation:

- Determine possible scales of anomalies
- Different representations allow comparison of different models
- Evaluation of non-unique model structures and artifacts

Westfälische Wilhelms-Universität Münster

GEOPHYSIK WWU MÜNSTER

References

Daubechies, I., (1992). Ten lectures on wavelets, Society for Industrial and Applied Mathematics (SIAM).

Daubechies, I., Defrise, M., & De Mol, C., (2004). An iterative thresholding algorithm for linear inverse problems with a sparsity constraint, Communications on Pure and Applied Mathematics, 57(11), 1413-1457.

Donoho, D. L. (2006). Compressed sensing. Information Theory, IEEE Transactions on, 52(4), 1289-1306.

Kingsbury, N. (2001). Complex wavelets for shift invariant analysis and filtering of signals. Applied and computational harmonic analysis, 10(3), 234-253.

Lee, S. K., Kim, H. J., Song, Y., & Lee, C.-K., (2009). Mt2dinvmatlab -a program in matlab and fortran for two-dimensional magnetotelluric inversion, Computers & Geosciences, 35(8),1722-1734.

Loris, I., Nolet, G., Daubechies, I., & Dahlen, F., (2007). Tomographic inversion using l1-norm regularization of wavelet coffecients, GJI, 170(1), 359-370.

Selesnick, I. W., Baraniuk, R. G., & Kingsbury, N. C., (2005). The dual-tree complex wavelettransform, Signal Processing Magazine, IEEE, 22(6), 123{151.

Instrument Pool, Permanent Reference Site, Archive and Data Publications

O. Ritter, G. Munoz, U. Weckmann, R. Klose, P. Rulff, R. Barth, G. Willkommen

Deutsches GeoForschungsZentrum GFZ

GIPP-MT (instruments / sensors)

- www.gfz-potsdam.de/gipp --> http://www.gfz-potsdam.de/sektion/geophysikalische-tiefensondierung/servicesinfrastruktur/geophysikalischer-geraetepool-potsdam-gipp/

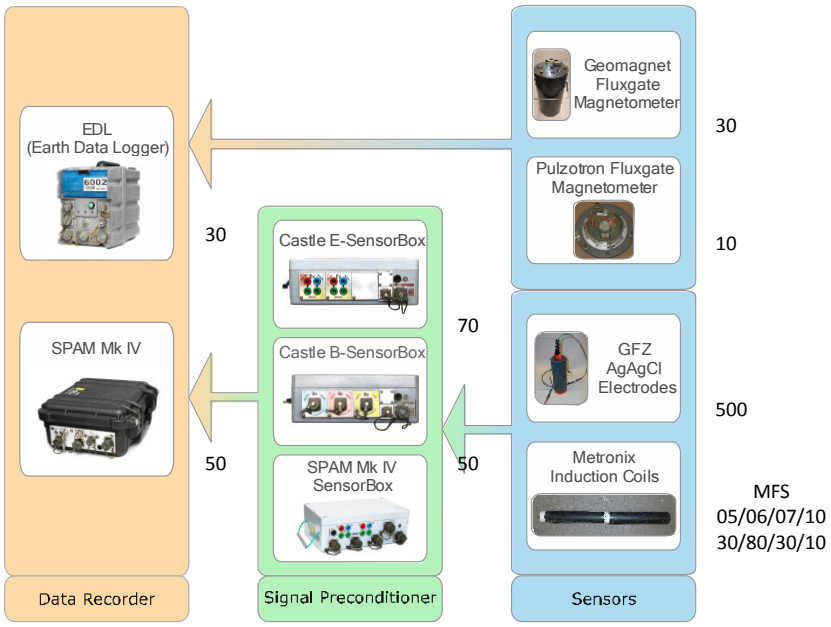

GIPP-MT (new sensors)

- Metronix MFS10 sensor: Optimized for Bz measurements.

length 853 mm
diameter 75 mm
Range: ~1 kHz – 1 mHz

GIPP-MT (how to get instruments?)

- Submit a proposal to the Steering Board of the pool:

The Steering Board for the Geophysical Instrument Pool	The Internal Advisory Board for the Geophysical Instrument Pool
Prof. Dr. W. Rabbel (Chairman, Univ. Kiel) Prof. Dr. D. Gajewski (Univ. Hamburg) Prof. Dr. F. Krüger (Univ. Potsdam) Prof. Dr. J. Ritter (Univ. Karlsruhe) Prof. Dr. B. Tezkan (Univ. Köln) Prof. Dr. Ch. Thomas (Univ. Münster)	Dr. Ch. Haberland (GFZ Potsdam) PD Dr. O. Ritter (GFZ Potsdam) Prof. Dr. M. Weber (GFZ Potsdam) Prof. Dr. F. Tilmann (GFZ Potsdam)

- The Steering Board meets twice a year (usually April and October).
- The deadline for applications is four weeks before the Steering Board meeting.
- The next steering board meeting will take place in **November 10, 2015;** the deadline for applications is **October 10, 2015**

GIPP-MT (who can get instruments?)

Prioritization of project applications

- The Steering Board discusses and evaluates the scientific content and feasibility of the project applications, sets up a priority list, and makes recommendations to the GFZ Executive Board. The GFZ Executive Board eventually makes decision based on the Steering Board recommendations.
- In addition to the scientific content, the following aspects are considered for the prioritization:
  1. Projects with German participation
  2. Projects of partners of the operators of European infrastructure networks
  3. other projects
- The instruments are provided free of charge in case of academic and non-profit projects. The provision to industry and commercial projects is subject of payment

GIPP-MT (but…)

Damage & Loss

- The user is liable for any damages and loss of the instruments. That is why an insurance particularly in case of operation abroad is highly recommended.

Data

- Raw data as well as a report have to be handed over to the GIPP within a year after completion of the experiment. Data is reserved for the user up to 4 years after the completion of the experiment. 4 years after the completion of the measurements, data gathered with GIPP-instruments have to be made freely available (through the "GIPP experiment- and data archive" under a Creative Common License.
- In case of citable data publication (having a DOI) scientists involved in the experiment have to be named.

Publication

- Publications related to experiments with GIPP instruments have to acknowledge the GIPP stating the GIPP- Grant-Number. The user sends electronic copies of these publications to the GIPP.
- The Helmholtz Association, … supports Open Access Publications ...

Failure to obey these guidelines will have consequences for further supply.

GIPP-MT (Experiment and Data Archive)

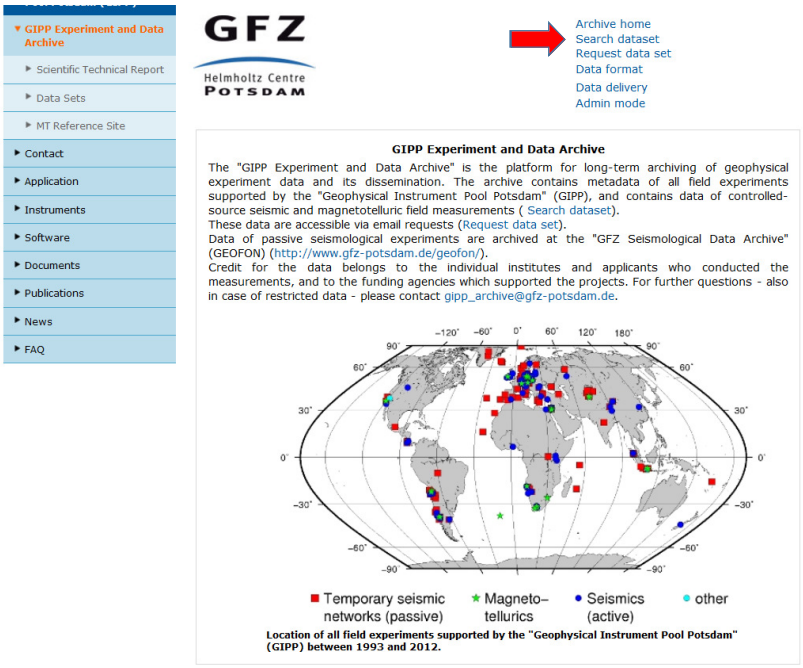

GIPP-MT (Experiment and Data Archive)

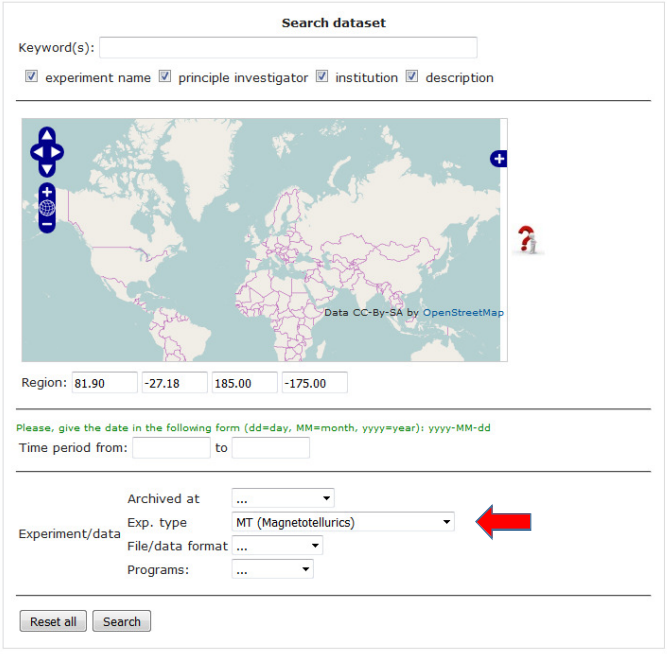

GIPP-MT (Experiment and Data Archive)

datasets found:: 39

ID	ExpName	ExpType	Start	End	Archiv	Program	Format	Ac
201418	DEEP/MT	MT (Magnetotellurics)	2014-09-21	2014-10-03	GIPP	GIPP		NOT_ARC
201309	GreenT/MT	MT (Magnetotellurics)	2013-08-01	2013-10-15	GIPP	GIPP		NOT_ARC
201306	MT_WNG	MT (Magnetotellurics)	2013-10-01	2013-12-31	GIPP	GIPP		UNKNOW
201217	TIPTIMON-MT	MT (Magnetotellurics)	2012-06-01	2012-08-30	GIPP	GIPP	MSEED	RESTRICT
201216	EOR	MT (Magnetotellurics)	2012-11-01	2012-11-30	GIPP	GIPP	MSEED	RESTRICT
201215	BRINE	MT (Magnetotellurics)	2012-03-01	2012-03-31	GIPP	GIPP	MSEED	RESTRICT
201203	ISOLDE	MT (Magnetotellurics)	2012-01-01	2013-05-01	GIPP	GIPP		UNKNOW
201117	HPT	MT (Magnetotellurics)	2011-10-01	2011-12-31	GIPP	GIPP	MSEED	RESTRICT
201116	SIPOHOLON-MT	MT (Magnetotellurics)	2011-07-15	2011-08-15	GIPP	GIPP	MSEED	RESTRICT
201115	GASH-MT	MT (Magnetotellurics)	2011-11-15	2011-12-15	GIPP	GIPP	MSEED	RESTRICT
201114	ELCONA	MT (Magnetotellurics)	2011-10-01	2011-11-30	GIPP	GIPP		UNKNOW
201018	GeoEn	MT (Magnetotellurics)	2010-10-01	2011-11-30	GIPP	GIPP		NOT_ARC
201012	ELIBABA/MT	MT (Magnetotellurics)	2010-06-25	2010-09-05	GIPP	GIPP		NOT_ARC
200907	EGS-MT	MT (Magnetotellurics)	2009-05-01	2009-05-31	UNKNOWN	GIPP		NOT_ARC
200904	Barberton-MT	MT (Magnetotellurics)	2009-03-15	2009-05-31	UNKNOWN	GIPP		NOT_ARC
200903	TIPAGE-MT	MT (Magnetotellurics)	2009-06-01	2009-09-10	UNKNOWN	GIPP		NOT_ARC
200902	GEO-EN MT Test (ex-COAST-MT)	MT (Magnetotellurics)	2009-03-01	2009-05-31	UNKNOWN	GIPP		NOT_ARC
200809	Tadshikistan/MT	MT (Magnetotellurics)	2008-06-15	2008-08-15	UNKNOWN	GIPP		NOT_ARC

GIPP-MT (Experiment and Data Archive)

Dataset details

Exp. id: 201309 **Status:** UNKNOWN

Project:	GreenT/MT Conductivity structure of a 1.9 Ga old fold belt in West Greenland to constrain the dip and depth extent of (thrust) faults, intrusions and possible remnants of subduction zones; comparison with corresponding MT-studies in Canada.
DOI:	
Principle investigator:	Andreas Junge junge@geophysik.uni-frankfurt.de Uni Frankfurt
Exp. type:	MT (Magnetotellurics)
Time period from:	2013-08-01 to 2013-10-15
Location:	[66.0;-53.0]
Recorder types:	EDL 12
Sensor types:	
Formate:	
Archived at:	GIPP
Programs:	GIPP

Request

Cancel

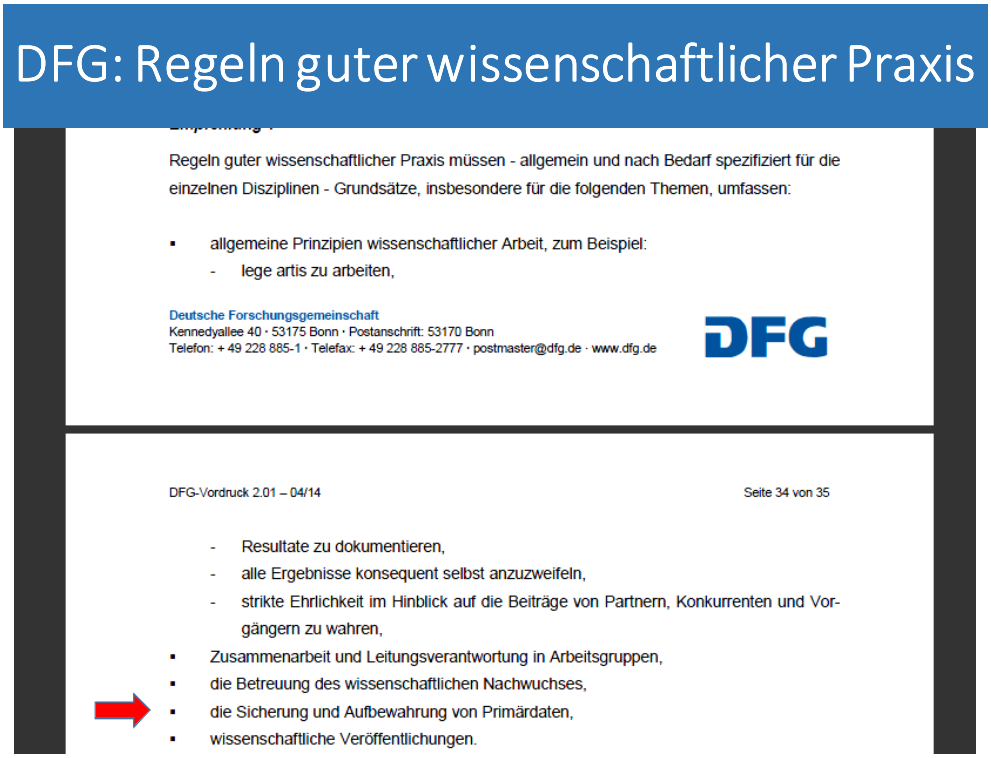
DFG: Regeln guter wissenschaftlicher Praxis
Regeln guter wissenschaftlicher Praxis müssen - allgemein und nach Bedarf spezifiziert für die einzelnen Disziplinen - Grundsätze, insbesondere für die folgenden Themen, umfassen:
allgemeine Prinzipien wissenschaftlicher Arbeit, zum Beispiel:
lege artis zu arbeiten,
Deutsche Forschungsgemeinschaft
Kennedyallee 40 · 53175 Bonn · Postanschrift: 53170 Bonn
Telefon: + 49 228 885-1 · Telefax: + 49 228 885-2777 · postmaster@dfg.de · www.dfg.de
DFG
DFG-Vordruck 2.01 – 04/14
Seite 34 von 35
Resultate zu dokumentieren,
alle Ergebnisse konsequent selbst anzuzweifeln,
strikte Ehrlichkeit im Hinblick auf die Beiträge von Partnern, Konkurrenten und Vorgängern zu wahren,
Zusammenarbeit und Leitungsverantwortung in Arbeitsgruppen,
die Betreuung des wissenschaftlichen Nachwuchses,
die Sicherung und Aufbewahrung von Primärdaten,
wissenschaftliche Veröffentlichungen.

A first step…

MT Reference Site

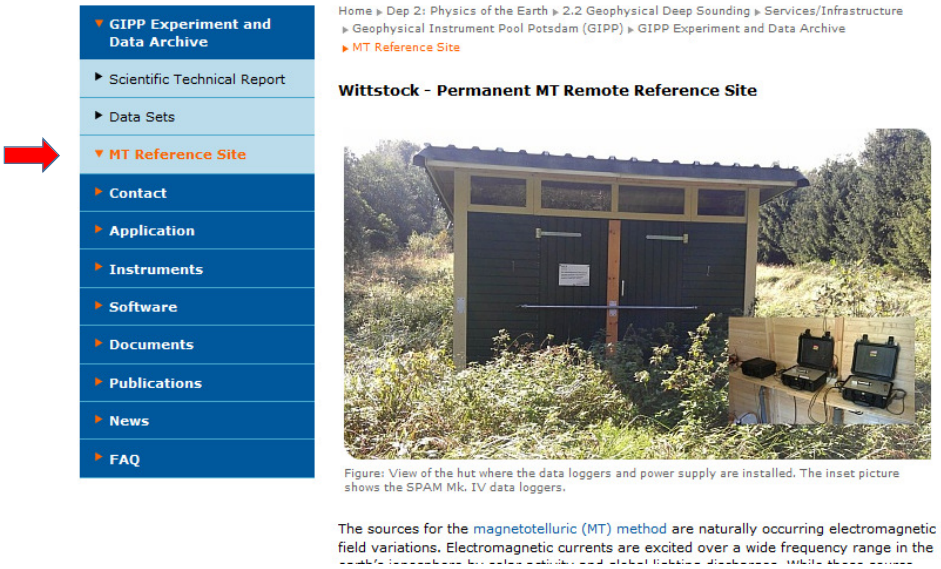

MT Reference Site

Archived time-series data

All data are recorded as time series using two SPAM Mk. IV systems. For ease of use, the data are re-organized as three virtual MT sites, covering a wide frequency range. Data streams can be continuous or in scheduled modes.

Site 991 comprises a 3-component Geomagnet fluxgate magnetometer (Bx, By, Bz) and electric field (Ex, Ey) recordings. Recording is continuous at a sampling rate of 5 Hz.

Site 996 comprises one (or more) continuously recorded data streams using MFS06 induction coil magnetometers (Bx, By, coil switch in LF mode, chopper on) and electric fields (Ex, Ey). Over time, a range of sampling rates were tested (50 Hz, 250 Hz, 500 Hz).

Site 997 records high frequency data which are typically sampled in scheduled mode. Over time, a range of sampling frequencies were tried (2.5 kHz, 5 kHz, 6.25 kHz, 12.5 kHz, 25 kHz). The magnetic fields are recorded with Metronix MFS07 sensors (Bx, By, coil switch in HF mode, chopper off).

For detailed information on available time-series for each site and year, please follow the links in the table below:

Site 991	Site 996	Site 997
		2011
2012	2012	2012
2013	2013	2013
2014	2014	2014
2015	2015	2015

MT Reference Site

Hardware Configurations and Recording Modes

Project: Wittstock Remote Reference
Site number: 996

Run: 001

Recording Period 18 Jan 2013 00:00:00 - 20 Jan 2013 23:59:59 (For 24 h every 24 h)							
Site	SPAM	Sensor Box	Sampling Frequency	Channel Nr.	Name	Sensor Type	Sensor Number
996	43	19	50.00 Hz	001	Bx	Metronix_Coil-----TYPE-006_LF	441
				002	By	Metronix_Coil-----TYPE-006_LF	395
	20	103		003	Ex	TelluricElectrode-TYPE-AgAgCl	0
				004	Ey	TelluricElectrode-TYPE-AgAgCl	0

Run: 002

Recording Period 06 Feb 2013 11:45:30 - 07 Feb 2013 01:59:59 (For 2 h every 2 h) 08 Feb 2013 00:00:00 - 12 Feb 2013 23:59:59 (For 24 h every 24 h) 14 Feb 2013 11:00:00 - 15 Feb 2013 23:59:59 (For 24 h every 24 h) 16 Feb 2013 00:00:06 - 16 Feb 2013 23:59:59 (For 24 h every once) 17 Feb 2013 00:00:06 - 18 Feb 2013 23:59:59 (For 24 h every 24 h) 19 Feb 2013 00:00:06 - 19 Feb 2013 23:59:59 (For 24 h every once) 20 Feb 2013 00:00:06 - 22 Feb 2013 23:59:59 (For 24 h every 24 h) 23 Feb 2013 00:00:06 - 26 Feb 2013 23:59:59 (For 24 h every 24 h) 27 Feb 2013 00:00:06 - 01 Mar 2013 23:59:59 (For 24 h every 24 h) 02 Mar 2013 00:00:06 - 02 Mar 2013 23:59:59 (For 24 h every once) 03 Mar 2013 00:00:00 - 04 Mar 2013 23:59:59 (For 24 h every 24 h) 05 Mar 2013 00:00:06 - 05 Mar 2013 23:59:59 (For 24 h every once) 06 Mar 2013 00:00:00 - 09 Mar 2013 23:59:59 (For 24 h every 24 h)							
Site	SPAM	Sensor Box	Sampling Frequency	Channel Nr.	Name	Sensor Type	Sensor Number
	43	19		001	Bx	Metronix_Coil-----TYPE-006_LF	441
				002	By	Metronix_Coil-----TYPE-006_LF	395

Citation Information

Citation Information

The magnetotelluric data of the Permanent Magnetotelluric Reference Station Wittstock, Germany is freely available upon request and may be used under the Creative Commons Licence (CC-by-sa 4.0 Unported). Please send your data requests to Oliver Ritter (oritter(at)gfz-potsdam.de).

Recommended citation of the datasets:
Ritter, O., Weckmann, U., Muñoz, G., Klose, R., Rettig, S., Schüler, M., Müller-Brettschneider, C., Willkommen, G., Rulff, P. (2015) Permanent Magnetotelluric Reference Station Wittstock, Germany. GFZ Data Services. DOI: http://doi.org/10.5880/GFZ.2.2.2015.001

Recommended citation of the data report:
Ritter, O., Muñoz, G., Weckmann, U., Klose, R., Rulff, P., Rettig, S., Müller-Brettschneider, C., Schüler, M., Willkommen, G., Eydam, D. (2015) A Permanent Magnetotelluric Remote-Reference Station in Wittstock, Germany. Scientific Technical Report 15/09 - Data, GIPP Experiment- and Data, GFZ German Research Centre for Geosciences. DOI: http://doi.org/10.2312/GFZ.b103-15092

The EMERALD Data Format for Magnetotelluric Data is described in detail in:
Ritter, O., Klose, R., Weckmann, U., EMERALD Data Format for Magnetotelluric Data, Scientific Technical Report - Data; 15/08, Potsdam: Deutsches GeoForschungsZentrum GFZ, DOI: http://doi.org/10.2312/GFZ.b103-15082, 2015.
http://doi.org/10.2312/GFZ.b103-15092

STR (scientific technical report)

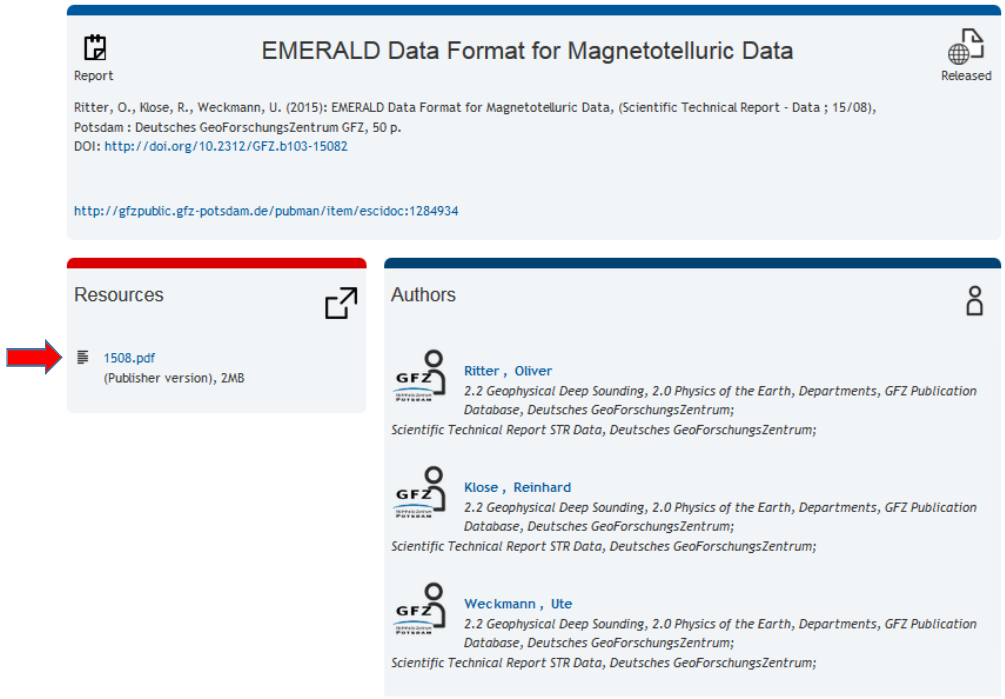

CC (creative commons)

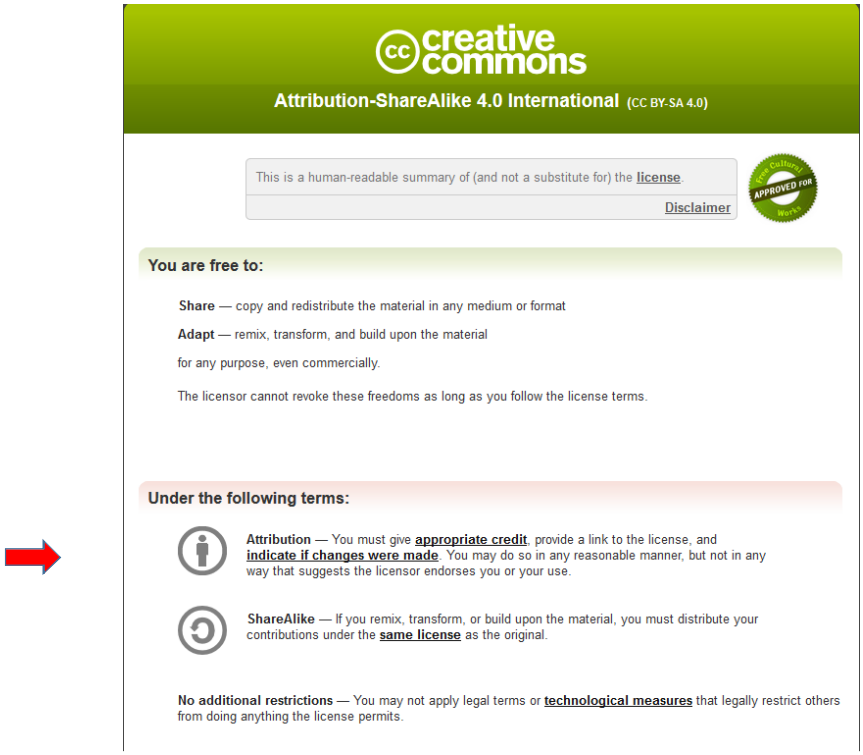

What (data) do I get ?

- Time series (binary)
- Meta-data (XML)
- Instrument responses
- Example programs (sources)

What (data) do I get and how?

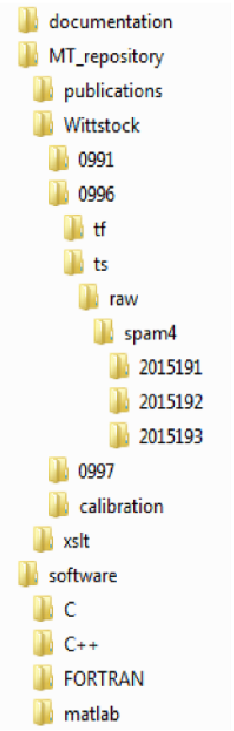

- **documentation**
- **MT_repository**: extract from GIPP-MT data repository
  - **publications:** folder containing relevant references in bibx format
  - **Wittstock**: data of the permanent remote reference site near Wittstock
    - **991**: site folder containing LF data (fluxgate sensor)
    - **996**: site folder containing BB data (MFS06 coils)
      - **ts / raw / spam4 / 201519x** subfolders containing time series data from days 191 - 193 of 2015
    - **997**: site folder containing HF data (MFS07 coils)
    - **calibration**: calibration data for magnetic field sensors
  - **xslt:** folder containing xslt style files to transform xml files to html formatted viewing in web browser
- **software**: folder with sample code to access EMERALD type data files (.RAW/.XTR/.XTRX)
  - **C:** examples in C
  - **C++:** examples in C++
  - **FORTRAN:** examples in FORTRAN
  - **matlab:** examples in matlab

Metadata? XML?

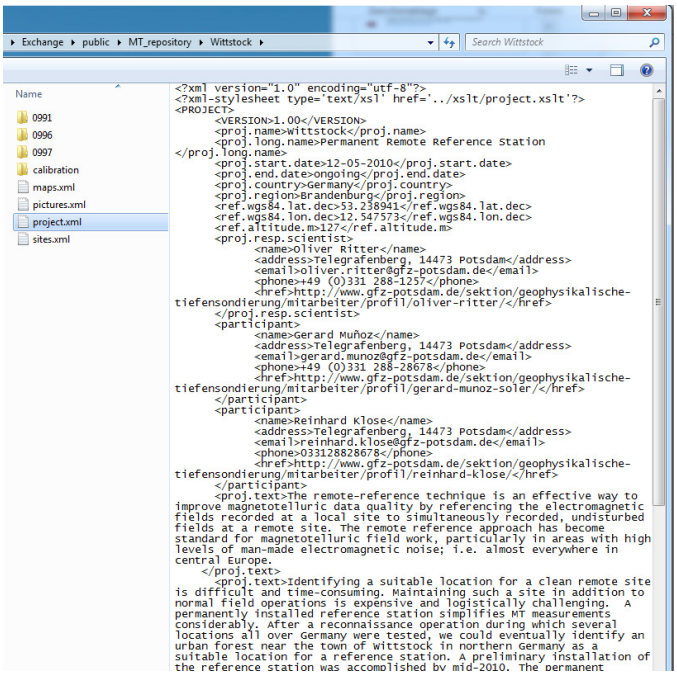

Your web browser knows what to do…

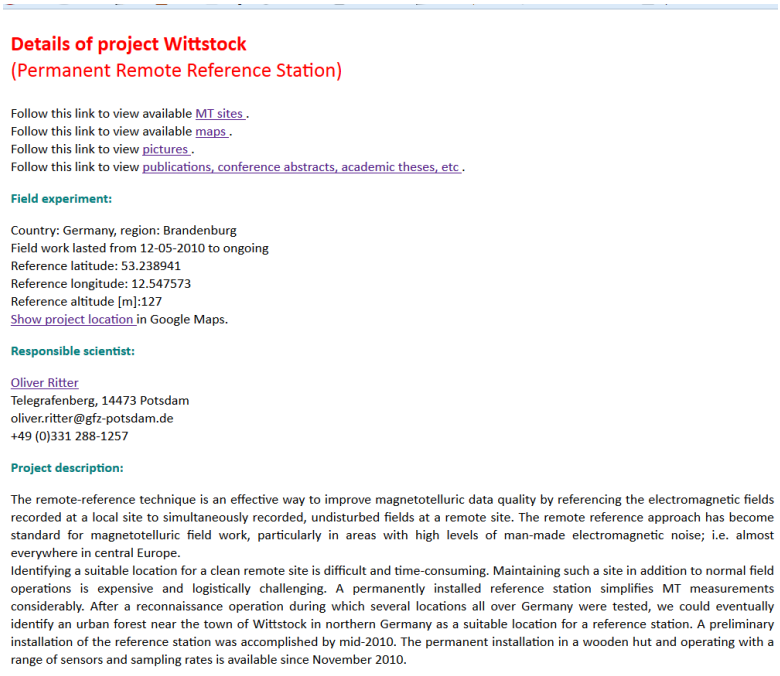

Details of project Wittstock
(Permanent Remote Reference Station)

Follow this link to view available MT sites .
Follow this link to view available maps .
Follow this link to view pictures .
Follow this link to view publications, conference abstracts, academic theses, etc .

Field experiment:

Country: Germany, region: Brandenburg
Field work lasted from 12-05-2010 to ongoing
Reference latitude: 53.238941
Reference longitude: 12.547573
Reference altitude [m]:127
Show project location in Google Maps.

Responsible scientist:

Oliver Ritter
Telegrafenberg, 14473 Potsdam
oliver.ritter@gfz-potsdam.de
+49 (0)331 288-1257

Project description:

The remote-reference technique is an effective way to improve magnetotelluric data quality by referencing the electromagnetic fields recorded at a local site to simultaneously recorded, undisturbed fields at a remote site. The remote reference approach has become standard for magnetotelluric field work, particularly in areas with high levels of man-made electromagnetic noise; i.e. almost everywhere in central Europe.
Identifying a suitable location for a clean remote site is difficult and time-consuming. Maintaining such a site in addition to normal field operations is expensive and logistically challenging. A permanently installed reference station simplifies MT measurements considerably. After a reconnaissance operation during which several locations all over Germany were tested, we could eventually identify an urban forest near the town of Wittstock in northern Germany as a suitable location for a reference station. A preliminary installation of the reference station was accomplished by mid-2010. The permanent installation in a wooden hut and operating with a range of sensors and sampling rates is available since November 2010.

Summary / Outlook

- Please acknowledge GIPP instruments on posters, presentations, theses, papers, …
- If acquired with GIPP instruments, please send us your data for archiving
- Consider using and citing data publications
- Wittstock is a beginning, more data will be released eventually (http://www.gfz-potsdam.de/en/section/geophysical-deep-sounding/infrastructure/geophysical-instrument-pool-potsdam-gipp/archive/mt-reference-site/)

? Use the archive for other MT data ?

? Should we be more restrictive with the licenses ?

? Automated downloads / web interface ?

? Integration with EPOS / similar platforms ?

Marine CSEM Site Survey on Gas Hydrate Targets in the Danube Delta, western Black Sea

Katrin Schwalenberg[1], Dennis Rippe[1,2], Romina Gehrmann[1], Sebastian Hoelz[3]

[1] Federal Institute for Geosciences and Natural Resources (BGR), Hannover, Germany,
katrin.schwalenberg@bgr.de

[2] now at GFZ Potsdam, Germany

[3] GEOMAR, Kiel, Germany

Burning Gas Hydrate

R/V Maria S. MERIAN in Varna, Bulgaria

BGR Bundesanstalt für Geowissenschaften und Rohstoffe
GEOZENTRUM HANNOVER

Project SUGAR-Site, RV MERIAN Cruise MSM35

Submarine Gas Hydrate Reservoirs

- German Joint Venture Project to investigate gas hydrates as a possible future energy resource and for CCS in hydrate form.
- 30 Partners, ~25 Mill. € in 6 years (2008-2014)

- MERIAN Cruise MSM 34: 06.12.2013 – 16.01.2014, Varna to Varna – Seismic, Geochemistry
- MERIAN Cruise **MSM 35:** 20.01. – 05.02.2014, Varna to Istanbul **- CSEM**
- **Objective:** geophysical **site survey** for a planned **test drill site** for methane production from gas hydrate

Cruise Track MSM 35

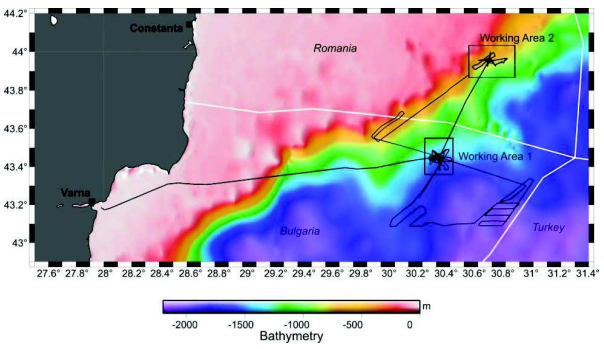

BGR Bundesanstalt für Geowissenschaften und Rohstoffe
GEOZENTRUM HANNOVER

Gas Hydrates in the Western Black Sea

- Quasi-closed marginal sea, up to **19 km sediment layer** in the Western basin
- **Anoxic conditions** favour the formation of methane
- Widespread presence of oil and gas
- **Presence** of submarine **gas hydrates** inferred from seismic **bottom simulating reflectors** (**BSR**) marking the **base** of the **gas hydrate stability zone** (GHSZ)
- **Multiple BSR** due to climate-related sea level changes
- **Danube Delta** considered as a possible **test drill site** for **methane production** from gas hydrate

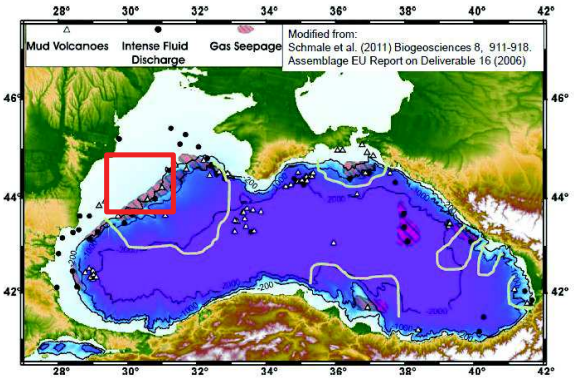

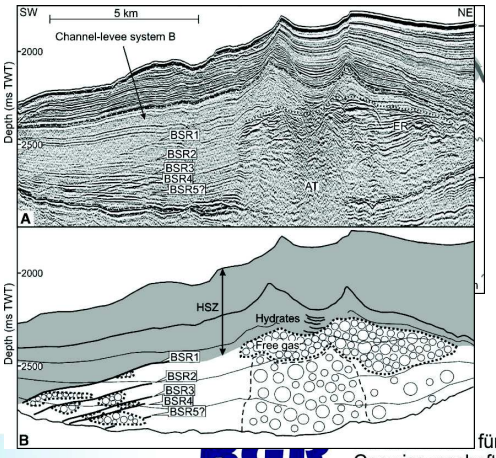

Popescu et al., 2006

für Geowissenschaften und Rohstoffe

GEOZENTRUM HANNOVER

Two Marine CSEM Experiments

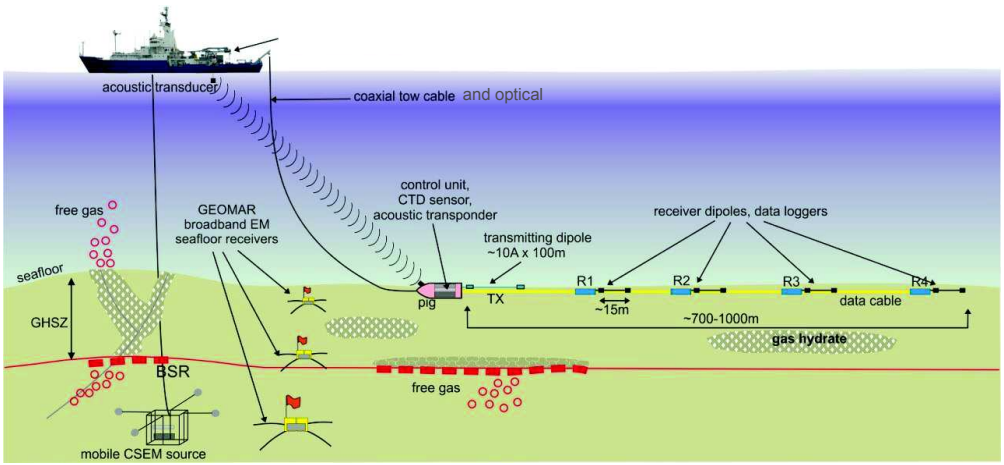

- HYDRA: seafloor towed electric dipole-dipole system → 2D profile data
- SPUTNIK: mobile CSEM Source & EM Receivers → 3D data set

Bundesanstalt für Geowissenschaften und Rohstoffe

GEOZENTRUM HANNOVER

HYDRA: seafloor-towed electrical dipole-dipole system

Receiver Unit

New Seafloor Signal Generator

Bundesanstalt für Geowissenschaften und Rohstoffe

GEOZENTRUM HANNOVER

SPUTNIK and Lobster EM Receiver

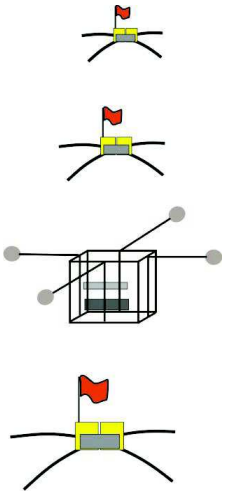

GEOMAR

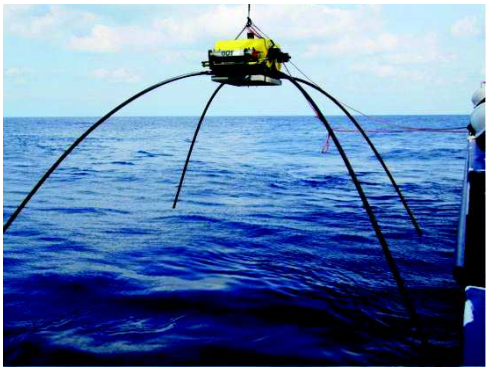

Seafloor EM receiver

2 orthogonal 10 m long source dipoles

Bundesanstalt für Geowissenschaften und Rohstoffe

GEOZENTRUM HANNOVER

Target Area: Danube Delta

Working Area 1

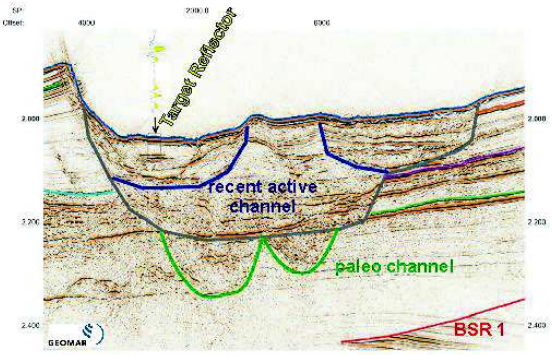

Timo Zander, Geomar, 2014

- Sediment filled Danube channel system
- High seismic amplitude reflections, partly inversed polarity
- Multiple BSR, BSR1 at ~330 mbsf
- High amplitude Target Reflector at about 100 mbsf

- 2D Survey with HYDRA, 3 profiles
- 3D Survey with SPUTNIK & LOBSTERS, 10 sites, 81 transmission points

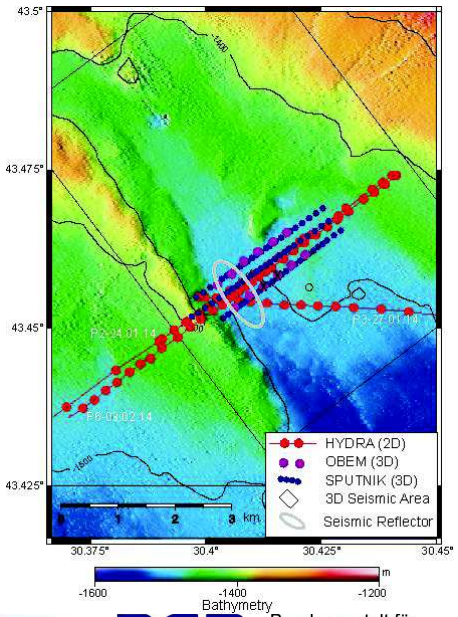

Bundesanstalt für Geowissenschaften und Rohstoffe

GEOZENTRUM HANNOVER

HYDRA Data Example

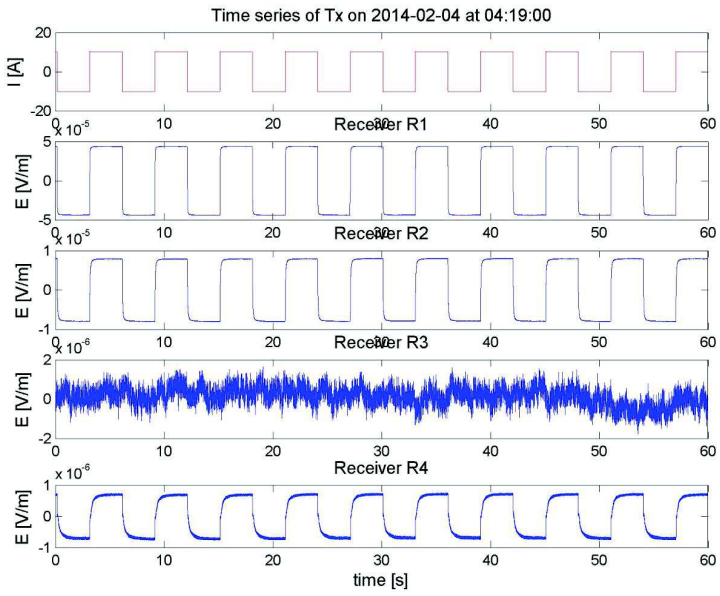

Tx - Rx1: 153 m

Tx – Rx2: 259 m

Tx – Rx3: 364 m

Tx - Rx4: 572 m

Bundesanstalt für Geowissenschaften und Rohstoffe

GEOZENTRUM HANNOVER

HYDRA Data Example

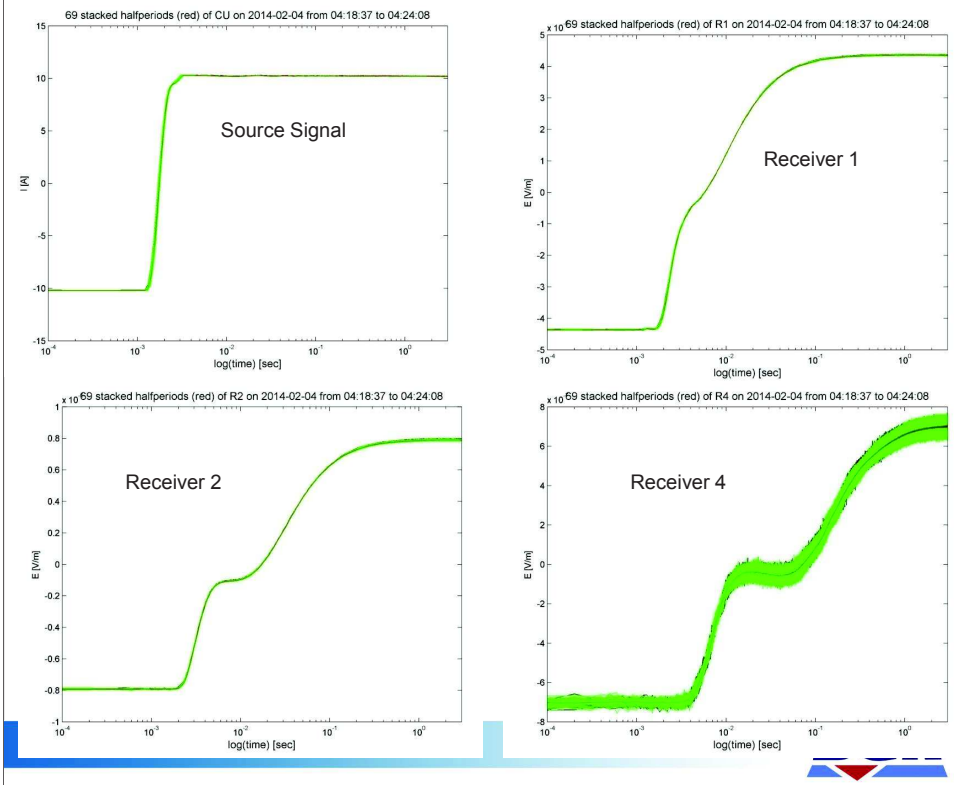

Bundesanstalt für Geowissenschaften und Rohstoffe

GEOZENTRUM HANNOVER

Overview: HYDRA Data Inversion

Profile MSM 35-7:

1) 1D Occam Inversion (*code by Carsten Scholl, CGG-EM*)
2) 2D Occam Inversion (*code by Carsten Scholl, CGG-EM*)
3) 2D Occam Inversion MARE2DEM (*Kerry Key, Scripps*)
4) Comparison: Seismic ←→ CSEM
5) 1D Resolution Study, Marquardt Inversion with Random starting models (*C. Scholl*)
6) 1D Bayesian Inversion (*Romina Gehrmann, UVIC / BGR*)

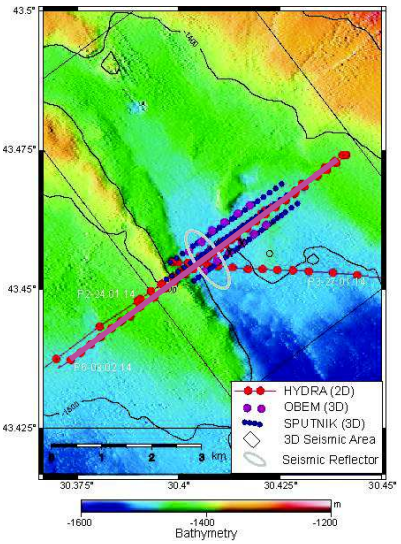

Bundesanstalt für Geowissenschaften und Rohstoffe

GEOZENTRUM HANNOVER

Inversion 1

Stitched 1D Occam Inversion, code by C. Scholl, CGG-EM

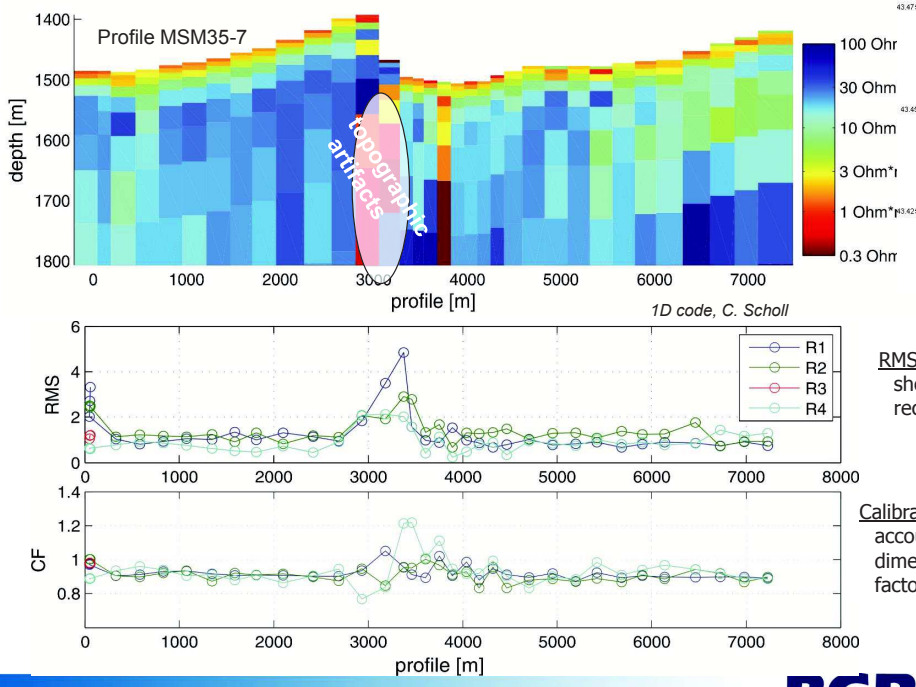

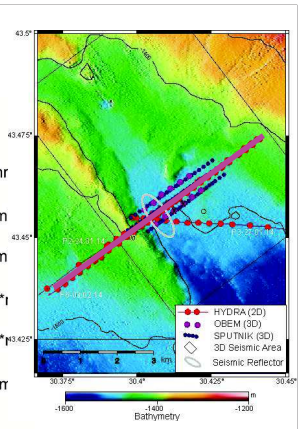

RMS Misfit:
should be balanced for all receivers → errors scaling

Calibration Factor:
accounts for geometry errors, dimensionality, amplitude factors

Bundesanstalt für Geowissenschaften und Rohstoffe

GEOZENTRUM HANNOVER

Inversion 2

2D Occam Inversion, code by C. Scholl, CGG-EM

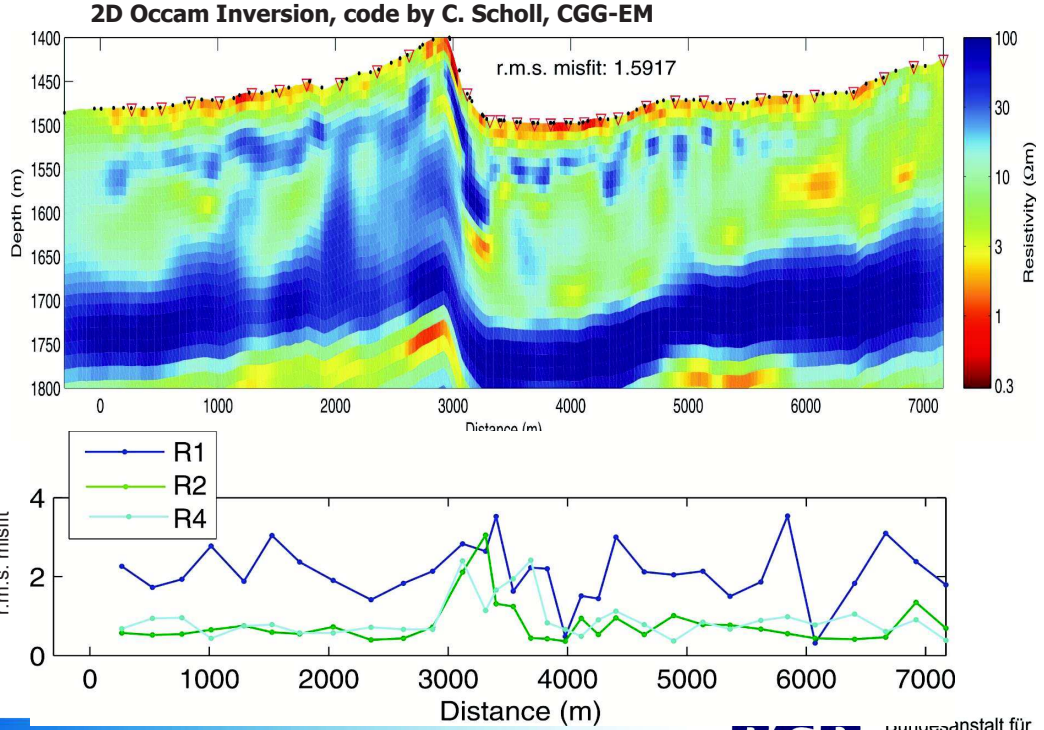

Bundesanstalt für Geowissenschaften und Rohstoffe

GEOZENTRUM HANNOVER

Inversion 3

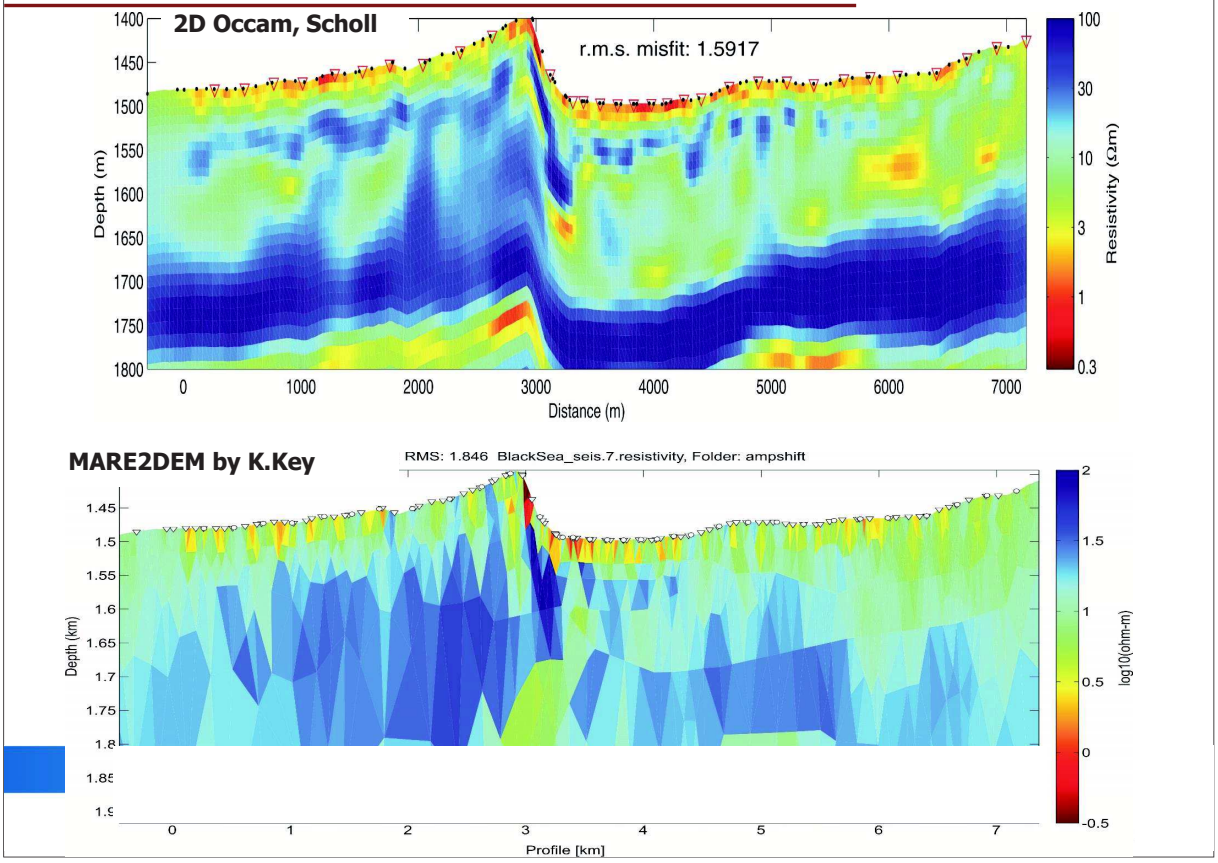

Comparison: Seismic & CSEM

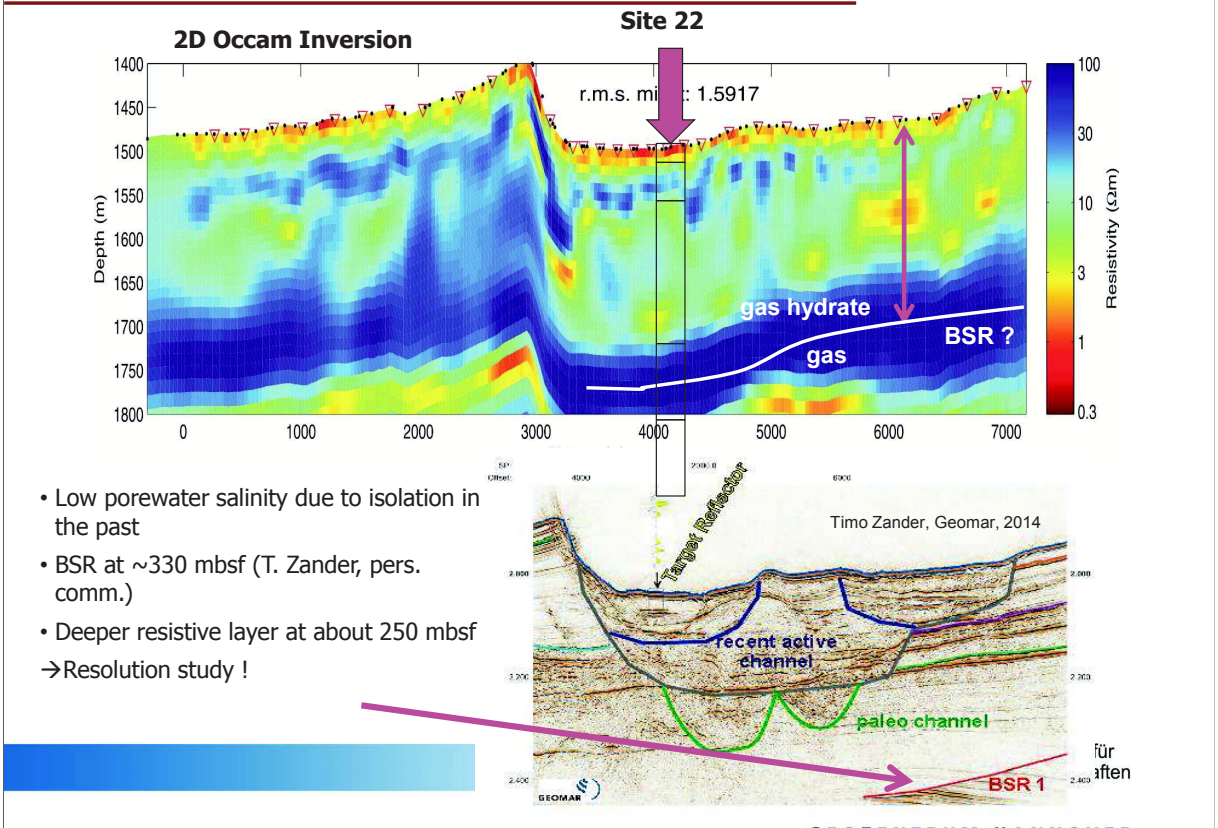

- Low porewater salinity due to isolation in the past
- BSR at ~330 mbsf (T. Zander, pers. comm.)
- Deeper resistive layer at about 250 mbsf

→Resolution study !

für ältere

GEOZENTRUM HANNOVER

1D Resolution Study

Random Starting Models for Marquardt Inversion

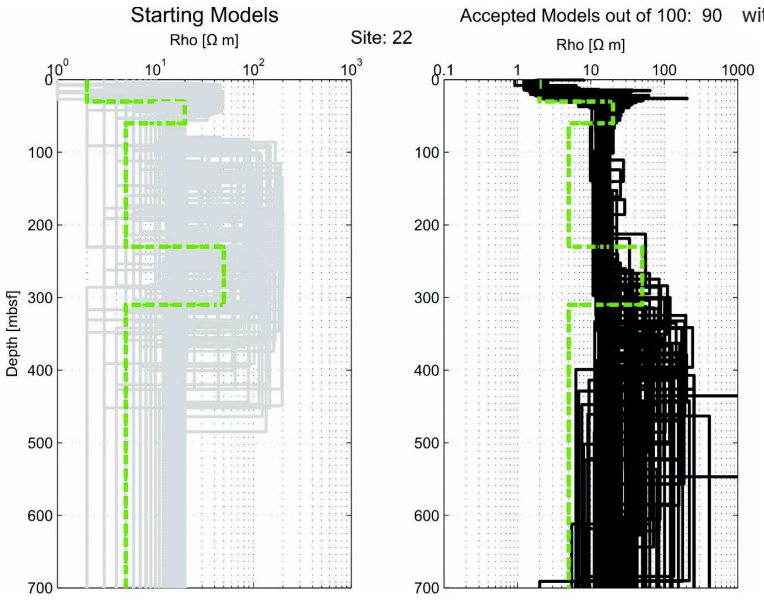

← Upper resistive layer is resolved

← Lower resistive layer exists.

← Depth could be deeper, but lower base is unresolved

Bundesanstalt für Geowissenschaften und Rohstoffe
GEOZENTRUM HANNOVER

1D Bayesian Inversion, Site 22

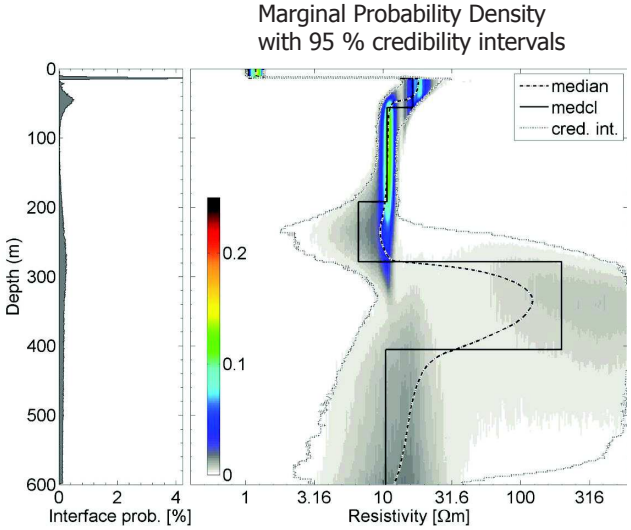

Romina Gehrmann (BGR)

- Top layers: High interface probability and low uncertainties
- Bottom resistive layer: Existing, but low credibility and interface probability

Bundesanstalt für Geowissenschaften und Rohstoffe
GEOZENTRUM HANNOVER

Interpretation

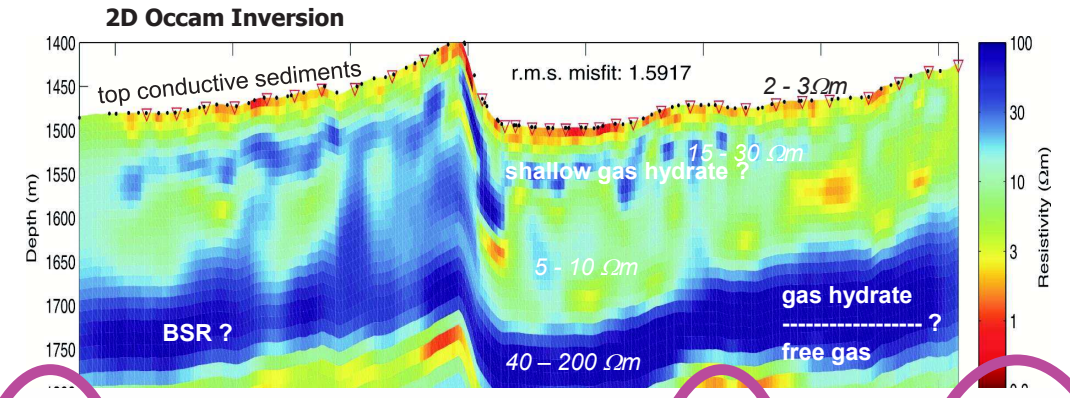

Depth [mbsf]	Salinity	Temperature	Porewater Conductivity / Resistivity	Formation Resistivity	Porosity a=1, m=2	GH Saturation a=1, m=n=2
At Seafloor	2 psu	9° C	2.5 S/m / 0.4 Ωm 0.397 : m [measured with CTD]	2-3Ωm	0.44 0.36	0 - 0.08 (background porosity: 0.4)
50 mbsf	psu	10-11° C	0.42 S/m / 2.38 Ωm	15-30Ωm	.40 .28	0.3 – 0.5 (background porosity: 0.6)
100 mbsf	psu	11-12.5° C	0.44 S/m / 2.27Ωm	5-10Ωm	.67 .48	0 – 0.04 (background porosity: 0.5)
200 mbsf	-5 psu	13-16° C	0.46-0.48 S/m / 2.17 – 2.08Ωm(3ps 0.74-0.76 S/m / 1.35 – 1.32Ωm(5ps			
300 mbsf	-5 psu	15-19.5° C	0.47-0.53 S/m / 2.13 – 1.89Ωm(3ps 0.75-0.84 S/m / 1.33 – 1.19Ωm(5psu	40-200Ωm	0.23-0.22/ 0.1 0.18-0.17 / 0.0	0.5 – 0.8 0.65 – 0.85 (background porosity: 0.5)

Preliminary Results 3D Survey, Lobster & Sputnik

GEOMAR

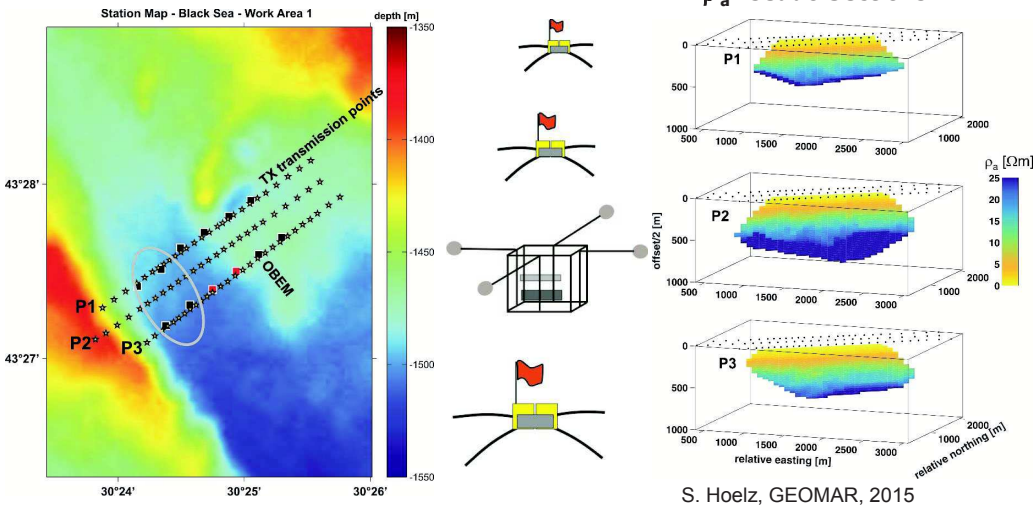

S. Hoelz, GEOMAR, 2015

- General increase in resistivity with depth
- Higher penetration depth at profile P2

→ Next step: 2D, 3D inversion

BGR Bundesanstalt für Geowissenschaften und Rohstoffe

GEOZENTRUM HANNOVER

Summary


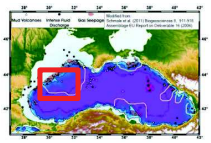


- Objective: Evaluation of submarine gas hydrates in the Western Black Sea using CSEM
- MERIAN Cruise MSM35, January 2014
- Site Survey, Test drill site

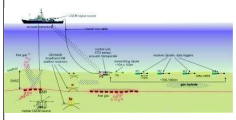

- 2 CSEM Systems: HYDRA – 2D profiles, Sputnik, Lobster - 3D survey

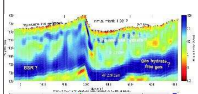
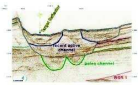
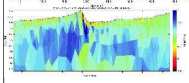
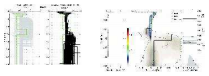

- HYDRA:1D/2D Inversion and Resolution Study.
- Comparison with seismic,
- High resistivity partly due to fresh porewater and high gas hydrate saturation

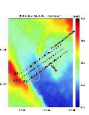
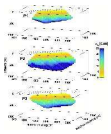

- 3D survey: Pseudo sections show increase in resistivity with depth

BGR Bundesanstalt für Geowissenschaften und Rohstoffe
GEOZENTRUM HANNOVER

Thanks for your attention!

Acknowledgements:

- We thank the Captain and Crew of M.S. MERIAN voyage MSM35
- Thanks to our technicians (Joachim Deppe, Boris Hahn, Martin Wollatz-Vogt, Patrick Schroeder)
- Carsten Scholl CGG-EM for 2-D Inversion of the data
- The SUGAR (CO_2 CH_4) Project was/is supported by BMBF Grant 03G0688A, and BMWi Grant 03SX32OZ
- Thanks to MAGSON GmbH, Berlin, for collaborations around electronic developments

BGR Bundesanstalt für Geowissenschaften und Rohstoffe
GEOZENTRUM HANNOVER

Poster

26. Schmucker-Weidelt-Kolloquium
Dassel, 21.–25. September 2015

Zweidimensionale Modellierungsstudie von long offset transient elektromagnetischen Daten: Untersuchung einer erzführenden Schicht in Thüringen

J. Böckmann, P. Yogeshwar, B. Tezkan

boeckmann@geo.uni-koeln.de, Institut für Geophysik & Meteorologie, Universität zu Köln

Einleitung

Als Voruntersuchung für das Forschungsprojekt DESMEX (**D**eep **E**lectromagnetic **S**ounding for **M**ineral **Ex**ploration) werden ein -/ und zweidimensionale Modellierungen von LOTEM Daten durchgeführt. Mittels 1D Modellierung kann die optimale Sender-Empfänger Geometrie und die maximal benötigte Aufzeichnungszeit festgelegt werden, um eine gutleitfähige Schicht in einer Tiefe von ca. 1 km detektieren zu können. Mit der anschließenden 2D Modellierung wird die gutleitfähige Schicht als nicht durchgehend und verschiedene Neigungen der Schicht angenommen. Durch den Vergleich der synthetischen 2D Daten mit den synthetischen 1D Daten für verschiedene Sender-Empfänger Lokationen entlang des Profils, kann der 2D Effekt abgeschätzt werden. Mit einer abschließenden 1D Inversion können Aussagen über die Angemessenheit einer 1D Inversion von 2D beeinflussten Daten getroffen werden und mögliche Fehlinterpretationen eingeschätzt werden.

1D Modellierung

Ausgehend von einem Modell mit einer 100 m mächtigen Deckschicht (ρ_1 = 100 Ωm) und einem guten Leiter (ρ_3 = 1 Ωm) in ca. 1000 m Tiefe, eingebettet zwischen einem schlechten Leiter ($\rho_{2,4}$ = 1000 Ωm), sind die vorwärts gerechneten Daten für einen Offset von 4000 m dargestellt (Abb. 2b und c). Die Modellrechnung wurde mit einer broadside Konfiguration berechnet (Abb. 1).

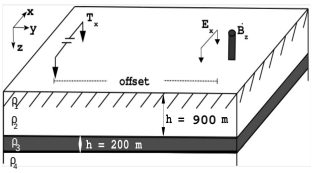

Abbildung 1: Broadside Konfiguration mit links einem Dipolsender von 1000 m Länge und rechts den Empfängereinheiten.

Unter der Annahme einer target response größer 10 % zeigt die 1D Modellierung des vertikalen Magnetfeldes $\dot{B}_z$, im Gegensatz zu der horizontalen Komponente des elektrischen Feldes E_x, eine deutlichere Detektierbarkeit der Unterkante der gutleitfähigen Schicht.

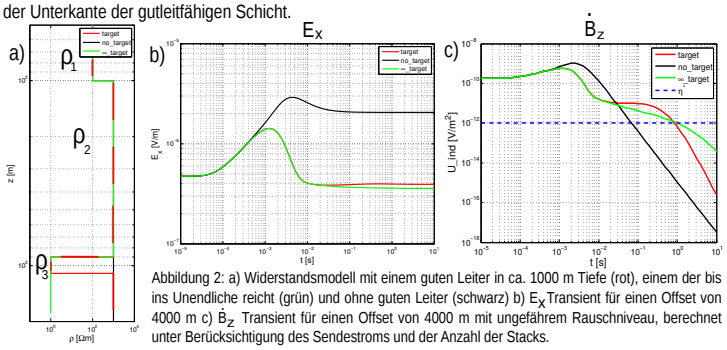

Abbildung 2: a) Widerstandsmodell mit einem guten Leiter in ca. 1000 m Tiefe (rot), einem der bis ins Unendliche reicht (grün) und ohne guten Leiter (schwarz) b) E_XTransient für einen Offset von 4000 m c) $\dot{B}_Z$ Transient für einen Offset von 4000 m mit ungefährem Rauschniveau, berechnet unter Berücksichtigung des Sendestroms und der Anzahl der Stacks.

2D Modellierung

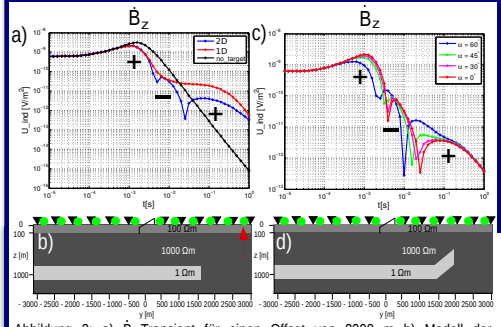

Abbildung 3: a) $\dot{B}_Z$ Transient für einen Offset von 3000 m b) Modell der unterbrochenen Schicht bei y = 1500 m. Die Kreise stehen für die Empfänger der magnetischen Feldkomponente, die Dreiecke für die der elektrischen Feldkomponente. Der Sender befindet sich bei y = 0 m. c) $\dot{B}_Z$Transient für verschiedene Neigungen der Schicht und d) Modell der geneigten Schicht.

Die 2D Modellierung wurde mit dem Finite-Differenzen Algorithmus SLDMem3t[1]durchgeführt. Die gutleitfähige Schicht wurde genau mittig zwischen Sender und Empfänger unterbrochen.
Dabei zeigt der $\dot{B}_Z$ Transient (Abb. 3a) für einen Offset von 3000 m einen doppelten Vorzeichenwechsel, der auf die 2D Struktur zurück geführt wird und somit nicht 1D interpretiert werden kann. Abb. 3c) zeigt die $\dot{B}_Z$ Transienten für drei unterschiedliche Neigungen der Schicht im Vergleich zu einer nicht geneigten, aber unterbrochenen Schicht. Eine größere Neigung der Schicht ist deutlich erkennbar im Verlauf des Transientens an der Position des Vorzeichenswechsel, verglichen mit der nicht geneigten Schicht (α = 0). Eine 1D Inversion ist somit für die 2D Daten der elektrischen Feldkomponente möglich.

Quasi 2D Darstellung der Inversionsergebnisse der E_X Komponente

Dargestellt sind die 1D Marquardt (vgl. Abb. 4a) - und Occam R1 (vgl. Abb. 4b) Inversionen der 2D Daten einer unterbrochenen Schicht bei y = 1500 m (schwarz markiert) für alle Stationen im Bereich von y = -3000 m bis 3000 m, wobei sich der Sender bei y = 0 m befindet. Das Modell des unterbrochenen gutleitfähigen Leiters (ρ = 1 Ωm) in einer Tiefe von ca. 1000 m wird trotzdem für alle Stationen rekonstruiert, wodurch es bei einer 1D Inversion zu Fehlinterpretationen kommen kann. Beispielsweise wird die gutleitfähige Schicht sowohl in der Marquardt - als auch in der Occam - Inversion für die Station bei y = 3000 m als weniger leitfähig, weniger mächtig und tiefer abgebildet. Auch zeigen die beiden Inversionen für die Stationen links vom Sender (s. y = -1500, -1000 und -500 m) eine geringere Leitfähigkeit und Mächtigkeit des guten Leiters. Lediglich für die ersten Stationen bei Profilmeter -3000 m und -2500 m wird der gutleitfähige Leiter für beide Inversionen exakt rekonstruiert. Die abgeleitenen Modelle zeigen aufgrund der Messgeometrie und der 2D Struktur, deutliche Unterschiede zu dem 1D Hintergrundmodell.

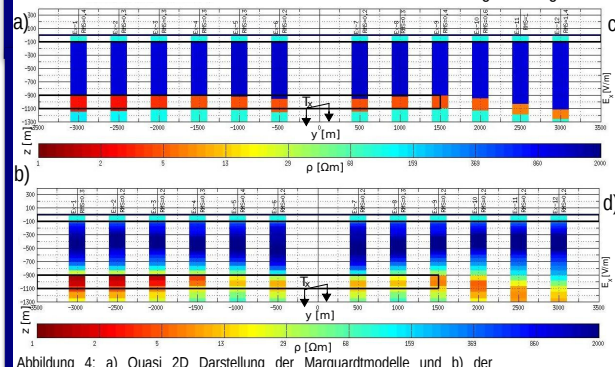

Abbildung 4: a) Quasi 2D Darstellung der Marquardtmodelle und b) der Occammodelle (R 1) für das Modell der unterbrochenen Schicht bei y = 1500 m mit der jeweiligen Datenanpassung für c) einen Offset von 500 m und d) einen Offset von 4000 m.

Fazit & Ausblick

Mit der 1D Modellierung hat sich gezeigt, dass für die Detektion des guten Leiters die magnetische Feldkomponente besser geeignet ist. Auch mit der 2D Modellierung erweisen sich die Vorzeichenwechsel in den Daten des magnetischen Feldes als Vorteil, da mit ihnen direkt der 2D Effekt nachgewiesen werden kann. Aufgrund des VZW lassen sich die 1D Inversionen nur für die Daten der elektrischen Komponente durchführen, auch wenn es mit dieser zu Fehlinterpretationen kommen kann. Untersuchungen an realistischeren Modellen und ein Vergleich mit LOTEM Feld Daten wird im Rahmen von DESMEX durchgeführt.

Referenzen: 1) Druskin & Knizhnerman, 1988

Dealing with static shifts in MT surveys using Airborne EM

R. Delhaye[1] (*rdelhaye@cp.dias.ie*), V. Rath[1] & the IRETHERM Team.
[1] Geophysics Section, Dublin Institute for Advanced Studies, Dublin, Ireland.

Introduction

Our work tests the feasibility of using regional airborne FDEM data in place of time domain EM data for static shift corrections in the manner of Sternberg et al. (1988) and Pellerin & Hohmann (1990). The test area is a sedimentary basin in Northern Ireland, concealed beneath flood basalts.

FDEM data were inverted with the Airbeo 1D inversion program (Raiche, 1999), and MT data were inverted with the ModEM 3D inversion program (Kelbert et al., 2014).

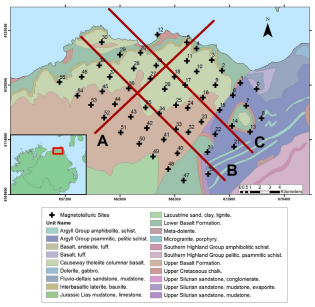

Figure 1: Location of MT sites, with surface geology and select profile locations overlain.

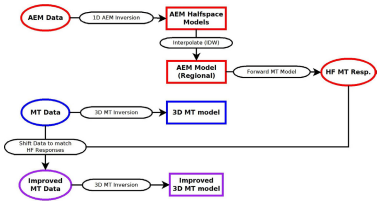

Figure 2: Flow chart showing the steps involved in correcting static shift of MT data with airborne FDEM data.

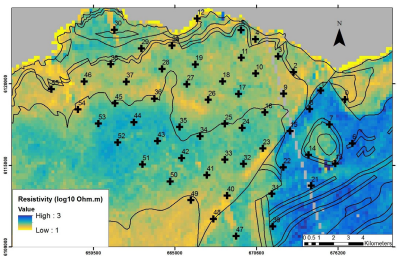

Figure 3: Halfspace resistivities found by 1D inversion with Airbeo, used as synthetic model for static-corrected MT responses.

Model Comparison

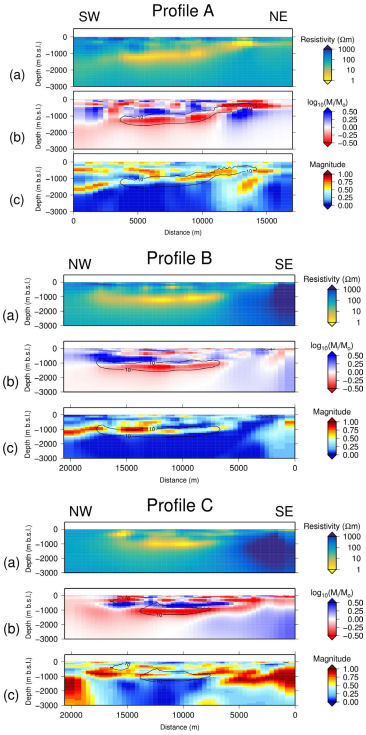

Figure 7: Profiles A, B, C taken through preferred model, with locations indicated in Figure 1. Subfigures (a) show the resistivity distribution, (b) show the logarithmic resistivity difference between the static-corrected model and the uncorrected model, and (c) show the normalised cross-gradient of the models.

Preferred Model - 10 Ωm isosurface

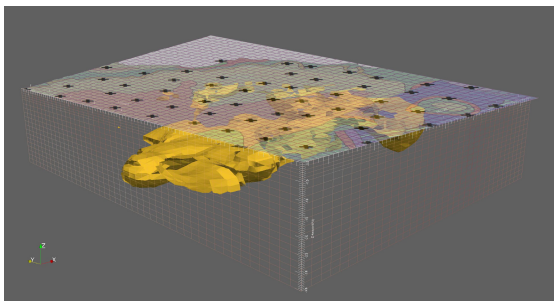

Static Shift Corrections

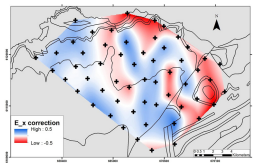

Figure 4: Spatial distribution of δ_{Ex}, the logarithmic static shift correction applied to E_x-dependent components.

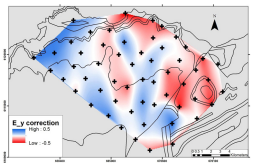

Figure 5: Spatial distribution of δ_{Ey}, the logarithmic static shift correction applied to E_y-dependent components.

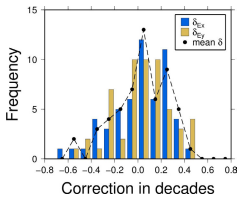

Figure 6: Logarithmic distribution of δ_{Ex}, δ_{Ey}, and the mean correction at each site, to examine the normality and central tendency of the respective distributions.

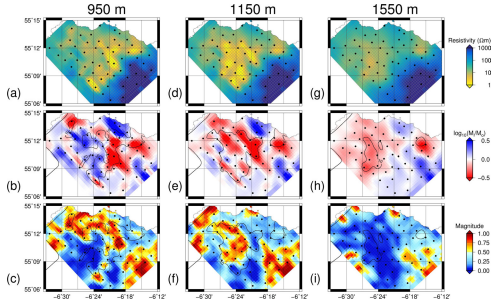

Figure 8: Depth slices taken through preferred model at 950, 1150 and 1550 m depth. Subfigures (a), (d), (g) show the resistivity distribution, (b), (e), (h) show the logarithmic resistivity difference between the static-corrected model and the uncorrected model, and (c), (f), (i) show the normalised cross-gradient of the models.

The static-corrected and uncorrected models were compared by two primary metrics, namely the logarithmic difference in resistivity (measured in decades), and the normalised cross-gradient (i.e. cross-product of gradient vectors of each model). The cross-gradient shows a maximum value in areas where the structures in each model differ significantly.

The IRETHERM team (www.iretherm.ie):

A.G. Jones[1,14], V. Rath[1], J.S. Daly[2], A. Allen[3], N. O'Neill[4], N.H. Hunter Williams[5], M. Lee[5], D. Reay[6], M. Feely[7], P. Hanly[8], R. Pasquali[9], N. Piana Agostinetti[3], S. Lebedev[1], M. Long[10], M. Moorkamp[11], T. Kalscheuer[12], A. Smyth[13], M. Muller[15].

[1] School of Cosmic Physics, Dublin Institute for Advanced Studies
[2] UCD School of Geological Sciences, University College Dublin
[3] Department of Geology, School of Biological, Earth and Environmental Sciences, University College Cork
[4] SLR Consulting Ireland Ltd, Dublin
[5] Geological Survey of Ireland, Dublin
[6] Geological Survey of Northern Ireland, Belfast
[7] Earth and Ocean Sciences, NUI Galway
[8] GT Energy, Dublin
[9] GeoServ Solutions, Enniskerry
[10] School of Civil, Structural and Environmental Engineering, University College Dublin
[11] Department of Geology, University of Leicester
[12] Uppsala University, Sweden
[13] Providence Resources, Dublin
[14] Complete MT Solutions, Ottawa

References:

Egbert, G.D., Kelbert, A., (2012) "Computational recipes for electromagnetic inverse problems." Geophysical Journal International 189:251-267.
Goodman, R., et al., (2004). Geothermal Energy Resource Map of Ireland. SEI report, July 2004.
Kelbert, A., Meqbel, N., Egbert, G.D., Tandon, K., (2014) "ModEM: A modular system for inversion of electromagnetic geophysical data." Computers & Geosciences 66:40-53.
Mitchell, W.I. (ed.), (2004). The Geology of Northern Ireland - Our Natural Foundation (Second Edition). Geological Survey of Northern Ireland, Belfast.
Pellerin, L., Hohmann, G.W., (1990) "Transient electromagnetic inversion: a remedy for magnetotelluric static shifts." Geophysics 55:1242-1250.
Raiche, A., (1999) "A Flow-through Hankel Transform Technique for Rapid, Accurate Green's Function Computation" Radio Sci. 34:343-50.
Rath, V., Mandea, M., Holmes, J.D.G., Newman., G.A., Amason., K., Lindsey., N.J. (2015) "Comparison of 3D MT Inversions for Geothermal Exploration: Case Studies for Krafla and Hengill Geothermal Systems in Iceland." Geothermics 57:258-274.

How to Find Buried and Inactive Seafloor Massive Sulfides using Transient Electromagnetics

–

A Case Study from the Palinuro Seamount

Sebastian Hölz & Marion Jegen
shoelz@geomar.de
GEOMAR Helmholtz Centre for Ocean Research Kiel

MARTEMIS

At GEOMAR we have built the new marine transient electromagnetic induction system MARTEMIS (➥Ⓐ), which is specifically designed for the detection and characterization of seafloor massive sulfides (SMS):

- operational depth up to 6000m,
- coincident loop with 4.3 x 4.3m^2,
- transmitter (TX) coil with 1-2 windings,
- TX current of 40A @ 50% duty cycle,
- TX turn-off time ~120µs,
- TX repetition frequency of 2.5Hz,
- receiver (RX) sampling frequency 10kHz.

Working Area

The Palinuro Volcanic Complex, located in the Tyrrhenian Sea, has some characteristics, which make it up to date a unique site for testing equipment on inactive and buried SMS:

- little to no hydrothermal activity,
- no surface expressions (e.g. black smokers),
- sedimentary cover,
- SMS verified by drilling (Petersen et al., 2014).

Experiment

After calibration in the water column (➥Ⓑ), demonstrating the quantitative functioning of the MARTEMIS system, it was lowered towards the seafloor. Measurements were then carried out at a total of 80 locations at heights of 2-6m above the seafloor along a ~750m long profile within 1.5h (➥Ⓒ).

Interpretation

A qualitative comparison of all measurements shows a subset of processed transients with increased amplitudes (➥Ⓓ, red lines). These correspond to locations (➥Ⓒ, red dots) in the vicinity of the area of previous drilling (➥Ⓒ, black rectangle).
While a 1D inversion of data at station TX12 shows, as expected, background resistivities (➥Ⓔ), the response at site TX38 requires a highly conductive layer (~15S/m) at a depth between 8–16m (➥Ⓕ), which is clearly indicative of SMS and may not be solely explained by warm saline fluids.
The display of all 1D models shows that the layer of high conductivity is evident in all measurements in the vicinity of the previous drilling (➥Ⓖ, marked). In addition, a second unknown conductive anomaly towards the E hints at a hitherhto unknown SMS occurrence at greater depth (➥Ⓗ, marked).

Outlook

Measurements with the MARTEMIS system will be carried out at the TAG hydrothermal field in summer 2016. For 2017 we have applied for shiptime to continue measurements at the Palinuro Volcanic Complex.

Acknowledgment
This project received funding as part of the EU-FP7 project Blue Mining ("Breakthrough Solutions for the Sustainable Exploration and Extraction of Deep Sea Mineral Resources", Grant No. 604500).

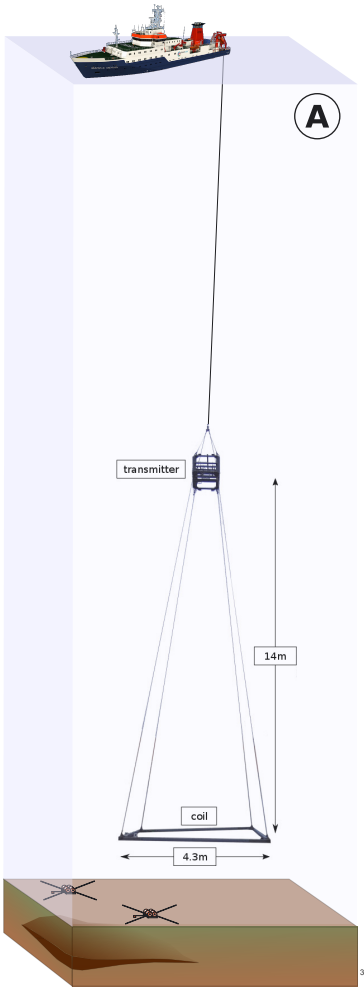

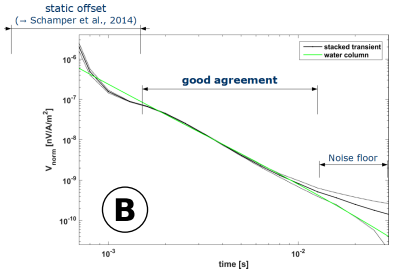

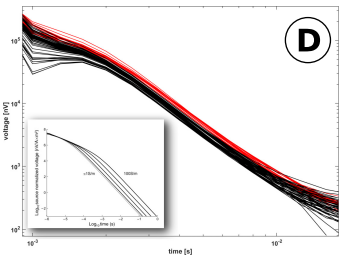

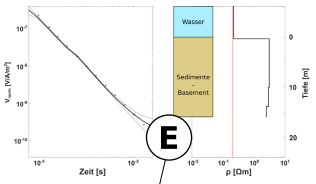

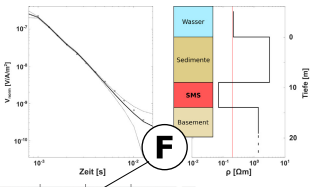

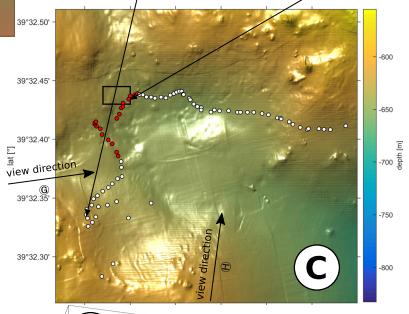

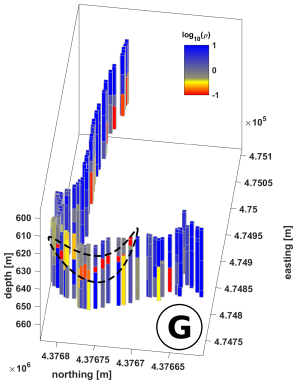

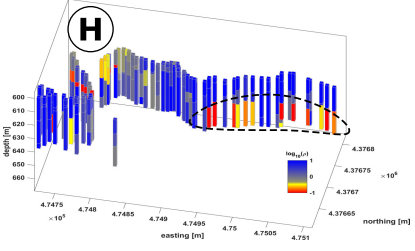

Auswertung von transient elektromagnetischen Messungen auf einer graphitisierten Störzone bei Bramsche

S. Janser*, M. Seidel, B. Tezkan

* janser@geo.uni-koeln.de, Institut für Geophysik und Meteorologie, Universität zu Köln

Einleitung

Auf einer geologischen Verdachtsfläche in der Ortschaft Wallenhorst bei Bramsche wurden drei transient elektromagnetische (TEM) Profilmessungen über einem geologisch interessanten Gebiet durchgeführt. Dieses Gebiet wurde bereits mit anderen Messmethoden, passiver als auch aktiver Natur, untersucht. Zu diesen zählen unter anderem die Gleichstromgeoelektrik, Radiomagnetotellurik und die Eigenpotentialmethode, wie sie durch Gurk et al. [2013] verwendet wurden. Die TEM-Inversionsergebnisse der Messungen eines Profils werden hier vorgestellt.

Geologie

Die gesamte Region um Bramsche herum wird im Untergrund durch einen großen Intrusivkörper geprägt, auch als Bramscher Pluton oder Bramscher Massiv bekannt, welcher die umliegenden und darüber gelegenen Schichten sowohl aufgewölbt als auch eine thermische Erwärmung zugeführt hat. Dies hatte zur Folge, dass sich oberflächennah eine fast senkrecht stehende Verwerfung gebildet hat, die zu großen Teilen aus elektrisch gut leitfähigem Graphit besteht. Diese Verwerfung soll zwischen zwei anderen geologischen Strukturen liegen, die vergleichsweise schlecht leitend sind. Somit liegt ein Leitfähigkeitskontrast vor, der mit elektrischen und elektromagnetischen Methoden untersucht werden kann.

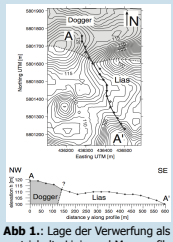

Abb 1.: Lage der Verwerfung als gestrichelte Linie und Messprofil der DC-Messung [Gurk et al., 2013]

Messgebiet

Die TEM-Daten wurden mit dem „TEM FAST 48" der Firma AEMR erhoben. Gemessen wurde dabei mit einer quadratischen single loop Auslage mit einer Kantenlänge von 25 m.

Abb. 2: links: Übersichtskarte zur Orientierung des Messgebiets. Rechts: Messprofile P1, P2 und P3. Als Oval gekennzeichnet ist die vermutete Lage der gutleitenden Verwerfung.

Die Transienten wurden im Zeitbereich von $4 \cdot 10^{-6}$ - $9{,}57 \cdot 10^{-4}$ s aufgenommen. Da keine Rauschmessungen durchgeführt wurden, wurden die Transienten in ungeschnittener Form bearbeitet.

Methodik

Die erhaltenen Transienten lagen in dekonvolutionierter Form vor und mussten nur noch auf Strom und Empfangsfläche normiert werden. Die nun vorliegenden Daten konnten anschließend mit dem Programm „emuplus" der Universität zu Köln 1D invertiert werden.

Zunächst wurden Occam R1 und R2 Inversionen durchgeführt um auf derer Grundlage Startmodelle für die RMS-gewichteten Marquardt Inversionen zu erstellen. Um die erhaltenen Ergebnisse adäquat beurteilen zu können wurden außerdem Äquivalenzmodelle erzeugt. Neben dem RMS der Anpassungen wurden auch die Importancewerte der einzelnen Modellparameter in die Analyse mit einbezogen, die während der Marquardt Inversion mit errechnet wurden. Eine qualitative Untersuchung der Transienten in Hinsicht auf mögliche Schichtungen erfolgte durch die Darstellung der Latetime-Näherung.

Literatur

Gurk, M., Bosch, F.P. und Tougiannidis, N., 2013: Electric field variations measured continously in free air over a conductive thin zone in the tilted Lias-epsilon black shales near Osnabrück, Northwest Germany, Journal of Applied Geophysics (91)

Exemplarisches 1D-Ergebnis

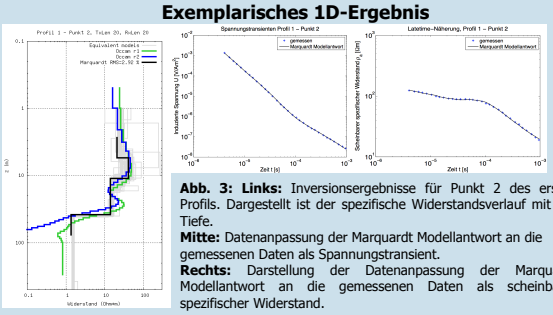

Abb. 3: Links: Inversionsergebnisse für Punkt 2 des ersten Profils. Dargestellt ist der spezifische Widerstandsverlauf mit der Tiefe.
Mitte: Datenanpassung der Marquardt Modellantwort an die gemessenen Daten als Spannungstransient.
Rechts: Darstellung der Datenanpassung der Marquardt Modellantwort an die gemessenen Daten als scheinbarer spezifischer Widerstand.

Das Marquardtergebnis aus Abb. 3 zeigt ein Vierschichtmodell, wobei die ersten beiden Schichten nicht gut aufgelöst sind. Dies hängt unter anderem mit einer minimalen Eindringtiefe von ca. 3 m zusammen. Die folgenden Schichten sind gut aufgelöst mit Importancewerten für die Widerstände und die Schichtdicken zwischen 0,91 - 0,97.
Der gemessene Transient zeigt eine gute Übereinstimmung zur Marquardt-Modellantwort mit einem RMS-Wert von 2,92 %. Die Latetime-Näherung zeigt ebenfalls ein mehrschichtiges Modell mit einem guten Leiter in der Tiefe.

Quasi-2D Darstellung des ersten Profils

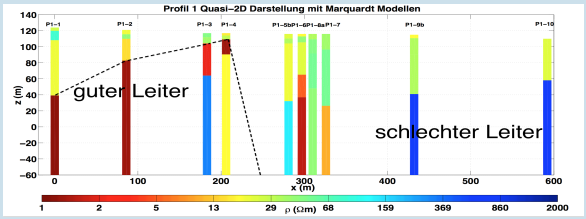

Abb.4: Quasi-2D Darstellung des ersten Profils mit Topographie über NN

Die profilweise Analyse der Marquardtergebnisse ergab, dass bei den Punkten 1 bis 4 eine gut leitfähige Struktur mit Widerstandswerten zwischen 1,2 – 2 Ωm detektierbar ist (Oberkante liegt in 8 m und höheren Tiefen Richtung Norden). Diese lässt sich im geologischen Rahmen als die graphitisierte Verwerfung interpretieren. Diese Werte lassen vermuten, dass das Graphit mit Sedimenten verunreinigt ist oder die anisotrope Struktur des Graphits Einfluss auf die Messung genommen hat. Die Mächtigkeit der Störzone nimmt vom vierten zum ersten Profilpunkt zu, wobei die Oberkante in die Tiefe absinkt. Nach Nordwest (linke Seite des Profils) als auch in die Tiefe lässt sich keine Begrenzung der Verwerfung feststellen. Die maximale Eindringtiefe beträgt ca. 80 - 100 m ausgehend von der Divergenz der Occam Modelle.

Vergleich mit einem DC-Inversionsergebnis

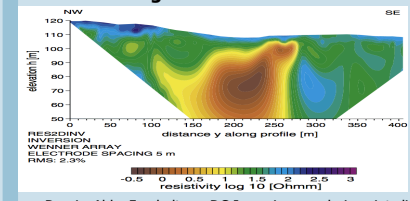

Abb.5: 2D-Inversionsergebnis der DC-Messung über die ersten 400 m des ersten Profils der TEM Messung unter Beachtung der Topographie mit Höhe über NN [Gurk et al., 2013].

Das in Abb. 5 erhaltene DC-Inversionsergebnis zeigt die Lage der Verwerfung, wobei auch hier die Unterkante nicht aufgelöst wird aufgrund einer mittleren Eindringtiefe von ca. 60 m. Die Widerstände variieren im gleichen Bereich wie das TEM-Ergebnis, jedoch wird das Kernmaterial nach dem DC-Ergebnis noch leitfähiger mit bis zu 0,2 Ωm.

Eine laterale Grenze der Verwerfung konnte durch TEM und DC abgeleitet werden. Die Eindringtiefe war jedoch nicht groß genug um die Unterkante aufzulösen.

In-Loop Transient Elektromagnetische Messungen im Kölner Grüngürtel: Vergleich der KMS-820 Empfangs-Einheit mit dem Zonge GDP32-II

M. Küpper, B. Tezkan, P. Yogeshwar, A. Haroon, R. Bergers, T. Hanstein

kuepper@geo.uni-koeln.de

Einleitung

In dieser Arbeit wurde erstmals eine KMS-820 Empfangsapparatur von KMS Technologies für In-Loop TEM-Messungen im typischen Zero-TEM-Zeitbereich eingesetzt. Dabei wurden Vergleichsmessungen in der Kölner Umgebung mit dem GDP32-II von Zonge Engineering durchgeführt.
Am Institut für Geophysik und Meteorologie der Universität zu Köln wird seit Jahren der GDP32-II als Empfänger für TEM-Messungen verwendet, sodass dieses Gerät und seine Eigenschaften bereits bekannt sind und sich die Ergebnisse gut als Referenz für Vergleiche mit der neuen KMS-820 Empfangseinheit eignen.
Das KMS-820 System ist für eine allgemeine Anwendung in der Elektromagnetik und Mikroseismik entwickelt worden. Zur Zeit ist der Haupteinsatz in der Magnetotellurik und LOTEM Sondierung. [1].

Messungen

Erste Messungen wurden im Vorgebirgspark in Köln durchgeführt mit typischen Sender-kantenlängen von 50 m und 100 m.
In Abb. 2 ist der Messaufbau skizziert. Hierbei wurde bei allen Messungen der GDP-32 zum Triggern des Senders NT-20 genutzt. Die Synchronisation der Zonge Apparatur erfolgt über eine Triggerverbindung, wohingegen mit der KMS-820, zusätzlich zur induzierten Spannung, die Stromfunktion über einen Shunt aufgezeichnet wurde. Bei LOTEM Anwendungen erfolgt die Zeit-Synchronisation typischerweise über GPS-Uhren und könnte hier alternativ auch verwendet werden.
Als Cycle-Frequenz wurde 32 Hz genutzt und an der KMS-820 die höchste Samplingrate (80 kHz) eingestellt.

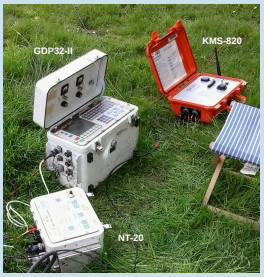

Abb. 1: Foto der verwendeten Messgeräte, NT-20 (vorne), GDP32-II von Zonge Engineering und KMS-820 von KMS Technologies (rechts)

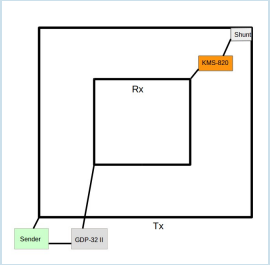

Abb. 2: Skizze des Messaufbaus. Bei der KMS-820 muss zusätzlich die Stromfunktion mitgeschnitten werden

Bestimmung des Zeitnullpunktes bei der KMS-820

Zur Bestimmung des Zeitnullpunktes wurde bei den Feldmessungen die gesendete Stromfunktion aufgezeichnet. Anhand derer wird der Zeitnullpunkt an den Punkt gesetzt, an dem der Strom komplett ausgeschaltet ist.
Dieser Punkt ist in der Praxis jedoch nicht eindeutig erkennbar, da die Stromfunktion Überschwinger haben kann oder oszilliert. Es kommen immer mehrere Punkte als Nullpunkt in Frage (vgl. Abb. 3). Da bei den Einstellungen der KMS-820 eine Samplingrate von 80 kHz gewählt wurde, liegen diese Punkte jedoch jeweils 12,5 µs auseinander.

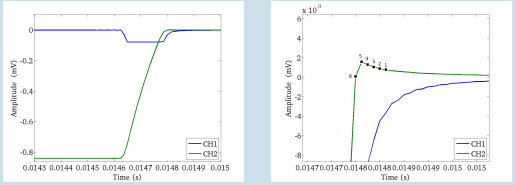

Abb. 3: Darstellung der induzierten Spannung (Channel 1) und der Stromfunktion (Channel 2) bei einer KMS-Messung, rechts: Vergrößerte Darstellung mit sechs beispielhaften Nullpunkten

Leichter ist der Nullpunkt am Anfang der Rampe ablesbar; die Transienten müssten dann um die bekannte Rampenzeit verschoben werden. Jedoch stimmen die Rampenzeiten der KMS-820 Messungen nicht mit den im Feld aufgenommenen Ozilloskop-Daten überein, sondern es gibt deutliche Abweichungen von bis zu 35 µs und die Rampe erscheint länger als im Oszilloskop. Der Grund hierfür ist der Einfluss des internen 20-kHz-Tiefpassfilters der KMS-820, der für eine zeitliche Verzögerung des Signals von 2-3 Abtastintervallen sorgt.
In Abbildung 3 fällt auf, dass die induzierte Spannung in die Sättigung geraten ist. Dies geschieht durch einen zu hoch gewählten Gain bei den KMS-820 Einstellungen.

Vergleich der Transienten

Die Wahl des Nullpunktes hat einen starken Einfluss auf den endgültigen Transienten. In Abbildung 4 sind beispielhaft die Transienten dargestellt, die durch die verschiedenen möglichen Nullpunkte (vgl. Abb. 3) entstehen. Dabei wird die beste Anpassung an den GDP-32 erreicht, wenn Punkt 5 als Nullpunkt gewählt wird. Als Referenz wird jeweils der Transient des GDP-32 (in Grün) betrachtet.

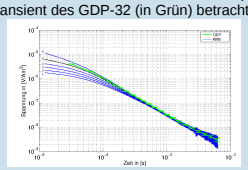

Abb. 4: Einfluss des Nullpunktes auf den KMS-820 Transienten, GDP-32 als Referenz

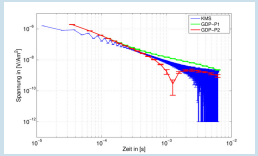

Abb. 5: Einfluss des internen Antialiasingfilters bei Messungen mit Senderkantenlänge 50 m

Um die Transienten quantitativ vergleichen zu können, werden die KMS-Daten auf die GDP-Stützstellen interpoliert (siehe Abb. 6)

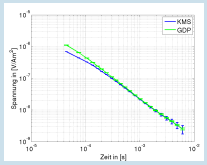

Abb. 6: KMS-820 Daten interpoliert auf GDP-32 Stützstellen

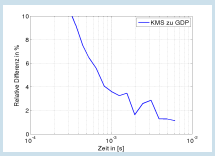

Abb. 7: Relative Differenzen zwischen GDP-32II und KMS820 und Transienten

An den relativen Differenzen ist erkennbar, dass die Tansienten zu frühen Zeiten, wegen der Wahl des Nullpunktes, deutlich abweichen. Zu späteren Zeiten ist diese Abweichung deutlich geringer. Problematisch ist ebenfalls der Einfluss des internen Antialiasingfilters der KMS-820. Der digitale Antialias-Filter erzeugt ein oszillierendes Einschwingen bei sehr schnellen Abschaltvorgängen wie bei 50 m X 50 m Senderspulen (vgl. Abb. 5). Bei größeren Sendespulenauslagen wie 100 m x 100 m oder einer Abschaltvorgang mit einer längeren Rampenzeit ist der Einfluss vernachlässigbar.

Vergleich der Inversionsergebnisse

Um abschätzten zu können, wie groß die möglichen Interpretationsfehler bei der Inversion sein können, die durch einen den gewählten Nullpunkt entstehen, werden für drei verschiedene Nullpunkte (Punkte 1, 3 und 5 aus Abb. 3) Inversionen durchgeführt und mit den Inversionsergebnissen des GDP-32 II verglichen (siehe Abb. 8). Im direkten Vergleich lässt sich erkennen, dass es zu Unterschieden bei den oberen Schichten der Modelle kommt.
Wird Punkt 5 als Nullpunkt gewählt, stimmen die Transienten von GDP-32 und KMS-820 überein und auch die Inversionsergebnisse sind vergleichbar. Die Anpassung ist insgesamt gut, mit $\chi \approx 1$.

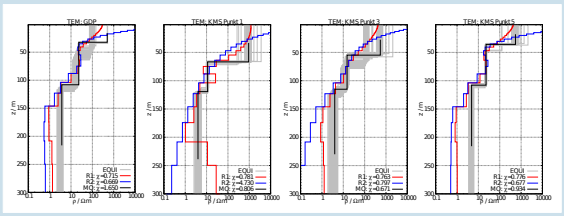

Abb. 8: Einfluss der Wahl des Nullpunktes auf das Inversionsergebnis, GDP-32 als Referenzmodell

Fazit

Erste Messungen ergeben, dass die gemessen Daten von KMS mit denen vom GDP übereinstimmen. Allerdings sind folgende Probleme bei der Datenprozessierung zu beachten:

- Ungenauigkeit beim Bestimmen des Zeitnullpunktes
- Verfälschung der Daten durch den internen Antialiasingfilter

Mögliche Lösungen:

- Nullpunktbestimmung am Anfang der Rampe (wie bei LOTEM), wenn genaue Verzögerung bei der Stomfunktion durch Tiefpassfilter bekannt ist
- Antialiasing verhindern durch längere Rampenzeit, vorgeschalteten externen Tiefpassfilter oder nachträgliche Dekonvolution

Referenzen:
[1] Haroon, A., Adrian, J., Bergers, R., Gurk, M., Tezkan, B., Mammadov, A. L. and Novruzov, A. G. (2015), Joint inversion of long-offset and central-loop transient electromagnetic data: Application to a mud volcano exploration in Perekishkul, Azerbaijan. Geophysical Prospecting, 63: 478–494. doi: 10.1111/1365-2478.12157

Technische Universität Braunschweig

IGEP TU Braunschweig — Institut für Geophysik und extraterrestrische Physik

Einfluss der Salinität und des pH-Wertes auf SIP Messungen

E. Kuhn, A. Hördt, H. Stebner
Technische Universität Braunschweig | Institut für Geophysik und extraterrestrische Physik
e.kuhn@tu-braunschweig.de | Telefon +49 (0) 531 391-5228

Einleitung

Durch Messung der Spektralen Induzierten Polarisation (SIP) sollen Interpretationen der hydraulischen Eigenschaften des Untergrundes ermöglicht werden. Voraussetzung dafür ist, dass die Abhängigkeit der elektrischen Parameter von der Geometrie des Porenraumes und damit von der hydraulischen Leitfähigkeit bekannt ist und diese nicht durch die chemischen Eigenschaften des Porenfluids verändert werden. In dieser Arbeit liegt der Fokus speziell auf dem Einfluss der Salinität und des pH-Wertes des Porenfluids auf SIP Messungen.

Messvorgang

Es wurden zunächst salinitätsabhängige Messungen mit Natriumchlorid-Lösungen im Frequenzbereich von 1 mHz bis 100 Hz bei Leitfähigkeiten von 0,4 mS/m bis 1200,0 mS/m durchgeführt. Bei der Untersuchung des pH-Wertes wurden die Proben mit Lösungen von pH=3,0 bis 5,3 bei einer konstanten Fluidleitfähigkeit gesättigt.

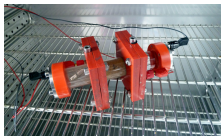

Abb. 1: Messzelle mit Elbsandsteinprobe.

Abhängigkeit von der Salinität

Abb. 2: Ausgewählte Impedanz Spektren bei Änderung der Salinität. Die Impedanz nimmt, wie durch Archie's Gesetzt zu erwarten ist, mit zunehmender Salinität ab.

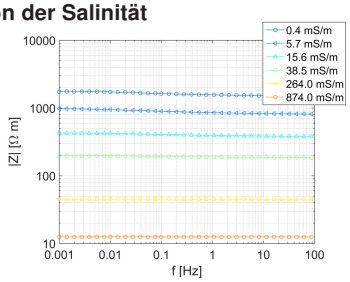

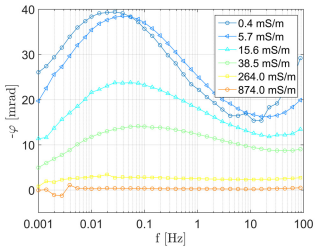

Abb. 3: Bei den zugehörigen Phasen-Spektren lässt sich ein abnehmender Trend mit der Leitfähigkeit (und damit der Salinität) feststellen. Dabei verschiebt sich das Phasenmaximum um knapp 100 mHz zu höheren Frequenzen. Die Phase verschwindet bei hoch-salinen Messungen vollständig.

Schlussfolgerungen

Die Salinität hat einen großen Einfluss auf die SIP-Spektren. Bei sehr hohen Salinitäten wird die Impedanz klein und der Phaseneffekt eliminiert. Der Imaginärteil steigt bis zu einem Maximum an und sinkt für sehr hohe Salinitäten wieder.
Der pH-Wert hat einen viel geringeren Effekt auf die Spektren als die Salinität.

Da sich die bisherigen Betrachtungen nur auf saure pH-Werte bis zu 5,3 konzentriert haben, werden Messungen bei höheren pH-Werten folgen.

Imaginärteil bei Variation der Salinität

Der Imaginärteil der Leitfähigkeit bei 1 Hz nimmt mit der Fluidleitfähigkeit zunächst monoton zu. Bei etwa 0,2 S/m beginnt der Imaginärteil jedoch wieder zu sinken, was bislang noch nicht vollständig erklärbar ist. Dieses Verhalten zeigt sich auch bei Weller, Zhang und Slater (2015), die ein Maximum des Imaginärteils bei Fluidleitfähigkeiten über 1 S/m mit einem anschließenden Abfall des Imaginärteils bei höheren Salinitäten finden. Hördt et al. (2015) erklären diesen Abfall durch einen Effekt des Zeta-Potentials bei der Membranpolarisation.

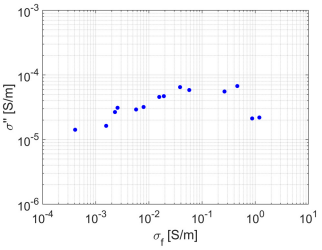

Abb. 4: Imaginärteil der Leitfähigkeit bei 1 Hz in Abhängigkeit der Fluidleitfähigkeit.

Einfluss des pH-Wertes

Um den pH-Wert kontrolliert zu variieren, wurden verschiedene Konzentrationen von Salzsäure und Natronlauge vermengt. Bei der Reaktion entsteht ein Überschuss an H^+- bzw. OH^--Ionen, die die Lösung sauer oder basisch machen.

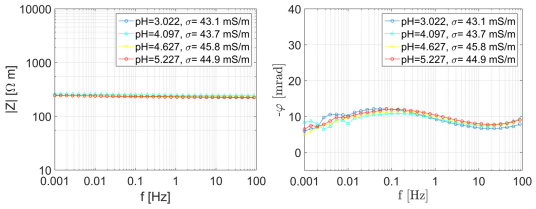

Abb. 5: SIP Spektren bei Variation des pH-Wertes bei konstanter Fluidleitfähigkeit.

Da bei Änderung des pH-Wertes auch die Salinität beeinflusst wird, wurde bei jedem neu angesetzten Porenfluid durch Hinzufügen von Natriumchlorid die Leitfähigkeit auf etwa 45 mS/m gebracht. Da Natriumchlorid-Lösungen im Mittel einen pH-Wert von rund 7 haben, bleibt der eingestellte pH-Wert unbeeinflusst.
Die Impedanz ist erwartungsgemäß nahezu konstant. Die Phasenwinkel und der Imaginärteil zeigen eine geringe Variation, die allerdings auch aus den leichten Salinitätsänderungen resultieren können.

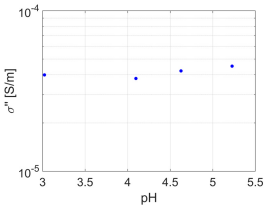

Abb. 6: Imaginärteil der Leitfähigkeit bei 1 Hz in Abhängigkeit des pH-Wertes.

Literatur

Hördt, A., K. Bairlein, A. Bielefeld, M. Bücker, S. Nordsiek, E. Kuhn und H. Stebner (2015). „The dependence of induced polarization on fluid salinity and pH, studied with an extended model of membrane polarization". Manuscript submitted for publication.
Weller, A., Z. Zhang und L. Slater (2015). „High-salinity polarization of sandstones". In: *Geophysics*.

Westfälische Wilhelms-Universität Münster

GEOPHYSIK WWU MÜNSTER

Processing and analysis of CSEM data acquired at a test site near Herford using Impressed Pipeline Currents as a source

T. Lindau, M. Becken, Institute of Geophysics, WWU Münster

Introduction

Impressed Current Cathodic Protection (ICCP) systems are extensively used for the protection of central Europe's dense network of oil-, gas- and water pipelines against destruction by electrochemical corrosion. Protection is provided by the injection of a DC current into the pipeline (Figure 2). However, occasional pipeline integrity surveys demand the protection current to be switched on- and off periodically. The resulting time varying pipe current induces secondary electric- and magnetic fields in the surrounding earth. While these fields are usually considered to be unwanted cultural noise, we aim at utilizing these fields for EM exploration, since the switching cycles typical fundamental periods roughly correspond to periods used in controlled source EM applications (CSEM).

We performed measurements on a test segment of 35km length near Herford, Germany (Figure 1) which is part of a gas pipeline operated by Westnetz. The DC current injected into the pipeline originates in a rectified 50Hz AC signal which can be switched on- and off periodically.

Figure 1: *Map view of the test area with the pipeline path depicted in red. The current is injected in the approximate center of the pipe from where it is flowing towards both ends. Source: maps.google.de*

The switching pattern typically employed by the pipeline operators has a fundamental period of 15s (12s on and 3s off), but for our study we chose a pattern with a fundamental period of 30s (25s on and 5s off, Figure 4). In order to describe the pipeline in terms of an EM source it is necessary to determine the current distribution within the pipeline, since the current decays away from the injecton point (current leakage). In addition the injected current signal needs to be recorded.

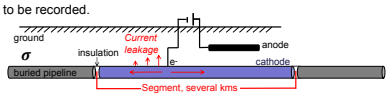

Figure 2: *Depiction of a typical ICCP Setup. The pipeline is split into multiple, electrically isolated segments. Each segment is equipped with ist own ICCP system which consists of an anode and a DC power source. In addition the pipeline is protected by an isolating coating (e.g. bitumen). The coating may be damaged at various locations, causing the current to leak into the surrounding earth.*

Data

Electric field measurements were performed at 45+ stations in an area close to the pipeline and at the current injection point. Each station recorded data for approximately two days at 500Hz sampling rate using the inhouse developed EDE32 dataloggers

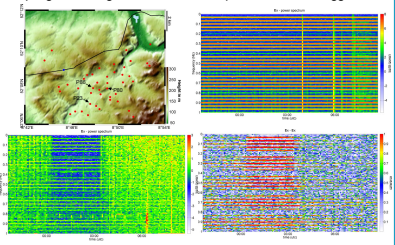

Figure 3: ***Top Left:*** *Map view of measurement area. Red dots show measurement sites, the blue dot indicates the injection site.* ***Top Right:*** *Spectrum of the recorded pipeline signal at the injection point for frequencies up to 1Hz.The spectrum shows high powers for the pipelines fundamental period of 30s and its harmonics and low power elsewhere.* ***Bottom Left:*** *Ex power spectrum for station labeled P23* ***Bottom Right:*** *Plot of coherency of injected current signal (Ex) and Ex component of measurement site P23.*

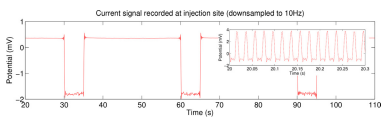

Figure 4: *Section of the recorded timeseries data of the injected current signal at the injection site downsampled to 10Hz. The switching of the pipe current is clearly visible. The snippet shows the signal at the 512Hz sampling rate.*

Transfer Function Estimates

From the data we estimate transfer functions describing the relationship between the recorded electric field and the injected protection current as

$$\underbrace{\begin{pmatrix} E_x \\ E_y \end{pmatrix}}_{\vec{E}} = \underbrace{\begin{pmatrix} T_x \\ T_y \end{pmatrix}}_{\vec{T}} I \quad , \vec{T} = \vec{T_{\Re}} + \vec{T_{\Im}} = \text{Telluric Vector}$$

Where E is the recorded electric field vector, I the injected protection current and T the univariate transfer function. The transfer functions are estimated in the frequency domain using a regression M-estimate (e.g. Egbert and Booker, 1986) and the data used for the estimate is chosen based on coherency between the electric fields and the protection current. In addition only coefficients of frequencies associated with the pipeline signal are used. For synthetic data transfer functions are calculated by division of the electric fields by a factor corresponding to the known total injected current of 2.5A.

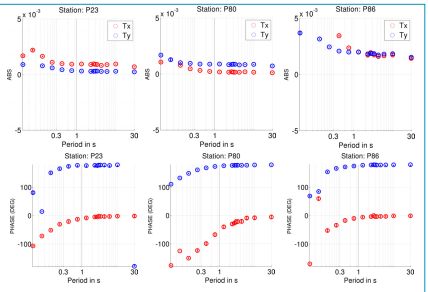

Figure 5: *Example of transfer functions estimated from the data for the stations labeled P23, P80 and P86. The transfer functions are smooth. While P23 shows only little dependence of the phase on the frequency, P86 shows a strong dependence.*

Modeling and Inversion

The pipe current was measured at discrete points using a pipeline detection tool and was found to decay exponentially towards the ends. An exponential function fitted to the measured values is used to be able to determine the source current at arbitrary points along the pipeline. 1D modeling is performed using the software EM1D (Streich and Becken 2011a). The pipeline model consists of 510 finite wire sources to approximate the pipeline geometry (Streich and Becken 2011b) and the individual sources current is determined from the fit to the measured data. Figure 6 shows the transfer functions (real part) computed for our model and various subsurface models in conjunction with the transfer functions estimated from the data.

The lenght of the real telluric vector was inverted for single stations and homogeneous half spaces at two neighbouring frequencies. We assumed 5% data error and error floors of 1e-5. Examples of the resulting resistivities are plotted on a map (see Figure 8). The results are consistent for single stations over the whole frequency range (0.03 Hz – 3 Hz), but may lack spacial consistency. The length of the imaginary telluric vector could not be fitted.

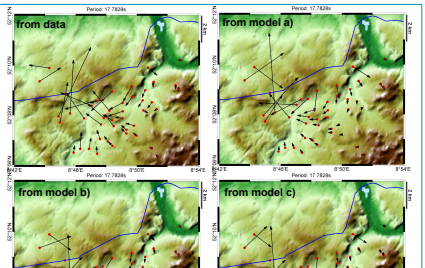

Figure 6: *Arrows indicating the direction and length of the real telluric vector.* ***Top Left****: Transfer functions estimated from the data* ***Top Right****: Transfer functions calculated for model a) in Figure 7* ***Bottom Left:*** *Transfer functions calculated for model b) in Figure 7* ***Bottom Right:*** *Transfer functions calculated for model c) in Figure 7.*

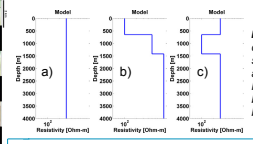

Figure 7: *Models used to calculate the transfer functions shown in Figure 6. Model labeled a) corresponds to values shown in Figure 6 top right, b) to Figure 6 bottom left, and c) Figure 6 bottom right.*

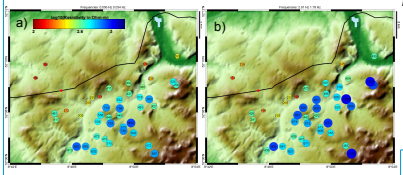

Figure 8: *Results from inverting the length of the real telluric vector. Inversion was performed for each station separately and frequencies of* ***a)*** *0.03 Hz and 0.06 Hz* ***b)*** *1Hz and 3 Hz. The numbers give the half space resistivity in Ohm-m (also indicated by size and color of the circles).*

Inversion of the data for layered subsurface models for single stations or carefully chosen combinations of multiple stations were partially successful. Again, only the length of the real telluric vector could be fitted with 10% error assumption. The modelled data shows a frequency dependent amplitude comparable to the frequency dependence observed in the transfer functions estimated from the data (Figure 9).

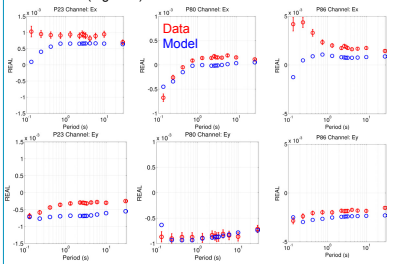

Figure 9: *Real- parts of transfer functions estimated from the data (red) and forward modeling (blue). The forward modeling was performed using the model resulting from a single station 1D inversion of the measured data for the lenght of the real telluric vector. 10% errorbars are plotted for the measured data.*

Conclusion

- Signals originating from the ICCP current are clearly visible in the recorded electric field data
- Transfer functions obtained from modeling show similar behavior as the transfer functions estimated from the data
- Inversion of single station data for narrow frequency bands give reasonable apparent resistivities for the subsurface
- However, generally inverting the data for 1D resistivity models proves difficult
- The lenghts of the real telluric vector observed in the data can be matched by the synthetic models
- Further attempts aim at using improving the 1D inversions. Additionally, 3D inversion approaches will be used in order to fit both, the real- and imaginary- parts of the transfer function data, ideally for the whole dataset rather than single stations.

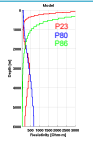

Figure 10: *Models used in calculations shown in Figure 9.*

Literature

Egbert, G. D. and J. R. Booker (1986): Robust estimation of geomagnetic transfer functions. *Geophysical Journal of the Royal Astronomical Society* 87, 173-194

Streich, R. and M. Becken (2011a): Electromagnetic fields generated by finite-length wire sources: Comparison with point dipole solutions. *Geophysical Prospecting* 59(2), 361-374

Streich, R. and M. Becken (2011b): Sensitivity of controlled-source electromagnetic fields in planarly layered media. *Geophysical Journal International* 187(2), 705-728

living.knowledge
WWU Münster

Acknowledgements

We would like to thank Westnetz for technical support and access to their pipeline infrastructure.

We thank the Department of Geophysics at the University of Frankfurt for their hospitality and support.

This project is funded by the Germany Science Foundation (DFG) under grant BE 5149/2-1

Controlled Source RMT Theoretical Modelling and Measurement in Vuoksa region Russia

Muttaqien, I.[1]*, Tezkan, B.[1]

[1]Institute of Geophysics & Meteorology, University of Cologne, Germany, *muttaqien@geo.uni-koeln.de

Introduction

Controlled source radiomagnetotelluric (CSRMT) is a modification of the RMT method. It uses horizontal electric dipole with length varying from 200 – 700 m as a source emitting frequency from 1–1000 kHz. This method is mainly intended for application in the remote area where there is no enough radio transmitter available. By lowering the frequency to 1 kHz, the skin depth is triple than standard RMT.

We present 2D theoretical study of CSRMT data. SLDMEM3F of Druskin and Knizhermann is used for forward modelling [1]. Inversion of synthetic data are done by using CS1D of Shlykov and Saraev [2]. The results of forward modelling and inversion show the effects of 2D conductivity structure.

Our first CSRMT measurement was made in Vuoksa Region, around 100 km north of St. Petersburg Russia. A 700 m dipole connected to GTS-1 transmitter was used as a source emitting rectangular signal with main frequency of 0.5 , 11.3, 30 and 105 kHz. 97 in-line soundings were made along a profile starting from 10 m with 20 m spacing, with 3 soundings addition off the profile. Thus we have a complete data of near field, transition and far field zones. 2 components of electric field E_x and E_y and 3 components of magnetic field H_x, H_y and H_z were measured in each sounding using RMT-5 receiving instrument.

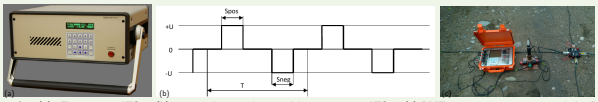

Fig. 1 : *(a). Transmitter GTS-1, (b) rectangular signal emitted by transmitter GTS-1, (c) RMT-5 receiver instrument and the field set up.*

CSRMT Theoretical Modeling

A 700 m dipole in x direction centered at $x = 0$ as shown in Fig. 2(a),(b), the soundings are made at 50 frequencies loglineary spaced from 1 to 1000 kHz in 10 stations starting from 1410 m with 20 m spacings, the fault located at $x = 1500$ m, 5 stations are located in the left and 5 are on the right of the fault.

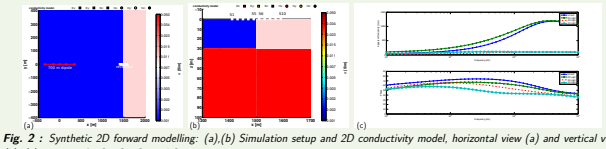

Fig. 2 : *Synthetic 2D forward modelling: (a),(b) Simulation setup and 2D conductivity model, horizontal view (a) and vertical view (b), (c) response for S1, S5, S6 and S10.*

The response of forward modelling shown in Fig. 2(c). It is clear seen that near the fault both overshoot and undershoot are present. The 1D responses are shown for S1 (1410 m) and S10 (1590 m), while 2D effects are seen in S5 (1490 m) and S6 (1510 m).

CS1D is an inversion code for CSRMT data in 1D. Displacement current is allowed in the ground and in the air in solving the forward problem [2]. Inversion results of the synthetic data are below:

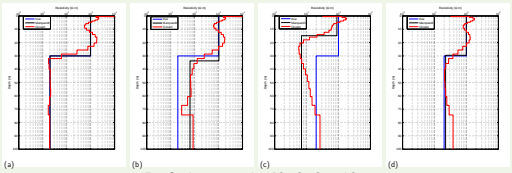

Fig. 3 : *Inversion results of S1, S5, S6 and S10.*

We see that for S1, S10, the inversion gives the correct model since they are located far from 2D structures, while for S5 and S6, the 2D structures effecting the synthetic data as shown in Fig 2(c) and also the inversion results.

CSRMT measurement in Vuoksa Region

Vuoksa region is located around 100 km north of St. Petersburg Russia. The profile in far field zone has been studied by RMT-F and RMT-M methods making this suitable for testing a new experiment method as well as new interpretation software. The profile is then extended to the direction of the source in order to have near field and transition zones data.

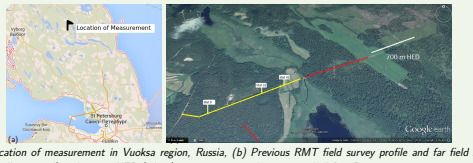

Fig. 4 : *(a) Location of measurement in Vuoksa region, Russia, (b) Previous RMT field survey profile and far field zone (yellow), CSRMT profile (yellow + red) and 700 m HED (white), station 8, 31 and 44 are marked for 1D inversion.*

Data Processing

The data are processed by calculating the surface impedance from the horizontal mutually orthogonal components of the electric and magnetic fields with minimum coherence of 0.8. From the surface impedance apparent resistivity ρ_a and phase Φ are calculated. Only emitted frequencies and their subharmonics are considered in the processing (neglecting available radio frequencies in far field zone) to have smooth apparent resistivity and phase data.

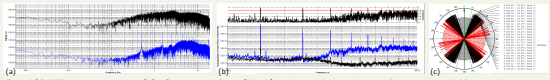

Fig. 5 : *CSRMT data processing (a). Spectrum of E_x (black) and H_y blue with main frequency 0.5 kHz at a distance 1750 m in 1-10 kHz frequency band. (b). Calculation of autospectra, the minimum coherence is 0.8 between mutually orthogonal electric and magnetic field. (c). Selection of frequencies in data processing.*

The pseudosection of far field data, (along RMT profile) is shown in Fig. 6

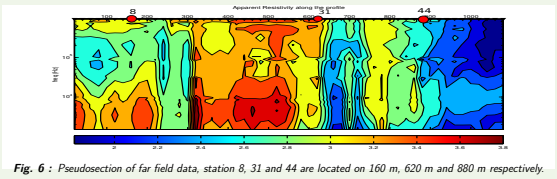

Fig. 6 : *Pseudosection of far field data, station 8, 31 and 44 are located on 160 m, 620 m and 880 m respectively.*

From the Fig. 6, 2D structure of the profile in far field zones are clearly seen with apparent resistivity range from 30–7000 Ω m. From 0– 630 m and 730– 900 m are resistive zone, and 630–730 m and 900–1060 m are conductive zone.

1D inversion of field data

Inversion results of real data in 3 stations, as shown in Fig. 4 c. are below:

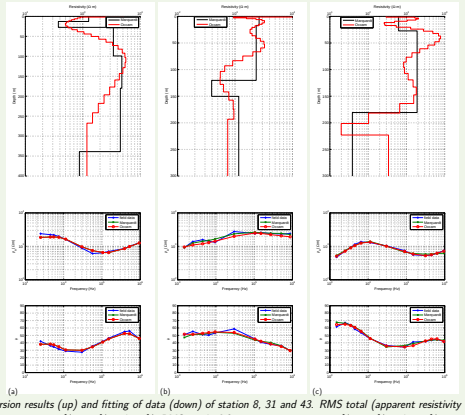

Fig. 7 : *Inversion results (up) and fitting of data (down) of station 8, 31 and 43. RMS total (apparent resistivity and phase) of Marquardt inversion are 3.3%, 3.82% and 4.7%, RMS total of Occam inversion are 2.98%, 3.48% and 6.82% respectively.*

The field data in station 8, 31 and 44 are smooth well fitted by CS1D. The inversion yields 6, 4 and 3 layers with for station 8, 31 and 44 respectively. Most of the layers are resistive > 375 Ωm with one exception in station 44 after depth of 180 m, the resistivity is around 20 Ωm.

Conclusion and Outlook

- **Conclusion:**
  - SLDMEM3F is a very fast and accurate in modelling 2D of CSRMT data.
  - CS1D can be applied to interpret CSRMT data.
- **Outlook:**
  - 2D inversion in far field.
  - 2D modelling in near field and transition zones.
  - Inversion (1D and 2D) of field data in all zones.

References:

[1] Druskin, V. L. and Knizhnermann, L. A., Spectral approach to solving three-dimensional Maxwell's diffusion equations in the time and frequency domains. *Radioscience*, 29(4), 1994.

[2] Shlykov, A. A. and Saraev, A. K., Estimating the Macroanisotropy of a Horizontally Layered Section from Controlled-Source Radiomagnetotelluric Soundings. *Izvestiya, Physics of the Solid Earth*, Vol. 51, No. 4, 2015.

Erste TEM-Messungen in Schleiz, Thüringen im Rahmen des DESMEX-Projekts

D. Ossen[1], B. Tezkan[1], P. Yogeshwar[1]

[1] Institut für Geophysik und Meteorologie, Universität zu Köln
Kontakt: ossen@geo.uni-koeln.de

DESMEX

DESMEX (*Deep electromagnetic sounding for mineral exploration*) ist ein Verbundprojekt, das vom Bundesministerium für Bildung und Forschung im Rahmen der Fördermaßnahme *r⁴ – Innovative Technologien für Ressourceneffizienz – Forschung zur Bereitstellung wirtschaftsstrategischer Rohstoffe* gefördert wird.
Primäres Ziel des Projektes ist die Entwicklung neuer geophysikalischer Verfahren für die Erkundung von heimischen Rohstoffpotenzialen, im Speziellen von Erzen. Im besonderen Fokus steht die Entwicklung zur flächenhaften und möglichst hochausflösenden Abdeckung durch elektromagnetische Verfahren mit Eindringtiefen bis 1000 Metern Tiefe. Weiterhin sollen bekannte Lagerstätten sowie bekannte Datensätze neu bewertet und Konzepte entwickelt werden zur Erfassung von bisher unbekannten Rohstoffvorkommen, beispielsweise von Hochtechnologiemetallen, die bisher nicht Gegenstand der Bergbauaktivitäten waren.
Als Untersuchungsgebiet wurde das ostthüringer Schiefergebirge in der Gegend von Schleiz bis Greiz ausgewählt, da hier das Vorkommen von antimonitführenden Gängen bekannt ist.

Messgebiet

Das Untersuchungsgebiet ist geprägt vom Bergbau. Es gibt viele alte Gruben, in denen früher Antimonit und andere Erze abgebaut wurden. Dementsprechend sind weite Teile des Gebietes mit Schächten unterhöhlt. Für das südliche Messgebiet ist vor allem die Grube Halber Mond zu nennen. Die unterirdischen Schachtsysteme verlaufen hier in Richtung Oberböhmsdorf und erstrecken sich über eine Länge von ca. 600, eine Breite von ca. 200 und bis in eine Tiefe von ca. 250 Metern auf verschiedenen Sohlen. Auch nördlich von Schleiz sind Schachtsysteme vorhanden. Genauere Informationen liegen allerdings nicht vor. Desweiteren verläuft um Schleiz eine Gaspipeline, die von Süden kommt und östlich an Schleiz vorbei und richtung Oettersdorf läuft (siehe Abb. 1).

Daten

Die Daten werden zusammengesetzt aus 3 Transienten. Der NanoTEM low gain Modus wird mit wenig Strom (I = 0.3 A) und ohne Verstärkung der Empfängersignals gemessen, der NanoTEM high gain Modus mit mehr Strom (I = 2.7 A) und mit Verstärkung und der ZeroTEM Modus mit viel Strom (I = 10 A). Zusammengesetzt ergeben sie einen langen Transienten.
Die Qualität der Daten im Untersuchungsgebiet ist gemischt. Auf den Profilen im Norden von Schleiz (2b bis 4b) sind sie weitgehend sauber (siehe Abb. 2a). In der Nähe der Pipeline fallen die Transienten zu mittleren bis späten Zeiten häufig sehr steil ab, während die Fehlerbalken extrem klein sind (siehe Abb. 2b). Außerdem kommen hier Vorzeichenwechsel vor wie in Abb. 2c zu sehen ist. Weiter im Süden des Messgebietes auf Profil 4a sowie in der Nähe der Grube Halber Mond sind die Daten meist stark gestört (siehe Abb. 2d).

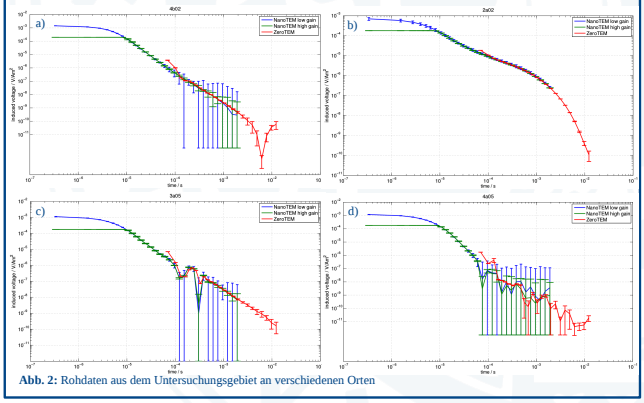

Abb. 2: Rohdaten aus dem Untersuchungsgebiet an verschiedenen Orten

Rauschmessungen

Um mögliche Störquellen zu identifizieren, wurden an einigen Punkten Rauschmessungen durchgeführt. Dazu wurde eine TEM-3 Spule von Zonge Engineering und eine KMS-820 von KMS Technologies benutzt.

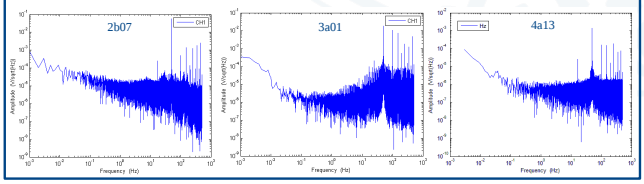

GEFÖRDERT VOM
Bundesministerium für Bildung und Forschung

Messungen in Schleiz

Im Rahmen einer Vorerkundung des Projekts wurde die Transient-Elektromagnetik (TEM) angewandt, um erste Ergebnisse für das Gebiet zu erhalten. Die Messungen wurden vom 18.08.2015 bis zum 05.09.2015 in der Umgebung von Schleiz bei den Orten Oberböhmsdorf und Oettersdorf durchgeführt. Bereits im Mai 2015 hat das BGR Hubschraubermessungen durchgeführt und dabei eine Fläche von mehr als 400 km² vermessen.
Die TEM-Messungen wurden entlang von Profilen durchgeführt, die auf den Fluglinien des BGR liegen. Insgesamt wurde an 69 Punkten mit der Inloop Konfiguration gemessen, mit einer 100x100 m² Sendespule und einer 25x25 m² Empfängerspule für frühe Zeiten und einer TEM-3 Spule von Zonge Engineering für späte Zeiten. Als Sender diente der NT-20 und als Empfänger der GPD32-24 von Zonge Engineering. Der Messpunktabstand betrug soweit möglich 100 Meter.

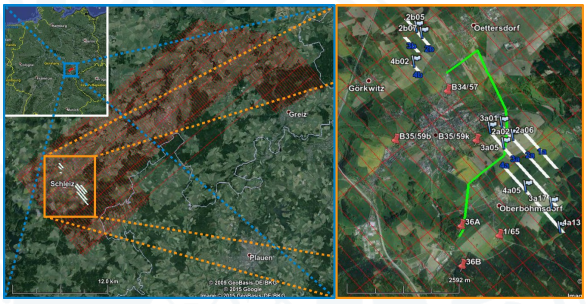

Abb. 1: Überblick über das Messgebiet. Rote Linien: Fluglinien des BGR. Weiße Linien: TEM-Profile. Grüne Linie: Ungefährer Verlauf der Gaspipeline. Rote Pins: Bohrlochlokationen

Erste 1D-Inversionsergebnisse

Für ausgewählte Puntke wurden erste 1D-Inversionen durchgeführt. Inwiefern diese aussagekräftig sind, muss noch diskutiert werden. Es bleibt zu klären, ob die 1D-Annahme gerechtfertigt ist, oder ob die Daten zumindest in 2D ausgewertet werden müssen.
Zunächst wurden Occam-Inversionen mit vielen Schichten und zwei verschiedenen Glättungsparametern durchgeführt. Die Ergebnisse legen einen 3- bis 4-Schichtfall nahe und wurden genutzt, um ein Startmodell für eine Marquardt-Inversion zu wählen. Zuletzt wurden äquivalente Modelle berechnet, die die gemessenen Daten ebenfalls gut erklären können.
Aus den ersten Inversionen lässt sich ein generelles Modell ableiten. An der Oberfläche findet man eine ca. 10 Meter mächtige Schicht mit einem Widerstand von 50 bis 100 Ωm. Darunter folgt eine sehr resistive Schicht mit einem Widerstand von 300 bis 10000 Ωm wobei dieser Wert meist nicht gut aufgelöst ist. In einer Tiefe von ca. 100 Metern fällt der Widerstand wieder auf 100 Ωm ab. Möglicherweise findet man hier noch geringere Widerstände bis 20 Ωm.

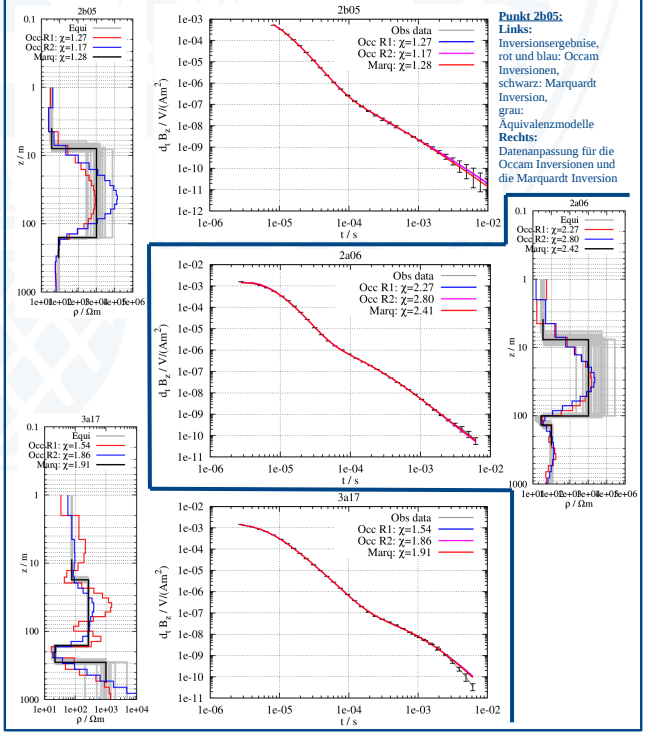

Punkt 2b05:
Links: Inversionsergebnise, rot und blau: Occam Inversionen, schwarz: Marquardt Inversion, grau: Äquivalenzmodelle
Rechts: Datenanpassung für die Occam Inversionen und die Marquardt Inversion

Gemeinsame Anwendung von Magnetik und EMI auf dem archäologischen Fundort Elusa (Israel)

N. Pickartz[1], B. Tezkan (Institut für Geophysik und Meteorologie, Universität zu Köln),
M. Heinzelmann (Archäologisches Institut, Universität zu Köln) [1]*pickartz@geo.uni-koeln.de*

Einleitung

Abb. 1: Lage von Elusa

Die antike Stadt Elusa, am nördlichen Rand der Negev-Wüste gelegen, wurde im 3. Jh. v. u. Z. vom Volk der Nabatäer als Karawanserei an einer Handelsroute für Gewürze und Weihrauch von der Arabischen Halbinsel über Petra bis hin zum Mittelmeer gegründet. Während der Kaiserzeit entwickelte sich Elusa zum größten städtischen Zentrum mit dem einzigen bekannten Theater des Negev. In frühbyzantinischer Zeit erlebte die Stadt eine zweite Phase der Prosperität, in der ein Bischofssitz eingerichtet und neben einer Kathedrale weitere Kirchen erbaut wurden. Die Stadt wurde vermutlich im 7. Jh. n. u. Z. aufgegeben. 2005 wurden Elusa und weitere Städte im Negev als Kulturdenkmal "Weihrauchstraße und Wüstenstädte im Negev" ins UNESCO-Welterbe aufgenommen. Trotz der großen Bedeutung der Stadt ist, abgesehen von punktuellen Ausgrabungen, bislang wenig über ihre städtebauliche Gestalt und Entwicklung bekannt.

Kampagnen

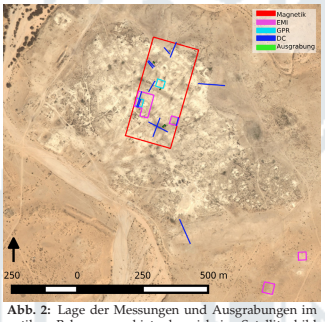

Abb. 2: Lage der Messungen und Ausgrabungen im antiken Bebauungsgebiet, das sich im Satellitenbild (Google Earth) abzeichnet.

In Zusammenarbeit mit dem Archäologischen Institut der Universität zu Köln wurden neue Untersuchungen durchgeführt.

April 2013:

- Magnetik: Cäsiumdampfsensoren (GeoMetrics)
  - großflächige Kartierung der Totalfeldstärke (ca. 7 von 40 ha)
- Bodenradar (GPR): 400 MHz Antenne (GSSI)
  - zwei Flächen à 30 m × 30 m innerhalb der Magnetikkartierung

Februar und März 2015:

- Archäologische Ausgrabungen und Surveys
- Elektromagnetische Induktion (EMI): CMD Mini-Explorer (GF Instruments)
  - insgesamt 6100 m^2 in unzusammenhängenden Teilstücken kontinuierlich gemessen
  - teils in horizontal (HCP) und vertikal (VCP) koplanarer Spulenanordnung, teils nur VCP
  - Vergleichsprofile mit Punktmessungen für HCP und VCP
- Multielektrodengeoelektrik (DC): Lippmann 4 Point Light (LGM)
  - 12 Profile u.a. zur Kalibrierung der EMI-Messung

Magnetik

Abbildung 3 zeigt das magnetische Anomaliefeld basierend auf den Messungen der Totalfeldstärke. Die Daten wurden mit fünf Prozessierungschritten aufbereitet (vgl. hierzu [1], [2] und [3]). Die archäologische Interpretation der Daten, im Rahmen derer bisher unbekannte Straßen und Mauerzüge lokalisiert wurden, lieferte neue Erkenntnisse über den innerstädtischen Aufbau von Elusa.
Die Flächen für die Testmessungen mit dem EMI-System sowie die Bereiche der Ausgrabungen wurden u.a. auf Grundlage dieser Messungen ausgewählt. Die 30 m × 30 m große Vergleichsfläche (Abbildung 3, rechts) wurde ausgesucht, da sich in der Magnetik deutliche Anomalien abzeichnen, die mit archäologischen Befunden korelliert werden können.

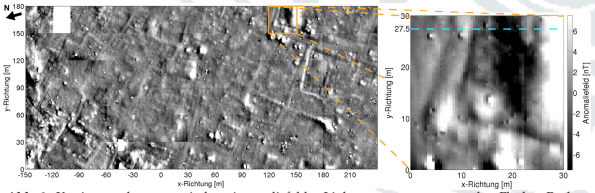

Abb. 3: Kartierung des magnetischen Anomaliefelds. Links: gesammte untersuchte Fläche. Rechts: Ausschnitt zum Vergleich mit EMI- und DC-Messungen. Das DC-Profil liegt bei y = 27.5 m (blaue Strichlinie).

Referenzen

[1] Ciminale, M. und M. Loddo (2001), Aspects of Magnetic Data Processing, *Archaeological Prospection*, *8*, 239-46.

[2] Eder-Hinterleitner, A., W. Neubauer, und P. Melichar (1996), Restoring Magnetic Anomalies, *Archaeological Prospection*, *3*, 185-97.

[3] Pickartz, N. (2014), *Über die Auswertung und Modellierung von Magnetik- Bodenradardaten des archäologischen Fundorts Elusa (Israel)*; Köln: Universität zu Köln, Institut für Geophysik und Meteorologie, Masterarbeit.

EMI

Die Rohdaten der scheinbaren spezifischen Leitfähigkeit und der In-Phase-Komponente für HCP und VCP des CMD Mini-Explorers auf der Vergleichsfläche sind in Abbildung 4 dargestellt. Das Gerät besitzt drei verschiedene Empfängerspulen im Abstand s von 0.32 m, 0.71 m und 1.18 m zur Sendespule, woraus sich jeweils drei verschiedene Erkundungstiefen von 0.25 m, 0.5 m und 0.9 m für VCP sowie 0.5 m, 1.0 m und 1.18 m für HCP ergeben.
Ebenso wie in der Magnetik (Abbildung 3) ist in den EMI-Messungen die L-förmige Anomalie zu erkennen, allerdings deutlicher in den scheinbaren spezifischen Leitfähigkeiten als in der In-Phase. Die zwei parallelen Linien dieser Struktur werden jedoch durch die EMI-Messungen nicht aufgelöst, es ist nur eine breite Anomalie zu erkennen. Auch die flächige Anomalie in der rechten oberen Ecke des Messfelds hat eine unterschiedliche Form in den Ergebnissen der beiden Methoden.

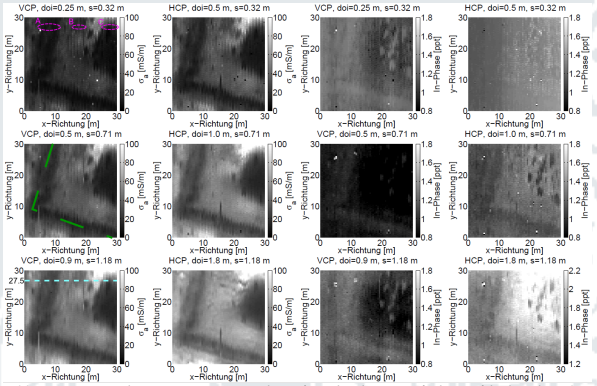

Abb. 4: Kartierung der EMI-Messwerte. Linke Häfte: scheinbare spezifische Leitfähigkeit der VCP- (erste Spalte) und HCP- (zweite Spalte) Messung der drei verschiedenen Spulenabstände s und der daraus resultierenden Erkundungstiefe *doi*. Rechte Hälfte: entsprechende Abbildungen wie oben für die In-Phase-Komponente. In der linken Spalte sind zusätzlich markiert: Korellation zum DC-Profil (magenta, vgl. Abb. 6), Skizzierung der archäologischen Anomalie (grün) und Lage des DC-Profils (hellblau).

Insbesondere in der In-Phase-Komponente sind in der rechten oberen Ecke des Messfelds viele kleinräumige Anomalien zu sehen. Vor Ort im Messgebiet wurden die dort größten wachsenden Sträucher, mit einer Höhe von bis zu 50 cm, mit einem Differential GPS eingemessen (Abbildung 5). Die Auswertung mit einem GIS zeigt eindeutig, dass diese Anomalien mit dem Bewuchs und der damit verbundenen Änderung der Tragehöhe des EMI zusammenhängt.

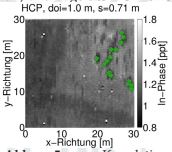

Abb. 5: Korrelation zwischen per DGPS eingemessenen Bewuchs und Anomalien in der In-Phase-Komponente.

DC

Das Inversionsergebnis der Dipol-Dipol-Messungen mit einem Elektrodenabstand von 50 cm des Profils bei 27.5 m auf der Vergleichsfläche (vgl. Abbildung 3) ist in Abbildung 6 dargestellt. Die scheinbaren spezifischen Leitfähigkeiten aller EMI-Kombinationen korellieren qualitativ vor allem mit dem oberflächennahen Bereich des DC-Modells (magentafarbene Markierung).

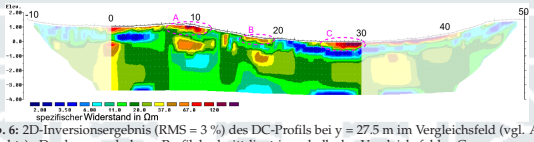

Abb. 6: 2D-Inversionsergebnis (RMS = 3 %) des DC-Profils bei y = 27.5 m im Vergleichsfeld (vgl. Abb. 3, rechts). Der hervorgehobene Profilabschnitt liegt innerhalb des Vergleichsfelds. Gemessen wurde in Dipol-Dipol-Konfiguration mit einem Elektrodenabstand von 50 cm. Die mit A, B und C markten schlechten Leiter korellieren gut mit den EMI-Messungen.

Ausblick

Auswertung der Messungen der Kampagne 2015:

- Inversion der DC-Profile
- Kalibrierung der EMI-Messungen mithilfe der DC-Modelle
- 1D-Inversion der EMI-Messungen und Erstellung von Quasi-2D- und Quasi-3D-Untergrundmodellen

Für Frühjahr 2016 ist eine weitere Kampagne mit Ausgrabungen und der Erweiterung der Magnetikprospektion geplant.

Danksagung

Besonderer Dank gilt dem Forschungszentrum Jülich für die Zuverfügungstellung des CMD Mini Explorers für die Kampagne im Jahr 2015.

Weiterhin danke ich allen Teilnehmern der Ausgrabungskampagne 2015 für die Unterstützung und die angenehme Atmosphäre vor Ort.

First 3D inversion results from magnetotelluric data of the Eastern Karoo Basin, South Africa

Anna Platz [1,2], Jade Greve [1,3,4], Ute Weckmann [1,2], Moctar Doucouré [3,4]

[1] Helmholtz Centre Potsdam - German Research Centre for Geosciences GFZ, Potsdam, Germany
[2] University of Potsdam, Institute of Geosciences, Potsdam, Germany
[3] Nelson Mandela Metropolitan University, Port Elizabeth, South Africa
[4] Africa Earth Observatory Network, Port Elizabeth, South Africa

Aim of project

- *General:* Fundamental understanding of the geology, petrology and hydrology of the Karoo Basin
- *Magnetotellurics (MT):* 3D-model of the subsurface

→ Imaging potential shale gas bearing formations

→ Imaging shallow aquifers for a better understanding of fresh and brackish water reservoirs

Photo of the Karoo Basins landscape in the study area (M. Schüler, GFZ Potsdam)

Study area

- *Eastern Karoo Basin:* Sedimentary basin stretching across most of southern Africa with a size of nearly 600,000 km²
- *Geology:* The basin contains two supergroups: Cape & Karoo Supergroup
- *Karoo Supergroup:* Contains Whitehill Formation with carbon rich shales

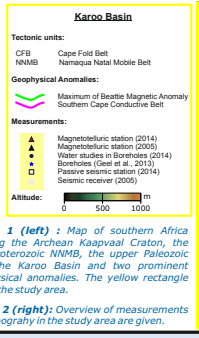

Figure 1 (left) : *Map of southern Africa showing the Archean Kaapvaal Craton, the Mesoproterozoic NNMB, the upper Paleozoic CFB, the Karoo Basin and two prominent geophysical anomalies. The yellow rectangle marks the study area.*

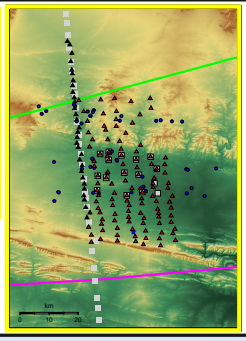

Figure 2 (right): *Overview of measurements and topography in the study area are given.*

Conclusion and future work

- 3D inversions started with standard single-site processing results → conductive layer (Whitehill?) mapped
- At shallow depth the Whitehill Formation is weathered and therefore not conductive
- Indications for shallow conductivity anomalies → aquifers?

→ Advanced processing of data

→ 2D inversion models along all profiles

→ 3D inversion models

→ Constraints from lithology/ hydrology

MT experiment 2005

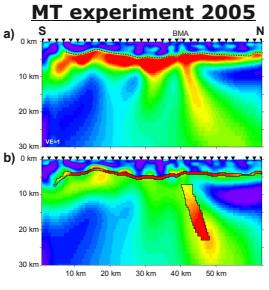

Figure 3: *2D inversion results from Weckmann et al. (2007) without (a) and with (b) tear zones. The rms of 2.3 for model a) could be reduced to 1.8 in model b) with the inclusion of tear zones. The most prominent conductivity anomalies are a shallow sub-horizontal high conductive band in the upper 5 km and a sub-vertical conductive feature beneath the maximum of the BMA going down to middle/ lower crust.*

Geology study

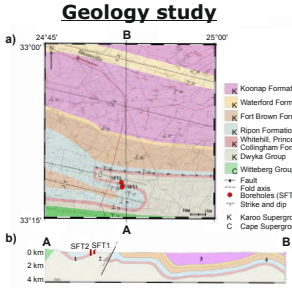

Figure 4: *(a) Geological map and (b) cross section after Geel (2013). Both were developed by using data collected from field outcrops and borehole logs. The Whitehill Formation in the metaanthracite window has a high total organic carbon content and correlates with a high electrical conductivity. The two boreholes reached a depth of 100 m (SFT1) and 300 m (SFT2) and intersected the Whitehill Formation.*

Data fit

Figure 5 (below): *Data fit of two sites for Model 1 and one site for Model 2. Site 0104 is located in the south of the study area. Site 0323 represents the middle part and is located near the maximum of the BMA. The data fit is quiet good except for the long periods at site 0323 for Model 1. For the same site the data might explained by Model 2. The reason is the high horizontal smoothing parameter of 0.4 in Model 1, which „smooths away" vertical structures. Furthermore, due to the high smoothing parameter the shallow conductivity horizon is interconneted even between profiles and sites in Model 1.*

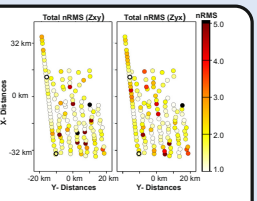

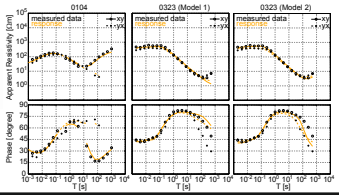

Figure 6 (above): *Total normalized rms for both off-diagonal components for each station for Model 1. Blacks dots mark stations for which all data for the special component are masked. There is no concentration of high rms values in one specific region or for one of the component. Site 0104 and 0323 are marked with thicker black circles.*

3D Inversion results

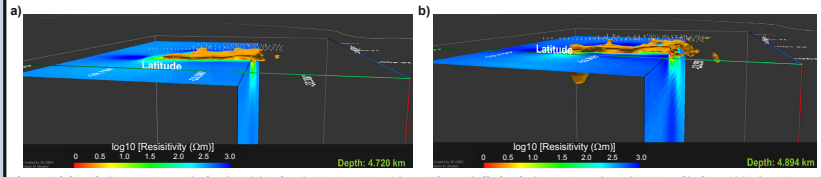

Figure 7 (above): *3D inversion results for a) Model 1 after the 91st iteration with a total rms of 2.4 and b) Model 2 after the 54th iteration with a total rms of 2.7. Off-diagonal components of the impedance tensor for MT data from 2005 and 2014 are used for the inversions. The isosurfaces of 3 Ωm are plotted in orange-brown. Furthermore a XY-slice is plotted together with a ZY-slice. In Model 2 a sub-vertical conductive body beneath the maximum of the BMA can be resolved. This feature does not appear in Model 1.*

Figure 8 (below): *2D sections along the MT profile from 2005 (see Figure 3) including the additional three sites measured in 2014. The maximum of the BMA is marked with a purple triangle and the sites depicting the data fit are shown as black filled triangles. A shallow sub-horizontal high conductive band in the upper 3-8 km is visible in both models, very similar to the results from Weckmann et al. (2007). In contrast to former MT studies no sub-vertical high conductor can be resolved beneath the maximum of the BMA in Model 1. In Model 2 this conductor is resolved.*

More 2D sections of Model 1

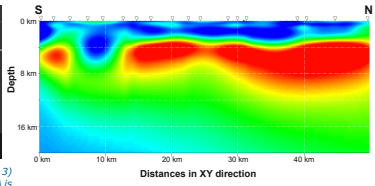

Figure 9 (above): *2D section along the third profile from the West. This profile is shorter than the most western profile and therefore it does not cross the maximum of the BMA. The sub-horizontal high conductive zone can be resolved in a depth of 3-10 km. Some shallow zones of reduced resistivities are observed in the high resistive body in the upper 2 km.*

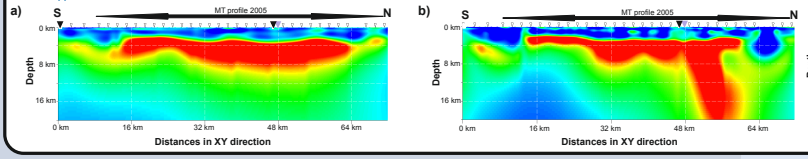

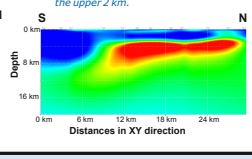

Figure 10 (left): *2D section along the most eastern profile. This profile is the shortest of all. The sub-horizontal high conductive zone is resolved in a depth of 3-8 km. Shallow zones of higher conductivity, as in the other profiles, can be resolved.*

MT 2014

- 111 five component stations
- 2-3 km site spacing along, and 5 km between profiles
- Frequencies: 10kHz-1mHz

Photo of the Karoo Basin and a flock of sheep in the study area (A. Dingle)

3D Inversion settings

- Using ModEM inversion code (Egbert & Kelbert, 2012; Meqbel 2009)
- Start from homogenous half-space with 400 Ωm (Model 1) and 500 Ωm (Model 2)
- Cells in x,y and z-direction with boundary cells : 100, 100, 55 (Model 1) and 110, 110, 60 (Model 2)
- Only use off-diagonal components of impedance tensor with 5% errorfloor on Zxy, Zyx
- Smoothing (α_x,α_y, α_z): 0.4, 0.4, 0.2 (Model 1) and 0.3, 0.3, 0.3 (Model 2)

Literature

Weckmann, U., Jung, A., Branch, T. and Ritter, O., 2007. Comparison of electrical conductivity structures and 2D magnetic modelling along two profiles crossing the Beattie Magnetic Anomaly, South Africa, *South African Journal of Geology*, 449-464

Geel, C., 2013. Shale gas characteristics of Permian black shales in the Ecca Group, near Jansenville, Eastern Cape, South Africa, *Unpublished Master thesis*, NNMU, South Africa

Egbert, G.D. and Kelbert, A., 2012. Computational recipes for electromagnetic inverse problems, *Geophy. J. Int.*, 189, 251-267

Meqbel, N., 2009: The electrical conductivity structure of the Dead Sea Basin derived from 2D and 3D inversion of magnetotelluric data, *Dissertation*, Freie Universität Berlin, Germany

Acknowledgments

Field work in South Africa was funded by the Africa Earth Observatory Network (AEON) and was supported by the Nelson Mandela Metropolitan University (NNMU). We thank the Geophysical Instrument Pool Potsdam for providing the MT instruments. This experiment would not have been possible without the generous permission of the local farmers to access their premises. We also appreciate the help of B. Morkel, V. Wagener, L. Bezuidenhout, A. Dingle, B. Linol, S. Brina, M. Schüler, C. Patzer and N. Meqbel during our fieldwork.

www.gfz-potsdam.de

Untersuchung von Fehlerquellen bei CMD Explorer Messungen: Detektion einer städtischen Wasserleitung in Köln

N. Pützer, B. Tezkan, P. Yogeshwar
Institut für Geophysik und Meteorologie, Universität zu Köln

puetzer@geo.uni-koeln.de

Motivation und Messgebiet

Oberflächennahe elektromagnetische Induktionsverfahren (EMI) zeichnen sich durch hohe Effizienz und Mobilität aus. In kurzer Zeit lassen sich große Flächen kartieren, was einen schnellen Überblick über das Messgebiet ermöglicht. Da es sich bei dem CMD Explorer von GF-Instruments um ein relativ neues Messgerät handelt, wurden im Rahmen dieser Arbeit Fehlerquellen wie beispielsweise verschiedene Tragehöhen, Neigungen und Schrittgeschwindigkeiten genauer unter-sucht. Es wurde ein Messgebiet auf einer Grünfläche des Hiroshima-Nagasaki-Parks am Aachener Weiher in Köln ausgewählt, da dort in ca. 1 m Tiefe eine aktive städtische Wasserleitung aus metallischem Material (mit Kunststoff ummantelt) verläuft. Es wurden zwei Profile in SW-NO Richtung ausgelegt, P1 mit 50 m Länge und P2 mit 10 m Länge. Unterschiedliche Messpunktabstände wurden auf den Profilen für verschiedene Tests verwendet (0.5 m und 1 m).
Die Wasserleitung befindet sich bei Profilmeter 28 – 29.

Abb. 1: Übersicht zur Lage und zur Aufteilung des Messgebietes am Aachener Weiher.

Messmethode

Der CMD Explorer besteht aus einer Senderspule sowie drei Empfängerspulen und arbeitet mit einer festen Sendefrequenz von 10 kHz. Es kann eine kontinuierliche oder eine Punktmessung vollzogen werden. Darüber hinaus besteht die Wahl zwischen horizontal koplanarer (HCP) oder vertikal koplanarer (VCP) Spulenausrichtung. Dabei beträgt die maximale Erkundungstiefe 6.7 m in der horizontal koplanaren Spulenauslage (HCP). Aufgezeichnet wird die Quadratur und die Inphase, wobei ersteres proportional zur scheinbaren elektrischen Leitfähigkeit und letzteres proportional zur magnetischen Suszeptibilität des Untergrundes ist. Zur Kalibrierung wurde über Profil 1 eine Geoelektrik-Messung vorgenommen und mit Hilfe der Software *EMI-Inversion* wurden die CMD Daten kalibriert (Mester et al., 2011).

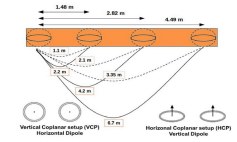

Abb. 2: Spulenabstände und Eindringtiefen

Inversionsergebnisse der CMD Daten

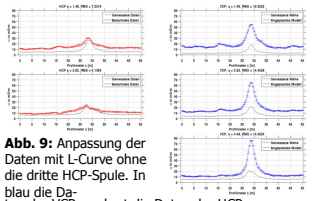

Abb. 9: Anpassung der Daten mit L-Curve ohne die dritte HCP-Spule. In blau die Daten der VCP- und rot die Daten der HCP-Anordnung.

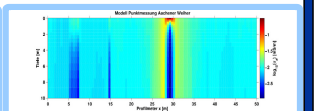

Abb. 10: Inversionsmodell nach der Anpassung mit dem L-Curve Verfahren

Für die Inversion wurde die Software *EM1DFM* verwendet (Farquharson et al, 2000). Zur Bestimmung des Trade-Off-Parameters wurde das L-Curve Verfahren ausgewählt. Da unkalibrierte Daten invertiert wurden, wodurch der Shift in Abb. 9 hervorgerufen wird, ist eine quantitative Aussage über die Leitfähigkeitsverteilung schwer zu treffen. Dennoch ist im Modell ein guter Leiter in Oberflächennähe dargestellt, der auf die Wasserleitung schließen lässt.

Kalibrierung der EMI-Daten

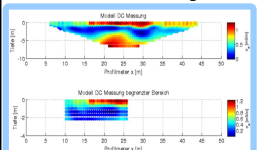

Abb. 11: Geoelektrik-Modell und der ausgewählte Bereich von 10 m bis 26 m, der für die Kalibrierung genutzt wurde.

Zur Kalibrierung der Daten wurde das Programm *EMI-Inversion* verwendet, das ausgehend von einem DCR Modell synthetische EMI Daten berechnet. Diese werden gegen die gemes-senen CMD Daten aufgetra-gen. Anschließend wird die Regressionsgerade ermit-telt, welche die Kalibrie-rungsfaktoren liefert. Für die Kalibrierung wurde ein Bereich aus dem ERT-Modell ausgewählt (vgl. Abb.11). Hier konnte nicht das gesamte ERT-Modell verwendet werden, da DCR die Leitung wegen der Plastikummantelung als schlechten Leiter repräsentiert. Der Gütefaktor R^2 liegt bei HCP zwischen 0.76 und 0.89 und zeigt somit eine gute Korrelation der Daten (> 0.85). Bei VCP liegen die R^2–Werte deutlich unter 0.85. Unter Beachtung der Skalenunterschiede ist das Modell der kalibrierten Daten sehr glatt im Vergleich zum unkalibrierten Modell. Dennoch ist auch hier eine gut leitende Struktur in Profilmitte abgebildet.

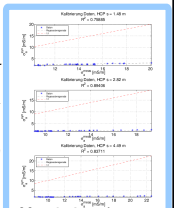

Abb. 12: Streudiagramme mit Regressionsgeraden, HCP

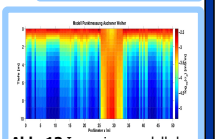

Abb. 13 Inversionsmodell der kalibrierten Daten

Fehlerquellenanalyse

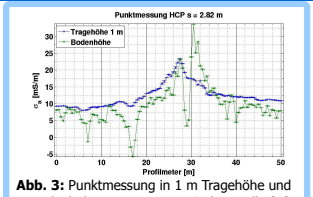

Abb. 3: Punktmessung in 1 m Tragehöhe und in Bodenhöhe gemessen in HCP beispielhaft für Spulenabstand s = 2.82 m. Leitung bei Profilmeter 28-29

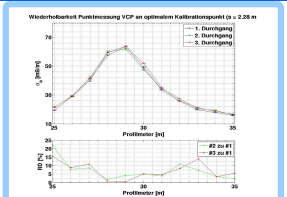

Abb. 4: Wiederholung Punktmessung in 1 m Tragehöhe in VCP für s = 2.82 m. Leitung bei Profilmeter 28-29

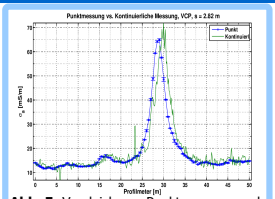

Abb. 5: Vergleich von Punktmessung und kontinuierlicher Messung in VCP mit Spulenabstand s = 2.82 m

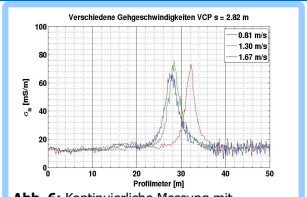

Abb. 6: Kontinuierliche Messung mit verschiedenen Schrittgeschwindigkeiten in VCP für s = 2.82 m Spulenabstand

Die Wasserleitung konnte mit dem CMD Explorer detektiert werden. In Profilmitte ist deutlich die gutleitende Stuktur zu erkennen. Die Oszillation der Messdaten in Bodenhöhe aus Abb. 3 lassen darauf schließen, dass Punktmessungen in Bodenhöhe im Vergleich zu Punktmessungen in 1 m Tragehöhe sensitiver für kleinräumige Strukturen in Oberflächennähe sind und zu weniger glatten Daten führen. Eine wiederholte Punktmessung hat ergeben, dass im Mittel Messfehler von ca. 7 % entstehen. Darüber hinaus zeigt der Vergleich zwischen Punkt- und kontinuierlicher Messung, dass beide Methoden ähnliche Ergebnisse liefern. Bei der kontinuierlichen Messung muss jedoch auf eine konstante Schrittgeschwindigkeit geachtet werden, da es sonst zu Verzerrungen der Messergebnisse kommt (vgl. Abb. 6). Wird das Messgerät nicht parallel zum Erdboden getragen oder die kalibrierte Tragehöhe nicht eingehalten, führt das zu Messfehlern (vgl. Abb. 7 und 8). Die relative Differenz zwischen einer Tragehöhe von 1 m und 0.95 m beträgt 6.4 %. Die Neigung des Messgerätes aus Abb. 8 hat eine Abweichung von 1.9 % bei einem Winkel von 5°.

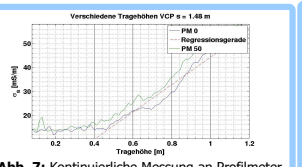

Abb. 7: Kontinuierliche Messung an Profilmeter 0 und 50, wobei das Gerät während der Messung von einer Starthöhe h bis zum Boden abgesenkt wurde.

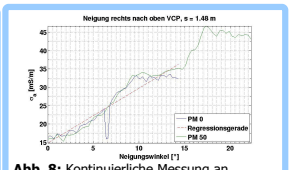

Abb. 8: Kontinuierliche Messung an Profilmeter 0 und 50, wobei die rechte Seite des Gerätes während der Messung nach oben geneigt wurde.

Zusammenfassung

Die Fehlerquellenanalyse hat hervorgebracht, dass der CMD Explorer empfindlich auf verschiedene Tragehöhen und Neigungen reagiert. Darüber hinaus muss auf eine korrekte Geräteeinstellung (Messung in Boden- bzw. Hüfthöhe) geachtet werden und eine konstante Schrittgeschwindigkeit bei kontinuierlichen Messungen eingehalten werden. Ein Messfehler von 7% wurde bei wiederholten Punktmessungen berechnet, welcher deutlich höher ist als der vorgegebene Stackingfehler (<2%). Das Modell der unkalibrierten Daten ist plausibel. Die Kalibrierung mit DCR ist an dieser Stelle problematisch, da die Leitung im DCR-Modell als schlechter Leiter repräsentiert wird.

Referenzen

- **McNeill J.D.**, Electromagnetic Terrain Conductivity Measurement at Low Induction Numbers, Geonics Limited, Technical Note TN-6, 1980.
- **Lavoue F.**, van der Kruk J., Rings J., Andre F., Moghadas D., Huisman J.A., Lambot S., Weihermüller L., van der Borght J. und Vereecken H., Electromagnetic induction calibration using apparent electrical conductivity modelling based on electrical resistivity tomography, Near Surface Geophysics, 8:553-561, 2010.
- **von Hebel C.**, Multi-Layer Conductivity Inversion of Calibrated Multi-Configuration Electromagnetic Induction Measurements; Aachen: TU Delft, ETH Zürich, RWTH Aachen und Forschungszentrum Jülich GmbH, Institute of Bio- and Geosciences: Agrosphere, 2013.
- **Farquharson C.**, Inversion and modelling of applied geophysical electromagnetic data, Background for Program 'EM1DFM', UBC- Geophysical Inversion Facility, 2000.
- **Mester A.**, van der Kruk J., Zimmermann E., Vereecken H., Quantitative Two-Layer Conductivity Inversion of Multi-Configuration Electromagnetic Induction Measurements, Vadose Zone Journal, 10, 1319- 1330, 2011.

Joint Inversion of DC and TEM data from a geothermal area in Mexico

D. Ruiz-Aguilar & B. Tezkan

Institute of Geophysics and Meteorology, University of Cologne

Introduction

San Felipe's area has many evidences of hydrothermal alteration, recent volcanism and hot springs. Also, there are many normal faults nearby the hot springs zone. The chemical composition of these hot springs indicates the presence of adequate temperatures to produce geothermal energy (Barragan et al., 2001). It is expected to obtain a potential between 100 and 120 MW for the geothermal reservoir, assuming a reservoir volume of 1 km³ (Prol-Ledesma et al., 2012). It is feasible to realize a geophysical exploration survey in the area in order to characterize the geothermal system (Fig. 1).

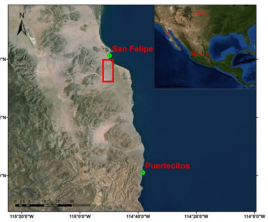

Figure 1. Localization of San Felipe.

Data acquisition

17 TEM and MT soundings were recorded along 4 lines, 1 NW-SE and 3 SW-NE, with 4 km of sounding spacing (Fig. 2). TEM soundings were acquired in the same spots in order to correct the static shift effect of MT data. Also, DC soundings that were found in literature are being used.

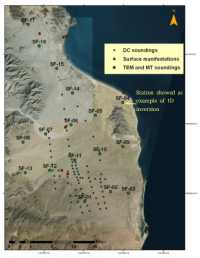

Figure 2. Localization of the soundings recorded.

TEM data

- TerraTEM of Monex Ltd.
- Single loop configuration
- 50 x 50 m loop size
- Four different gains: 1, 32, 100, 1000


Figure 3. TerraTEM device used in the field.

MT data

- Metronix devices
- Dipole length 50 m
- Induction coils
- Non-polarizable electrodes
- Frequency sampling of 4096 and 1 Hz
- Transfer functions in period range of 0.001-100 s


Figure 4. a)Layout of a sounding in the survey area. b) Induction coil. c) Metronix device. d) Field area.

1D Inversion of TEM data

1D inversion of TEM data has been performed with Occam and Marquardt inversion techniques.

Occam inversion was done for 30 layers with logarithmically equidistant layer thicknesses. The thickness of the first layer used is 1 m and the depth of the last layer 200 m.

The number of initial layers for Marquardt inversion was derived from the Occam models. A three-layers model is sufficient to fit the data. Equivalent models and parameter importances were calculated to reflect the model uncertainty and the quality of the inversion. In general, the resistivity and depth of the first layer have the greatest uncertainty. In the figure 7 we present the results of station SF-04, where a good conductive layer can be seen at depth of 90 m. This layer can be correlated to material exposed to hydrothermal alteration. D.C soundings confirm this interpretation. Finally, all the models generated present comparable values of resistivity and depth.

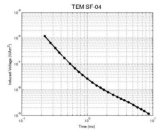

Figure 5 Example of data recorded with gain of 100.

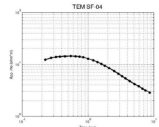

Figure 6. Example of Late-time apparent resistivity curve.

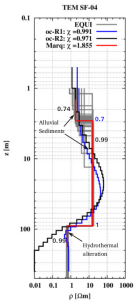

Figure 7. Example of model generated. Parameter importances are marked, in black for resistivities and in blue for depths.

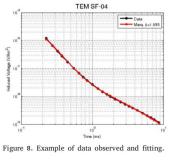

Figure 8. Example of data observed and fitting.

Spatially Constrained Inversion (SCI) of TEM data

Since 1D inversion results are similar for all TEM soundings, we assumed the subsurface is homogenous and decided to perform the Spatially Constrained Inversion scheme.

- SCI constraints are set laterally in two dimensions

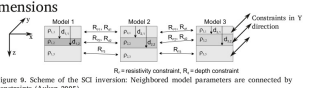

R_x = resistivity constraint, R_z = depth constraint
Figure 9. Scheme of the SCI inversion: Neighbored model parameters are connected by constraints (Auken,2005).

1. The first step for constraining the soundings is to perform a Delaunay triangulation (Fig. 10).


Figure 10. Delaunay triangulation of the soundings.

2. Second step is to decide how many neighboring soundings each sounding should be constrained to.

3. Final step is setting the strength of the constraint, following the formula:

$$C\_\mathrm{SCI}(d) = 1 + (A - 1)\left(\frac{d}{B}\right)^{a}$$

Where:
- d is the distance between two constrained soundings
- B is the reference distance
- A the reference constraint value
- *a* determines how the constraints loosen up with distance

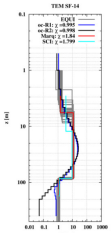

Figure 11. Example of model generated with SCI inversion scheme. Models generated with Marquardt and Occam inversions are also showed.

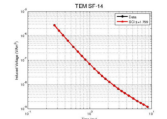

Figure 12. Example of data observed and fitting.

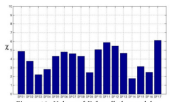
Figure 13. Values of χ for all the models.

SCI results are similar to conventional 1D inversion. We generated a pseudo-3D model of the subsurface from survey area (fig. 14). The good conductive layer associated to hydrothermally altered material can be seen since 90 m deep.

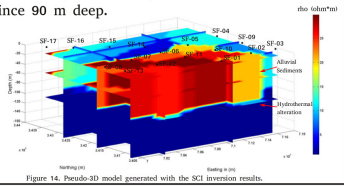

Figure 14. Pseudo-3D model generated with the SCI inversion results.

Joint DC-TEM Inversion

We could find information about a D.C survey exploration for groundwater purposes realized by the Mexican Commision of Water during the end of the 80's. D.C soundings were acquired with Schlumberger configuration and the maximum AB/2 was of 1000 m. Since some of their D.C soundings are between 300-800 m near from the TEM stations, we decided to perfom D.C-TEM Joint inversions to them. In order to be able to do the Joint Inversion, we calculated Forward Modeling to the D.C resulted models that we found in the literature and added 1 % of error to the synthetic data. In the figure 15 we show the 1D results of Occam and Marquardt joint inversion schemes for the stations: SF01-VES216, SF10-VES108 and SF12-VES13. We can see an important conductivity contrast at depths of 90 to 100 m. This conductivity layer can be associated to material that has been exposed to hydrothermal alteration.

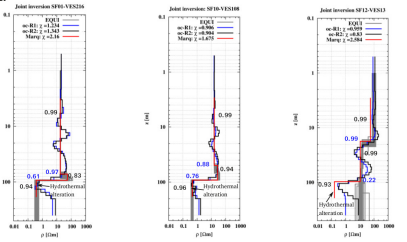

Figure 15. Results of Occam and Marquardt joint inversions. Equivalent models are also showed. Parameter importances are marked, in black for resistivities and in blue for depths.

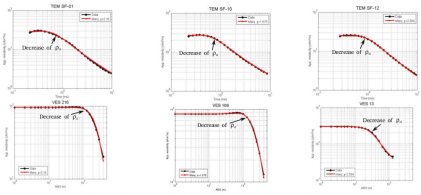

Figure 16. Data observed and data fitting of TEM and D.C soundings.

Conclusion & Outlook

The 1D models generated with TEM data describe the resistivity distribution of the shallow area from the subsurface in the survey area. Spatial Constrained Inversion results are consistent and comparable to the 1D Marquardt and Occam results. Joint inversion results of DC and TEM data are also comparable to the single 1D models obtained. We were able to obtain better results for the resistivity and depth of first layer with the help of D.C data.

Main goal of this project is to generate a 3D model with the Magnetotelluric data. We are going to use the TEM results as constraints for the MT data inversion in order to characterize accurately the geothermal system of San Felipe.

Acknowledgements

We would like to thank to the Institute of Geophysics of UNAM (National Autonomous University of México), specially to Prof. Dr. Rosa María Prol-Ledesma and Dr. Claudia Arango-Galván, for providing the data for this project. This doctoral project is funded by DAAD.

References

Auken, E., A. V. Christiansen, B. H. Jacobsen, N. Foget and K. I. Sørensen, 2005. Piecewise 1d laterally constrained inversion of resistivity data, Geophysical Prospecting, 53, 497–506.

Barragán, R. M., Birkle, P., Portugal M, E., Arellano G, V. M., and Alvarez R, J., 2001. Geochemical survey of medium temperature geothermal resources from the Baja California Peninsula and Sonora, México. Journal of Volcanology and Geothermal Research 110, 101-119.

Prol-Ledesma, R.M., Villanueva-Estrada, R., Arango-Galvan, C. and Flores-Marquez, L., 2012. Evaluation of the geothermal resources in Baja California peninsula. Technical report. SENER-CONACYT 152823.

GFZ Helmholtz Centre Potsdam

HELMHOLTZ CENTRE POTSDAM
GFZ GERMAN RESEARCH CENTRE FOR GEOSCIENCES

Mare2DEM on land: MT Data from the Cape Fold Belt (South Africa) revisited

Paula Rulff[1,2] & Ute Weckmann[1]
[1]Helmholtz Centre Potsdam, GFZ German Research Centre for Geosciences
[2] Institute of Earth and Environmental Science, University of Potsdam

INTRODUCTION

Mare2DEM is a parallel adaptive finite element code for 2D forward and inverse modelling for electromagnetic data (Key & Ovall, 2011), which is now being made freely available. Mare2DEM was originally designed with marine controlled-source electromagnetic (CSEM) and marine magnetotelluric (MT) applications in mind, but it can also be applied to onshore data. Important features of Mare2DEM are:

- automatic mesh generation and refinement
- triaxial (intrinsic) anisotropy
- topography

To test this inversion code with onshore MT data we use the data set measured in 2005 in the Cape Fold Belt, South Africa. The stations are aligned along a ~ 100km long profile with significant topography and a close-by ocean. Several stations indicate the existence of electrical anisotropy in the subsurface through phases > 90°. Commonly, these phases out of quadrant are explained by an anisotropy strike oblique to the main conductivity structures.
While in earlier inversion studies only data without 3D/anisotropy effects were inverted using WinGLink, we can now compare inversion results of this study, in particular how Mare2DEM deals the anisotropy effects in the MT data.

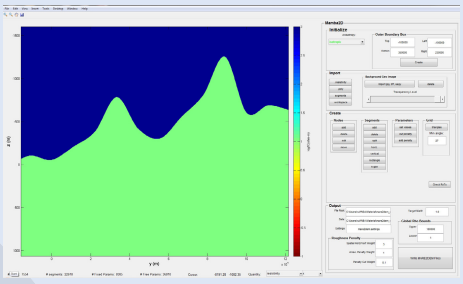

Figure 1
User interface Mamba2D for Mare2DEM to specify the following settings:
- *grid dimensions*
- *isotropic / anisotropic conductivities*
- *import a priori information, e.g. topography*
- *create and modify nodes and segments*
- *set conductivities / lock cells*
- *generate mesh*
- *target rms*
- *conductivity bounds*
- *regularization parameters*

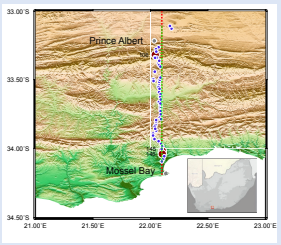

Figure 2
Map of the study area in South Africa. The blue dots show the location of the MT-Stations, which were projected onto the . dashed profile line. The MT profile consists of 54 stations and was measured in 2005. It crosses the Cape Fold Belt in South Africa between Prince Albert and Mosselbay.

2D Models

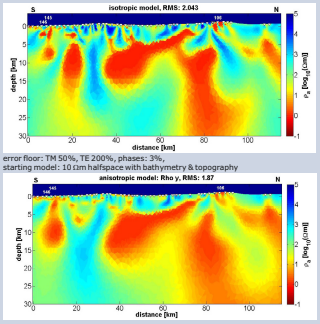

Figure 3
Isotropic conductivity model calculated with Mare2DEM [Key and Ovall, 2011]. White triangles show the location of the MT stations. The topography was included with 50m resolution together with the Ocean (rough bathymetry) at the southern end of the profile. Total rms: 2.04

Figure 4
Anisotropic conductivity model allowing for triaxial anisotropy. Here we present the y component of the conductivity which shows similar features compared to the isotropic inversion. The anisotropy introduced did not exeed a ratio of 2, but phases >90° cannot be modelled. Total rms: 1.87

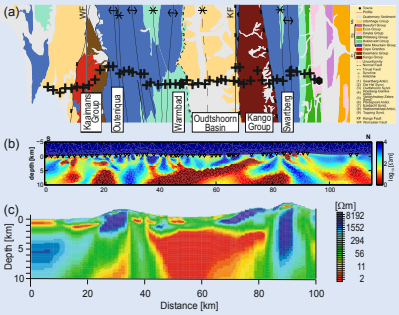

Figure 5
Comparison between (a) surface geology, (b) 2D isotropic inversion model (Mare2DEM) and (c) 2D isotropic inversion model (RLM2DI) [Weckmann et al., 2012]. Prominent conductors e.g. under the Oudtshoorn Basin are included in both inversions, but have different shapes. FE inversion shows more structures (overfitting?), but vertical anomalies seem to correlate with positions of syn- and anticlines and might image fluid pathways. Including topography in FE inversion was vital to improve data fit. While the FD inversion did not include structures outside the station coverage, 2 stations north of the profile had to be included an a-prioiri conductivity structure beneath fixed.

MT Data & fit

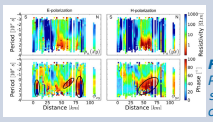

Figure 6
Pseudo-sections of TE and TM apparent resistivity and phase. Phases >90° (circled) are observed in the middle of the profile at periods >1s in both modes [Chen, 2012].

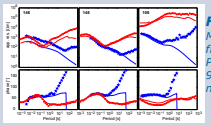

Figure 7
MT data & fit (lines); Phases > 90° could not be fit.

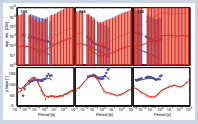

Figure 8
Data fit (lines) of the inversion after omitting data with phases >90°. The total rms improved, but phases approaching or higher than 90° usually correlate with decrasing resistivities. The apparent resistivites can be fitted, but not the phases approaching 90°.

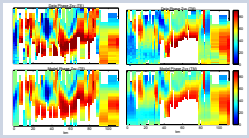

Figure 9
Pseudosections of observed and modelled TE and TM mode phases along the profile. White areas at long periods show omitted data due to phases >90°. Because of static shift, apparent resistivities were downwaited in the inversion and not shown here.Therefore only phases are presented, which could be explained well by the inversion model.

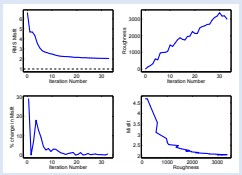

Figure 10
Development of total rms and roughness during the inversion run. While the rms does not change a lot after the 20th iteration the model includes more complex structures. The final iteration and „reasonable" inversion results have to be compared, to prevent overfitting of the data.

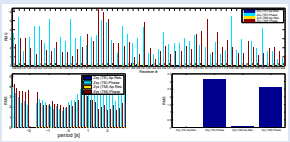

Figure 11
rms for each
- *station (in dependance of data type)*
- *period (in dependance of data type)*
- *data type*

Conclusions & References

- Mare2DEM works with land MT data.
- Only triaxial anisotropy --> phase values over 90° cannot be reproduced.
- Anisotropic inversion absorbes 3D effects
- topography has improved data fit
- Development of rms and roughness as indicator for overfitting
- General conductivity structure comparable to FD inversion, but shapes seem to be more detailed and complex.

Chen, X.: *Two-dimensional anisotropic inversion of magnetotelluric data, 2012*
Key, K.: *MARE2DEM: Tutorial and Training, Scripps Institution of Oceanography, UC San Diego, 2014*
Key, K., *Ovall, J.: A parallel goal-oriented adaptive finite element method for 2.5-D electromagnetic modelling, Geophysical Journal International, 2011*
Rodi, W., Mackie, R.: *Nonlinear conjugate gradients algorithm for 2-D magnetotelluric inversion, Geophysics, 2001, volume 66, No.1, S. 174-187*
Rulff, P.: *Vergleich isotroper und anisotroper 2-D Inversion (MARE2DEM) von magnetotellurischen Daten aus dem Cape Fold Belt, Südafrika, Bsc Thesis 2015*
Weckmann et al.: *Magnetotelluric image linked to surface geology across the Cape Fold Belt, South Africa, Terra Nova, 2012*

www.gfz-potsdam.de

HELMHOLTZ ASSOCIATION

Investigating sedimentary deposits in the East-African Rift Valley using Transient Electromagnetics

M. Seidel, P. Yogeshwar, B. Tezkan (Institute of Geophysics and Meteorology, University of Cologne, Germany)
Shimeles Fisseha (Institute of Geophysics, Space Science and Astronomy, University of Addis Ababa, Ethiopia)

CRC 806
Our way to Europe

Culture-Environment Interaction and Human Mobility in the Late Quaternary
Cluster A: Northeast Africa - Ways of Dispersal from the Centre of Origin

IGM Geophysik Köln

DFG Deutsche Forschungsgemeinschaft

Introduction

In the framework of the Collaborative Research Centre (CRC) 806 „Our way to Europe“, a 2D transient electromagnetic survey was conducted on three different sedimentary basins in southern and central Ethiopia. Combining geoscientific and archaeological methods, the CRC 806 is designed to reconstruct the passageway of Modern Man from eastern Africa to central Europe over the last 200,000 years. Geophysical measurements assist with the identification and definition of possible palaeoenvironmental archives such as sedimental deposits.

Survey Area

Three sedimentary basins within the East-African Rift System (EARS) have been investigated, see Fig. 1. Lake **Chew Bahir** ("Salty lake" in Amharic, approx. 500 m a.s.l.) is a 30 x 70 km² saline mudflat that episodically fills to a shallow lake during rainy season. According to airborne gravity and seismic reflection data, the thickness of its sedimentary deposits is assumed to be of several kilometers. Therefore, the basin potentially provides sedimentary archives that extend far beyond the Quaternary.
The source area of **Bisare River** is located within the Hobitcha Caldera near Wolaita Sodo in southern Ethiopia. Former sedimentological results indicate a continuous sedimentation process and Tephra layers.
The double crater system of the **Dendi Lakes** is located at Mount Dendi (3,270 m asl) 80 km west of Addis Ababa. First drillings revealed holocene deposits within the lake sediments. Our results indicate sediment thicknesses comprising quaternary sediments.

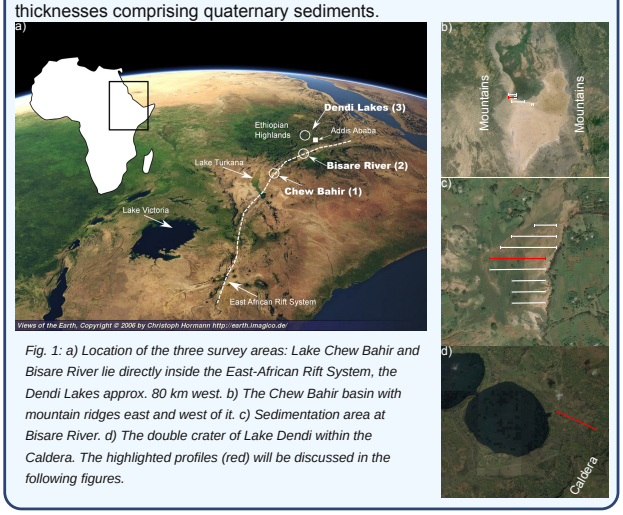

Fig. 1: a) Location of the three survey areas: Lake Chew Bahir and Bisare River lie directly inside the East-African Rift System, the Dendi Lakes approx. 80 km west. b) The Chew Bahir basin with mountain ridges east and west of it. c) Sedimentation area at Bisare River. d) The double crater of Lake Dendi within the Caldera. The highlighted profiles (red) will be discussed in the following figures.

Survey Description

In December 2014 and February 2015, a total of 125 2D transient electromagnetic measurements were conducted in the central-loop configuration utilizing 50 x 50 m² and 100 x 100 m² transmitter loops. TEM/3 induction coils from Zonge International served as receivers of the vertical and one horizontal component of the time derivative of the magnetic field. All profiles are located perpendicular to the boundary of each basin to investigate possible 2D effects from the surrounding mountain ridges or calderas. The vertical component is used for the estimation of sediment thicknesses and stratigraphic layers. The horizontal component will be used to study 2D effects generated by lateral resistivity variations.
At Bisare River and Lake Dendi, 4-point DC soundings were additionally taken to enhance the quality of the estimation of sediment thicknesses.

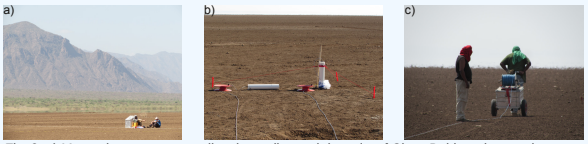

Fig. 2: a) Mountain range surrounding the sedimental deposits of Chew Bahir and transmitter station. b) Zonge TEM/3 receiver coils for the horizontal and vertical component of the magnetic field. c) Placement of a 100 x 100 m² transmitter loop.

Quasi-2D Results

Fig. 3 shows quasi-2D results of Chew Bahir profile P1, Bisare profile 3 and Lake Dendi profile P1 through the stitching together of the resulting 1D-models of the Marquardt inversions. The Chew Bahir profile (fig. 3a) starts on the western boundary of the basin, near the slope of the mountains see fig. 1b). Note that the resistivities vary between 0.3 and 1 Ωm which is due to the hypersalinity of the subsurface. No rock basement could be found. The same applies for profile P1 of Lake Dendi (fig. 3c). Only in the area of Bisare River, a rock basement may have been found (fig. 3b).

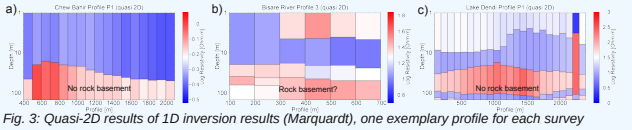

Fig. 3: Quasi-2D results of 1D inversion results (Marquardt), one exemplary profile for each survey location. a) Chew Bahir P1,b) Bisare River 3, c) Lake Dendi P1. The resistivities are displayed logarithmically.

Comparison: TEM, DC and Joint Inversion

For station F3 of Bisare profile 3, we recorded an additional DC sounding. Fig. 4 shows the measured data and the fitting of the inversion. The last 6 to 7 data points cleary indicate a deep resistive layer which we interprete as the rock basement. Fig. 5a shows the according 1D inversion result (Marquardt). Fig. 5b shows the 1D inversion results of the TEM data (Marquardt and Occam). Slight indications of a deep resistive layer can be seen but not as clear as in the DC results. The result of the joint inversion of TEM und DC data is displayed in fig. 5c. Here, the resistivity of the last layer is not as resistive as in the inversion result of the single DC inversion.

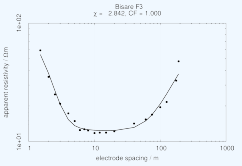

Fig. 4: Original DC data und fitting of Station F3 of Bisare River profile 3.

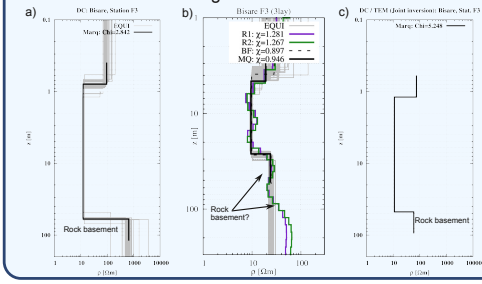

Fig. 5: Inversion results of Station F3, Bisare River profile 3. a) 1D inversion result of the DC measurement (Marquardt + equivalent models) . b) 1D inversion result of TEM (Marquardt, equivalents and Occam). c) 1D joint inversion result of DC and TEM (only Marquardt).

Horizontal component $\dot{H}_x$

With TEM, we recorded a horizontal component of the magnetic field for each station. Typically, we found one or more local minima in all transients (see fig. 6). Fig. 7 shows the time of the first local minimum (yellow), the time of the subsequent local maximum (green) and the respective magnitude of that maximum (purple) for each station of profile P1 in Chew Bahir. Station 4 is next to the mountains, station 20 towards the center of the basin.

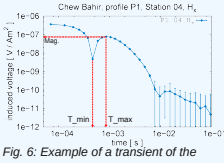

Fig. 6: Example of a transient of the horizontal component. T_min is the time of the first local minumum, T_max the time of the following local maximum.

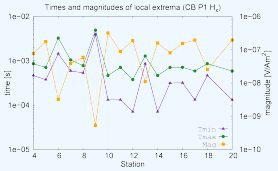

Fig. 7: Time of the first local minimum (yellow), the subsequent local maximum (green) and the magnitude of that maximum for the horizontal component of all stations of Chew Bahir profile P1.

Outlook

The horizontal components of the magnetic field will be subject to further investigations with respect to 2D effects of the surrounding and underlying bedrock. The results of the vertical component will be used to identify further suitable borehole locations for subsequent palaeoclimatological researches.

Acknowledgements

We thank the *Institute of Geophysics, Space Science and Astronomy (IGSSA)* of the University of Addis Ababa, Ethiopia, for the collaboration and the great assistance during our fieldwork.
We thank the *German Research Foundation* (Deutsche Forschungsgemeinschaft) for the funding of this project.

Analyzing Two-Dimensional Effects in Central Loop Transient Electromagnetic Data

Yogeshwar, P.[1]* & Tezkan, B.[1]

[1]Institute of Geophysics & Meteorology, University of Cologne, Germany, *yogeshwar@geo.uni-koeln.de

Abstract

Thick sedimentary sequences are deposited in the central area of the Azraq basin/Jordan consisting mostly of hyper-saline clay and various evaporates. These sediment successions form the 10 km × 10 km Azraq mudflat and are promising archives for a palaeoclimatical reconstruction within the Collaborative Research Centre 806 (CRC-806) entitled "Our Way to Europe" [1]. We utilized the central loop Transient Electromagnetic (TEM) method to identify the subsurface resistivity structure along two 7 km and 5 km long transects and, furthermore, to provide a basis for future drilling activities within the CRC-806 [5, 6].
The subsurface resistivity structure varies from around 50 Ωm on the basalt formation to around 0.3 Ωm inside the alluvial mudflat. Therefore, a 1D interpretation may not be adequate. Here we present the calculation of a semi-synthetic TEM Tipper to quantify a probable 2D effect. Although the horizontal component of the magnetic field was not measured in the field, it is possible to use the TEM Tipper to investigate if the derived subsurface model generates a 2D effect, which is e.g. larger than the data error-floor.

Survey area and TEM setup

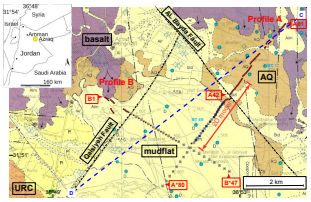

Fig. 1 : Geological map of the survey area in the central part of the Azraq area, Jordan [4].

A total of 150 TEM soundings were recorded with an inter-station distance of generally 50 m up to a maximum distance of 200 m and a transmitter loop size of either 50^2 m^2 or 100^2 m^2. The investigated profiles cross four geological formations (cf. Fig. 1 & 2(a)):

- AQ: Quaternary sediments.
- AOB: Basalt.
- ALM: (alluvial) mudflat sediments with hyper-saline shallow groundwater.
- URC: Chert limestone formation. Base layer below mudflat sediments.

Quasi 2D resistivity-depth sections

The 1D models along both profiles are stitched together as quasi 2D sections (cf. Fig. 2(b,c)). The derived resistivity depth section along profile A is in excellent agreement with the corresponding geological cross-section and the depth to uncertain geological boundaries (dashed lines in Fig. 2(a)) are well detected. Moreover the transition zone from fresh to saline groundwater is identified along both profiles resulting in a resistivity decrease from moderate to extremely low values. Around sounding A42 the Al Bayda Fault is expected. The resistivity structure exhibits maximal lateral variation in that zone. Therefore, the 1D interpretation may be inadequate and lead to miss-interpretations.

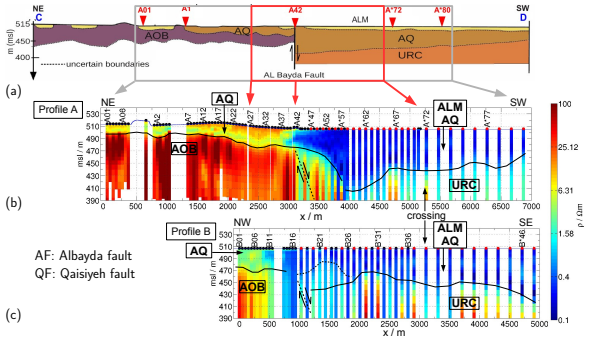

Fig. 2 : (a) Geological cross-section [4], which is representative for profile A. Quasi 2D resistivity-depth sections for (b) profile A and (c) profile B derived from the 1D Occam R1 models. The profile locations are shown on the map in Fig. 1.

Conclusions

- The 1D inversion results are consistent and in good agreement with the geology.
- Considering the derived 2D model, the semi-synthetic TEM-Tipper approach indicates that 8 soundings exhibit a 2D effect. Moreover, the zone where the 2D effect is maximal correlates partly with larger data residuals.
- The presented approach can be used to analyze if a 2D interpretation is required.
- The U_x-response is very sensitive to sensor placement and, therefore, difficult to measure.

Acknowledgements:
The project was funded by the German Research Foundation (DFG) and hosted in the frame of the CRC-806 'Our Way to Europe'. We thank all our colleagues from the Natural Resources Authority, Jordan for great support and hospitality during the field surveys.

References:
[1] CRC 806,. OUR WAY TO EUROPE. Culture-Environment Interaction and Human Mobility in the Late Quaternary. *Online: www.sfb806.uni-koeln.de*, 2012.
[2] Bedrosian, P. A., Burgess, M. K. and Nishikawa, T., Faulting and groundwater in a desert environment: constraining hydrogeology using time-domain electromagnetic data. *Near Surface Geophysics*, 11(11), 2013.
[3] Druskin, V. L. and Knizhnerman, L. A., Spectral approach to solving three-dimensional Maxwell's diffusion equations in the time and frequency domains. *Radioscience*, 29(4), 1994.
[4] Ibrahim, K.M., The Regional Geology of Al Azraq Area. *Hashemite Kingdom of Jordan, Geological Mapping Division, Natural Resources Authority, Bulletin*, 36, 1996.
[5] Yogeshwar et al., Investigation of the Azraq sedimentary basin, Jordan using integrated geoelectrical and electromagnetic techniques. *NSG*, 11, 2013.
[6] Yogeshwar, P., A resistivity-depth model of the central Azraq basin area, Jordan: 2D forward and inverse modeling of time domain electromagnetic data. *Ph.D. thesis, University of Cologne, Inst. of Geophysics and Meteorology*, 2014.

Analyzing 2D effects in synthetic TEM data

Although the 1D interpretation of TEM field data has proven its feasibility in various case studies, data may be 2D affected for certain subsurface situations. The 1D inversion of such data can lead to significant miss-interpretations (cf. Fig. 4).
In order to quantify if a certain model generates a 2D effect in TEM data, we calculate a TEM-Tipper from the ratio of the horizontal and vertical induced voltage components: $T_U = U_x/U_z$ (cf. Fig. 3(c,d)). As a cross-check for the TEM-Tipper approach we compare it to the relative difference calculation between the 2D model and a 1D background model response: R-diff $= \frac{U_{ind}^{2D} - U_{ind}^{1D}}{U_{ind}^{2D}} \times 100$ (cf. Fig. 3(b), [2]). Both approaches yield comparable results and allow to quantify which soundings and transient times are influenced by a 2D effect. The maximum 2D response is directly on the contact zone. The TEM-tipper approach is convenient, as it does not require to construct a 1D background model, which is rather complicated for realistic 2D models.

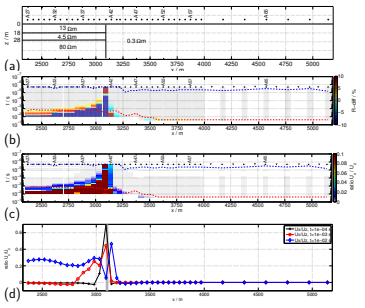

Fig. 3 : (a) 2D model with vertical contact zone at sounding A41. (b) Relative difference calculated from the 2D response and 1D background model response. (c) Tem tipper $T_U = U_x/U_z$. (d) T_U for three distinct time points.

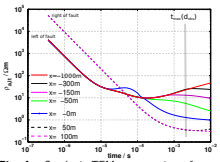

Fig. 4 : Synthetic TEM $\rho_{a,U}$ transients for several distances from vertical contact zone.

Analyzing 2D effects in TEM field data

The application of the above presented TEM-Tipper approach to the field data is straight forward. Herewith it is possible to quantify which soundings and transient times are 2D affected, although only U_z was measured in the field. We conclude the following:

- Good global fitting for 2D model with $\chi = 1.47$ (cf. Fig. 3(a)).
- Larger residuals partly between sounding A34 and A59. This zone correlates with the lateral conductivity change (cf. Fig. 3(a) and (b)).
- Significant 2D effect between sounding A35 and A42 (cf. Fig. 3(c) and (d)). In that zone also larger residuals are present. At sounding A37 the 2D effect is maximal and occurs earliest.
- U_x response strongly depends on Rx-location and is difficult to measure (cf. Fig. 6).

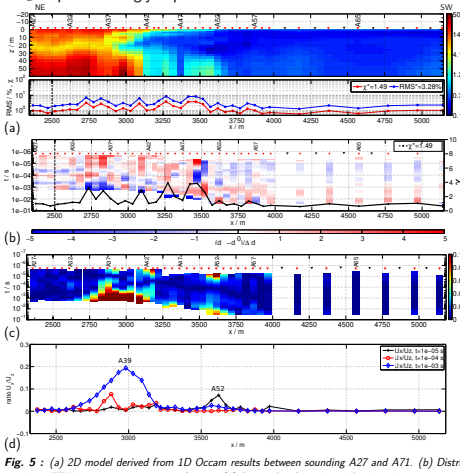

1D stitched models between sounding A27 and A71

2D data fitting of 1D stitched models (relative difference)

Semi-synthetic TEM-Tipper $T_U = \frac{U_{x,synt}}{U_{z,obs}}$

Semi-synthetic TEM-Tipper for distinct transient times

Fig. 5 : (a) 2D model derived from 1D Occam results between sounding A27 and A71. (b) Distribution of residuals. (c) Semi synthetic TEM-tipper $T_U = U_{x,synthetic}/U_{z,obs}$. (d) Ratio of U_x/U_z plotted for three distinct time points along the profile line.

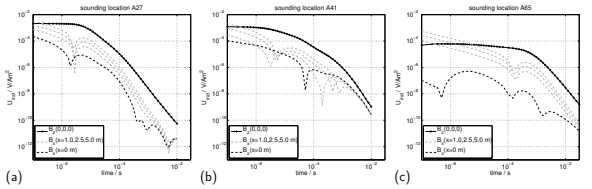

Fig. 6 : Synthetic induced voltage response U_z and U_x for sounding locations A27, A41 and A65. Additionally U_x is plotted as gray dashed lines for 1.0, 2.5 and 5.0 m offset to the center of the transmitter.

Contact: yogeshwar@geo.uni-koeln.de, www.geomet.uni-koeln.de

Sonderbeitrag von Volker Haak zum Thema „Johann von Lamont and his magnetotelluric experiments in 1862", vorgetragen auf dem 22nd EM Induction workshop in Weimar, 2014.

Johann von Lamont and his magnetotelluric experiment in 1862

Volker Haak, Blankenfelde

SUMMARY

Earth currents were first observed in the middle of the 19th century, closely related to magnetic field variations. Particularly the magnetic storms of 1859, which belong to the strongest ones ever experienced, destroying telegraphic constructions in the USA, Europe and Australia, made Johann von Lamont start with experiments about the nature and origin of earth currents. Among these experiments he presented for the first time a method to calculate the thickness of a high conductivity layer in southern Germany.

Keywords: earth-electric current, magnetic storms, Lamont

INTRODUCTION

The geophysical sounding method “magnetotellurics” was formulated and published by Louis Cagniard in 1953, in particular in Western Europe. Later on it became known that even before in 1950 A.N. Tikhonov published an equivalent theory in Eastern Europe, in Russian. Both were henceforth appreciated as the discoverers of magnetotellurics. However, a few years ago we could read that a Japanese author, M.H.Hiramaya, published an equivalent theory already in 1934.

Quite recently the question came up somewhere in the MT community whether Johann von Lamont could have been the very first who “invented” the magnetotelluric method. He actually published in 1862 a book about earth currents. There he describes an experiment to measure electrical currents in the earth and the corresponding magnetic field. He then uses the ratio of the amplitudes to calculate the depth range of the sediments beneath his geomagnetic observatory close to the capital of Bavaria, now known as Fürstenfeldbruck (FUR). It appears thus clearly as a magnetotelluric experiment and Lamont as a pioneer of that geophysical method.

This remarkable historical event fell completely in oblivion till K.-P.Sengpiel mentionend this experiment and the surprising result in his dissertation at the University in Munich in 1968, however without discussing any detail of that work. In 1991 a special issue of the “Münchener Geophysikalische Abhandlungen (Munich Geophysical Treatises)” in honour of the 150th birthday of the observatory a number of contributions appeared, also to honour the founder of this geomagnetic observatory, Johann von Lamont in 1840. One of the contributions was written by Gustav Angenheister, the former director of the institute and observatory, about those experiments to discover the unknown nature of earth currents.

Johann von Lamont was at his lifetime a well-known and appreciated scientist. His name and his merits in experimental discovery of the magnetic field of the Earth are well known up to the present. He was member in almost all scientific academies in Europe; he was professor at the Munich University, director of the astronomical and geomagnetic observatory. And he was ennobled by the Bavarian King Ludwig the 2nd. Mares on the planet Mars and on our Moon bear his name.

Lamont’s scientific interests were very broad, in particular in astronomy. Among them, for a few years, the study of the origin of electrical currents in the Earth which received global attention with a magnetic storm on 1st September 1859 which destroyed telegraphic constructions worldwide. Already in October of that year he installed several experiments in his observatory and started observations one month later. In 1862 he published the experiments already in a book (Lamont, 1862).

This book is actually a comprehensive final report on a research project of only 2 years with the aim to identify the nature of the Earth currents. On pages 32-38 Lamont describes an experiment to measure electrical currents at the Earth's surface and develops a mathematical algorithm to calculate their depth range which we now interpret as the depth range of well conducting sediments.

In this contribution I will try to reformulate the mathematical and physical deduction of Lamont, both in the original as well as in modern terminologies. Reading and understanding texts from earlier centuries, written in their national languages, the wording and the style, of that time, is a difficult piece of work, possibly subjected to ambiguous interpretations.

Additionally, the formulation of physics relations in a rather archaic state of knowledge as here of EM, in particular before James Clark Maxwell cannot be translated in modern terms at all.

The knowledge and understanding of the origin and effects of electrical currents were still at its very beginning in that time not much more than 60 years after Luigi Galvani and Alessandro Volta in Italy discovered the first electrical phenomena on frogs. Still at the time of Lamont electrical currents were due to electrochemical (galvanic) or thermoelectrical origin, induction currents just started their career. The idea of Lamont was that earth currents are either one these three types or a completely new type of electrical current. This was the aim of this research project where the following "magnetotelluric" experiment only plays a minor role.

THE EXPERIMENT

The construction and the properties of the instruments for measuring the magnetic fields and the electric currents occupy a large part of the book. Lamont was a very gifted maker of instruments. It is startling, however, that none of these instruments were calibrated in any unit other than the number of scale divisions of the deflection of the needles: the most basic unit.

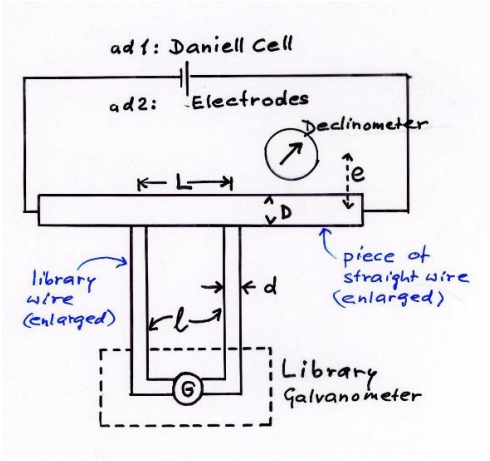

Following Lamont, we will use the original terminology g for current intensity, instead of the modern expression current density j. Lamont measures the earth current intensity with two buried iron plates (0.98x0.79 m²) about 100 m apart, connected by a copper wire. The current is the product of current intensity and cross section of the wire, resistance the product of a resistivity (which never appears since it will always cancel out) and length divided by the cross section of the wire. The electric current flows from the electrode plates through the wire and the galvanometer, its strength is designated as N, i.e.:

$$N = g\,B\,H \qquad (1)$$

with N the number of divisions taken from the galvanometer, B = breadth (width) and H = height of the electrode-plates.

Lamont's primary aim was to determine the depth of origin of the currents. He introduced a simple model of a plate with thickness k on top of the region in which this current was flowing. To solve the problem mathematically, he applied the method of Biot-Savart.

The result was

$$Y' = 2\pi g\,k \qquad (2)$$

The equation looks familiar as it resembles the gravity formula for the corresponding Bouguer-plate, with g as mass density and k as thickness of the plate. The factor 2π may be due to a unity system which, however, is never mentioned and does not play a role here because this relation will appear finally only in ratios of different depths k such that this factor cancels out.

The declinometer indicates the according magnetic field Y' as a deflection of the needle

$$\Delta\delta = \frac{2\pi g k}{X}$$ (3) with X as the restoring force of the magnetic needle.

k could not be calculated since $\Delta\delta$, g and X were unknown. Therefore he set up the experiment in two steps:

> A long straight wire is suspended parallel to the magnetic meridian above the ground and a current of strength I is fed in with a battery. The needle of the declinometer will be deflected by "m" divisions and the galvanometer connected in a by-pass circuit is deflected by " m' " divisions. If the battery is disconnected, the current flow is underground from the electrode plates. While the galvanometer shows no change, the declinometer will now also indicate the magnetic field from the underground layer of depth k according to Equation 2.

The mathematical formulation of both parts of the experiment is:

Ad 1. The magnetic field of a current through the long straight wire, measured at a distance e perpendicular to it, is:

$$\delta Y = \frac{1}{2}\frac{D^2\pi}{e}\, g \;\{= \frac{2I}{e}\}$$ (4)

D is the cross section of the long wire. The term in curly brackets {} is added to show Biot-Savart's law in the modern customary expression for comparison.

δY is acting perpendicular to X, the horizontal magnetic field strength, which serves as the restoring force on the magnetic needle

$$m = \frac{D^2\pi g}{2e\,X}\;\{= \frac{2I}{eX}\}$$ (5)

To determine the current through the galvanometer Lamont attached the galvanometer with two clips c and d (terminals) somewhere towards the middle of the long straight wire. The length of the shorter of both pieces c-d is L with cross section D, the longer piece of the wire (indeed reaching until the library of the observatory where the galvanometer was installed) is l with the cross-section d.

The resistance of the short piece is thus:

$$R_{short} = \frac{L}{(D/2)^2\pi}$$ (6)

The resistivity of the wires will cancel out in the following since the material is always copper.

For the longer "library" segment, we yield:

$$R_{long} = \frac{l}{(d/2)^2\pi}$$ (7) The current through the galvanometer circuit will approximately be equal to the current though the long straight wire multiplied by the ratio of the resistances of the short wire and the long wire. Instead of writing the current strength I, the deflection in number of divisions on the scale is given by (in curly brackets again the modern expression):

$$m' = \{I\,\frac{R_{short}}{R_{long}+R_{short}} \approx I\,\frac{R_{short}}{R_{long}}\} =$$

$$(D/2)^2\pi g\,\frac{L}{(D/2)^2\pi}\,\frac{(d/2)^2\pi}{l} =$$

$$\frac{1}{4}\,d^2\pi\,\frac{L}{l}\,g$$ (8)

Ad 2: According to Equation 2 the deflection of the declinometer needle is:

$$N = \frac{2\pi g H}{X} \qquad (9)$$

for a layer with thickness H (the electrode depth range) and

$$\hat{N} = \frac{2\pi g k}{X} \quad \text{for a layer with thickness k} \qquad (10)$$

From Equation 5 we take g

$$g = \frac{2mXe}{D^2\pi} \qquad (11)$$ and insert it into Equation 9

$$N = \frac{2\pi H}{X}\,\frac{2mXe}{D^2\pi} = \frac{4mHe}{D^2} \qquad (12)$$

The current flows from the electrode plates through the galvanometer

$$N' = gBH \qquad (13)$$

B and H specify the dimensions of the electrode plates.

The current density g is now expressed by the current density causing the battery driven deflection m' in Equation 8:

$$g = 4m'\,\frac{l}{L}\,\frac{1}{d^2\pi}$$ and inserted in (13): (14)

$$N' = 4m'\,\frac{BHl}{\pi d^2 L} \qquad (15)$$

Now Lamont uses these observables as defined in Equations 9, 10 and 15 in pairs of impedance-like (E/H) combinations:

$$p = \frac{N'}{N} = \frac{BHl}{\pi d^2 L}\,\frac{D^2}{4mHe} = \frac{m'BD^2 l}{md^2 Le} \qquad (16)$$

And for the "layer of thickness k":

$$f = \frac{N'}{\hat{N}} = \frac{4m'BHl}{\pi d^2 L}\,\frac{D^2}{4mke} = \frac{m'BD^2 l}{m\pi d^2 Le}\,\frac{H}{k} = p\,\frac{H}{k} \qquad (17)$$

RESULT

N' and $\hat{N}$ are the observed deflections of the declinometer and the galvanometer in scale-divisions. Lamont reports that he observed on 17th September 1861 exactly the same deflections on both scales, such that f = 1.0. p can then be calculated from the experimental set-up which consist only of length measures in Bavarian Foot bf (1 bf = 0.2920 m),
L = 5.0 bf,
l = 272.7 bf,
H = 3.35 bf,

B = 2.69 bf,
e = 1.9bf ,
m = 8.17,
m' = 83.57,
D^2/d^2 = 5.407 (by weighing of equally long pieces of both types of wire).
Using these values, with Equation 16 yields p = 1360.
The experiment was repeated several times, the final mean value was p = 1483.
The thickness of the electric current layer, and thus of the conductive subsurface layer can be calculated using Equation 17:
k = p H = 4968 bf = 1450 m.
The geomagnetic observatory at that time 1861 was built on the sedimentary Molasse basin. The depth of the sedimentary sequences beneath the observatory as determined by seismological experiments and by drilling 100 years later is close to the value determined by Lamont.

DISCUSSION

Lamont himself mentioned aspects which could influence his results:

Current concentration: From his own experiments he knew that the currents, flowing primarily straight and parallel to each other, will concentrate towards the electrodes. His calculations did not consider this concentration effect and he therefore assumed that this neglect may be a sensitive source of an inaccurate result. The concentration effect should be determined experimentally but was not pursued further.
The current density may differ in all earth layers due to different conductivities. He discussed some solutions which, however, will not be discussed here.

A question not really answered by Lamont was whether the observation of f = 1.0 was mere coincidence or on purpose. In a footmark he remarked that the wire to the galvanometer was extended by a piece of 133.3 bf, up to 272.7 bf. This changed the resistance R_{long} and thus the factor p: It is likely that Lamont adjusted this part of the experimental set-up to yield f = 1.0. This arrangement was at least one of the means of observing accurately two simultaneous and independent variables in one experiment at a time when recording techniques not yet existed.

The derivation of Lamont's Formula by the Thin Sheet approximation of Waits recursion algorithm:

The model of a low resistive layer with the conductivity σ_1 and the thickness d upon the substratum of lower conductivity σ_2 is indeed very convenient for the applied method: Starting with C at the upper surface of the second layer $C_2 = 1/K_2$, it follows

$$C_1 = \frac{1}{K_1}\frac{K_1/K_2 + \tanh(K_1 d)}{1 + K_1/K_2 \tanh(K_1 d)} \approx$$

$$\frac{1}{K_1}\frac{K_1/K_2 + K_1 d}{1 + K_1^2/K_2 d} =$$

$$\frac{1/K_2 + d}{1 + K_1^2/K_2 d} = \frac{\frac{1}{K_2}}{\frac{K_2 + K_1^2 d}{K_2}} = \frac{1}{K_2 + K_1^2 d} \approx$$

$$\frac{1}{K_1^2 d} = \frac{1}{i\omega\mu_0\sigma d}$$

with $K_n = \sqrt{i\omega\sigma_n \mu_0} = \frac{1+i}{p_n}$ p = depth of penetration

$C_1 = \frac{E}{i\omega B} = \frac{E}{i\omega\mu_0 H}$, and $j = \sigma_1 E$,

we get $\frac{E}{H} = i\omega\mu_0 C_1 = \frac{1}{\sigma_1 d}$, thus $\frac{j}{H} = \frac{1}{d}$

This is the relation which Lamont used instead of the traditional E/H relation in magnetotellurics – of course without the knowledge of this derivation.

I will demonstrate these relations with a simple numerical model as in the case discussed here. We consider a layer of 30 Ohm m and 1500 m above a basement of 10000 Ohm m, in a period range 0.1 to 10000 sec. The result shown in Fig.2 displays clearly the thin sheet approximation with the almost 45° rise and the vanishing phase. The calculation of the thickness of that upper layer is in that period range almost independent of the periods. All this shows that Lamont was a fortunate scientist.

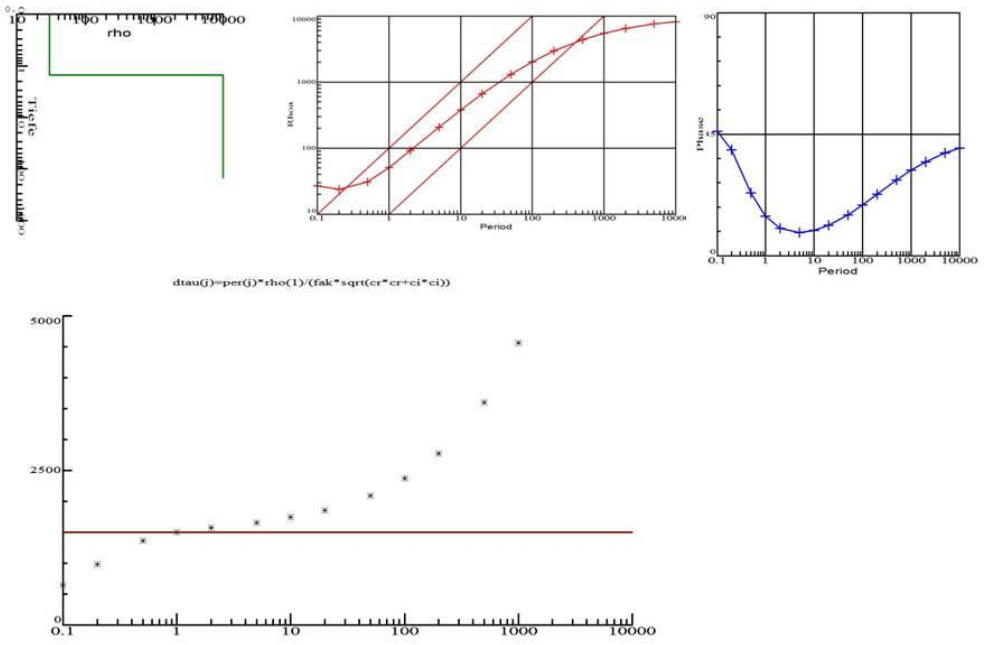

G. Angenheister also discussed whether Lamont's result could be seriously considered as a real achievement. He did not take up his detailed derivation of the mathematical and physical formula. Instead he took up the critical though qualitative remarks of Lamont, which in particular considered the intensity of concentration of the current lines towards the electrodes and the calculation of the current density, by taking the total current and the dimensions of the electrode plates into account. He concludes that the result (the 1450 m) is just accidental and could have been any number.

It may be a philosophical problem: there are only 3 quantities: j, H, d. If H and d are correct, why should and can j be wrong? Probably Lamont's and Angenheister's doubts are not justified so firmly. In each case, Angenheister's final remark holds still true: This experiment was probably the first one to investigate the subsurface with electromagnetic methods.

CONCLUSION

Forgotten and vanished names of pioneers of science are not rare; the reasons for it are numerous. One reason may be after a century or even more the style of their quaint writing is hard to understand. This problem came up when the scientific language of communication changed from classical Latin which remained unchanged since the time of Cicero to the different national languages. The classical Latin could be understood over the centuries and everywhere. It is interesting that Galvani has still written his most important work "De Viribus Electricitatis Artificialias in Motu Musculari" 1791 in Latin (W. Stroh 2007). Lamont was writing in German in the style and wording of the mid 19th century. German language has changed over these 150 years, and nobody would describe a simple geoelectric experiment as Lamont has done it. This was indeed the difficulty in reading and understanding the text, which required sometimes a break of days to even weeks and months to understand and then to proceed. The almost forlorn and forgotten pioneers of MT, A.N.Tikhonov and M. Hirayama have written in their national languages, i.e. Russian and Japanese. L. Cagniard however published in English, not in his native language French.

Lamont did not only write in a time dependent national language, but he considered also only a small part of the MT method, i.e. its thin sheet approximation. One could now argue that also Cagniard considered only a small part of the MT method, i.e. the 1D version. But the deciding aspect of Cagniard, Tikhonov and Hirayama was that they constructed a solution on the full induction problem.

If we could ask Lamont himself today whether he would feel as the first man who did magnetotellurics he would probably disagree. He was a strong character and – following his book about earth currents - was amused, sometimes disgusted by colleagues who believed in more than they could measure. It is not unlikely that Lamont would have been sceptical about the equations introduced some years later by James Clerk Maxwell, even though he was native Scotsman like him.

Final remark: Lamont did this experiment to find out about the nature and origin of the earth currents. He discussed the reasons to discard the currents of galvanic type, then the currents of thermoelectric type and to our surprise also the currents of induction type. For this latter type he even performed an experiment, which he described briefly in a footnote. The mistake was that he did not consider the small induction number of the experimental setup which of course was not yet invented before Maxwell's theory. Therefore he proposed an interesting philosophy on the true nature of the earth currents: Since it was for more than 100 years known that the earth globe is negatively charged (with 5.9×10^5, Erich von Kilinski, 1958), there should exist a negatively charged fluidum more or less close to the earth's surface. The problem left was to find out how to move this electric negative fluidum such that the observed electrical currents appear. He left this problem unsolved.

ACKNOWLEDGEMENT

Martin Beblo, the seventh successor of Johann von Lamont at the Geomagnetic Observatory of the Ludwig-Maximilians-University of Munich, now located near Fürstenfeldbruck, made the copy of the original book available for this study. I am very grateful for this.

REFERENCES

Angenheister, Gustav (1991) Die Beobachtungen des Erdstromes von Johann von Lamont in den Jahren 1856 – 1862, Münchener Geophysikalische Abhandlungen (M.Beblo, H.Soffel, eds), 25-30.

Cagniard, Louis (1953) Basic Theory on the Magnetotelluric Method of Geophysical Prospecting. Geophysics 18, 605-635

Hirayama, M. (1934) On the relations between the variations of the Earth potential gradient and terrestrial magnetism., J. Meteorol.Soc.Jpn. (in Japanese)

Kilinski, Erich von (1958) Lehrbuch der Luftelektrizität. Leipzig, Akademische Verlagsgesellschaft.

Lamont, Johann von (1862) Der Erdstrom und der Zusammenhang desselben mit dem Magnetismus der Erde. Leipzig, Leopold Voss,74 pages.

Sengpiel, K.-P. (1968) Das induzierte erdelektrische Feld im Süddeutschen Alpenvorland und seine Abhängigkeit vom Untergrund, untersucht mit neuen Methoden der Auswertung und Interpretation. Diss.Naturw.Fak.Univ. München

Stroh, Wilfried (2007) Latein ist tot, es lebe Latein. Kleine Geschichte einer grossen Sprache. Seite 239.-List-Ullsteinverlag

A.N.Tikhonov (1950) On determining electrical characteristics of the deep layers of the Earth's crust. Dokl. Akad. Nauk. SSSR, 73, 295-297

The original publication

The experiments of Johann von Lamont in 1861 with E and H

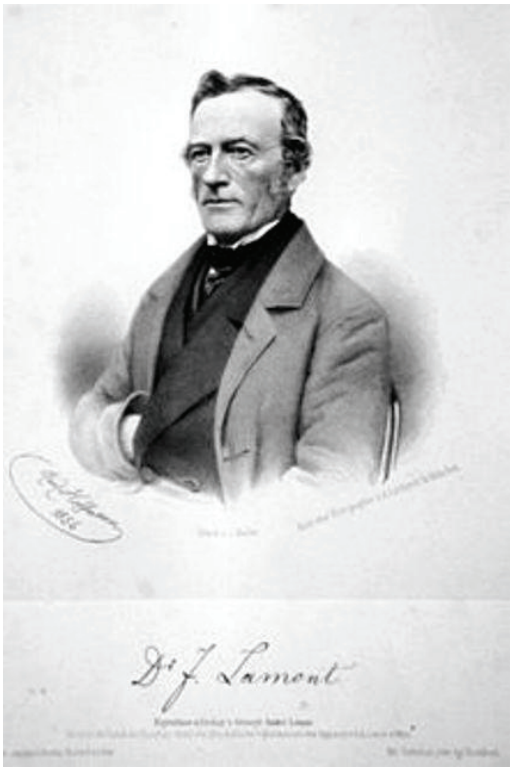

The 19th century in culture and science

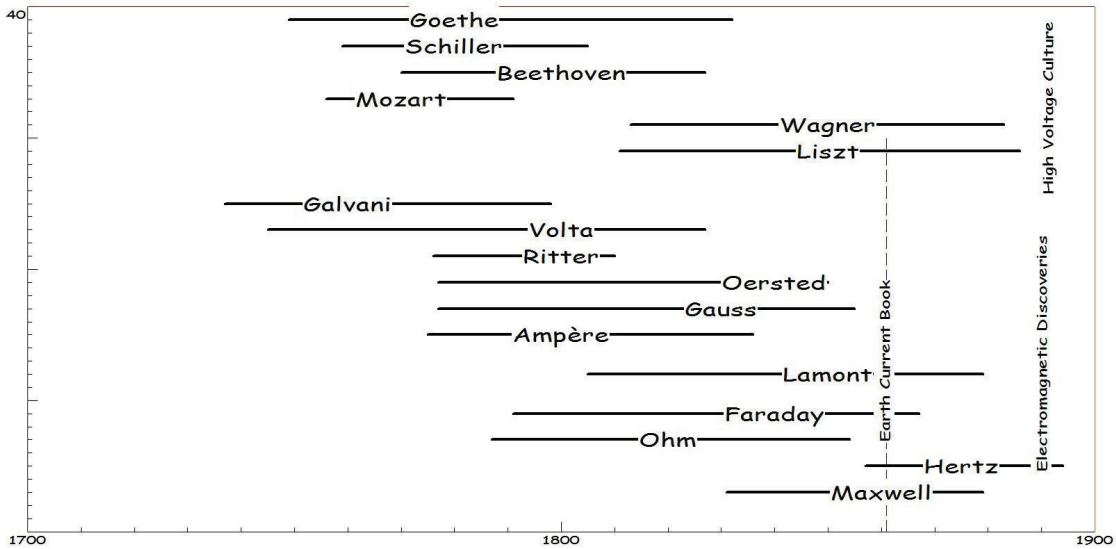

A demonstration of „old“ and „modern“

If you see this

$$f = \frac{j_y}{H_x} = \frac{1}{\Delta z}$$

It seems rather clear to us what it will say. However if you see this

$$f = \frac{N'}{\hat{N}} = \frac{4m'BHl}{\pi d^2 L}\frac{D^2}{4mke} = \frac{m'BD^2l}{m\pi d^2 Le}\frac{H}{k} = p\frac{H}{k} \qquad (17)$$

at least it needs a longer explanation in order to understand that it means the same, in Lamont‘s formulation.

The life of John Lamont and Johann von Lamont

Born 1805 in Corriemulzie, Scotland as John Lamont

After the death of his father he was sent at the age of 12 by the family to the catholic priest school in Regensburg in Bavaria.
Studied German, Latin, Greek, Hebrew, French, but liked much more mathematics and physics.

After school he went to Munich, Bogenhausen, to the astronomic institute

In 1830 promotion, 1833 director of the Astronomic institute, till his death in 1879.
In 1840 he convinced the king Ludwig I to finance a new Geomagnetic Observatory. This has moved later to Fürstenfeldbruck.
In 1853 professor of astronomy at the university of Munich.
He was nobled to Johann von Lamont by king Ludwig II.

Two Mare are named after him, one on the Moon, the other on Mars and one Street in Munich.
He never returned to Scotland. He is buried about 500 m from his observatories, where he lived and worked for 51 year


Blick von Oberföhring auf München. Lenbachhaus, München
Church of Bogenhausen
Ernst Kaiser,1835/40


St. Georgs Kirche, Bogenhause/München


Johann von Lamont, Bogenhausener Friedhof